

Processing and interpretation of reflection seismic data from Isfjorden, Svalbard

Master of Science thesis

Linea Ågesen



Department of Earth Science

University of Bergen

June 2021

Abstract

In august 2002, four 2D multichannel reflection seismic lines were acquired in the inner Isfjorden and Sassenfjorden, Svalbard. The study area has a complex history affecting the evolution of the North Atlantic. The area has been subjected to repeated orogenic events in the pre-Caledonian period, transcurrent, contractional and extensional faulting from the Caledonian to Devonian, Carboniferous and Jurassic rifting, and contractional reactivation during the Cenozoic era. Intense deformation, uplift and erosion during the Cenozoic era have resulted in large-scale deformational structures, in addition to an abnormally hard seabed with P-wave velocities estimated to over 4.5 km/s.

This thesis presents processing and interpretation of the four seismic lines. First, the data were processed focusing on attenuating the strong water layer multiples in order to optimize the image of the subsurface. The processed data were then interpreted with regard to the stratigraphic units and structural features, in order to obtain a good understanding of the geological features, which have affected the subsurface in the study area.

The water layer multiples were challenging to remove due to the hard and shallow seabed, causing the multiples to become very strong and repeat at short intervals. Several velocity filters in the f_k -domain and surface predictive deconvolution were utilized to remove most of the multiple energy. The remaining energy were attenuated through pre-stack migration, mute and stacking.

Stratigraphic units from the seabed to Hecla Hoek were interpreted. Some very high amplitudes in the Late Carboniferous to lowermost Jurassic successions were interpreted as dolerite intrusions. The fault geometry in the BFZ were interpreted as a supra-detachment basin, which formed as a result of crustal scale extension related to the Caledonian orogenic collapse. The fault zone is dominated by steep normal faults that root in the detachment. Hecla Hoek is dominated by steep normal faults that are likely to be a part of a bigger fault-bounded rift basin that characterises the basement on Svalbard.

Acknowledgements

I would like to use this opportunity to thank and express my gratitude towards those who have supported and helped me during the course of this master thesis!

First and foremost, I would like to thank my supervisor Rolf Mjelde (UiB) for his supervision, support and helpful insight through the past years. You have been open and available for questions, in addition to devoting a lot of time to me and my thesis. I would like to thank my co-supervisor Bent Ole Ruud (UiB) for his guidance and immense help during the data processing. You have provided a lot of helpful insight and are always available for questions.

Further, I would like to thank my fellow students and friends that I have met over the years for your all the good times, your patient, encouragement, and motivation. I would also like to thank my family, friends and boyfriend for listening during times of frustration and for all the support and encouraging words.

Thank you!

Linea Ågesen

Bergen, June 2021

Innholdsfortegnelse

1 INTRODUCTION	1
1.1 STUDY AREA	1
1.2 SEISMIC DATA	1
1.3 AIM OF STUDY	3
2 GEOLOGICAL FRAMEWORK	4
2.1 TECTONIC SETTING	4
2.2 GEOLOGICAL HISTORY	8
2.2.1 <i>Precambrian</i>	8
2.2.2 <i>Paleozoic</i>	8
2.2.3 <i>Mesozoic</i>	11
2.2.4 <i>Cenozoic</i>	13
2.3 DEFORMATION STRUCTURES	15
2.4 STRATIGRAPHY	21
2.4.1 <i>Hecla Hoek</i>	22
2.4.2 <i>Devonian</i>	22
2.4.3 <i>Billefjorden Group</i>	22
2.4.4 <i>Gipsdalen Group</i>	22
2.4.5 <i>Tempelfjorden Group</i>	23
2.4.6 <i>Sassendalen Group</i>	23
2.4.7 <i>Kapp Toscana Group</i>	23
2.4.8 <i>Adventdalen Group</i>	23
2.4.9 <i>Van Mijenfjorden Group</i>	24
3 METHODS	25
3.1 SEISMIC REFLECTION DATA ACQUISITION	25
3.1.1 <i>Source</i>	28
3.1.2 <i>Receiver</i>	30
3.2 SEISMIC PROCESSING	31
3.2.1 <i>Editing</i>	31
3.2.2 <i>CMP sorting</i>	32
3.2.3 <i>Amplitude recovery</i>	32
3.2.4 <i>Frequency filtering</i>	33
3.2.5 <i>Deconvolution (inverse filtering)</i>	34
3.2.6 <i>Velocity filtering</i>	35
3.2.7 <i>Static correction</i>	36
3.2.8 <i>Velocity analysis</i>	36
3.2.9 <i>NMO correction</i>	37
3.2.10 <i>Muting</i>	38
3.2.11 <i>Stacking</i>	38
3.2.12 <i>Migration</i>	39
3.3 SEISMIC INTERPRETATION	41
3.3.1 <i>Structural analysis</i>	44
3.3.2 <i>Stratigraphic analysis</i>	45
3.3.3 <i>Seismic resolution</i>	46
4 DATA ACQUISITION	49

5 PROCESSING	56
5.1 SOFTWARE – GEOCLUSTER.....	56
5.1.1 Xjob	56
5.1.2 Teamview	56
5.1.3 GeoVel	57
5.1.4 Xps.....	57
5.2 PROCESSING SEQUENCE.....	57
5.2.1 Editing	61
5.2.2 Filtering and deconvolution	64
5.2.3 Static correction	68
5.2.4 Velocity model.....	69
5.2.5 Velocity analysis.....	69
5.2.6 Stacking.....	72
5.2.7 Migration.....	73
5.2.8 Muting with stack	75
5.2.9 Converting to SEG-Y format.....	77
6 INTERPRETATION	83
6.1 SOFTWARE – PETREL	83
6.2 BASIS FOR THE INTERPRETATION	84
6.2.1 Previous studies in the area	84
6.2.2 Seismostratigraphic framework.....	85
6.2.3 Data quality	87
6.3 STRATIGRAPHIC INTERPRETATION.....	90
6.3.1 Seabed.....	94
6.3.2 Reflection R.....	94
6.3.3 Top Permian.....	95
6.3.4 Top mid Carboniferous	96
6.3.5 Top Hecla Hoek	97
6.3.6 Stratigraphic units.....	98
6.4 STRUCTURAL INTERPRETATION	107
6.4.1 Fault structures in BFZ.....	108
6.4.2 Stratigraphy in BFZ.....	108
6.4.3 Structures in Hecla Hoek.....	112
7 DISCUSSION	114
7.1. PROCESSING.....	114
7.2 INTERPRETATION	116
7.2.1 Stratigraphic units.....	116
7.2.2 Stratigraphy and structures in BFZ.....	119
7.2.2 Stratigraphy and structures in Hecla Hoek	128
7.2.4 Other observations.....	131
8 CONCLUSION	134
8.1 PROCESSING.....	134
8.2 INTERPRETATION	135
REFERENCES	137
APPENDIX A	142
APPENDIX B	154

Abbreviations

AI – acoustic impedance

BFZ – Billefjorden Fault Zone

BP – band-pass filter

BR – band-reject filter

CDP – common depthpoint

CMP – common midpoint

CSP – common shotpoint

CTB - Central Tertiary Basin

HFC – Hornsund Fault Complex

HP – high-pass filter

LAFZ - Lomfjorden-Agardhbukta Fault Zone

LP – low-pass filter

NMO – normal moveout

RC – reflection coefficient

RMS – root mean square

TWT – two-way traveltime

WSFTB – West Spitsbergen Fold-and-Thrust Belt

Chapter 1

Introduction

1.1 Study area

Svalbard is a highly glaciated and mountainous archipelago that is located between 74-81 °N and 10-35 °E. It is situated on the north-western corner of the Eurasian continental shelf between the Barents Sea, North Atlantic and Arctic oceans (Dallmann, 2015). Svalbard consists of several large and smaller islands, some of the larger ones are Spitsbergen, Nordaustlandet, Barentsøya and Edgeøya. The archipelago provides a unique insight to the geological evolution from Precambrian to today (Hjelle, 1993).

During the evolution of the Arctic and North Atlantic oceans, tectonic forces caused the uplift of the archipelago. The uplift is the reason why the archipelago is exposed today (Dallmann, 2015). Svalbard is the only exposed area in the Barents Sea, hence field observations and studies on the archipelago can be used as an analogue to the offshore subsurface areas. While Svalbard was uplifted and exposed because of tectonic forces, the surface morphology was shaped by ice movements during the Pleistocene glaciations along with on-going Arctic weathering (Dallmann, 2015).

1.2 Seismic data

The study area is located in the inner Isfjorden and Sassenfjorden (Fig. 1.1). Several 2D multichannel reflection seismic lines were acquired as a part of the student course SVALEX in august 2002 (Mjelde, 2003), where four of these lines have been used in this study; line 2, line 11, line 12 and line 15 (Fig. 1.1C).

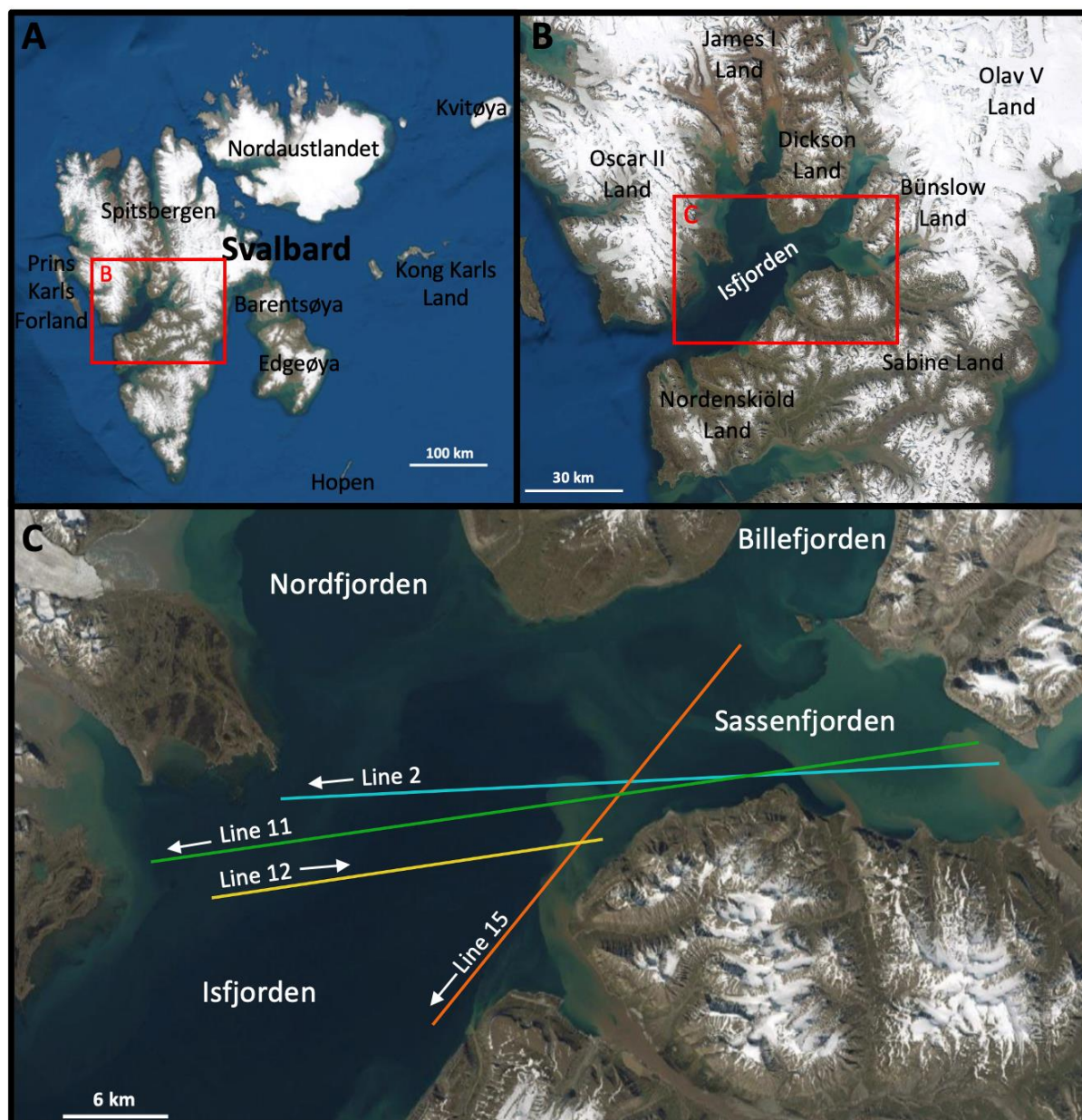


Figure 1.1: The maps illustrate the study area on Svalbard. A shows an overview of the main part of the archipelago. B shows a closer overview of Isfjorden and the land areas around. C shows the approximate location of the four lines that have been used in this study. The arrows point the direction the lines were shot in.

1.3 Aim of study

The intense deformation and uplift during the Cenozoic era have contributed to making the seabed in Isfjorden very hard, which in return cause extremely high velocities at the seabed. These factors cause strong water layer multiples that dominate the seismic data. The goal during the processing will be to find the processing sequence that provide the best possible image of the subsurface. The main focus will thus be aimed at effectively attenuate or remove the water layer multiples, without significantly affecting the quality of the data. After the processing is done, the lines will be used to interpret the subsurface geological features in the area. It will be important to map the stratigraphic units and the structural features that are present in the seismic sections to obtain a good understanding of the subsurface. Several studies have previously been conducted in the area and will be important as background for this study.

This study will provide a better understanding of the subsurface geology in the inner Isfjorden and Sassenfjorden area. It will be particularly important to map the stratigraphic units and fault structures in the basement and Billefjorden Fault Zone. The processing will contribute to give a better understanding of the challenges related to water layer multiples in marine seismic data, and how such data should be treated to provide the best possible image of the subsurface.

Chapter 2

Geological framework

This chapter describes the geological framework of Svalbard, which includes the present-day tectonic setting, the geological history, deformation structures and the stratigraphy of the study area. The chapter will provide a deeper understanding of the different processes that have affected Svalbard, where the different sections provide the basis for the complex geology seen on the archipelago today.

2.1 Tectonic setting

Svalbard is located at the north-western corner of the Barents Sea Shelf (Fig. 2.2.1). In contrast to the rest of the shelf, the archipelago is exposed. The uplift and exposure of the land areas happened as late as the late Mesozoic and Cenozoic era (Dallmann, 1999; Dallmann, 2015), thus making Svalbard an excellent site to study the geological record of the Barents Sea Shelf. The record ranges from Archean to Recent age. The Barents Sea Shelf cover an area of about 1 300 000 km², making it one of the most extensive continental shelf seas in the world. Svalbard's land areas cover less than 5% of the total Barents Sea area (Worsley, 2008; Dallmann, 2015).

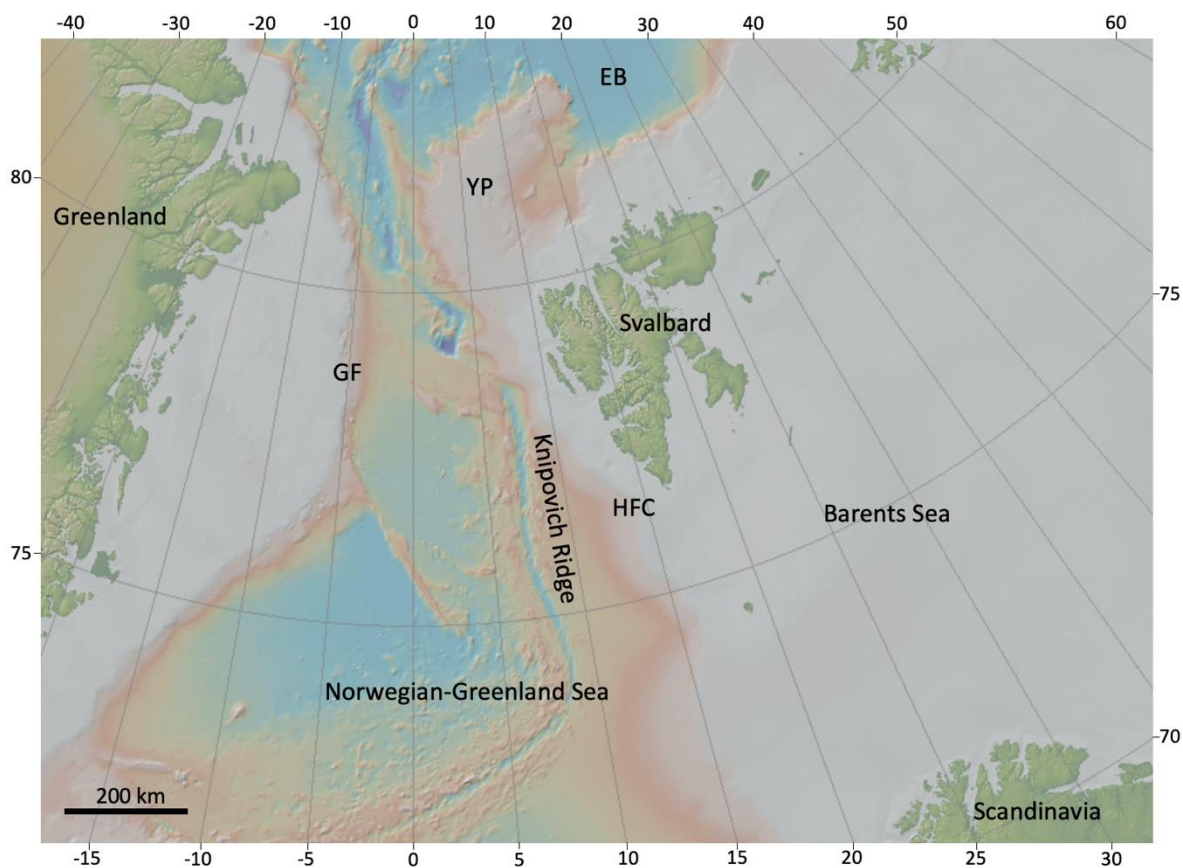


Figure 2.1.1: The figure shows a bathymetric map of the North Atlantic, modified from NOAA. The map shows areas around Svalbard; Eurasia Basin (EB), Yermak Plateau (YP), Knipovich Ridge, Greenland Fracture Zone (GF) and Hornsund Fault Complex (HFC).

Offshore to the west the main island, Spitsbergen, is separated from the Knipovich Ridge by a 40-80 km wide shelf (Fig. 2.1.1). The Knipovich Ridge is an oceanic spreading ridge which is segmented by a few transform faults. These transform faults includes the Spitsbergen Fracture Zone in the north and the Greenland Fracture Zone in the south (Dallmann, 1999; Dallmann, 2015). The Yermak Plateau is located northwest of Svalbard and is bordered by the shelf. The eastern part of the plateau is volcanic and is thought to be derived from a hotspot during Cretaceous (Dallmann, 2015). About 50-100 km north of the shore of Svalbard, a steep passive continental margin forms the boundary with the Eurasian Basin in the Arctic Ocean. The Eurasian Basin developed when the continental transform fault system, the De Geer Fault and Greenland Fracture Zone, tectonically separated Svalbard from Greenland (Dallmann, 1999; Faleide et al., 2008; Dallmann, 2015). This happened as a response to the start of seafloor spreading in the North Atlantic and Arctic oceans. Today the De Geer Fault is a part of the Hornsund Fault Complex.

The Barents Sea Shelf between Svalbard and Fennoscandia south of the archipelago is a platform area. During the formation of the North Atlantic Ocean, influence of transform faulting and crustal extension formed structural basins and highs in this platform area (Dallmann, 2015). Two large rotated downfaulted blocks dominate a zone with crustal thinning on the shelf area between Sørkapp and Bjørnøya (Faleide et al., 2008). The bathymetric features around Svalbard show a seafloor that is strongly influenced by seafloor spreading, dynamics of past ice sheets, varying stability of continental slopes, action of water currents, and leakage of fluids from the sub-seafloor (Dallmann, 2015).

Svalbard is strongly influenced by the West Spitsbergen Fold-and-Thrust Belt (WSFTB). The fold belt is located on the western part of Spitsbergen and extends from Kongsfjorden in the north to Sørkapp in the south. The WSFTB consists of a western thick-skinned zone and an eastern thin-skinned zone (Dallmann, 2015). Isfjorden crosses central parts of the WSFTB. This is the largest fjord on Spitsbergen and is oriented in an east-west direction. The fjords in Svalbard are predominantly oriented in an east-west or south-north direction, reflecting the main drainage directions of past glaciations. Fjords with a south-north orientation are generally parallel to large fault systems, while fjords that are oriented east-west seem to be controlled by strike-slip systems (Blinova et al., 2009; Dallmann, 2015).

Most of the fault zones on Svalbard are old and have been reactivated several times during various geological periods (Dallmann, 2015). These fault zones strike approximately N-S to NNW-SSE and vary from being dominated by dip-slip to strike-slip movements. In addition to characterising the geology of Svalbard (Fig. 2.1.2), the fault zones are also responsible for the distribution of depositional areas across the archipelago (Dallmann, 2015). Apart from the Western Spitsbergen Fold-and-Thrust Belt, the Hornsund Fault Complex (HFC), Billefjorden Fault Zone (BFZ), and Lomfjorden-Agardhbukta Fault Zone (LAFZ) dominate. These dominantly dip-slip to strike-slip fault systems have gone through several reactivations.



Figure 2.1.2: The figure shows the bedrock geology of Svalbard with associated major fault systems, modified from Dallmann (2015). Lomfjorden-Agardhbukta Fault Zone (LAFZ), Billefjorden Fault Zone (BFZ), Hornsund Fault Complex (HFC), Central Spitsbergen Basin (CSB), Western Spitsbergen Fold-and-Thrust Belt (WSFTB).

2.2 Geological history

2.2.1 Precambrian

The oldest and most altered rocks on Svalbard is the basement rocks, often referred to as Hekla Hoek. The basement originated during the pre-Caledonian period from middle Hadean to Silurian, and has gone through a complex geological evolution with repeated orogenic events. The oldest rocks found on Svalbard date back to the Late Archean age and are zircon grains found in rocks that contain other minerals that show younger ages (Worsley, 1986; Dallmann, 2015). A possible explanation for this can be that these old rocks have been metamorphosed during several orogenic events, causing the rocks to partly rejuvenate. The youngest Proterozoic strata are tillite beds. These beds formed as moraines, glaciofluvial deposits and drop deposits under cold periods with glaciations from melting icebergs (Hjelle, 1993).

2.2.2 Paleozoic

The Cambrian-Ordovician succession, predominantly consisting of carbonate rocks, overly the Neoproterozoic tillites (Dallmann, 2015). The change in lithology marks a change in the climatic conditions as the tillites formed under a cold period with glaciations, and the carbonates under warm to tropical climatic conditions. By the end of the Ordovician period persistent cooling led to widespread glaciations of the supercontinent Gondwana, which lasted into the Early Silurian. Warm temperatures were again established during the Silurian period (Dallmann, 2015).

During the Early Ordovician to Early Devonian a mountain range the size of today's Himalaya, the Caledonian mountain range, formed. The two continents Laurentia and Baltica, as well as minor continental plates collided, resulting in the closing of the Iapetus Ocean. In the collision zone the continental crust thickened, rocks were compressed, folded and partly metamorphosed. The mountain belt can be distinguished by the large thrust systems that have been displaced several hundreds of kilometres (Hjelle, 1993; Dallmann, 2015). Figure 2.2.1 shows how the Caledonides was affected by strike-slip faults towards the end of the orogeny. The Caledonian Orogeny affected all rocks of pre-Devonian age in Svalbard. The

collision and horizontal convergence was followed by orogenic collapse, extension and the formation of the Devonian depositional basin (Dallmann, 2015).

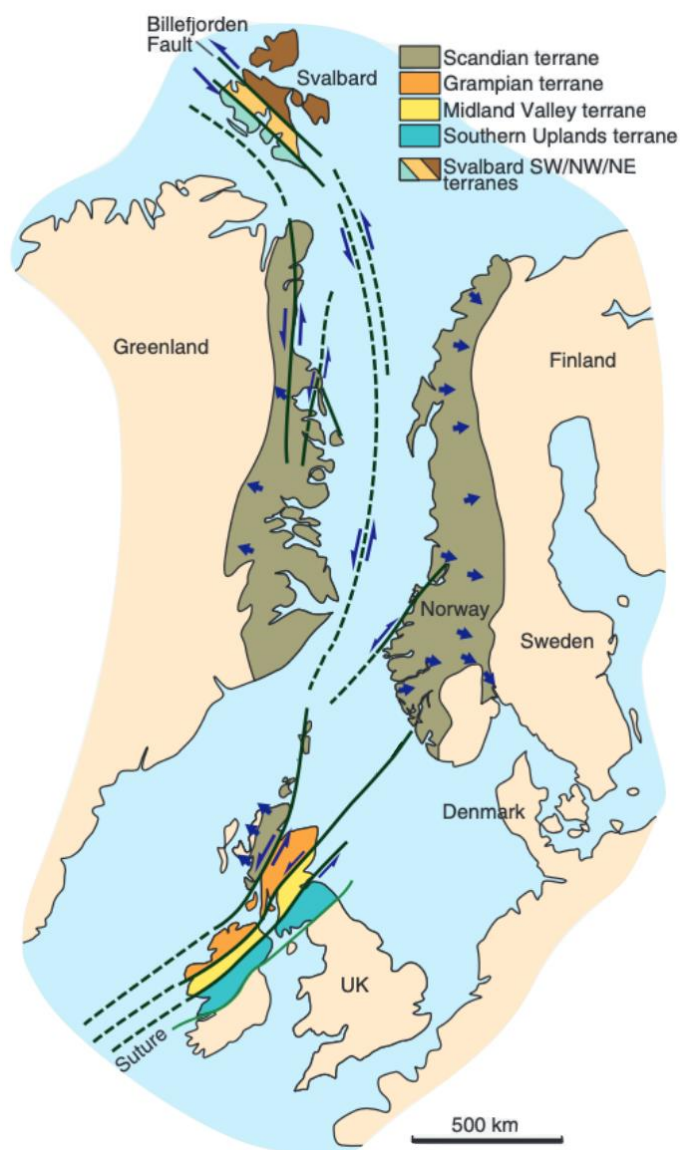


Figure 2.2.1: The figure shows a simplified map of the North Atlantic Caledonides, modified from Fossen (2010). The Caledonides was affected by large-scale strike-slip movements towards the end of the orogeny. The Billefjorden Fault Zone are one of many faults that was involved in the displacement.

The regime change from compression to extension was followed by a prolonged period of weathering and denudation during the Devonian period. The eroded material accumulated in fault-bounded rift basins, including enormous amounts of molasse fill from the surrounding mountains. A common term for the Devonian terrestrial bedrock is Old Red Sandstone, which accumulated in the rift troughs. The siliciclastic sediments reflects dry, desert-like depositional

environments (Worsley, 1986; Piepjohn and Dallmann, 2014; Dallmann, 2015). During the Devonian period Svalbard drifted from about 5°N to 20°N, experiencing a hot, arid to semi-arid climate marked by seasonal, monsoon-like precipitation. These extreme conditions caused the mountains to quickly wear down. In the Late Devonian a new phase of tectonic activity, Svalbardian Event, caused the folding and faulting of the previously deposited Devonian rocks (Worsley, 1986; Dallmann, 2015).

The warm and humid climate from the Devonian period continued into the Early Carboniferous before it shifted to become drier by the end of Early Carboniferous. Svalbard drifted from about 20°N at the beginning of the period to about 35°N at the end. This northward migration and change in geological, climatic, and environmental setting are reflected in the varying sedimentary bedrocks. Active rifting and extension started around the end of Early Carboniferous, where rift valleys subsided along major, pre-existing fault zones, leading to the formation of horst-graben structures (Dallmann, 2015). Most of Svalbard's land areas were gradually submerged during Late Carboniferous because of a major marine transgression caused by globally rising sea levels. This submergence caused the terrestrial sediments to gradually become replaced by marginal marine deposits. By Moscovian times most of the remaining highs were flooded and the active rifting had ceased (Hjelle, 1993; Dallmann, 2015).

During the Permian period, Svalbard was located at the northern margin of Pangaea, whose consolidation was complete by the end of the period (Fig. 2.2.2A). Svalbard drifted from about 30°N to 45°N during the period and formed part of a broad, epicontinental shelf sea, called the Franklinian Shelf, comprising a series of shallow platforms and deeper basins. The fundamental climatic, environmental and palaeoceanographic changes during the period resulted in a highly varied depositional environment (Hjelle, 1993; Dallmann, 2015). The land areas became exposed again at the beginning of the Permian period due to a long-term sea-level fall. This emergence of Svalbard caused associated weathering and erosion of exposed deposits, resulting in a major hiatus in the Artinskian. The end of the Permian period and the Paleozoic era is marked by the most devastating mass extinction in Earth's history, making the transition into the Mesozoic Era (Dallmann, 2015).

2.2.3 Mesozoic

While the Paleozoic climate was characterised by hot equatorial to subtropical conditions, the Triassic period represented a change in the climate to dry and temperate conditions (Dallmann, 2015). The change in climatic conditions resulted in a drastic lithological change. The depositional area during the period was a large shelf sea, an embayment bordered in the south, southwest and northwest. This large depositional basin was totally filled with sediments during the Triassic. During the period, Svalbard was relatively tectonically stable (Dallmann, 2015).

During the transition to the Jurassic period, the Triassic dry to temperate climate shifted to a humid, warm climate, with the possible existence of minor polar ice sheets. The present distribution of tectonic plates is a consequence of the Early to Late Jurassic break-up of the supercontinent Pangaea, which was complete by the end of the Late Jurassic (Fig. 2.2.2B; Dallmann, 2015). The reorganisation of the continental plates during the period resulted in numerous sea-level changes. In the Middle Jurassic the uplift of Svalbard and several internal basin highs in the Barents Sea resulted in a relative sea level fall. A swarm of generally north-south striking continental rifts were created from the Middle Jurassic until the Late Jurassic due to intensified crustal extension with some associated volcanism. These continental rifts were part of the Arctic-North Atlantic rift system, where rift basins formed on either side of the North Atlantic margins (Dallmann, 2015). Dolerite intrusions from the latest Jurassic through the Early Cretaceous was the first sign of the opening of the Arctic and North Atlantic oceans, as well as the continental break-up between Europe and Greenland (Dallmann, 1999; Senger et al., 2013). The dolerite intrusions most commonly occur as sills in Carboniferous through Jurassic strata.

Svalbard was situated in the northern boreal region between 60°N and 70°N in Early Cretaceous, and had a warm and humid climate. During the period, the former supercontinent Laurasia started to break apart (Fig. 2.2.2C). This break-up led to the formation of the North Atlantic Ocean, which joined with the South Atlantic Ocean during the Late Cretaceous. The massive volcanic activity related to the early phase of seafloor spreading made the period the warmest in Earth's history (Worsley, 1986; Dallmann, 2015). The volcanic activity also caused a high eustatic sea level by displacing seawater and increasing its volume, this caused the sea

level to increase to more than 250 m above present levels. Uplift and intense erosion in the Arctic region created a hiatus, where the entire Upper Cretaceous strata is lacking on Svalbard (Dallmann, 1999, 2015).

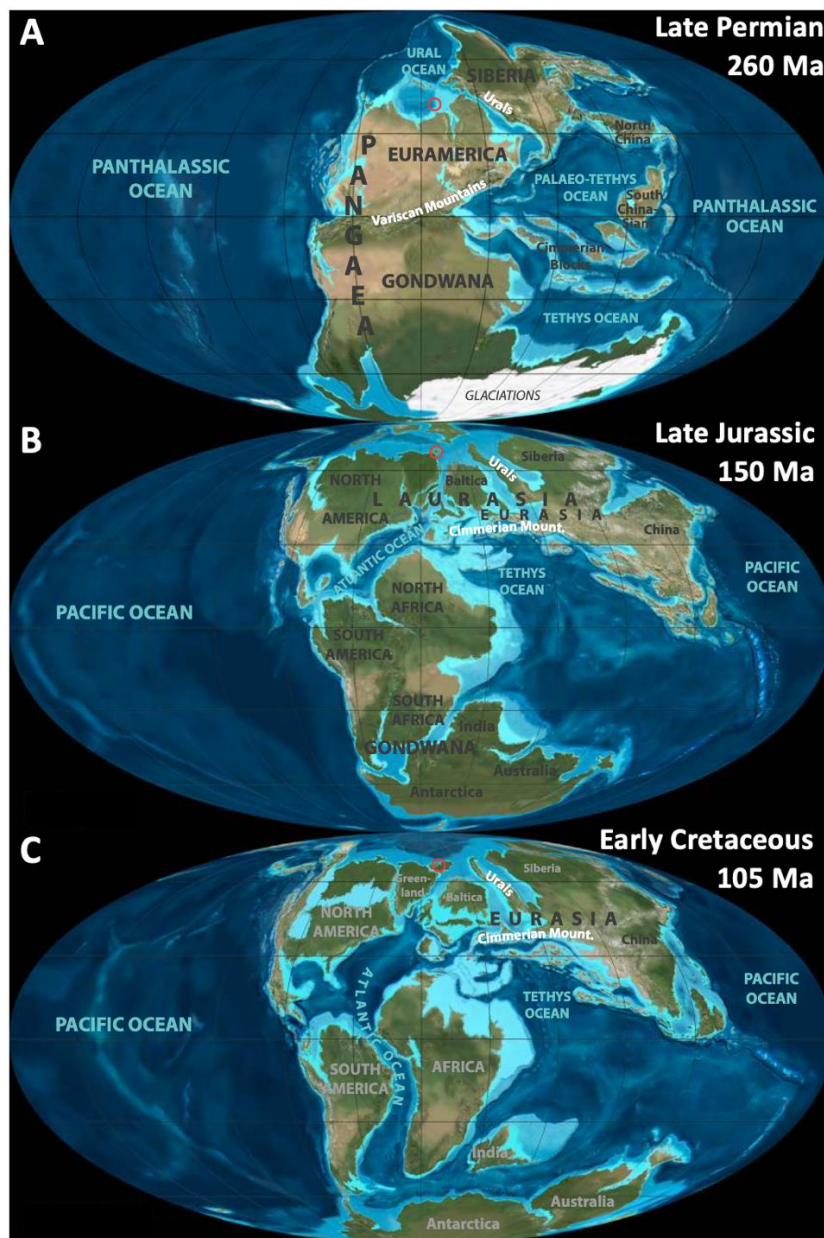


Figure 2.2.2: The figure illustrates the global palaeogeography at three separate times; Late Permian (A), Late Jurassic (B), Early Cretaceous (C). Svalbard is marked by the red circle. A) The consolidation of Pangaea was complete by the end of the Permian period, where Svalbard was located at the northern margin of the supercontinent. B) Break-up of Pangaea from Early to Late Jurassic. C) The former supercontinent Laurasia started to break apart, which led to the formation of the North Atlantic Ocean. At this time the North Atlantic was a continental rift, which broke up at ~53 Ma. Modified from Dallmann (2015).

2.2.4 Cenozoic

The warm and humid climatic conditions from the Cretaceous period gradually became cooler and drier during the Paleogene period. The evolution of the North Atlantic and Arctic oceans dominated the plate tectonics in Paleogene, eventually forming the connection between the two oceans and thereby separating Svalbard from Greenland (Fig. 2.2.3; Dallmann, 2015). The continued rifting in the Labrador Sea and Baffin Bay during the Paleocene epoch caused north-eastward movement of Greenland along the Wegener Fault Zone against the Barents Shelf. These movements caused the development of a major depression known as the Central Tertiary Basin (CTB). The sedimentation in the CTB started in the early Paleocene and probably went into the Oligocene. As the rifting gradually increased in the North Atlantic during the Paleocene, the rift motion in the Labrador Sea decreased (Worsley, 1986; Dallmann, 2015).

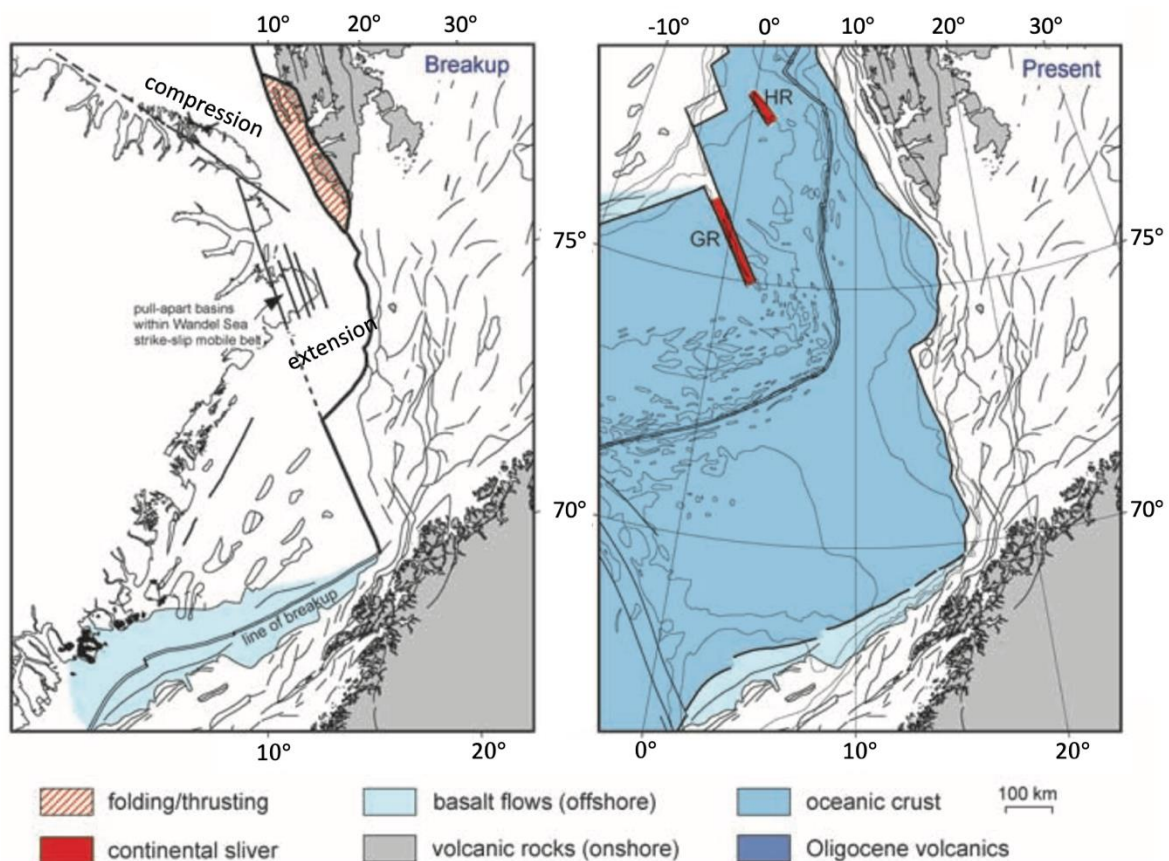


Figure 2.2.3: The figure illustrates the Cenozoic plate tectonic evolution of the Norwegian-Greenland Sea. Greenland Ridge (GR), Hovgård Ridge (HR), modified from Faleide et al. (2008). The figure to the left shows the evolution at the time of the break-up, where both extensional and compressional forces affected the area. The figure to the right shows how the evolution has reached today, where the sea-floor spreading continued and resulted in Svalbard moving farther away from Greenland.

In the early Eocene continuous plate motion led to the formation of the Eureka Fold Belt which formed when Greenland slid past Svalbard, which in Svalbard often is referred to as the Western Spitsbergen Fold-and-Thrust Belt (Faleide et al., 2008; Dallmann, 2015). During Eocene the WSFTB was uplifted and served as the main sediment source as the sediment transport changed from northeast to west into the CTB. The HFC started as a major continental transform fault and cut off the last continental bridge between Eurasia and Greenland-North America by the end of Eocene. The plate tectonic motion changed by about 25° NNW-SSW to WNW-ESE when the continental connection broke. The HFC suddenly experienced extension with depositional basins developing alongside with sediments from late Eocene to Oligocene age (Faleide et al., 2008; Dallmann, 2015).

The sea-floor spreading in the North Atlantic and Arctic oceans continued throughout the Neogene and Quaternary, causing Svalbard and the Barents Shelf to move farther away from Greenland (Fig. 2.2.3). While transform faults developed in the Fram Strait, the continental margin to the west of Spitsbergen and Prins Karls Forland kept broadening by rifting and accumulation of clastic sediments (Dallmann, 2015). Svalbard's landscape was dominated by erosion and denudation during the Neogene period, with the WSFTB developing an erosional relief and eastern parts of Svalbard forming low-relief plateaus or peneplains. This Neogene peneplain is slightly inclined to the north, which possibly happened during the Neogene after the extrusion of the Miocene lavas (Dallmann, 2015). The north-western parts of Svalbard experienced volcanism during Miocene and Pleistocene, where the volcanism was related to the presence of a hotspot under the Yermak and Morris Jesup plateaus (Dallmann, 2015).

The climatic cooling trend continued through the Neogene when the land bridge between North and South America emerged during the Pliocene epoch and prevented warm Pacific waters from entering the Atlantic Ocean. This event resulted in the formation of ice caps at the poles, in addition to a series of continental glaciations that started in Quaternary (Dallmann, 2015). Today, these series of continental glaciations are better known as the Ice Age. The previous ice caps played a large role in sculpting the landscape on Svalbard, where glaciers and rivers are still shaping it (Hjelle, 1993).

2.3 Deformation structures

This part will describe the deformation structures that occur in contractional and extensional regimes. In the contractional regime tectonic forces cause the convergence of plate boundaries and collisional orogens. These movements cause deformational structures as a consequence of shortening and thickening of the crust. In extensional regimes the tectonic forces cause the divergence of plate boundaries leading to extensional deformation structures. These movements cause the extension and thinning of the crust. When these two regimes are combined, they can lead to the formation of extremely complex structures (Van Der Pluijm and Marshak, 2004; Fossen, 2010).

Deformational structures record the permanent change in shape that occur in natural rocks as a response to the forces that act on the bodies (Van Der Pluijm and Marshak, 2004). The deformational changes can include distortion, translation and rotation. Both brittle and ductile deformation is nonrecoverable, which means that the deformational changes remain when the forces that act on the bodies are removed (Van Der Pluijm and Marshak, 2004). The differences between the two is that for brittle deformation the rock breaks, while for ductile deformation the rock does not break. In this sense faulting is brittle deformation whereas folding is ductile deformation.

Extensional faults are commonly normal faults, but can be other fault types as long as the reference layer gets extended (Van Der Pluijm and Marshak, 2004). Extensional faults are commonly estimated to initiate at dips around 60° , and yet, both high- and low-angle extensional faults are common (Fossen, 2010). The easiest explanation for this is that the rock could be affected by earlier phases of deformation (Fossen, 2010). Thereby, high-angle normal faults can represent reactivated joints or strike-slip faults, and low-angle normal faults can represent reactivated thrust faults. At the same time, both high- and low-angle extensional faults can form without pre-existing weak structures (Fossen, 2010). Rotation on normal faults can lead to the formation of several deformational structures, as rollover anticlines and synclines, and the formation of horst-graben structures (Fig. 2.3.1; Van Der Pluijm and Marshak, 2004).

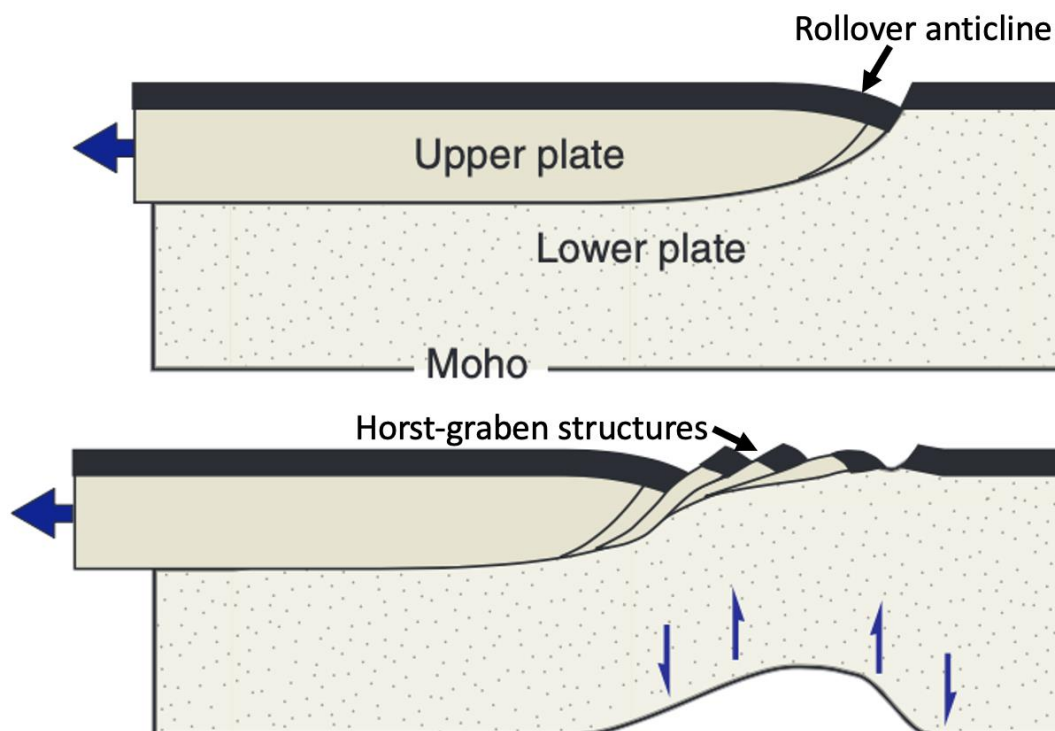


Figure 2.3.1: The figure illustrates the principle of the fault rotation model, modified from Fossen (2010). Listric normal faults form in the upper crust and flatten along a weak detachment zone. After a certain amount of extension, new faults form in the hanging wall. The arrow points to the related formation of a rollover anticline and horst-graben structures.

In an extensional regime the formation of a rift can be either active or passive. In an active rifting model the rifting is caused by hot mantle material or mantle plumes that rise in the asthenosphere creating a dome (Fossen, 2010). The dome is affected by tensile stresses and eventually cause the formation of a rift. In a passive rifting model the rifting is caused by plate tectonic stresses, and tend to form along zones in the lithosphere that have already been exposed to weakness (Fossen, 2010).

Extension can also occur in conjunction with orogens and orogenic collapse (Fig. 2.3.2). In the early stages of a collision, extension can occur as a result of back-arc rifting as well as stretching of the upper part of the down-going slab in a subduction zone (Fossen, 2010). Extension can also occur during the later stages when the orogenic wedge becomes unstable and causes the formation of extensional faults and shear zones (Fossen, 2010). The orogenic collapse can also be gravity driven. When the crust becomes too weak, potentially due to heating, or too thick to support its own weight, it will collapse along extensional faults and shear zones (Fossen, 2010).

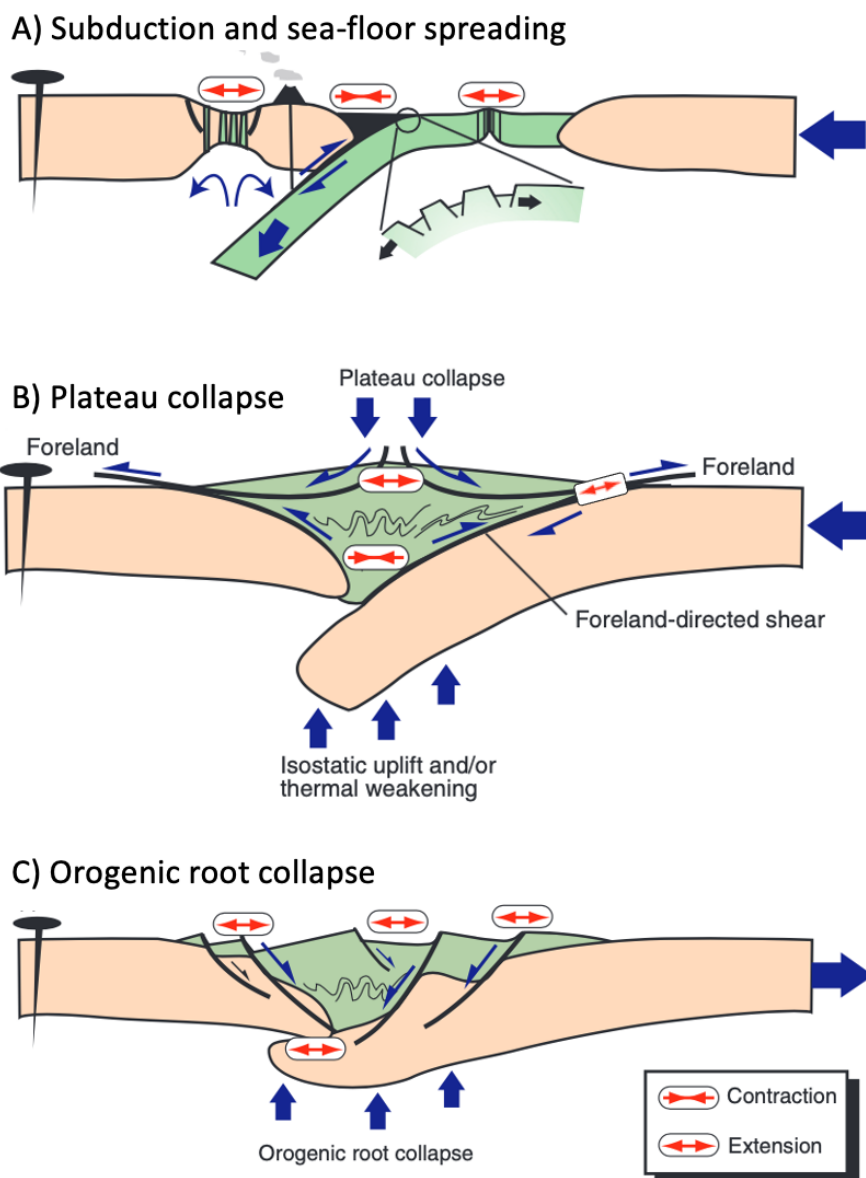


Figure 2.3.2: The figure illustrates how extension can occur in conjunction with the formation of orogens and orogenic collapse. A illustrates how subduction zones have extension in the back-arc basin and down-going slab. B illustrates how extension occurs during a plateau collapse, where the subduction slab is exposed to extension. C illustrates extension related to orogenic root collapse. Modified from Fossen (2010).

Contractional faults are primarily reverse faults and thrust faults, but can also be other fault types as long as the reference layer gets shortened. In contrast to reverse faults, thrust faults have large displacements and form at angles below 30° (Fossen, 2010). The thrust fault can cause the stratigraphy to change by displacing older rocks on top of younger ones. A thrust separates the substrate from an overlying thrust sheet, where a thrust sheet is a rock unit that

has been transported several kilometres or more on a thrust fault (Fossen, 2010; Dallmann, 2015). The sole thrust can also be referred to as a detachment, or *décollement*, and separates the thrust sheets from the basement (Fossen, 2010). Detachments tend to form in weaker rock types like shale or evaporite (Van Der Pluijm and Marshak, 2004). The term detachment is also used to describe low-angle extensional faults.

Contractional faults typically form imbrication zones (Fig. 2.3.3), where the complete structure when bounded by a roof thrust is called a duplex structure (Fossen, 2010). The duplex consists of horses that are arranged piggy-back where the thrusts generally initiate in a break-forward sequence (Van Der Pluijm and Marshak, 2004; Fossen, 2010). Major thrust faults have a stair-step profile where ramps typically form in stronger units and flats in weaker ones (Van Der Pluijm and Marshak, 2004). Thrusting can also cause sediments to fold, where the folds form as a result of development of slip on thrust faults (Van Der Pluijm and Marshak, 2004). The term detachment folds is used to describe folds where the layers above the detachment shorten more than their substrate (Fossen, 2010).

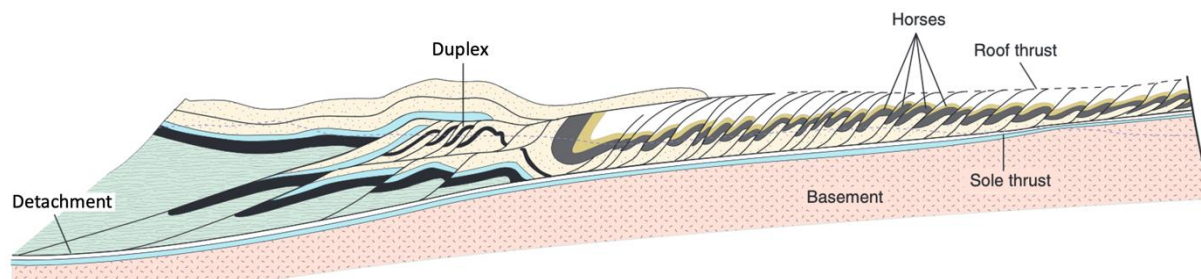


Figure 2.3.3: The figure illustrates how contractional faults typically form imbrication zones, modified from Fossen (2010).

The roof and sole thrust bind the duplex structure, where the horses are arranged piggy-back and root in a detachment.

In some tectonic settings, arrays of thrust faults form in conjunction with folds. These systems are called fold-thrust belts, and occur when a layer of the upper crust undergoes significant horizontal shortening under conditions that are low-grade or sub-metamorphic (Van Der Pluijm and Marshak, 2004). A fold-thrust belt can be divided into different zones that have different characteristics (Fig. 2.3.4). The foreland is located at the flanks of the collisional orogen, while the hinterland is located in the central area and is subjected to more intense deformation. Overall, fold-thrust belts show a wedge-shaped geometry in cross-sections (Fig. 2.3.4), where the hinterland is the thickest part with gradual thinning towards the foreland

(Fossen, 2010). This geometry occurs because sediments get scraped off the surface and collected in wedges. The geometry can be compared to the wedge-shaped build-up of snow from a snowplough (Fossen, 2010). Typically, numerous thrusts will merge at depth with a shallowly dipping detachment.

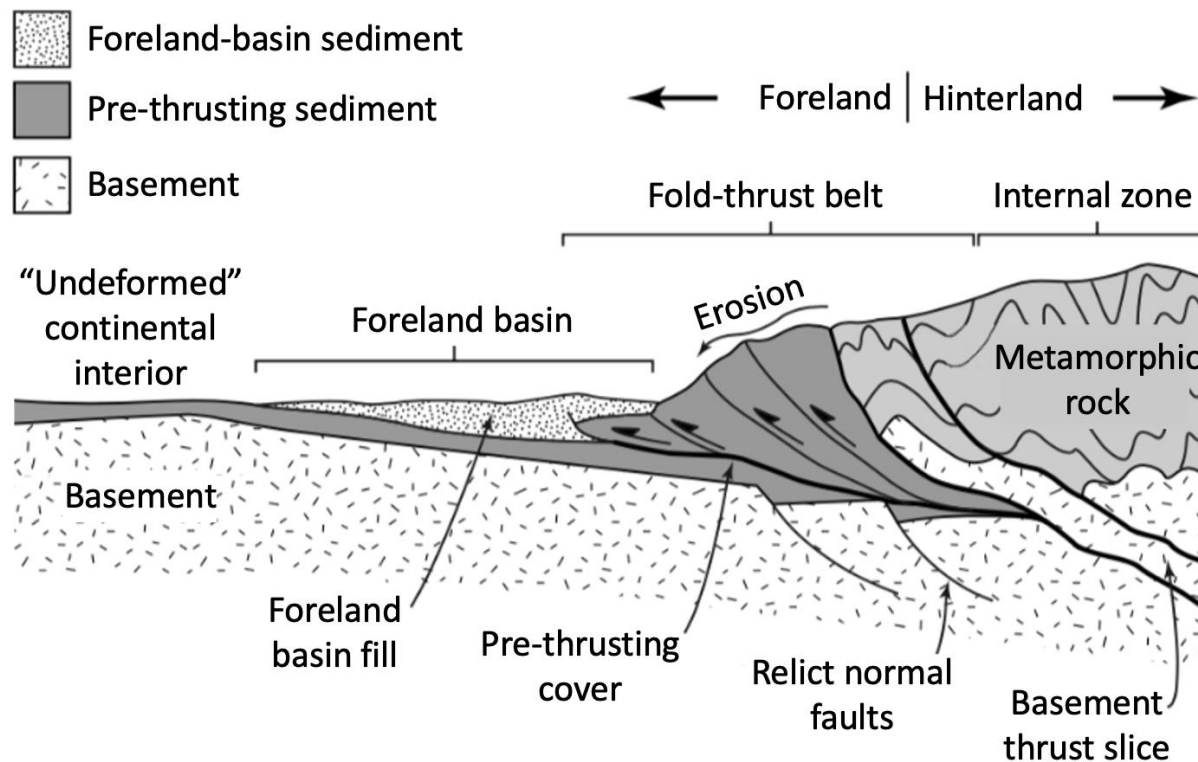


Figure 2.3.4: A schematic cross section that illustrates the location of the different zones in a fold-thrust belt in an orogen. The fold-thrust belt has a wedge-shaped geometry when viewed in a cross section. Modified from Van Der Pluijm and Marshak (2004).

In the foreland region, the deformation is restricted to the rocks above a regional fault called the basal detachment which lies at or near the basement-cover contact (Van Der Pluijm and Marshak, 2004). This type of deformation is referred to as thin-skinned. A foreland basin will form in front of a rising orogen as a result of a stack of thrust sheets that acts as a weight (Van Der Pluijm and Marshak, 2004). The thrust sheets will bend down the surface and create a depression that collects sediments eroded from the orogen. In the hinterland region, the basement rocks are incorporated in thrust sheets. This type of deformation is referred to as thick-skinned. Structures in the hinterland region tend to form at greater depths than in the foreland region. Thus, the deformation occurs under metamorphic conditions making it

possible for sedimentary rocks to deform plastically (Van Der Pluijm and Marshak, 2004; Fossen, 2010). Sedimentary layers can therefore fold into fold nappes, which are huge recumbent folds underlain by a detachment (Van Der Pluijm and Marshak, 2004).

In a tectonic regime, both contraction and extension can occur alongside strike-slip movements. The entire strike-slip fault, or bends in the fault, can contain additional components of shortening or extension (Van Der Pluijm and Marshak, 2004; Fossen, 2010). This type of deformation is referred to as transpression or transtension. Transpression occurs where there is a combination of strike-slip movement and shortening, whereas transtension occurs where there is a combination of strike-slip movement and extension (Fig. 2.3.5A; Van Der Pluijm and Marshak, 2004; Fossen, 2010). Transpression and transtension can lead to the formation of flower structures which occurs when an array of faults merges at a depth to near-vertical, and diverges to shallower dips near the ground surface (Fig. 2.3.5B; Van Der Pluijm and Marshak, 2004). Transpression can produce an uplift along the fault, leading to a positive flower structure, and transtension can produce a subsidence along the fault, leading to a negative flower structure.

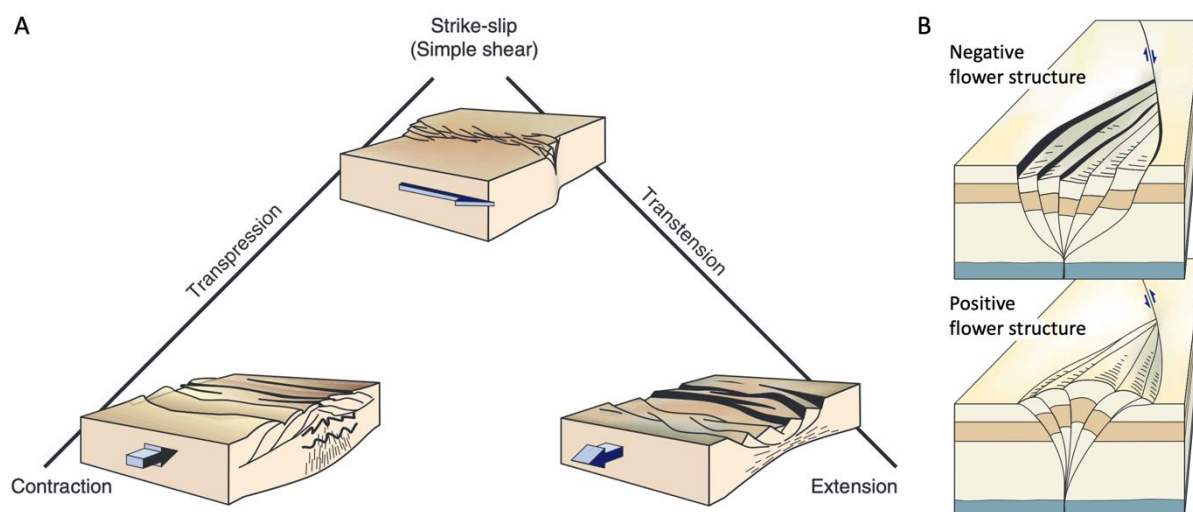


Figure 2.3.5: A) The relationship between different deformation types, where transpression occurs where strike-slip movements and shortening occur together. Whereas transtension occurs where strike-slip movements and extension occur together. B) Flower structures, where negative flower structures can be produced by transtension, whereas positive flower structures can be produced by transpression. Modified from Fossen (2010).

2.4 Stratigraphy

The stratigraphy on Svalbard represents different geological times from the Precambrian until present. During this time Svalbard has moved from the southern to the northern hemisphere and been subjected to changing climatic conditions and a variety of tectonic regimes. This section will give a short description of the main units that are included in Figure 2.4.1, showing their name, age, lithology and thickness.

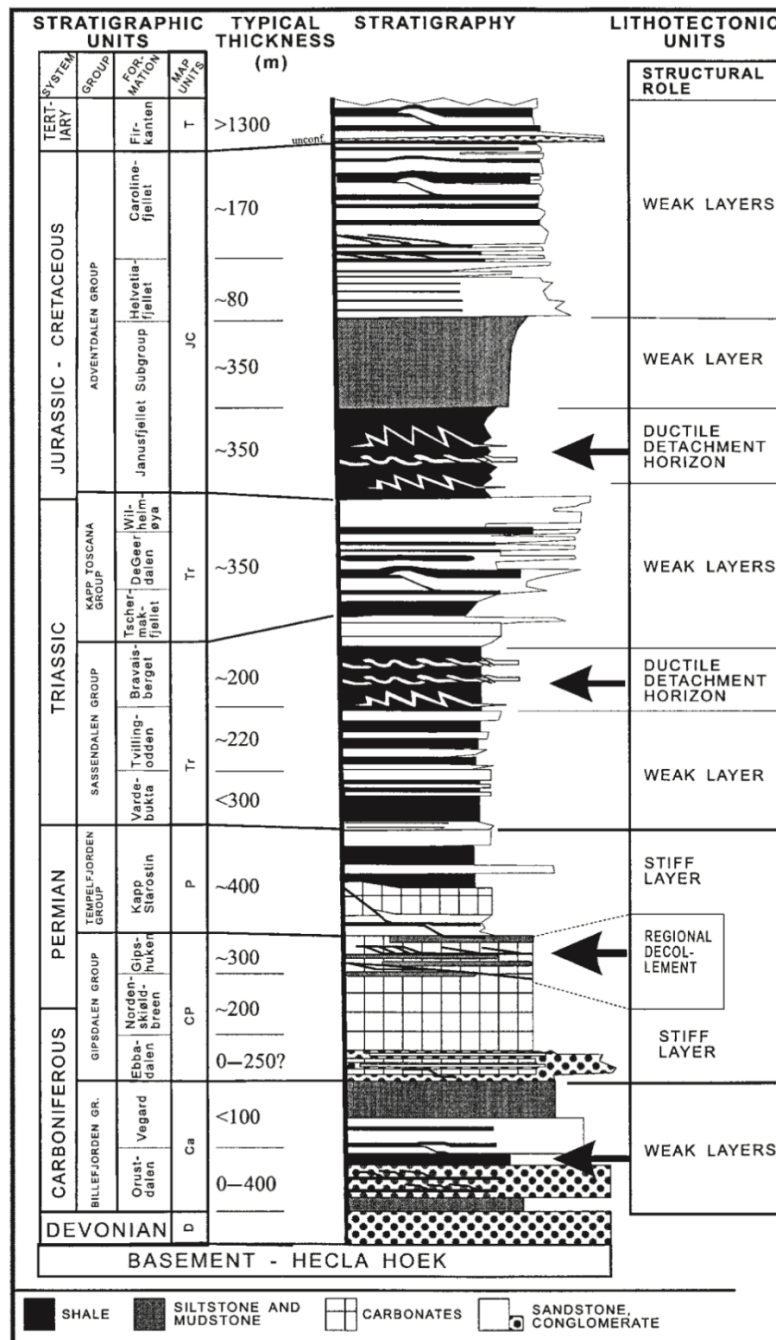


Figure 2.4.1: Stratigraphic scheme for Svalbard. The figure includes the stratigraphic units, their age, thickness, and lithology with their structural role (Braathen et al., 1999).

2.4.1 Hecla Hoek

The basement at Svalbard is often referred to as Hecla Hoek and comprises rocks from the Precambrian to Silurian. The succession mainly represents magmatic and metamorphic rocks that have been strongly deformed due to repeated orogenic events. Even though Hecla Hoek has been affected by poly-orogenic development, it is mainly considered to be the product of the Caledonian Orogeny (Dallmann, 1999).

2.4.2 Devonian

During the Devonian period a vast thickness of Old Red molasse sediments were deposited on Svalbard (Dallmann, 1999). The sediments reflect a dry, desert-like depositional environment. These coarse grained sediments were deposited during active rifting in fault-bounded rift basins, and are separated from the overlying Carboniferous rocks by an angular unconformity (Dallmann, 2015).

2.4.3 Billefjorden Group

The Billefjorden Group was deposited from Late Devonian to Early Carboniferous in tectonic depressions that developed subsequent to the deposition of the Old Red sediments (Dallmann, 1999). The sediments from the Billefjorden Group differs from the Old Red Sandstones by mainly consisting of greyish sandstones and siltstones with minor amounts of conglomerates and shales. The sediments are predominantly of fluvial and lacustrine origin and represent a change towards a humid and warm environment (Worsley, 2008; Dallmann, 2015).

2.4.4 Gipsdalen Group

Various carbonate and clastic rocks deposited from Middle Carboniferous to Early Permian make up the Gipsdalen Group (Dallmann, 1999). The lower part of the group consists of conglomerates, sandstones, siltstones and shales deposited during semi-arid to arid climatic conditions in separate basins. The coastal land and lowlands were flooded in Late Carboniferous causing the formation of various marginal marine deposits like sabkha

evaporites and shallow marine carbonates (Worsley, 1986; Dallmann, 1999; Worsley, 2008; Dallmann, 2015).

2.4.5 Tempelfjorden Group

The Tempelfjorden Group was deposited from Middle to Late Permian and mainly consists of cherts, siliceous shales and siltstones with intercalated minor sandstones and limestones (Dallmann, 1999). The lithofacies of the Tempelfjorden Group is in strong contrast to those of the underlying Gipsdalen Group, where the Tempelfjorden Group was deposited on deeper water in temperate to cold water with high-energy conditions. The lithofacies reflect the changes in depositional environment through the regional transgression, prograding from foreshore to shore-face and finally to the deeper offshore environments (Dallmann, 2015).

2.4.6 Sassendalen Group

The main lithologies of the Sassendalen Group are shale, siltstone and sandstone deposited in Early and Middle Triassic (Dallmann, 1999). The main sediment source was located in the west where the sediments represent coastal, deltaic to shallow shelf deposits (Dallmann, 1999; Dallmann, 2015).

2.4.7 Kapp Toscana Group

The Kapp Toscana Group were deposited from Late Triassic to Middle Jurassic and mainly comprises shales, siltstones and sandstones (Dallmann, 1999). The main sediment source shifted to the east with uplift, erosion and drainage from the Ural Mountains, where the Lower and Middle Jurassic succession exhibit several hiatuses. The sediments were generally deposited in a nearshore, deltaic environment, and are characterised by shallow marine and coastal reworking (Dallmann, 1999).

2.4.8 Adventdalen Group

The Adventdalen Group mainly comprises shales, siltstones and sandstones deposited from Late Jurassic to Early Cretaceous (Dallmann, 1999). The Late Jurassic succession consists of organic-rich, dark marine mudstones deposited in an inner to outer shelf environment (Dallmann, 1999; Dallmann, 2015). The Early Cretaceous succession consists of shales,

sandstones, siltstones and subordinate coals, conglomerates and rare bentonites. The sediments were deposited in varying environments with transitions from a deeper outer shelf to a shallow inner shelf, as well as delta-front and fluvio-deltaic systems. The bentonites originate from igneous activity due to the opening and development of the Amerasian Basin (Dallmann, 2015). The group was eroded to varying levels due to the Cretaceous uplift, which also is the reason why the entire Upper Cretaceous is missing, thus creating a hiatus (Dallmann, 1999; Dallmann, 2015).

2.4.9 Van Mijenfjorden Group

The Van Mijenfjorden Group was deposited from Paleocene to Eocene and is a clastic sedimentary succession consisting of sandstones, siltstones, shales and subordinate coals and conglomerates (Dallmann, 1999; Dallmann, 2015). The lower coal-bearing part of the group is interbedded with marine and non-marine sandstones, siltstones and shales. While the lower part is of deltaic origin, the upper part represents a series of barrier shoreline developments and contain marine sandstones interbedded with minor conglomerates, siltstones and clay-ironstones (Dallmann, 1999; Dallmann, 2015).

Chapter 3

Methods

This chapter will describe important principles for acquisition of marine multichannel seismic reflection data, including seismic resolution, which will greatly affect the final product. In addition, theory and principles for seismic data processing and interpretation will be discussed.

3.1 Seismic reflection data acquisition

Seismic reflection surveying is the most extensively used and well known geophysical method (Kearey et al., 2002; Gelius and Johansen, 2010). The method is used to produce detailed and highly resolved images of subsurface geology. There are three fundamental purposes for collecting seismic data, which are to obtain information to image stratigraphic features, structural elements and rock properties (Hart, 2000).

During the acquisition of seismic data, a controlled source emits an acoustic pulse that propagates through the subsurface (Hart, 2000; Kearey et al., 2002; Gelius and Johansen, 2010). As the wave propagates through the subsurface it will be affected by the elastic moduli and density of the material it passes. When the wave reaches a material with different properties, the energy will partition. Different physical properties will give a contrast in acoustic impedance (AI), which is a product of the P-wave velocity and density. The reflection coefficient (RC) is dependent on the AI contrast, where RC is a measure that defines how much energy that will be reflected at an interface. A large AI contrast will give a large RC, and thus, a strong reflection. Whereas a small AI contrast will give a small RC and a weak reflection (Hart, 2000; Kearey et al., 2002; Herron, 2011). The reflections from the interfaces can be recorded at the surface by receivers that measure the strength (amplitude) of the reflected energy, and the time it takes the waves to travel, known as two-way traveltime (TWT). The recorded information can be presented as seismic traces, which is a graph that plot variations in amplitude as a function of time. The traces reflect changes in physical properties in the

subsurface geology, and can be examined and processed to map the subsurface (Hart, 2000; Kearey et al., 2002).

During seismic reflection surveying, the desired data are primary reflections, which are rays that reflect at a single interface (Fig. 3.1.1). However, the recorded signal can be complicated by various types of noise. Noise can be divided into coherent and random noise, where the latter is usually not connected to the survey. Examples of random noise can be high frequency signals from rain, wind and other boats, and low frequency swell noise generated by waves. Coherent noise is generated from the survey and surveys nearby, but are of no direct interest. This type of noise can for instance be refractions, diffractions and multiples (Kearey et al., 2002; Gelius and Johansen, 2010). Unlike primaries, multiples reflect at more than one interface, and generally tend to have lower amplitudes due to energy loss at each reflection. However, water layer multiples (Fig. 3.1.1) can have amplitudes comparable to the primaries, where the ray repeatedly reflects at the seabed and sea surface. These multiples will look like repeated events down the seismic section. The arrival times of multiples are predictable, and it is important that they are identified correctly so they can be suppressed by data processing techniques, so they are not confused as primary events. A ghost reflection forms when the source and/or receiver lies at a depth below the water surface, and the ray travels upward and reflects off the water surface before it travels downward. In some cases, the ghost can be a type of multiple where it creates a double appearance of each event that arrives shortly after the primary (Sheriff and Geldart, 1995; Kearey et al., 2002; Gelius and Johansen, 2010). However, in this case, the ghost is not a multiple, as the depth of the source and receiver is chosen to obtain constructive interference between the ghost and the primary pulse (Mjelde, 2011).

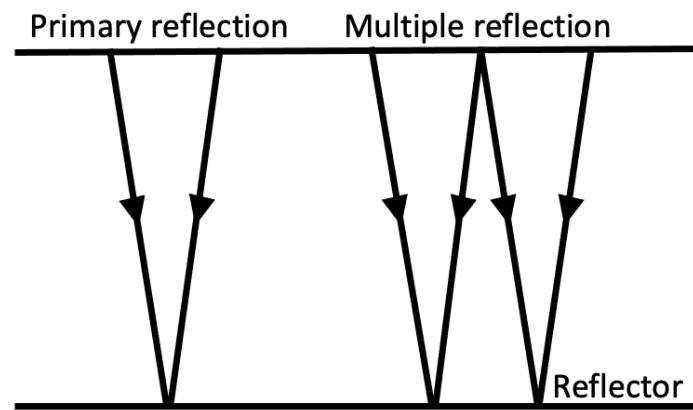


Figure 3.1.1: The figure shows a primary and a multiple reflection outlined after Kearey et al. (2002). There are several types of multiples, this is a double-path multiple and one example of how a multiple can reflect within a layer.

Seismic reflection data can be acquired in 2D, 3D or 4D. In 2D surveys the data are collected in two dimensions along a survey line, where the resulting image represents a 2D section below the line (Kearey et al., 2002; Gelius and Johansen, 2010). The method is often used to get a rough overview over a larger area. A 3D survey can achieve a higher degree of resolution, and can therefore be used to provide a detailed overview of the area. The data collected in a 3D survey samples a volume of the subsurface, as opposed to 2D surveys that samples an area in a vertical plane (Kearey et al., 2002). A 4D survey is a series of 3D surveys that are shot repeatedly over time, at the same location. The purpose is to monitor changes in the subsurface conditions, like pore fluids in a reservoir during production (Kearey et al., 2002; Gelius and Johansen, 2010; Herron, 2011).

The acquisition method used in this study is 2D multichannel marine seismic data. In a standard 2D marine survey a boat is towing a single or an array of sources, followed by a single streamer with receivers that is towed behind the source (Fig. 3.1.2; Kearey et al., 2002; Gelius and Johansen, 2010). The seismic data recorded from the receivers needs to be amplified, filtered necessary, digitised and stored with the appropriate information (Kearey et al., 2002).

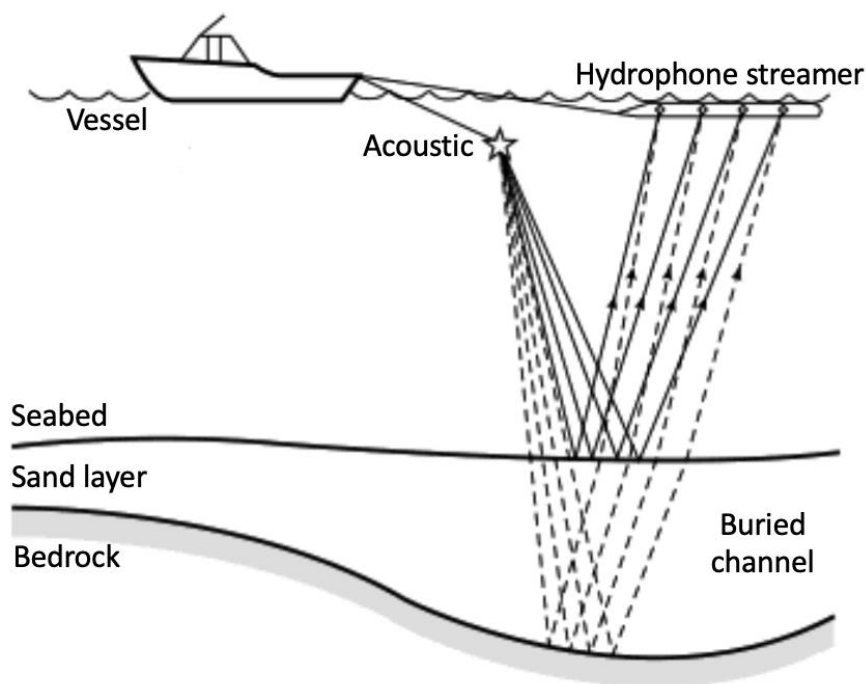


Figure 3.1.2: The figure shows the survey set-up for a multichannel 2D seismic reflection survey, modified from Kearey et al. (2002).

3.1.1 Source

A seismic source must have a waveform that is repeatable, and it needs to be safe, efficient, and environmentally acceptable. It also needs to emit sufficient energy across a broad frequency range, and concentrate the wave energy towards the area that is the target for the survey. The factors that determine what kind of source to use are primarily the depth and thickness of the target area and cost-efficiency (Hart, 2000; Kearey et al., 2002). Air-guns are the most commonly used source in the marine realm, and is also the one used in this study. Air-guns (Fig. 3.1.3) store highly pressurised (10-15 MPa) air in a chamber, where an electrical triggering discharges the air into the water (Hart, 2000; Kearey et al., 2002; Gelius and Johansen, 2010). The released air forms an expanding bubble that generates the primary pulse. The primary pulse is followed by a train of bubble pulses caused by the oscillatory expansion and collapse of the gas bubbles. The bubble pulses lengthen the seismic pulse, and is regarded as noise as it affects the seismic resolution (Kearey et al., 2002).

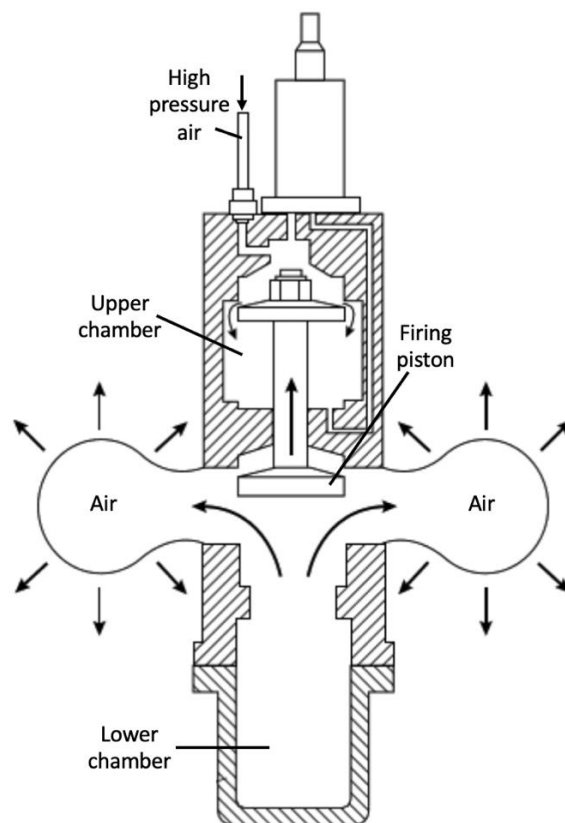


Figure 3.1.3: The figure shows the schematic structure of an air-gun, modified from Kearey et al. (2002). High-pressured air is injected at the top of the air-gun. Air from the lower chamber is released when the firing piston is activated.

It is possible to use one or multiple air-gun arrays for sources. There are several advantages of using arrays of air-guns with different chamber volumes that are fired simultaneously. The first one is that the total amount of transmitted energy increases, which is beneficial for deep penetration surveys. Secondly, the different chamber volumes will result in different bubble pulse periods. The primary pulses will interfere constructively, while the bubble pulses interfere destructively as a result of differing arrival times (Fig. 3.1.4; Kearey et al., 2002; Gelius and Johansen, 2010). Finally, it improves the signal-to-noise ratio and induces directivity of the source. Some frequencies, that are not directly below the source array, will be attenuated by the array design. The long array, which is along the direction of the vessel, focuses the energy downward. The bubbles will “cancel-out”, making the frequency content much flatter (Gelius and Johansen, 2010). It is possible to avoid the ghost by placing the source array at the surface, but this will increase the effect of weather noise caused by rough waves. The source has therefore been placed at 7 m depth to reduce the weather noise and create maximum constructive interference between the ghost and the primary pulse.

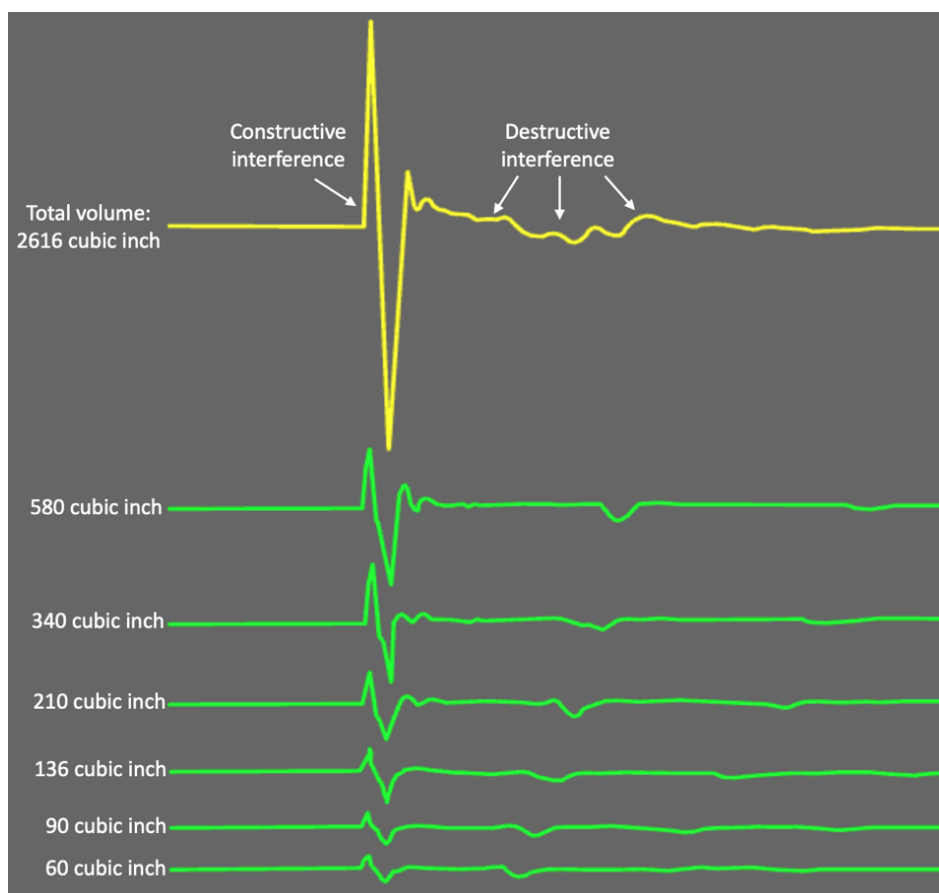


Figure 3.1.4: Air-gun signature of 6 air-guns with chamber volume varying from 60 to 580 cubic inches, modified from Mjelde (2011). The green signals are from the individual air-guns, whereas the yellow signal is the resulting pulse from shooting the air-guns simultaneously.

3.1.2 Receiver

A marine seismic receiver must be sensitive to variation in pressure, and be able to record the required range of frequencies and amplitudes without distorting the signal. In marine seismic surveys it is common to use hydrophones. The hydrophone is a piezoelectric device that generates a voltage to convert the mechanical pressure changes from the reflected pulse into electrical energy that can be recorded digitally (Hart, 2000; Kearey et al., 2002; Gelius and Johansen, 2010). The influence of movements due to currents and wave actions are minimized by connecting and polarizing two piezoelectric elements in one hydrophone so that voltages from directional acceleration will cancel (Fig. 3.1.5; Gelius and Johansen, 2010).

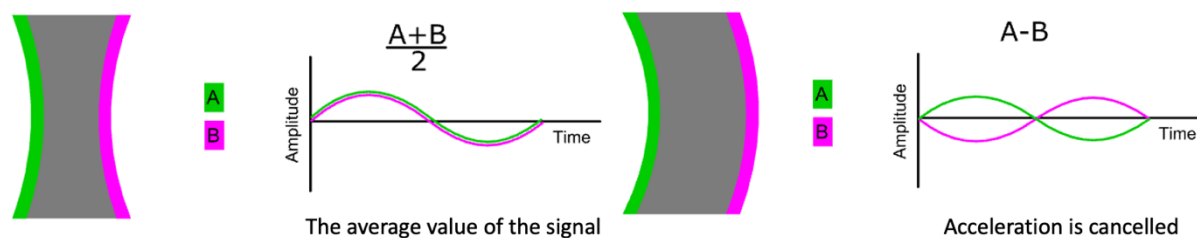


Figure 3.1.5: The figure illustrates the two piezoelectric elements, A and B, modified from Mjelde (2010). The figure on the left shows how the signal register at pressure variations, while the figure on the right shows how the signal is cancelled due to acceleration.

Individual hydrophones can be distributed in a streamer, where the streamer has neutral buoyancy and is manufactured to ensure good transmission of seismic energy to the hydrophone elements. The streamer is typically several kilometres in length, where the hydrophones are grouped together into linear arrays of a pre-defined length, commonly 12.5 or 25.0 m. This is done to reduce the amount of data and to enhance the signal-to-noise ratio by providing detectors with a directional response and to suppress horizontally travelling coherent noise (Hart, 2000; Kearey et al., 2002; Gelius and Johansen, 2010). Streamers are equipped with birds that are used to control the depth of the streamer. This is done by utilising a built-in pressure transducer that reads a depth deviation to adjust the angle of their depth fins (Gelius and Johansen, 2010).

3.2 Seismic processing

The data recorded during the acquisition bears little resemblance to geology, and contains noise and unwanted frequencies that makes it difficult to interpret the seismic data. The objective of seismic processing is to increase the signal-to-noise ratio and improve the seismic resolution to produce the clearest image possible of the subsurface geology (Hart, 2000; Kearey et al., 2002; Gelius and Johansen, 2010).

3.2.1 Editing

Editing is a quality control of the seismic traces where bad traces that are dead or exceptionally noisy can be removed. The bad data can be zeroed out or replaced with interpolated values to the levels of the surrounding data (Sheriff and Geldart, 1995). Traces that are noisy, have transient glitches or mono-frequency signals are deleted, while traces

with polarity reversals are corrected (Yilmaz, 2001). Bad traces can affect the signal-to-noise ratio, which is why it is important to remove them as early as possible to prevent further complications.

3.2.2 CMP sorting

The seismic traces can be sorted in different ways. The data acquisition is done in shot-receiver coordinates, sorting the seismic traces into common shotpoint (CSP) gathers (Fig. 3.2.1A). The processing, on the other hand, is done in midpoint-offset coordinates, which means that the trace coordinates needs to be sorted into common midpoint (CMP) gathers (Fig. 3.2.1B; Yilmaz, 2001; Kearey et al., 2002; Gelius and Johansen, 2010). The idea behind the CMP method is that each reflection point should be imaged several times to produce a stronger and clearer image of the subsurface by constructive interference of the primary reflections (Hart, 2000).

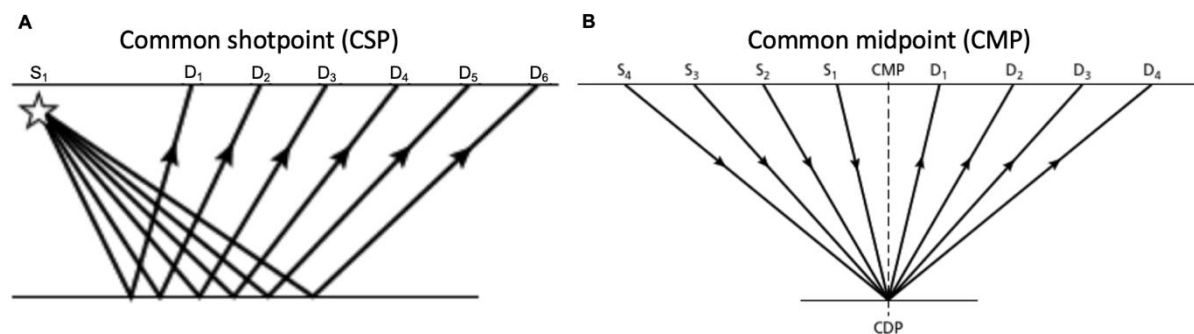


Figure 3.2.1: The figure illustrates common shotpoint (A) and common midpoint (B), modified from Kearey et al. (2002). The sources are represented by S and the receivers by D . B, shows that common midpoint (CMP) is the midpoint at the surface, whereas common depthpoint (CDP) is the midpoint at depth.

3.2.3 Amplitude recovery

Gain is a time-variant scaling which is used to recover reflection amplitudes. There are three major factors that cause seismic amplitude losses. The first is geometrical spreading which causes amplitude attenuation from wavefront divergence. The second is intrinsic attenuation where internal friction causes energy losses. The third is transmission losses where the amplitude attenuates due to reflections at interfaces (Gelius and Johansen, 2010). Amplitude

recovery attempts to compensate for these amplitude losses, but needs to be used with care as it can destroy the character of the signal (Yilmaz, 2001; Gelius and Johansen, 2010).

3.2.4 Frequency filtering

Frequency filtering is used to increase the signal-to-noise ratio by filtering out frequency ranges where noise dominates over the primary reflection signals, and passing frequency ranges where the primaries dominate (Sheriff and Geldart, 1995). Because the signal is recorded in the time-domain it needs to be converted to the frequency-domain before filtering, this is done by using the Fourier transform. Frequency filtering can be done in different ways (Fig. 3.2.2). A high-pass (HP) filter cut low frequencies, which can help attenuate ship-generated noise. Whereas a low-pass (LP) filter cut high frequencies, which for instance can help attenuate wind noise in land-seismic surveys (Kearey et al., 2002). An anti-alias filter is a low-pass filter with steep slope set at 70 dB/octave. This is used to prevent aliasing during acquisition by removing frequencies above the Nyquist frequency (Herron, 2011). A band-pass (BP) filter cut frequencies above and below a set value and keeps the frequencies in between. A band-reject (BR) filter does the opposite to the BP filter, where it keeps frequencies above and below a set value and cuts the frequencies in between. The signal is converted back to the time-domain by using the inverse Fourier transform. This process generates a “ringing” known as Gibbs’ phenomenon which happens due to discontinuities in the filter edges. A process known as tapering rounds the filter edges which minimises the ringing (Sheriff and Geldart, 1995). Frequency filtering can be performed at several stages in the processing, early to remove obvious noise, and later to remove artefacts produced by other processing stages (Yilmaz, 2001; Kearey et al., 2002).

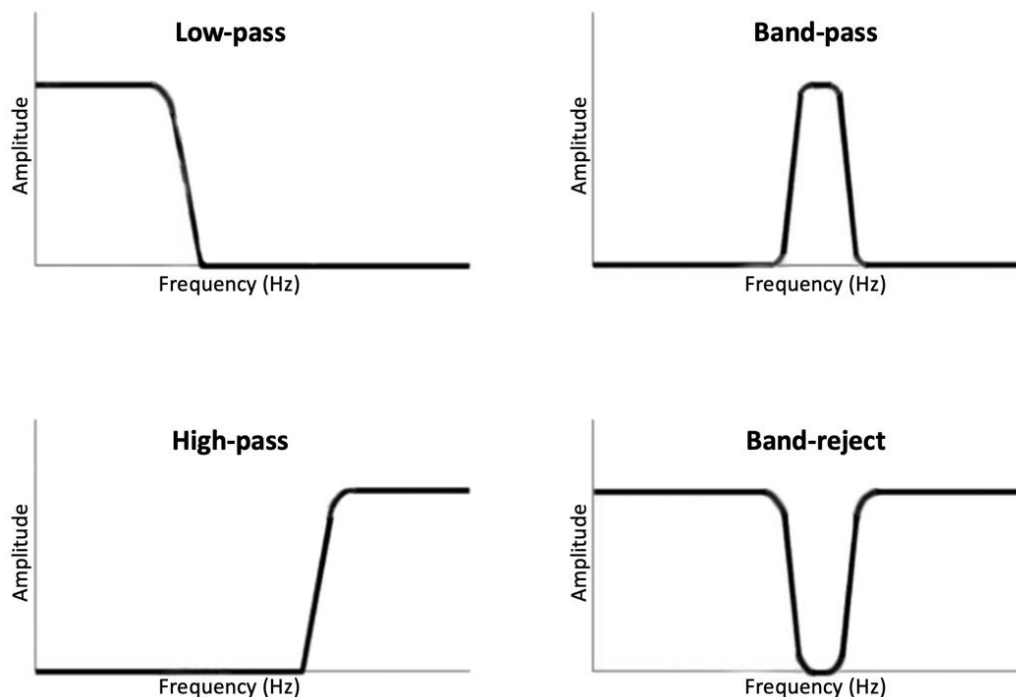


Figure 3.2.2: The figure shows low-pass, high-pass, band-pass and band-reject filters, modified from Obeid et al. (2017).

3.2.5 Deconvolution (inverse filtering)

Deconvolution is the process of removing the effect of previous filter operations by convolving the signal. It uses an inverse filter based on criteria other than frequency to suppress noise that have the same frequency characteristics as the primary reflection by removing, shorten or replace the wavelet (Sheriff and Geldart, 1995; Hart, 2000; Kearey et al., 2002). A wide range of inverse filters are available, where each is designed to remove some specific ground filtering effect, such as absorption or multiple reflections (Kearey et al., 2002). Examples of inverse filtering can be dereverberation to remove water layer multiple associated ringing, and de-ghosting to remove the ghost by shortening the pulse length and thereby improving the vertical resolution. After deconvolution, frequency filtering often need to be performed as the inverse filtering process sometimes tries to undo prior filtering effects (Sheriff and Geldart, 1995; Yilmaz, 2001).

3.2.6 Velocity filtering

The purpose of velocity filtering is to remove coherent noise events based on the angle the event dips. The dip is calculated from the apparent velocity, which is defined in formula 3.1. The apparent velocity v_a is calculated from frequency f and wavenumber k_a , where a wave travels with velocity v at angle α .

$$(3.1) \quad v_a = \frac{v}{\sin \alpha} = \frac{f}{k_a}$$

The data can be converted from time-distance (t-x) domain to frequency-wavenumber (f-k) domain by using the Fourier transform. By changing the domain, it is possible to use f-k filtering to remove unwanted noise events, as each f-k plot (Fig. 3.2.3) yield a straight-line curve with gradient v_a , where the events plot differently (Kearey et al., 2002).

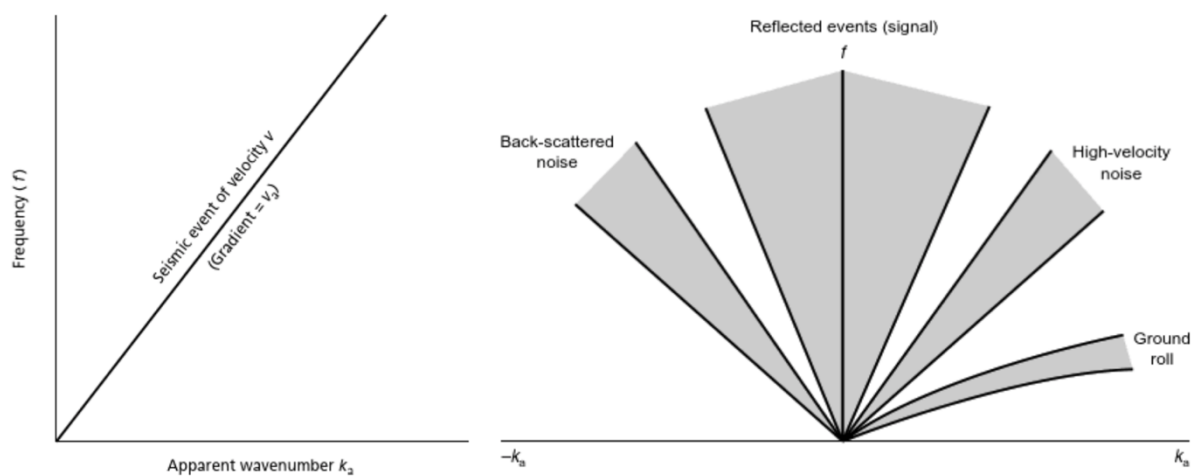


Figure 3.2.3: The figure illustrates the principles for velocity filtering, modified from Kearey et al. (2002). The example is taken from land seismic, where the ground roll will be higher than for marine seismic. The graph shows how a seismic pulse can be plotted in a f-k plot. The f-k plot contains reflection events and different types of noise events, where back-scattered noise can be multiples and high-velocity noise can be refractions. These are separated into different zones where it is possible to remove the unwanted events.

3.2.7 Static correction

The seabed is usually simple and laterally uniform, causing the events to be delayed with approximately the same time amount across the length of the streamer. Then, all the traces stack coherently as high quality data with a high signal-to-noise ratio (Samson and West, 1992). In areas where there are rapid changes in the seabed topography, the water depth variations cause velocity pull-up and push-down distortions that can severely damage the data quality. Abrupt water depth fluctuations across the length of the streamer delays event with different time amounts, which causes the traces in the CMP gather to stack incorrectly (Samson and West, 1992; Kearey et al., 2002). In return, this causes a degraded image. Static correction is a good method to correct for these problems without removing the effect of the water layer.

3.2.8 Velocity analysis

The velocity model of the Earth needs to be as accurate as possible to provide an accurate image of the subsurface geology. The velocity varies as a function of depth and is dependent on the physical properties of the individual units. Generally, velocity increases as a function of depth as the units become more consolidated. A velocity analysis is performed on CMP gathers where the objective is to provide correct stacking velocities to correct for normal moveout (NMO), which is a function of offset, velocity and reflector depth (Sheriff and Geldart, 1995; Yilmaz, 2001; Kearey et al., 2002). Figure 3.2.4 illustrates how the traces plot as a hyperbola, indicating that the NMO increases with increasing offset. A range of velocity values are used to calculate the corrections before the corrected traces are stacked (Kearey et al., 2002).

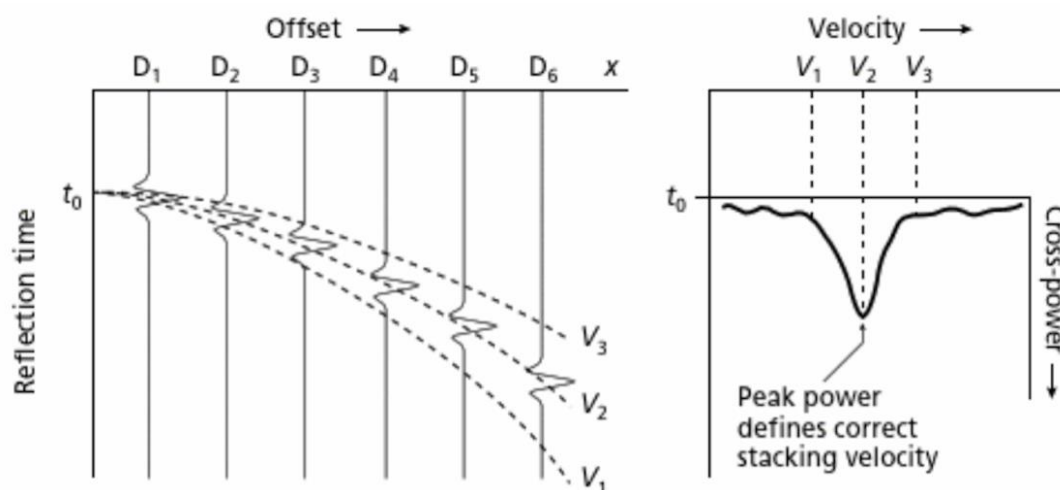


Figure 3.2.4: The figure illustrates how a set of reflection events in a CMP gather is NMO corrected by using different velocity values. The figure to the left illustrates how the traces plot as a hyperbola where the NMO increases with increasing offset. Both figures illustrate how correct velocity picking correct for the NMO. From the right figure it is possible to see that V_2 give the correct stacking velocity as it correlates with the peak power. Figure from Kearey et al. (2002).

There are several types of velocity analyses. The most common one is to compute the NMO corrections in discrete time windows along a hyperbola and down an entire trace, which is done for many different velocities. The velocity analysis produces a velocity spectrum which is a table of numbers as a function of velocity and two-way zero-offset time, which represent some measure of signal coherency (Yilmaz, 2001). The correct velocity will give the largest coherency, whereas too high or too low velocity will give little coherency. In general, the velocity increases with increasing depth. It is possible to distinguish primary energy from multiple energy by looking at the velocities. Multiple energy can be identified by its abnormally low velocity (Gelius and Johansen, 2010). Correct velocity picking will correct for the NMO and is illustrated in Figure 3.2.4, resulting in a successful velocity analysis.

3.2.9 NMO correction

After correct velocity picking, the NMO can be corrected for. NMO is the difference between traveltimes for reflected arrivals at a certain offset and at zero offset (Kearey et al., 2002; Gelius and Johansen, 2010). The NMO is a function of offset, velocity and reflector depth. When the traces are NMO corrected the offset effects are removed from the traveltimes, which results in the traces flattening across the offset range (Fig. 3.2.5; Yilmaz, 2001). If the picked velocities

are too high, the NMO corrected traces will be under-corrected and bend downwards. The NMO corrected traces can also be over-corrected and bend upwards when the picked velocities are too low.

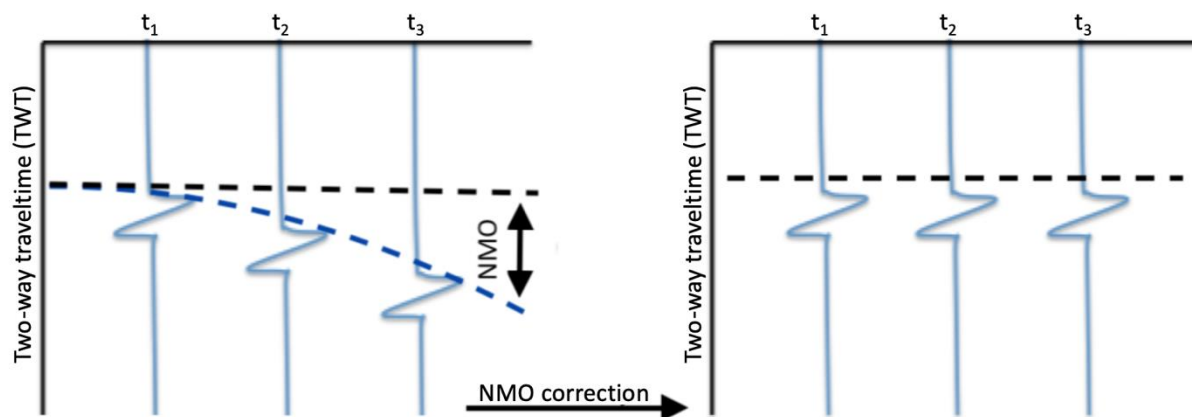


Figure 3.2.5: The figure illustrates the principles of NMO correction, modified from Skaara (2020). The different traces t_1 , t_2 and t_3 have different NMO which have to be corrected for. When the offset effects have been removed from the traveltimes, the traces flatten across the offset range.

3.2.10 Muting

Muting is done to exclude traces that reduces the quality of the seismic data by assigning zero values to the traces within the mute interval. After NMO correction the waveshape of reflections at shallow times and large offsets will be subjected to stretching (Sheriff and Geldart, 1995; Yilmaz, 2001). The stretching changes the frequency spectrum of the wavelet, which in result attenuate higher frequencies during stacking. It is common to mute large-offset traces before the stretching reaches 25% (Sheriff and Geldart, 1995).

3.2.11 Stacking

Stacking is the most important application in data-processing in improving the quality of the data, as it considerably increases the signal-to-noise ratio. The stacking process is carried out by combining the NMO corrected traces from a CMP gather. If the stacking velocities are correct, the primary reflections will align horizontally. When the stacking is done, the primary energy will amplify due to constructive interference, whereas multiple energy will attenuate where different arrival times cause the signal to interfere destructively (Fig. 3.2.6; Sheriff and Geldart, 1995; Gelius and Johansen, 2010).

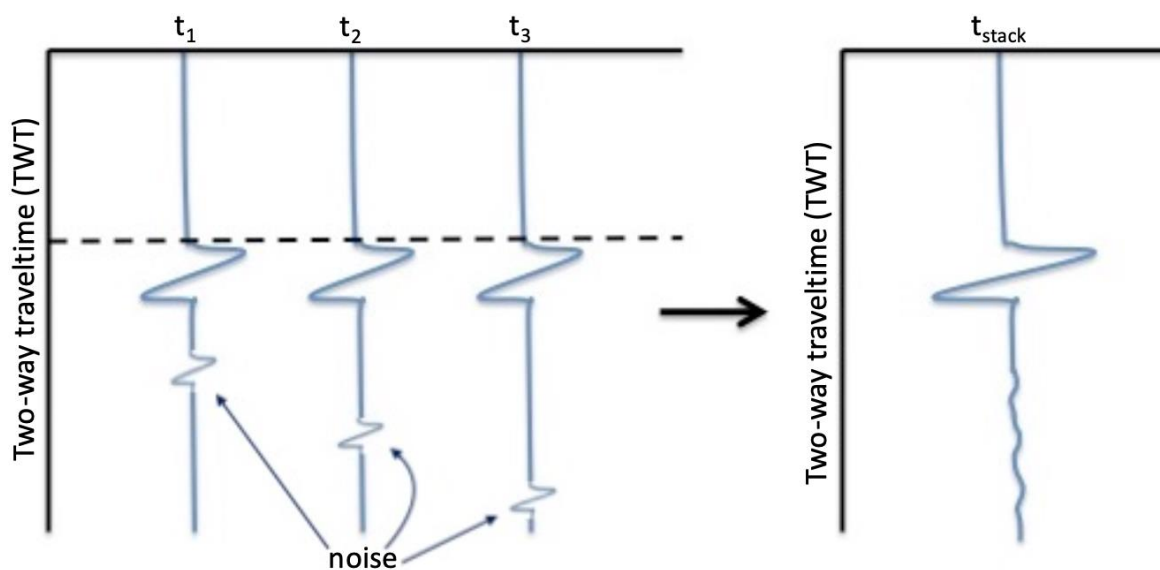


Figure 3.2.6: The figure illustrates how the NMO corrected traces (t_1 , t_2 , t_3) have been added together to a stacked trace (t_{stack}), modified from Skaara (2020). The signal-to-noise ratio will improve as the primary energy will interfere constructively, whereas the noise will interfere destructively due to different arrival times.

3.2.12 Migration

Until now it has been assumed that the reflection points lie in the subsurface at the mid-point between the shot and receiver. If the layers are horizontal this is an accurate assumption, but in cases of dipping layers, this needs to be corrected for. Dipping layers and complex structures cause the reflection points to register at the wrong location, leading to an incorrect image of the subsurface. This is illustrated in Figure 3.2.7 where the result of incorrect reflection positioning is a bow-tie shape. Migration is the process of moving events to their true subsurface locations and thereby assigning them to their correct vertical reflection time (Fig. 3.2.8; Hart, 2000; Yilmaz, 2001; Kearey et al., 2002). Migration also improves the resolution of the seismic section by collapsing diffractions and shrinking the Fresnel zone. 2D survey data does not provide any information on cross-dip and, hence, the migrated reflection points are constrained to lie within the plane of the section. This means that the true reflection points may lie out of the vertical section, thus, making 2D migration an imperfect process (Kearey et al., 2002). Migration can be performed in time or depth, and before or after stacking. In general, migration is carried out after the data have been stacked, but in areas of structural complexity, e.g. below thrust sheets, migration may be carried out before stacking (Hart, 2000; Yilmaz, 2001).

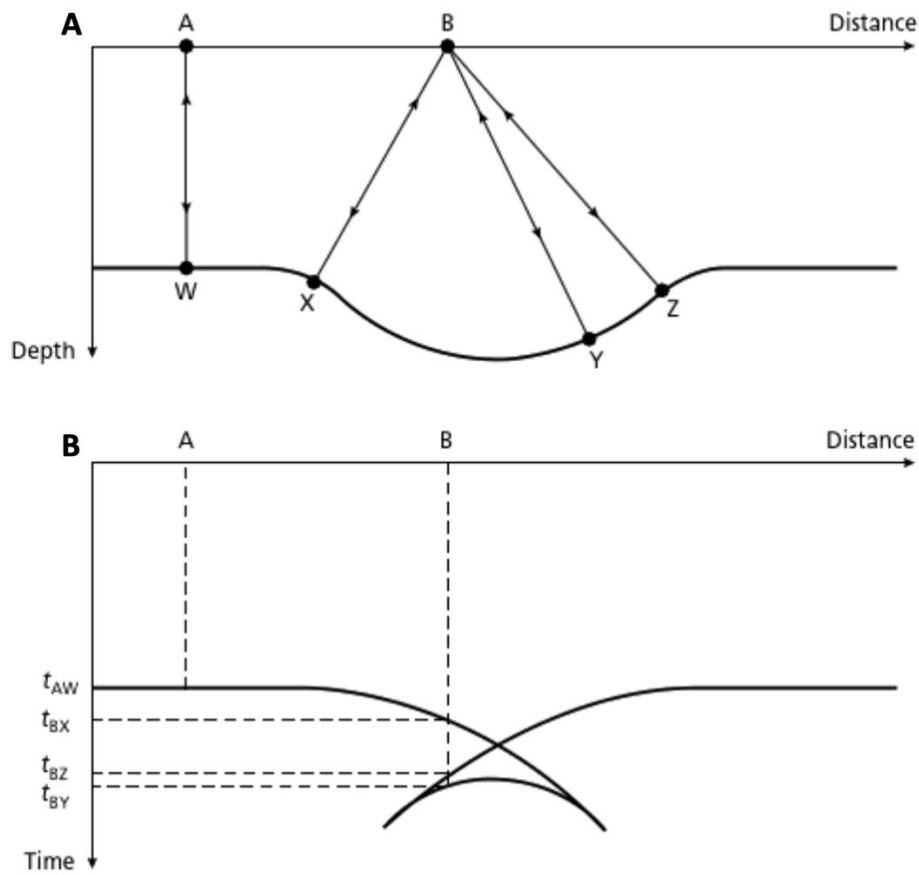


Figure 3.2.7: Figure A) illustrates a sharp syncline in a reflecting interface, and B) illustrates the resulting bow-tie shape that will occur in the non-migrated section. Figure from Kearey et al. (2002).

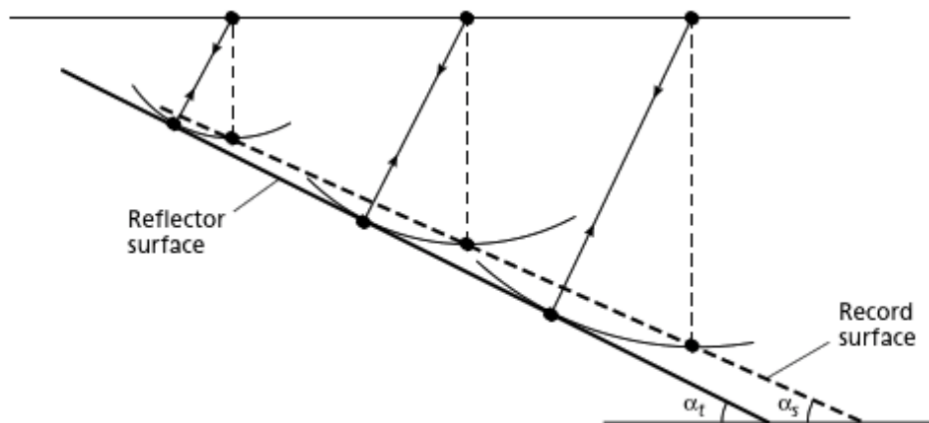


Figure 3.2.8: The figure illustrates where the reflection points in a planar-dipping reflector surface are assumed to be located directly underneath a CMP in a non-migrated seismic section. Thus, the recorded surface will deviate from the true reflector surface. Figure from Kearey et al. (2002).

3.3 Seismic interpretation

The data are ready for interpretation after the processing is done. The interpretation itself already begins at the survey design phase, when choices that influence the interpretability of the data are made. This may involve decisions where a survey designed for deep targets does not have the fold or high frequencies needed for imaging of shallow level geology (Hart, 2000). Interpretative choices are also made during the processing phase, as it also affects the character and interpretability of the data. Figure 3.3.1 shows the relationship between lithology, acoustic impedance, reflection coefficient and seismic response (Kearey et al., 2002).

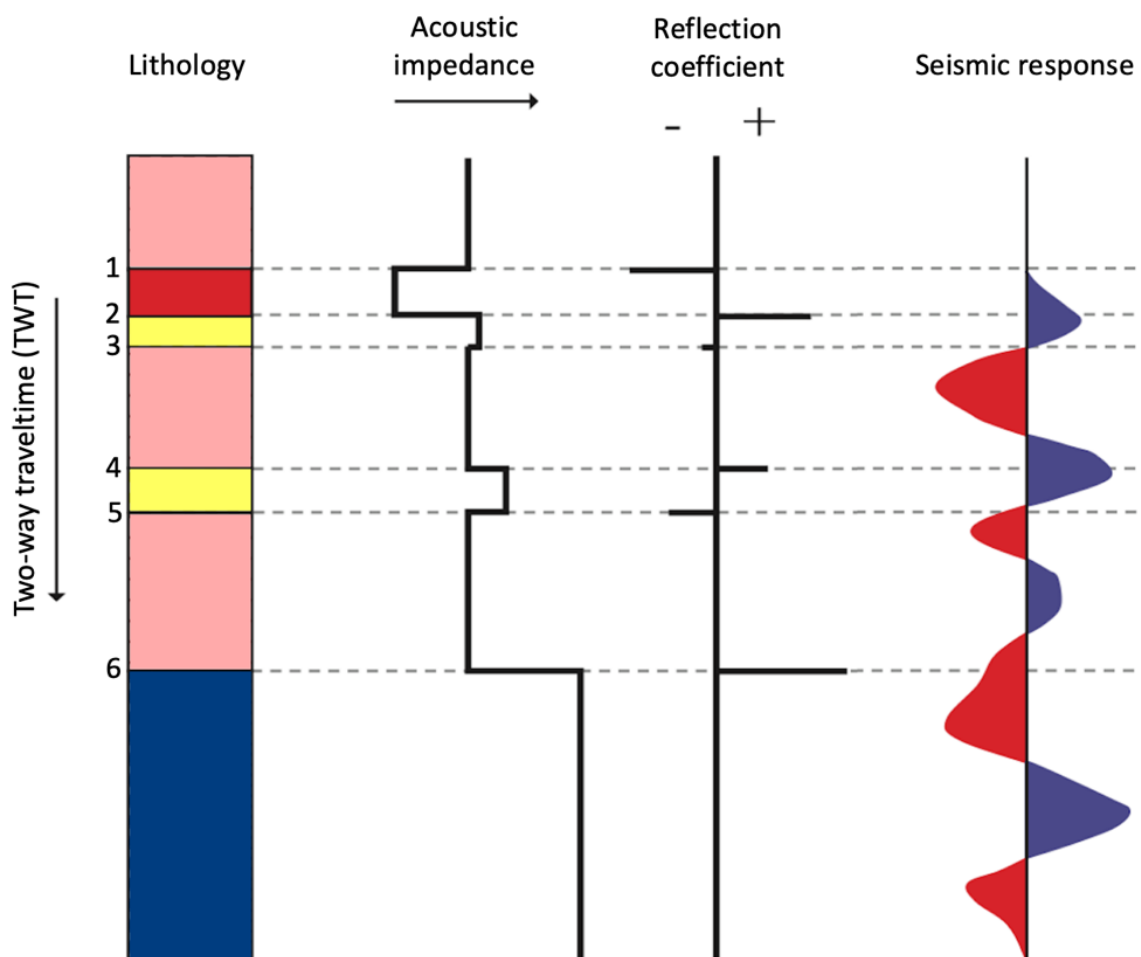


Figure 3.3.1: The figure illustrates how lithology, acoustic impedance and reflection coefficient influence the seismic response. Modified from Simm and Bacon (2014).

There are a few general assumptions that is important to be aware off before the interpretation process starts (Sheriff and Geldart, 1995). Firstly, the reflection events in the seismic sections are related to contrasts in acoustic impedance. Secondly, these impedance contrasts represent a change in the geology. Finally, details like waveshape and amplitude are related to geological properties.

Seismic data are nonunique and highly subjective, thus, seismic sections may look similar even though the depositional environment and tectonic setting are different (Herron, 2011). Thus, a good understanding of the geology in the area can help the interpretation. In 2D seismic data the interpretations are correlated from line to line, and the reflection times are compared directly at the profile sections. The two main approaches to seismic interpretation are structural analysis (Section 3.3.1) and stratigraphic analysis (Section 3.3.2).

Display

2D reflection seismic data are generally displayed in seismic sections as individually stacked zero-offset traces that show amplitude variations as a function of time. The vertical axis represents the depth as time, while the horizontal axis represents distance (Hart, 2000). The seismic section can be displayed in different ways (Fig. 3.3.2). The traces are displayed as a continuous curve, whereas for the variable wiggle display, the peaks are filled with black. The variable density display is the one most commonly used as a workstation display (Herron, 2011). It has a user-defined or customised colour scheme, usually red-blue-white, where near-zero amplitudes are coloured in white and red and blue represents a peak or trough. It is also possible to combine the variable wiggle with the density display to get more information from the seismic section (Hart, 2000).

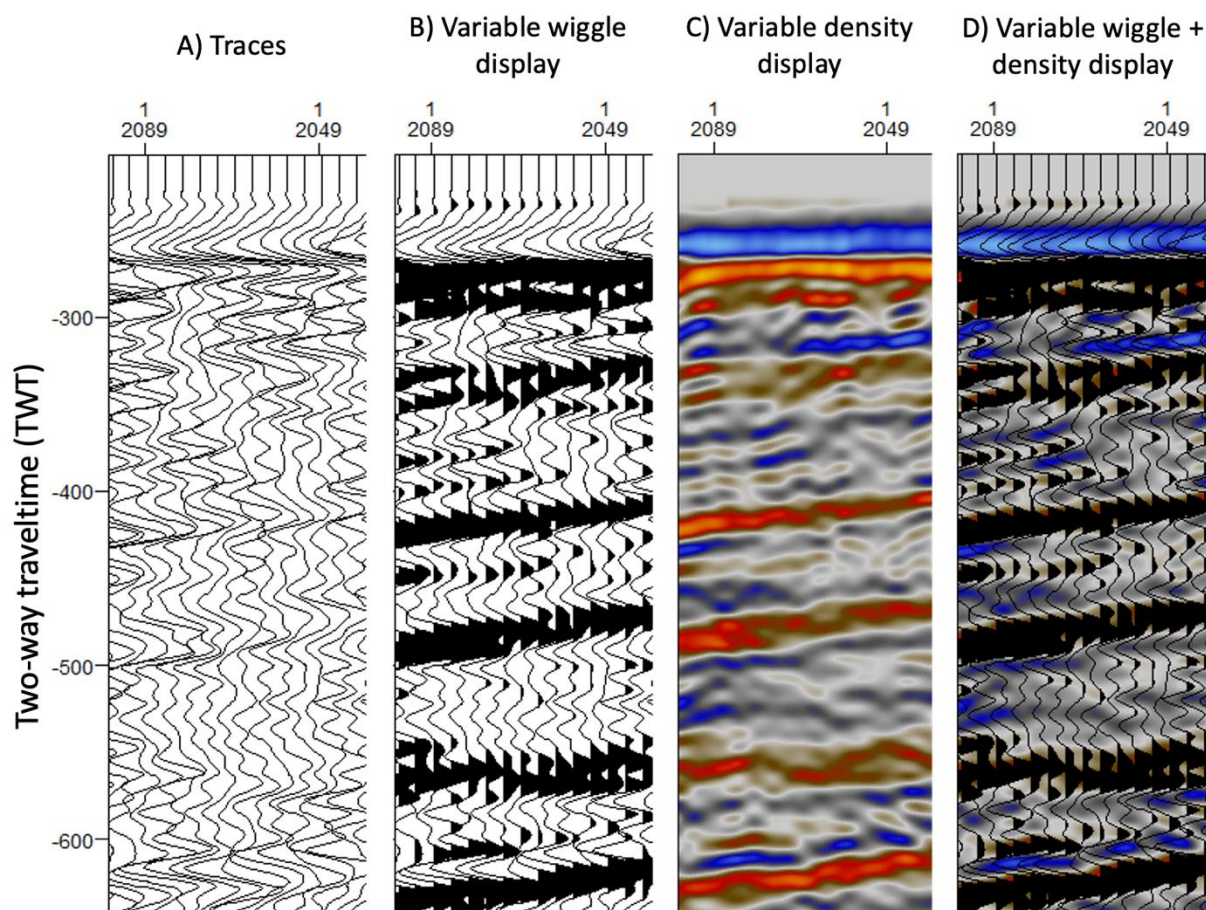


Figure 3.3.2: The figure shows different ways of displaying the seismic, where A) shows the traces, B) variable wiggle display, C) variable density display, and D) which is a combination of B) and C). The examples are from line 11 between trace 2089 and 2049. The seismic has SEG normal polarity as positive reflection coefficient is shown as a peak.

Polarity

The polarity of the dataset determines whether a positive reflection coefficient will be displayed as a peak or a trough (Hart, 2000). There has not been defined a universally accepted standard polarity, however, SEG has defined normal polarity as positive reflection coefficient, represented by a peak. Others will consider this as reverse polarity, although this is less common (Herron, 2011; Simm and Bacon, 2014). In regards of colour, it is common for seismic peaks to be coloured in blue and troughs in red, but there are exceptions (Simm and Bacon, 2014). The seismic data in this study is displayed as SEG normal polarity, where peaks are coloured in red and troughs are coloured in blue (Fig. 3.3.2). An easy way to check this is to display “variable wiggle” over “variable density”, or to control a specific event, e.g. seabed, against the acoustic impedance contrast.

Phase

The phase of a seismic signal determines the location of a peak or a trough, and thus where to interpret the event. By changing the waveform of a signal, the location of the peak or trough changes. Ideally a zero-phased wavelet is wanted. This wavelet is symmetrical with the amplitude centred on time zero (Fig. 3.3.3), which can be changed during processing (Sheriff and Geldart, 1995; Simm and Bacon, 2014). This is preferred, as the seismic event is symmetrical and thus the most easy and intuitive to visualise (Herron, 2011). Most sources, such as air-guns, generate near minimum-phase signatures. The wavelet has a fast build-up of energy after time zero, and no energy before time zero (Sheriff and Geldart, 1995; Simm and Bacon, 2014).

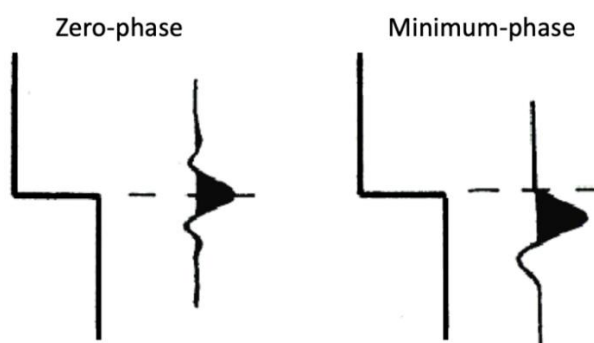


Figure 3.3.3: The figure illustrates the difference between zero-phase and minimum-phase. The line represents an increase in acoustic impedance along with the trace response. The zero-phased trace has the reflection point centred at the peak, whereas the minimum-phase has the reflection point centred before the peak. Modified from Sheriff and Geldart (1995).

3.3.1 Structural analysis

During a structural analysis the geometry of the reflectors are analysed. Usually major patterns are defined first, then more and more details are added. The geometry patterns can be used to indicate folds or fault geometries. When interpreting faults, one should begin by defining major faults, then add successive levels of detail. When the complexity of the faulting increases, it can be helpful to go back and forth between structural and stratigraphic interpretations to get a better understanding of the nature of the faulting (Hart, 2000). General knowledge of the tectonic setting in the area can also be very helpful. It is possible to generate structural contour maps to show the structures, where an isopach map shows the difference in TWT between two horizons. It is possible to convert the map from TWT to meters by using the appropriate interval velocities (Hart, 2000; Kearey et al., 2002).

3.3.2 Stratigraphic analysis

During a stratigraphic analysis, the seismic data are subdivided into discrete stratigraphic packages, before the variability and changes in seismic character of each package are analysed (Hart, 2000). The changes in seismic character will represent changes in depositional environment over time, where reflectors of the same character are assumed to have been deposited under the same conditions. The first step in a stratigraphic analysis is the seismic sequence analysis. Here, the major stratigraphic packages are defined by picking geological boundaries (Fig. 3.3.4). These boundaries are often unconformities, as they are easily recognised due to the change in reflection character on each side of the horizon (Hart, 2000; Kearey et al., 2002). After the major stratigraphic packages have been defined, the reflection character within each sequence is examined with objective of determining the depositional environments. This process is known as seismic facies analysis, where the reflection character is described in terms of frequency content, amplitude, continuity, and other shape descriptions (Fig. 3.3.5; Hart, 2000; Kearey et al., 2002). Finally, a reflection character analysis can be performed, which is generally done through modelling. The objective of reflection character analysis is to fully understand the links between seismic reflections, rock properties and geometries (Hart, 2000).

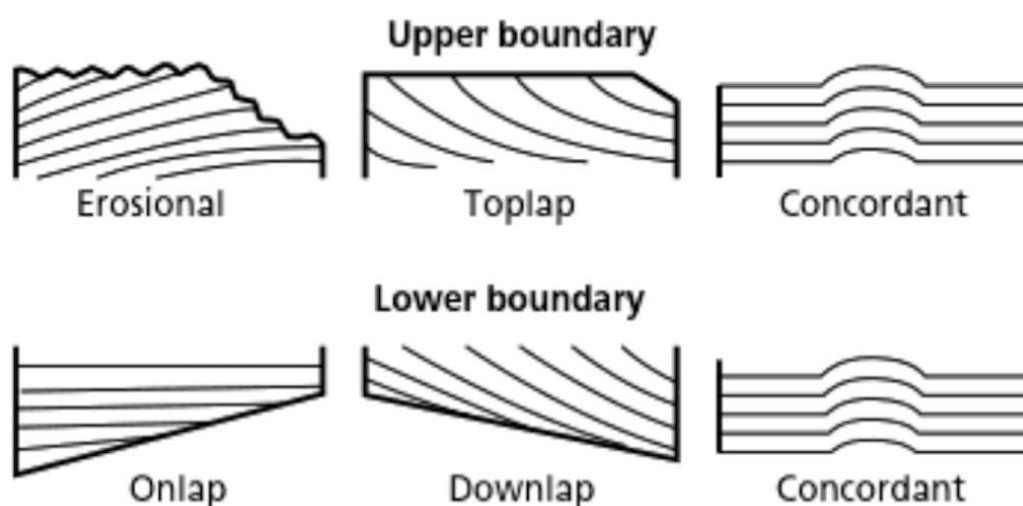


Figure 3.3.4: The figure illustrates different types of geological boundaries, from Kearey et al. (2002). These boundaries define seismic sequences where the upper three represent upper boundaries and the lower three represent lower boundaries.

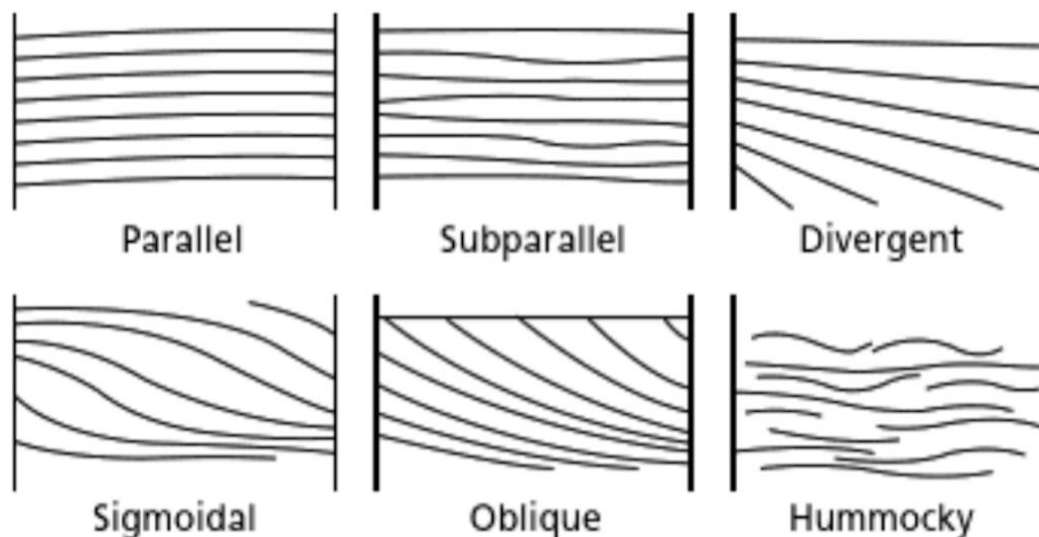


Figure 3.3.5: The figure illustrates different types of reflection characters, from Kearey et al. (2002). The reflection characters represent various internal bedforms that give rise to different seismic facies.

3.3.3 Seismic resolution

Seismic resolution is divided into vertical and horizontal resolution, where the seismic resolution is defined as the ability to separate two features that are closely spaced (Sheriff and Geldart, 1995; Herron, 2011). The resolution thus determines how large or thick the stratigraphic layers or the structural features needs to be in order to be visible in the seismic section. The seismic resolution is dependent on the signal-to-noise ratio, the acoustic impedance, the type of wavelet and the bandwidth (Hart, 2000; Simm and Bacon, 2014), where the resolving power of the data follows from the sampling theorem. The sampling theorem states that if there are fewer than two samples per cycle of a given signal, one signal may be mistaken for another. This is known as aliasing (Herron, 2011).

A thick bed with a high AI contrast compared to the surrounding beds will be visible in the seismic section, while a thin bed with low AI contrast will not be visible. However, if the changes in the physical properties of the surrounding beds are great enough, the thin bed may be visible. This means that there is a lower limit to the bed thickness that can be detected, where the thickness of the bed is related to the wavelength of the acoustic pulse (Hart, 2000; Kearey et al., 2002; Simm and Bacon, 2014).

Vertical resolution affects the ability to interpret stratigraphy and is determined by the wavelength (λ) of the seismic signal, which is given by formula 3.2. v is the vertical propagation velocity and f is the dominant frequency (Hart, 2000; Herron, 2011).

$$(3.2) \quad \lambda = \frac{v}{f}$$

The general rule is that the bed will not be visible in the seismic section if the bed thickness is less than $\frac{1}{4}$ of the wavelength. Shorter wavelengths will give better resolution than longer wavelengths, but will in return also attenuate faster. Because the velocities tend to increase with depth due to compaction, and deeper layers tend to have lower dominant frequencies due to attenuation, the vertical resolution decreases as a function of depth. (Hart, 2000; Kearey et al., 2002; Simm and Bacon, 2014). During processing, deconvolution can improve the vertical resolution by shortening the recorded pulse length.

Horizontal resolution is a measure of the lateral spacing between two points that determines how closely spaced they can be to be recognised as to separate points. The resolving power of the seismic data is described in terms of the Fresnel zone (Fig. 3.3.6). The Fresnel zone is defined as the portion of a reflector from which reflected energy can reach the detector with $\frac{1}{4}$ wavelength of the first reflected energy (Gelius and Johansen, 2010; Herron, 2011). Constructive interference over the Fresnel zone causes the reflections, whereas an area around the Fresnel zone tend to interfere destructively and cancel out. The width of the Fresnel zone represents a limit on the horizontal resolution, where distances smaller than this cannot be distinguished individually (Kearey et al., 2002). The Fresnel zone (F_r) is defined in formula 3.3, where λ is the dominant wavelength and Z is the depth to the target surface.

$$(3.3) \quad F_r = \sqrt{\frac{\lambda Z}{2}}$$

The width of the Fresnel zone almost always increases with depth. The velocities increase whereas the dominant frequencies decrease with depth. This results in a decrease in the horizontal resolution with depth. The Fresnel zones are measured with respect to unmigrated

seismic data, thus, doing migration during the data processing can help shrink the Fresnel zone and enhance the horizontal resolution (Hart, 2000; Herron, 2011; Simm and Bacon, 2014).

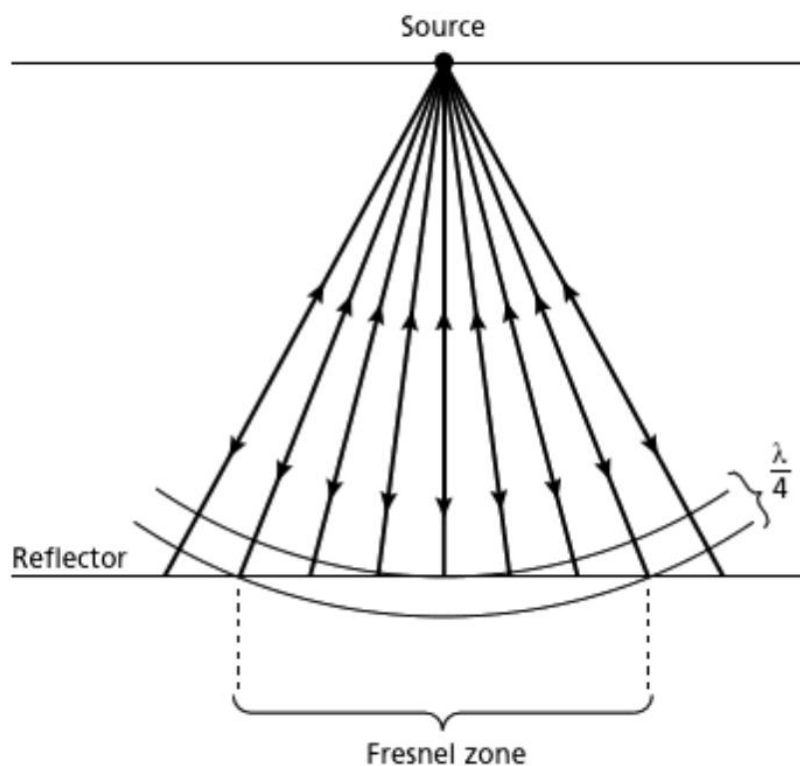


Figure 3.3.6: The figure illustrates how the energy is reflected from all points of a reflector. The Fresnel zone is the part of the reflector from which the energy is reflected from within $\frac{1}{4}$ of the wavelength of the initial reflected arrival. Modified from Kearey et al. (2002).

Chapter 4

Data acquisition

This chapter will go through the technical information of the data acquisition and the parameters that have been used. All of the information in this chapter has been collected from the cruise report by Mjelde (2003).

In 2002 from 30 August to 3 September a seismic survey was conducted in Isfjorden, Spitsbergen as a part of the student course SVALEX. This course was a collaboration between Statoil and the universities NTNU, UiB, UiO, UiS, UiT and UNIS. The 2D multichannel seismic reflection data were collected with the vessel R/V Håkon Mosby, with a total of 15 seismic lines and 517 km of data. The acquisition parameters are shown in Table 4.1, and were selected for the best imaging of structures at 3-5 km depth. All the lines were shot in fair weather conditions, with low streamer noise at 3-4 microbar. During acquisition a recording filter was used with a low-cut at 3 Hz and high-cut at 180 Hz. The recording filter removes low-frequency swell-noise, and it also acts as an anti-aliasing filter.

Table 4.1: The table shows the parameters that were used during acquisition.

Vessel	R/V Håkon Mosby
Speed	4.5 knots
Streamer	Length: 3 km Nessie 3 by WesternGeco
Recording system	Triacq by WesternGeco
Source	GEO, UiB air-gun string with 5 air-guns and one additional gun of 580 cubic inches
Shot-point interval	50 m
Sampling interval	2 ms
Group-length	12.5 m
Record length	12 s
Streamer depth	10 m
Air-gun depth	7 m
Channels	240
Distance from GPS antenna and centre of source	72 m
Distance from GPS antenna to first active channel	150 m
Low-cut filter	3 Hz and 18 dB/octave slope
High-cut filter	180 Hz and 72 dB/octave slope

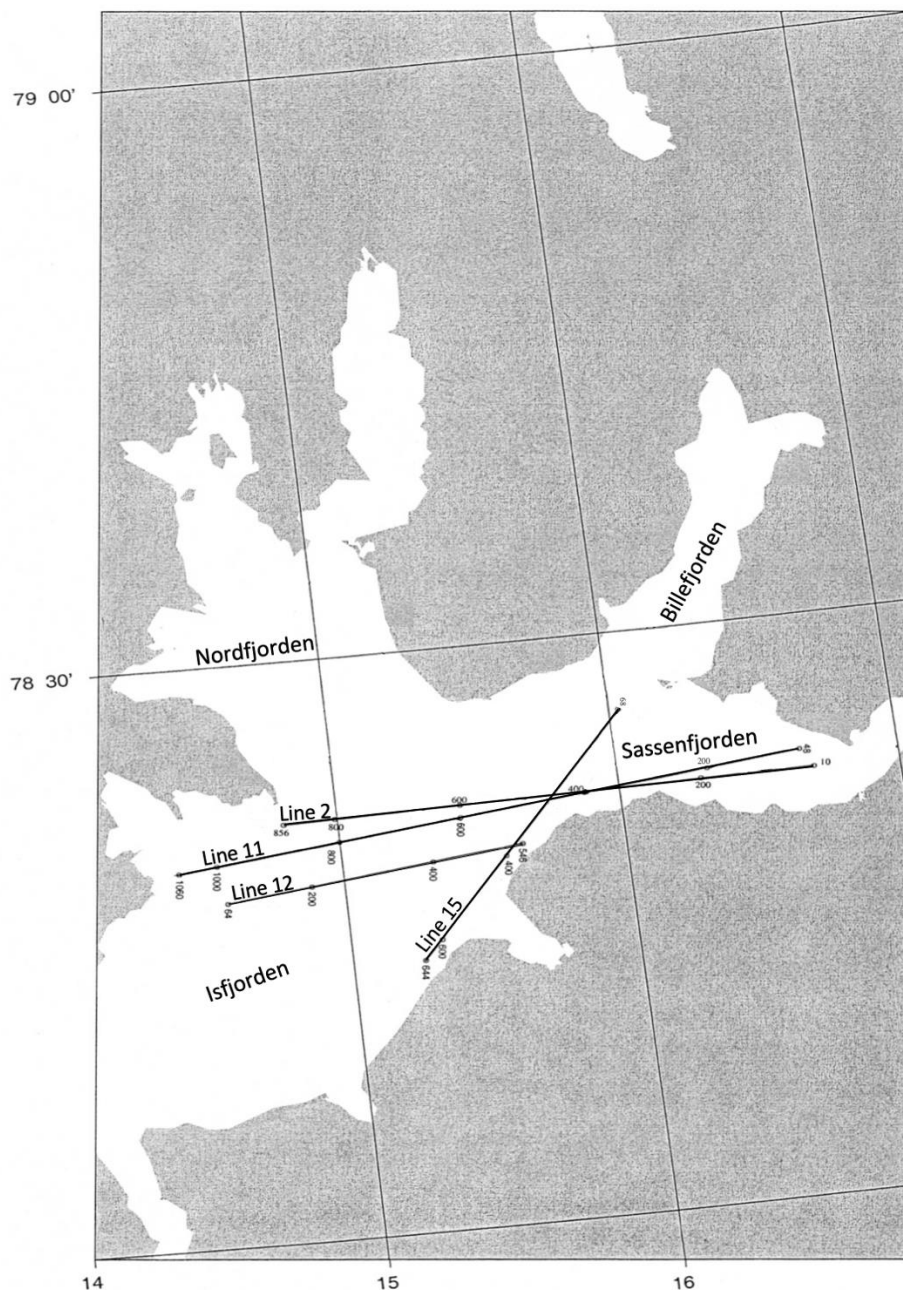


Figure 4.1: The figure shows an overview of the four multichannel 2D lines that have been processed and interpreted in this study. The lines were acquired during the SVALEX project in 2002. Modified from Mjelde (2003).

Figure 4.1 shows the four lines this thesis will study and the direction they were shot in. Line 2 and line 11 were shot in the same direction from Sassenfjorden across Isfjorden. Line 12 was shot in the opposite direction to the two other lines, from Gøtaneset eastwards across Isfjorden. The last line, line 15, was shot from the southern end of Billefjorden south-westwards along the north-eastern border of Isfjorden. The shooting direction can affect how the lines are imaged. This is because the source itself has a certain directivity, and because dipping structures in the subsurface image differently from different directions (Kearey et al., 2002). The geographical position of the lines is shown in Table 4.2, where the positions were recorded in UTM-datum, zone 33X.

Table 4.2: The table shows an overview of the geographical position of the lines. All the values are collected from the cruise report by Mjelde (2003).

Line no.	Event no.	Northing	Easting	°N	Nmin	°E	Emin	Length (km)
Line 2	10	ca.8734960	ca.807760	78	ca.22.5	16	ca.45	42.3
	856	ca.8728200	ca.764520	78	ca.22.0	14	ca.50	
Line 11	48	8736901.26	804253.15	78	23.024244	16	39.09012	52.5
	1060	8719781.76	756637.14	78	19.486674	14	25.613244	
Line 12	64	8717279.71	760604.68	78	17.76135	14	35.009628	26.55
	546	8725507.28	783256.85	78	19.587294	15	38.255316	
Line 15	68	8740763.06	789411.15	78	26.826504	16	2.833842	31.7
	644	8714855.05	776833.74	78	14.686764	15	15.385854	

There were some problems when acquiring two of the lines, line 2 and line 15. For line 2 the signal from gun 1 was lost close to the end of the line. This happened as a result of a loose signal cable, and even though the shot was shown as green on the gun-controller, the gun did not fire. For line 15, the last 244 shots were fired without gun 6. This happened as a result of a defect signal cable. During the generation of the shot-point map (Fig. 4.1) it was discovered that the navigation data for line 2 were lost, and that the plotted line coordinates for line 15 were incorrect. Because of this, the lines were drawn in manually based on the information from the planned survey and the field logs. This does not significantly influence the results, since the quality control performed during the shooting showed no anomalies.

The following figures shows the geometry of the air-gun configuration (Fig. 4.2), the far-field signature (Fig. 4.3) and the amplitude spectrum (Fig. 4.4). The geometry of the air-gun configuration is set up with 5 air-guns in a long array, i.e. along the direction of the vessel. The size of the air-guns decrease away from the vessel, where the total volume is measured at 2616.0 cubic inches. The last air gun has the largest volume and is placed 10 m to the left of the first air-gun. The total geometry is therefore a simple areal array. The long array focuses the energy vertically downward, where the decreasing air-gun size away from the vessel focuses the energy slightly backwards. The single air-gun located to the left provides attenuation of side reflections by ensuring that the source sends out a little less energy to the sides. The depth of the source and the receiver is chosen to create constructive interference with the direct wave and the ghost (Fig. 4.3 and 4.4). Because absorption causes higher frequencies to attenuate faster, the receiver needs to be located deeper than the source. Another reason for locating the receiver deeper is to reduce noise from the surface (Kearey et al., 2002).

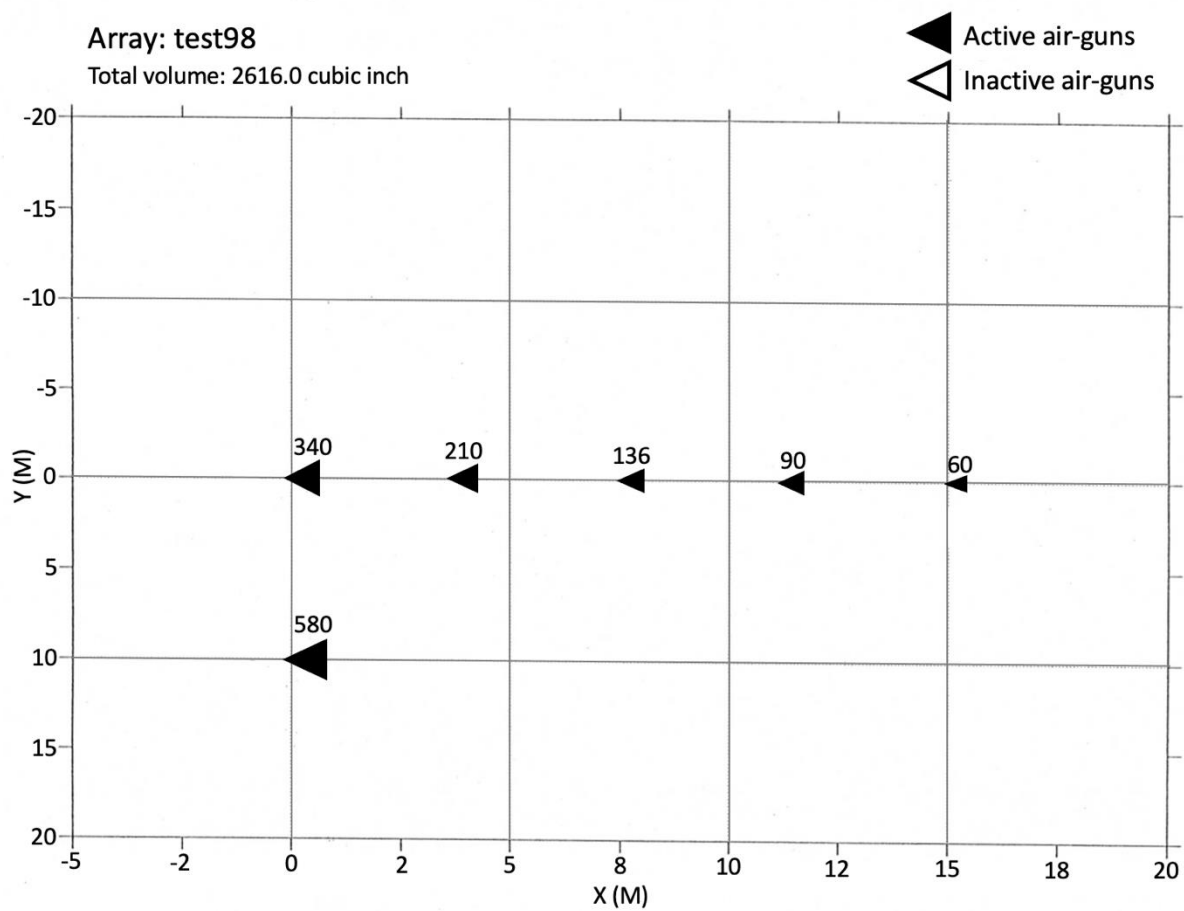
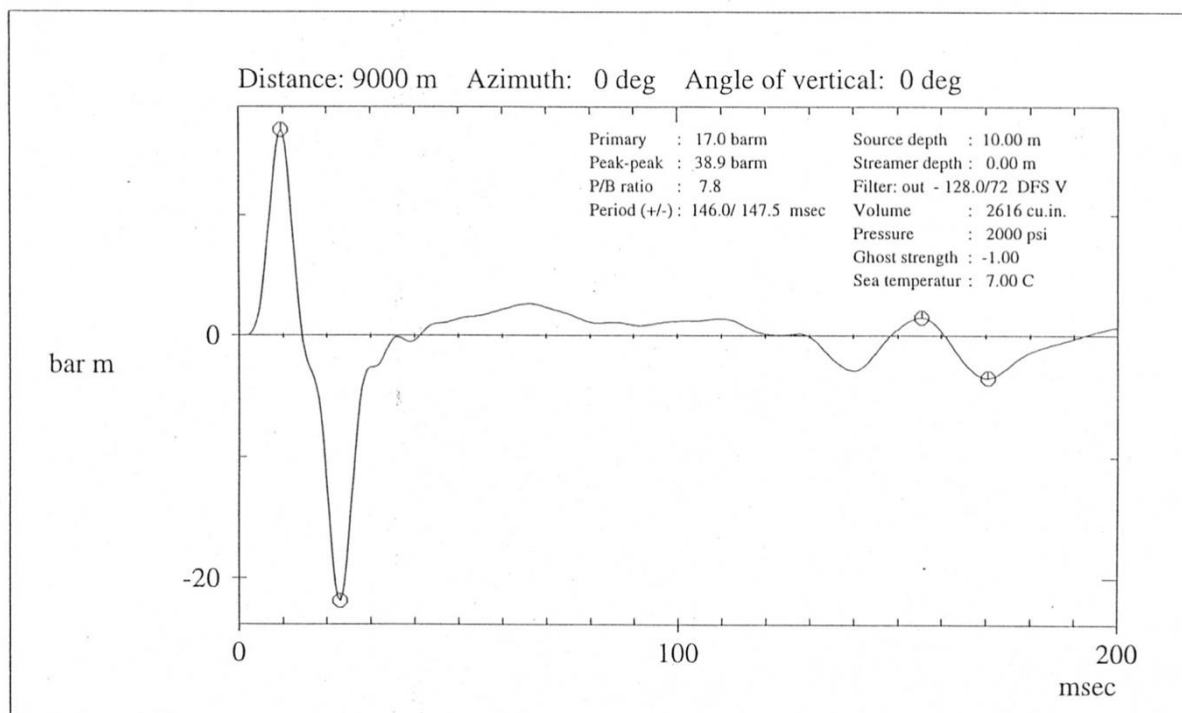


Figure 4.2: The source geometry (air-gun configuration) during the acquisition. The numbers over each air-gun states the volume in cubic inches. Modified from Mjelde (2003).

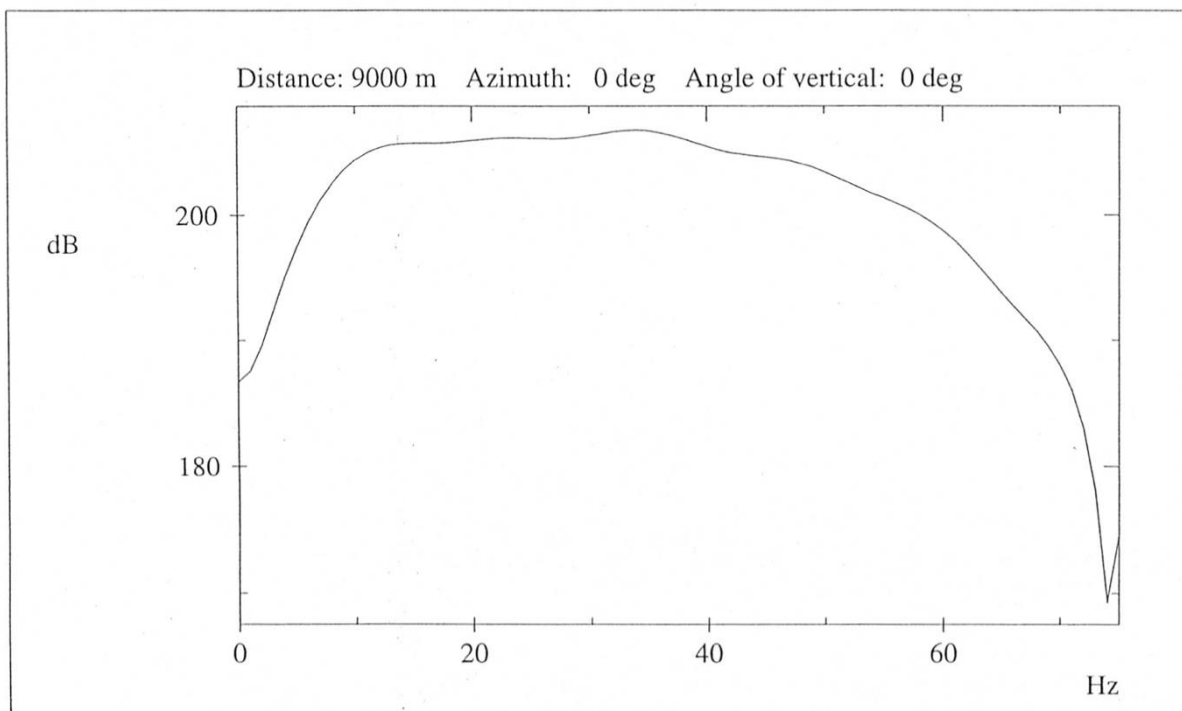
Far-field signature of array: test98



1200,580 10m

Figure 4.3: The far-field signature of the source array (Mjelde, 2003).

Amplitude spectrum of far-field signature of array: test98



1200,580 10m

Figure 4.4: The amplitude spectrum of the far-field signature of the source array (Mjelde, 2003).

Chapter 5

Processing

In this chapter the Geocluster software that have been used during the processing will be presented. The chapter also contain a review of the processing workflow that has been used, in addition to figures that illustrate how each processing job affects the seismic data.

5.1 Software – Geocluster

The whole processing has been done in Geocluster 5.0, which is a software developed by CGGVeritas. The software contains a variety of packages and tools that can be used during processing, where the tools used in this study are briefly described in the sections below. When opening the software, Geopad serves as the main page. It is a file manager that shows an overview of all the available data and the different jobs in the project. It is also possible to open all the different tools and applications from Geopad.

5.1.1 Xjob

Xjob is a tool used to build different processing jobs by setting up a workflow. A processing sequence consists of several processing jobs that run after another. A processing job is built by adding different modules in the desired order, where each module contain different parameters that need to be adjusted to the dataset.

5.1.2 Teamview

Teamview is an application that is used for displaying the seismic data. By displaying selected parts of the seismic data after each processing job, it is possible to get an overview of how each job influences the data, and thus see if the purpose of the job is achieved. It is also very useful in assessing which parameters to use in the different modules by comparing the results. Teamview can be used to visualise and assess a range of different factors, some that have been important during this processing are velocities, frequency content, fk-spectrum, manually picking of seabed and mute. It is possible to plot the data with different types of amplitude scaling, axis and colourmaps. The figures presented in this chapter have the same

amplitude scaling, which is RMS. This type of scaling is calculated from the root mean square (RMS) amplitude from all of the plotted traces. The colourmaps used are 'BlackWhite31' and 'BlueWhiteRed31' for the fk-spectra.

5.1.3 GeoVel

GeoVel is a part of the ChronoVista software package, and is used to perform the velocity analysis in time domain as well as quality control of the analysis (CGGVeritas, 2008). GeoVel contains a variety of different tools that can be combined with the velocity analysis. In 'Velocity Analysis Viewer' it is possible to pick stacking velocities and horizons. The quality control has been done in IsoVel, where it is possible to view the interval velocities. In this window it is possible to correct the velocities if any deviations are discovered. In order to use the picked velocities in Geocluster modules, they need to be exported to an Xps library.

5.1.4 Xps

Xps is an interface to a database which is used to store data, these can for instance be estimated velocity results from the velocity analysis or estimated sea bottom depths. The data are saved with an 'ident' and 'version' name, where the ident needs to be the same for all libraries used in the same job, and the version needs to be different. The data are stored in a library which makes up the Xps, where only certain modules can read the libraries. It is possible to view the values from the data in the library, and to edit them if necessary.

5.2 Processing sequence

The processing sequence consists of multiple steps, where the main purpose is to remove water layer multiples and other noise components from the seismic data. The processing sequence contain 11 jobs (Appendix A). Multiple jobs were repeated during the processing to assess which modules achieved the desired result, and which values that were the best. The assessment was done in Teamview. One of the biggest challenges during this processing sequence was to suppress the multiples without affecting and severely reducing the primary energy. Hence, the goal is to find a satisfying processing sequence that optimizes this task. Table 5.2.1 shows the processing sequence that was used during processing, where all the

lines have been processed in the same way. Line 2 has been used as an example of the processing.

Table 5.2.1: The table shows the processing sequence that have been used during the processing of the data.

Editing	
SEGIN	Read shot gathers in SEG-Y format
QCTRL	Quality control, check if all traces are present
HISTA	Reduce trace length
FILTR	Butterworth band-pass filter to remove noise from waves, wind, other vessels, and streamer noise
RSAMP	Resample traces from 2 to 4 ms, reduce data amount
SPASM	Remove noise known as noise burst
MODET	Calculate and update header words to GCT format, e.g., CDP number and offset



Signature deconvolution	
INPTR	Read output from editing
DESIG	Signature deconvolution to reshape signal and attenuate bubble pulse
SPARN	Remove incoherent noise between 7.5 Hz and 50 Hz
REFOR	Correction for spherical spreading
SPASM	Spatial amplitude smoothing to attenuate spikes
FKFIL	Velocity (FK) filtering to remove streamer noise and the direct wave

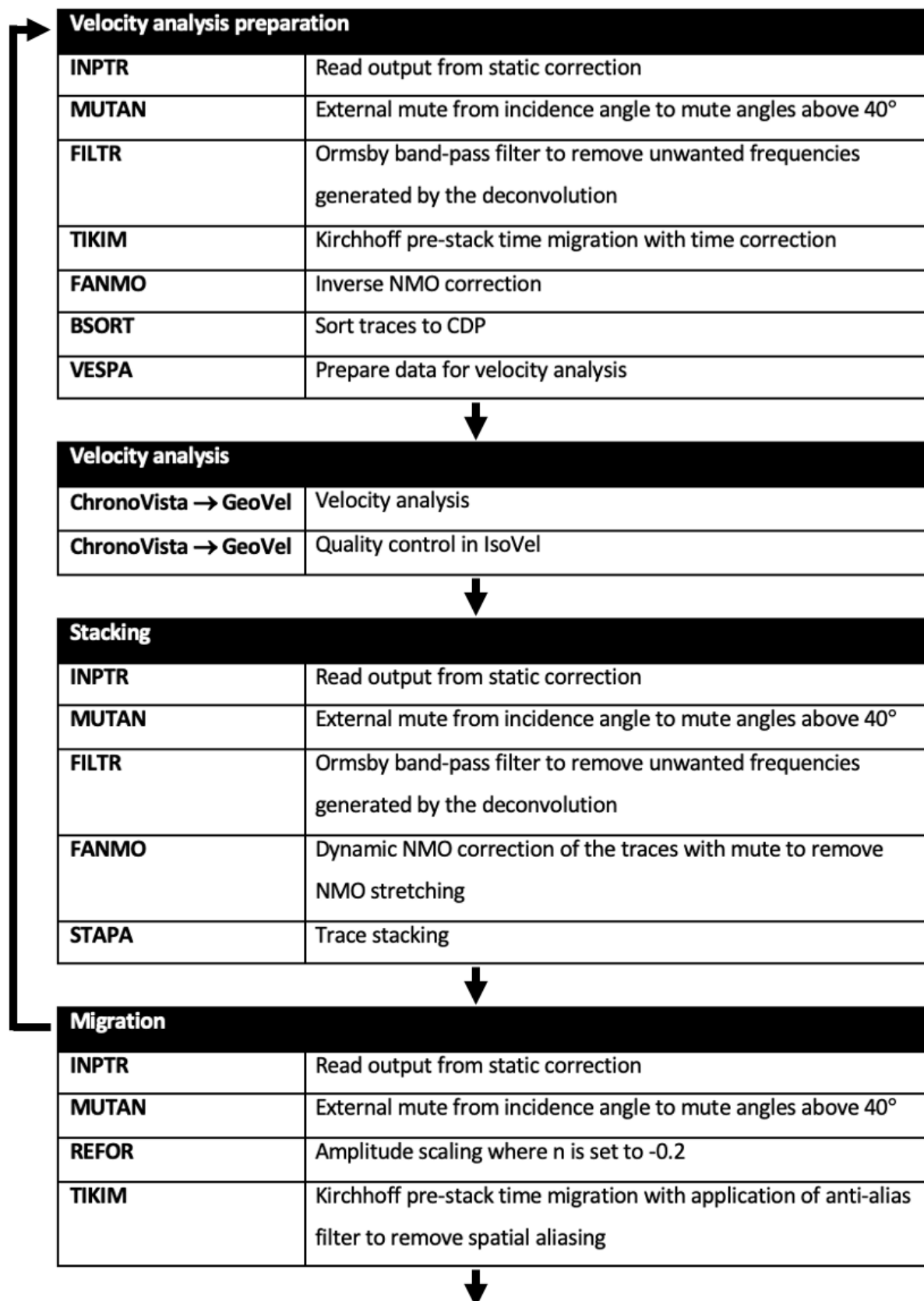


Filtering	
INPTR	Read output from deconvolution
FKFIL	Velocity (FK) filtering of shot gathers
BSORT	Sort to receiver gathers
FKFIL	Velocity (FK) filtering of receiver gathers
BSORT	Sort to CDP gathers
RECOV	Amplitude recovery to smooth anomalies and recover amplitudes of real reflection
DECSC	Surface consistent predictive deconvolution to remove water layer multiples



Static correction	
INPTR	Read output from filtering
HABIL	Read receiver water depth
MODET	Receiver side statics to calculate the receiver water depth correction
HABIL	Read shot water depth
MODET	Shot side statics to calculate the shot water depth correction
MODET	Total statics to calculate correction for all traces
HEDFI	Remove average statics for each CDP gather
HISTA	Apply statics to correct local variations





Mute with stack	
INPTR	Read output from migration
MUTES	Manual mute to remove migration-stretching and refractions
STAPA	Trace stacking
MNGTY	Merge traces into one gather
FKFIL	Dip filtering in fk-domain to remove spatial aliasing
TVDEF	Time variable band-pass customized to how the spectrum of the signal is expected to change with time
PFILT	Change pulse shape to zero-phase

↓

Write SEG-Y	
	Read output from mute with stack
HABIL	Get UTM coordinates
MODET	Copy UTM coordinates
SEGOU	Write SEG-Y

5.2.1 Editing

The vessel Håkon Mosby record the data in SEG-D format, but store it in SEG-Y because it is easier to work with. The first step in the processing is to read the SEG-Y data and reformat it to an internal Geocluster format, which is called GCT. The next step is to check if all the traces are present; this is done by performing a quality control on the data. If there are any deviations, it will be listed in the script. In this case, there were no deviations. The trace length is reduced from 12 288 ms to 6 144 ms, which will help the processing jobs to run faster, making the processing more effective.

After the trace length reduction, a band-pass filter is used to filter out low-frequency swell noise, and high-frequency noise from wind and other vessels. The low-frequency cut value is set to 8 Hz with a slope at 24 dB/octave, and the high-frequency cut value is set to 90 Hz with a slope at 48 dB/octave. This is known as a Butterworth filter. The next step is to resample the signal from 2 ms to 4 ms, where the purpose is to reduce the total data amount. By doubling the sampling interval, the Nyquist frequency halves to 125 Hz. Aliasing is prevented by the previous module, as frequencies above 90 Hz have already been cut. Spatial amplitude

smoothing is then used to remove noise bursts. All the traces are compared to neighbouring traces, where high amplitudes that are not repeated will be considered as noise and reduced.

An important part of the processing is to update the header words. The SEG-Y standard specifies a large number of header words that may vary from dataset to dataset, however, these are not exactly the same as in the GCT format. Important header words as shot number, channel number, number of samples per trace and sample interval, will be transferred. Important information about the traces are collected from the acquisition set-up (Table 4.1). Finally, the pre-processed dataset is saved.

Before the dataset is saved, some shots are selected for display. The results can be viewed in Teamview, where a quality control is performed. The first shot points are not included in the display as they are too noisy. The signals in these first shot points curve upwards. This happens because the streamer is in a curve when the boat turns to start the new line. Figure 5.2.1 shows an outcrop of some of these selected shots, where it is possible to see the different types of waves. The direct wave is recorded first as a straight line, followed by the bubble pulse. The weaker linear lines are the refracted waves. The first strong curved line is the seabed reflection, followed by several water layer multiples with decreasing amplitude downward in the section. These water layer multiples are considered as noise, and later processing jobs will try to remove these to the greatest extent possible.

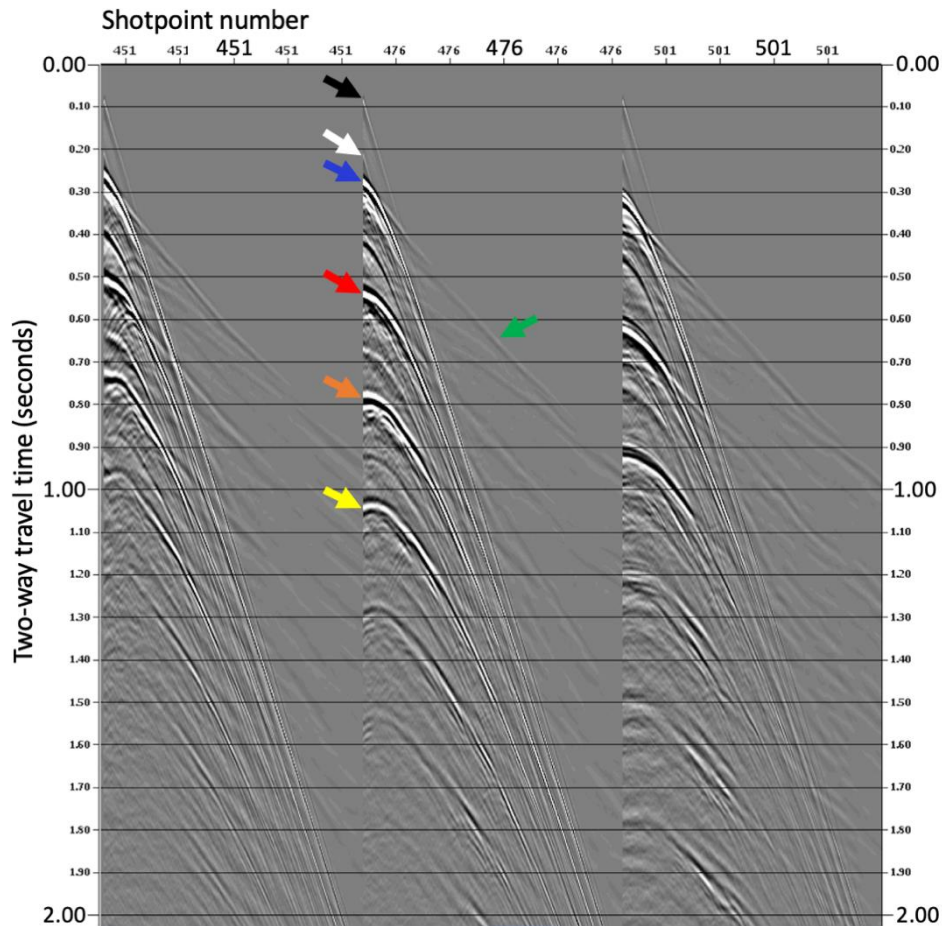


Figure 5.2.1: The figure shows selected shot gathers for line 2. On shot gather 476, arrows are used to show the direct wave (black), the bubble pulse of the direct wave (white), refracted wave (green), seabed reflection (blue), and the first (red), second (orange) and third (yellow) water layer multiple.

A near trace plot shows a collection of the first trace in every shot gather. It is important to generate a near trace plot early to get an overview of the profiles and possible challenges. The near trace plot (Fig. 5.2.2) shows that the seismic is strongly affected by water layer multiples that hide real structures in the section. To help remove the water layer multiples, the seabed is picked manually in Teamview. The picking is saved in a water bottom library in Xps; this can be used during later processing jobs to define the seabed, and thus, remove the water layer multiples.

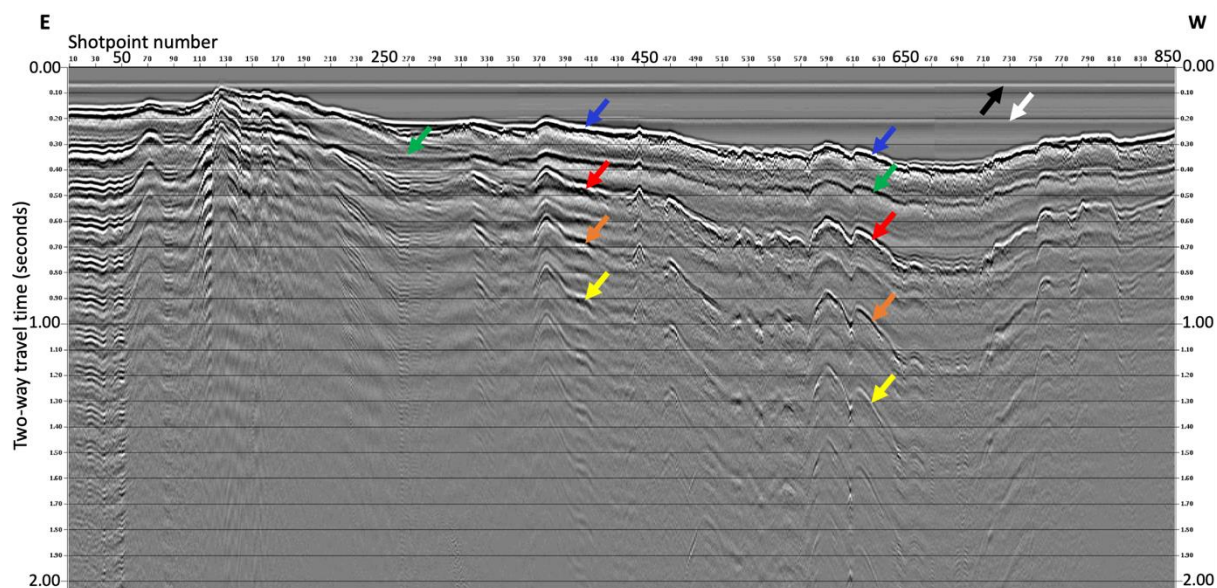


Figure 5.2.2: The figure shows a near trace plot of line 2 after editing. The arrows show the direct wave (black), the bubble pulse of the direct wave (white), seabed reflection (blue), the bubble pulse of the seabed (green) and the first (red), second (orange) and third (yellow) water layer multiple.

5.2.2 Filtering and deconvolution

The recorded seismic data contain abnormally high velocities in the shallow layers underneath the seabed, this causes the multiples to be especially strong. Because the seabed in general is very shallow, the multiples repeat at short intervals. Filtering and deconvolution steps can be used to attenuate or remove these multiples. Figure 5.2.3 illustrates how the f_k -spectra of the shots appear before filtering and deconvolution.

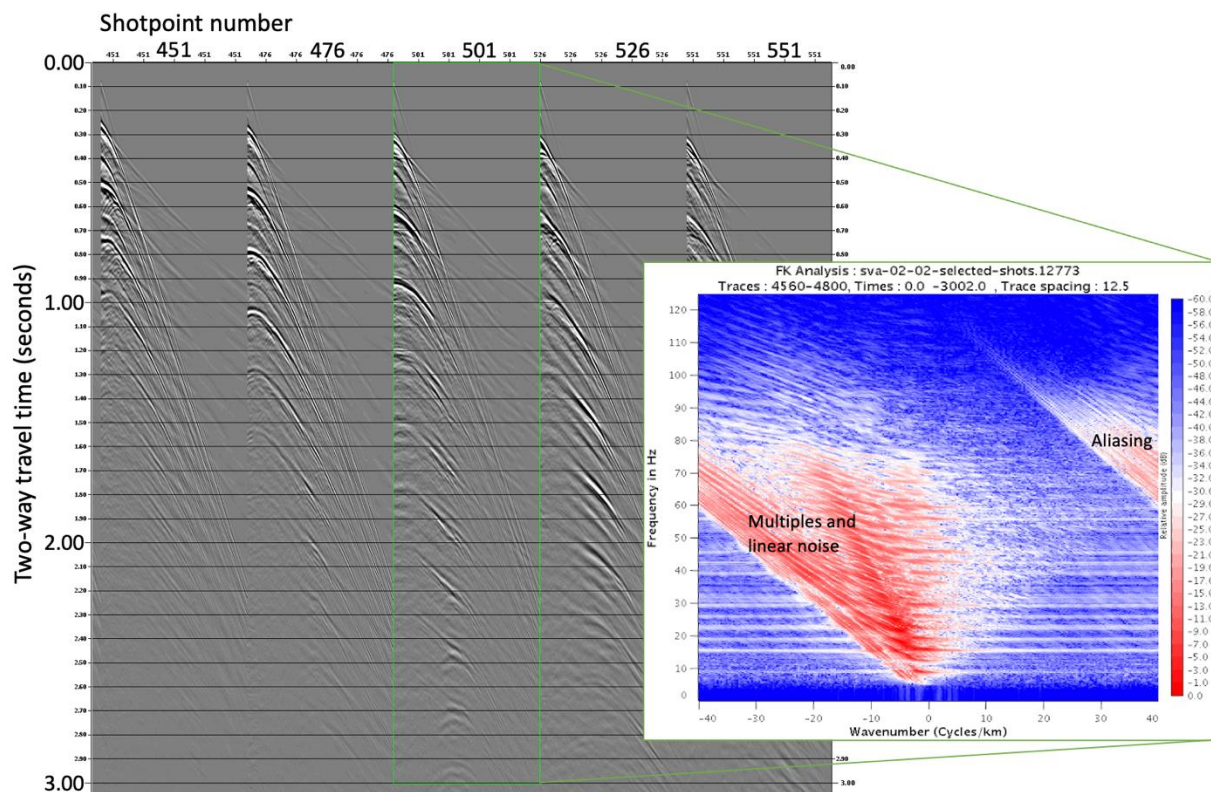


Figure 5.2.3: The figure illustrates a shot gather from line 2 before filtering and deconvolution. From this shot gather, a fk -spectra was generated. The spectra shows how the energy from the shot gather is partitioned, where multiples and linear noise dominates over the wanted energy. Aliasing occurs at high frequencies and high wavenumbers.

The first step is to perform a signature deconvolution on the shot gathers, where the main goal is to reshape the signal and attenuate the bubble pulse. Afterwards, a range of steps are performed to improve the quality of the dataset. The first one attempts to remove incoherent noise, where the minimum processing frequency is set at 7.5 Hz and the maximum at 50 Hz. The second is a spherical spreading correction, which uses a time-power method (Ruud, pers. comm.). The scaling is calculated as t^n , where t is time and n has been set to 1. This restores the amplitudes of reflectors in the deeper parts of the section, which is most affected by the spherical spreading. The third step is spatial amplitude smoothing to attenuate spikes.

Several fk -filters are added to remove multiples, refractions and other types of noise that occur outside the zone that is typical for reflections. The fk -filters use the apparent velocity to remove unwanted noise events that have velocities outside a set velocity boundary, and keep the energy inside the boundary (Fig. 5.2.4). The velocities of the refracted waves in the shallow layers are measured in Teamview and used to set the velocity boundary for the fk -filters. The

velocities are estimated to over 5 km/s, close to 6 km/s, for all the lines except line 12, which has somewhat lower velocities at around 4 km/s. By choosing a boundary value slightly higher than the measured velocities, a lot of the water layer multiples will be removed while the primary reflections will be retained. Velocities with high wavenumber and high frequency represent refractions or aliasing and needs to be filtered out.

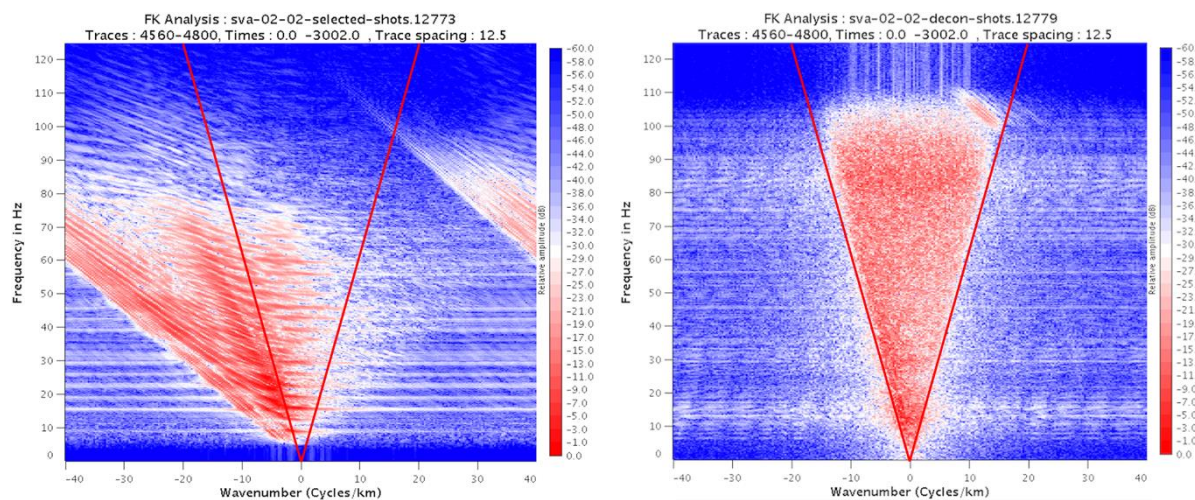


Figure 5.2.4: The figure to the left illustrates the *fk*-spectra before filtering and deconvolution, while the figure to the right illustrates the *fk*-spectra after filtering and deconvolution. The red lines represent the *fk*-filter as a triangle. The energy inside this triangle is kept, whereas the energy outside is removed.

The effect from the velocity filter will vary with the direction the line was shot in, since the seabed is not flat. To avoid an asymmetric effect in the *fk*-spectra, it is possible to apply the *fk*-filter twice. First for the shot gathers, then resort the data to receiver gathers and apply the *fk*-filter again. The data are then sorted into common depthpoint (CDP) gathers before amplitude recovery is attempted to improve the data quality. This is done by amplifying weaker amplitudes and smooth anomalies to recover true relative amplitudes of reflections (Hart, 2000). Surface consistent predictive deconvolution uses the water bottom library made from the near trace plot to attempt to remove the water layer multiples that remain after the *fk*-filtering. This is a statistical method, where separate filters are calculated for each source and receiver location (CGGVeritas, 2008).

By comparing the shot gathers in Figure 5.2.5 to Figure 5.2.3, it is possible to see that the direct wave, bubble pulse and refracted wave have almost been removed completely. When comparing the fk-spectra from the two figures, it is also possible to see that the multiples, linear noise, and aliasing are largely removed. The strong noise components pointed to by the red arrow in Figure 5.2.5 will be muted in a later processing job. The remaining multiples and noise, which have become clearer due to the amplitude recovery, can be removed by adjusting the fk-filter values. However, adjusting these values might in return also remove some of the reflected energy. Some of this strong energy might also represent real reflections from high-velocity magmatic intrusions, which are known to exist in the area (Senger et al., 2014). It was decided that the set values should be kept, as later processing jobs would attenuate the noise further.

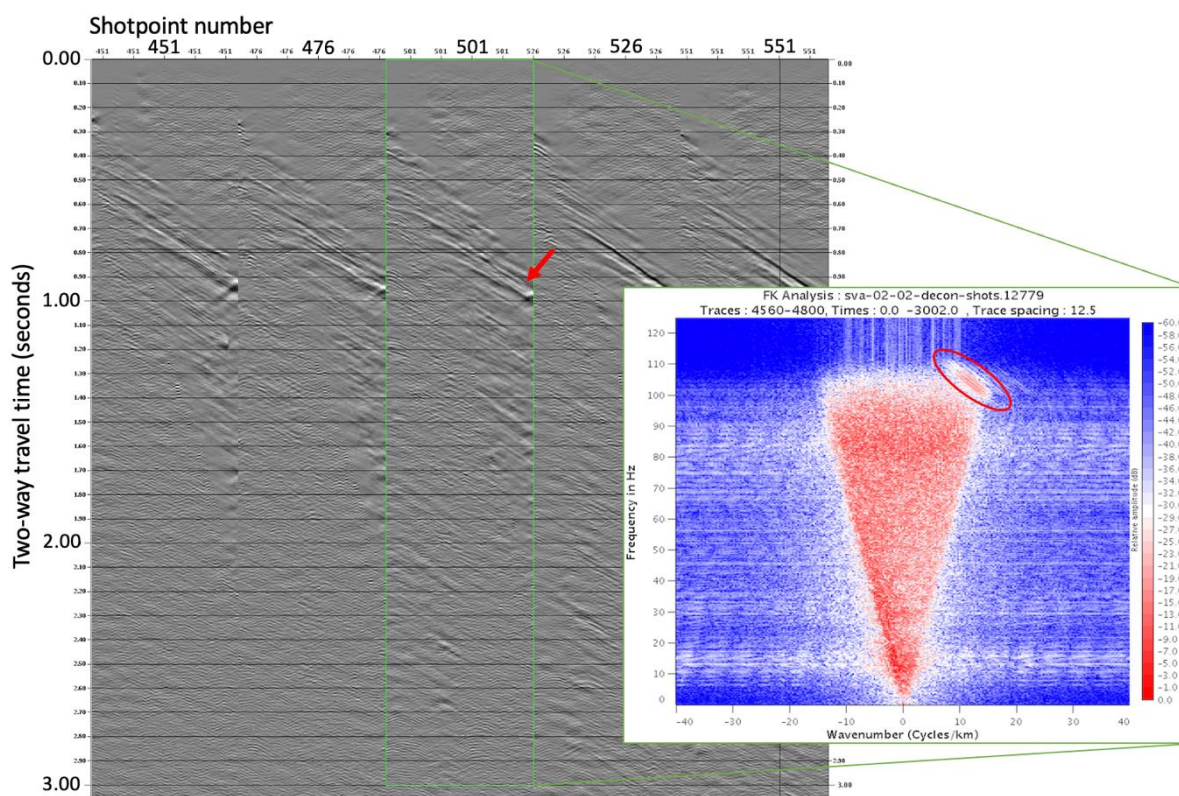


Figure 5.2.5: The figure illustrates a shot gather from line 2 after filtering and deconvolution. A new fk-spectra was generated from shot gather 501, which shows the improvement in energy partitioning. A lot of unwanted energy has been removed. However, some aliasing still remains and is marked by a red circle in the fk-spectra around wavenumber 10 and frequencies between 100-110 Hz. The red arrow points to some strong noise components that will be muted at a later processing stage.

5.2.3 Static correction

From the near trace plot (Fig. 5.2.2) it is clear that the seabed has large topographical changes. These changes were partly caused by glacial activity during the Quaternary period, as well as erosion and varying rock hardness. The water depth variations can cause unwanted velocity pull-up and push-down distortions that can severely damage the quality of the data. These distortions can cause local highs or lows in the topography to be repeated down the seismic section (Samson and West, 1992).

Static correction is performed on the data to correct for these pull-up and push-down effects. The correction is calculated as difference in TWT for vertical rays that travel through the water layer, compared with the time they would use if the water was replaced with rocks with the same velocity as the seabed (Ruud, pers. comm.). Hence, the water bottom library is used. The correction from the shot water depth and receiver water depth is added, then the correction is calculated for all traces before the average is removed from each CDP gather. At the end, the correction is applied to all the traces. The result from the static correction is presented in Figure 5.2.6.

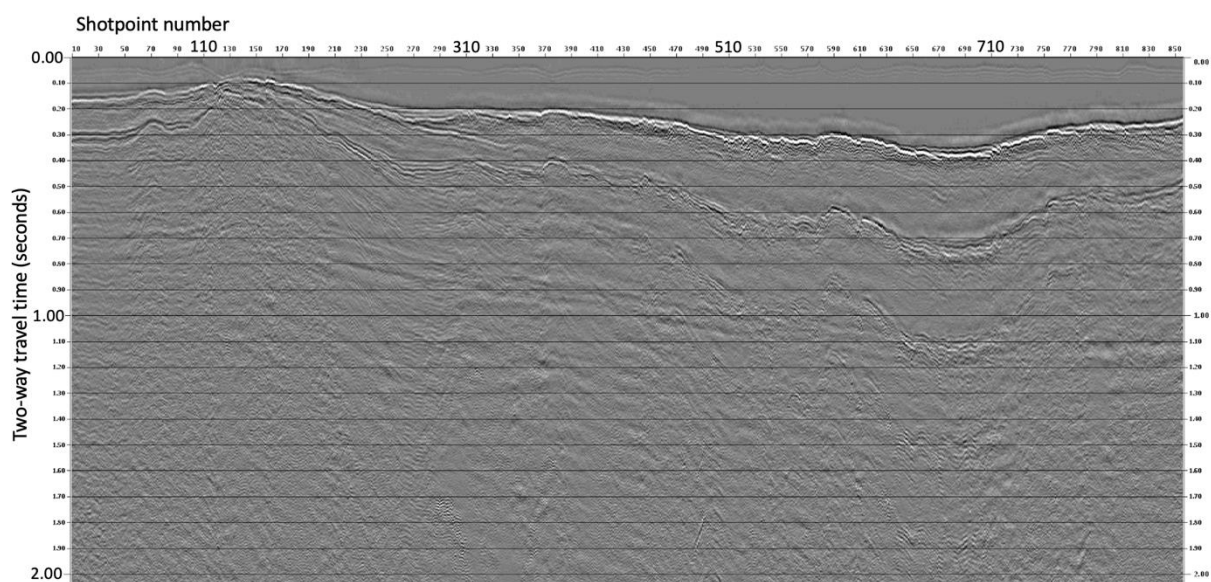


Figure 5.2.6: The figure illustrates a near trace plot of line 2 after static correction. When comparing this figure to the near trace plot after editing (Fig. 5.2.2), most of the multiples and bubble pulses have been removed. It is now possible to start to see some real reflections. Stacking will amplify these real reflections and attenuate the remaining multiples.

5.2.4 Velocity model

The next step in the processing sequence is to build a velocity model of the data. The purpose of this step is to estimate the velocities in the best way possible to obtain the clearest image of the subsurface. This is done by making a very simple velocity model as a starting point for the velocity analysis. By doing this, the velocity analysis will be simpler as it has a sensible model to proceed from. First, traces with zero amplitude are generated, and a range of CDP intervals are selected. CDP gathers are used because one would like to find the wave velocities when the layers are horizontal. The interval velocity below the seabed is first set to 3000 m/s, then a mute library and a water bottom library is added to mute above the seabed. Finally, 1500 m/s is added, resulting in the velocities above the seabed becoming 1500 m/s, and the velocities below becoming 4500 m/s. The velocities are converted from interval to RMS velocities, where the output from the job is a velocity library that are used as reference velocities in the velocity analysis (Ruud, pers. comm.).

5.2.5 Velocity analysis

After the velocity model has been built, the next step is to perform a velocity analysis. Before the velocity analysis can be performed, the data needs to be prepared. The preparation starts by muting traces based on incidence angle, which is calculated from the offset of the traces together with a velocity library generated from the velocity model. During the preparation for the first velocity model, the angle is set to 45°, where higher angles will be muted as they are mainly influenced by noise. An Ormsby band-pass filter is applied to remove noise, where the filter values are set to 5 Hz, 15 Hz, 75 Hz and 100 Hz. Then, Kirchhoff pre-stack time migration is performed, using the preliminary velocity model. The migration module also performs a time correction similar to NMO correction. An inverse NMO correction is performed on the data using the same velocities as the migration. By migrating the data before the velocity analysis, the velocity analysis becomes simpler and more correct, even if the preliminary velocity model is not entirely accurate (Ruud, pers. comm.). This process can be repeated with an improved velocity model. During the second preparation for the velocity analysis, the mute angle is changed to 40°, and the velocity library from the velocity model is replaced with the one created from the first velocity analysis. At the end, the traces are sorted into CDP gathers before the data are prepared for the velocity analysis by calculating the velocity spectrum and converting the data to velcom format.

The velcom file is imported to GeoVel, where the velocity analysis takes place. Tools in GeoVel are used to pick the velocities, and the velocities can be picked in the velocity spectrum or the mini-stack window (Fig. 5.2.7). The picked velocities are calculated and used to represent chosen velocities inside the interval velocity window. One window shows what the traces look like before NMO correction, and another window shows how the traces appear when NMO corrected. These windows can be used to check that the hyperbolas straighten out, or if they are under- or overcorrected, and thus, show if the correct velocity has been picked. It is also important to only pick primary energy, and not multiple energy, as this will affect the final result.

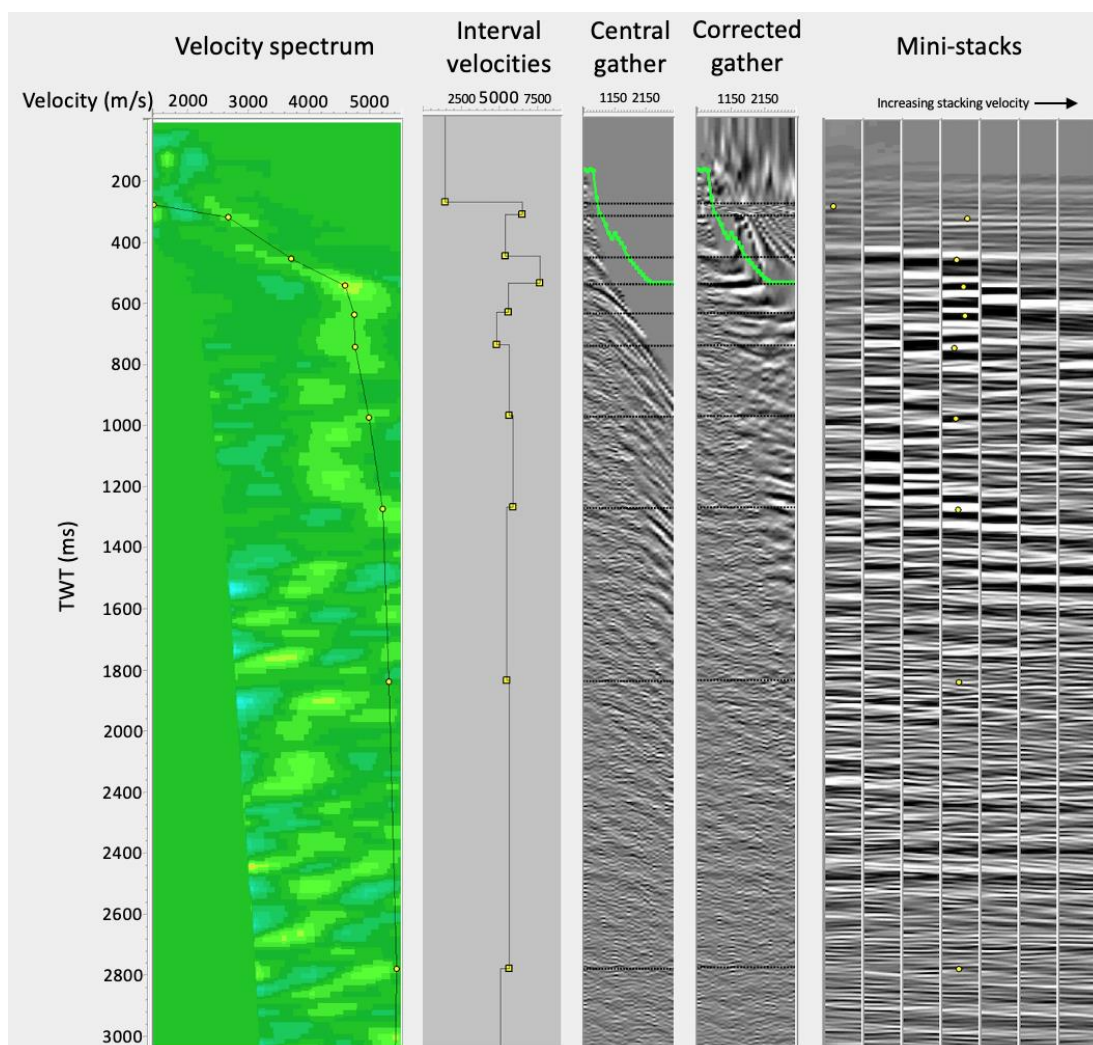


Figure 5.2.7: The figure shows a section from the velocity analysis of line 2 CDP 3124 in GeoVel. The first window shows the velocity spectrum, which is calculated from the velocities within a CDP interval. The second window shows the picked interval velocities. The third and fourth windows show the CDP gather with and without NMO correction, where everything above the green line is muted. The last window shows the mini-stack, where the yellow dots indicate the picked velocities.

Figure 5.2.7 shows picked velocities from a section of CDP 3124. For each of the seismic lines there are a range of such sections, where velocities have been picked. Velocities have not been picked from the first or last CDP gathers, as these contain few traces. Every other CDP gather was picked, where the remaining got assigned interpolated values calculated from the picked velocities. The distance between the picked CDP gathers is 2.0 km. The first picked velocity is the seabed, which should be around 1.5 km/s, and represents the water velocity. Then, the lines have a steep increase in interval velocity to around 4.5 and 6 km/s. The highest velocities might represent magmatic intrusions or high-velocity sedimentary rocks, like carbonates. In general, the velocities should increase down the profile. However, the rocks underneath the seabed have very high velocities. This can result in some local low-velocity layers where the velocity decreases before it increases again further down the profile. A quality control of the velocity analysis is performed in IsoVel, where Figure 5.2.8 illustrates the picked interval and RMS velocities for CDP 3124. Thus, it is easier to evaluate and check the picked velocities and to do changes.

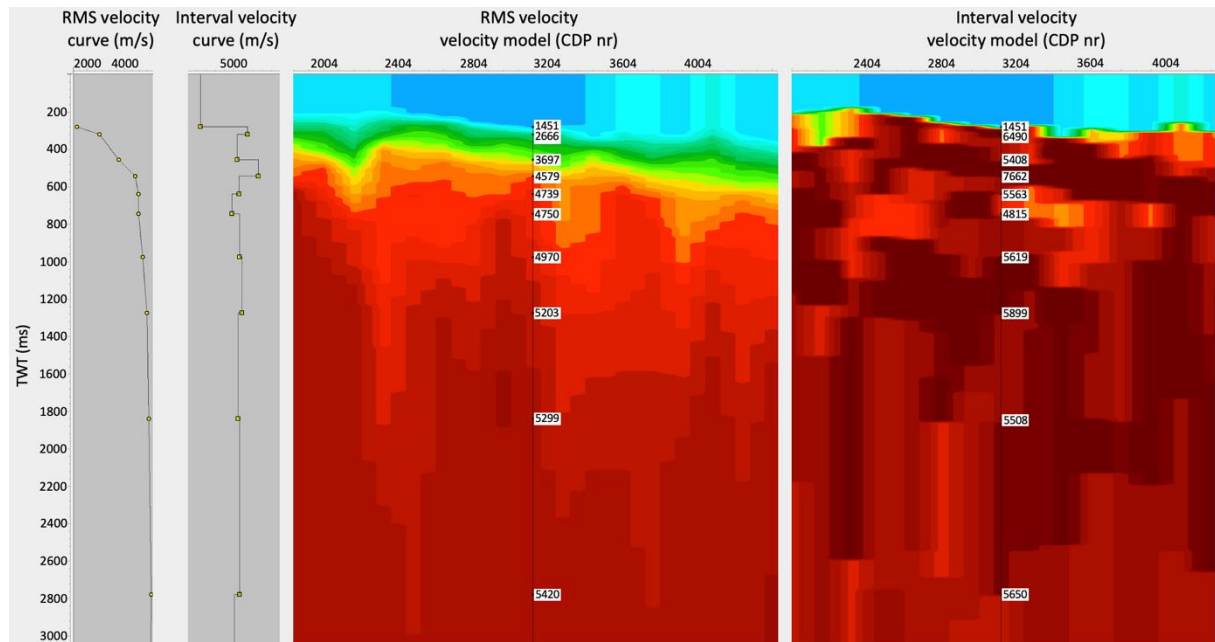


Figure 5.2.8: The figure shows a section from the quality control of line 2 CDP 3124 in IsoVel. The first two windows show the RMS velocity and interval velocity curves. The two last windows show the velocity model for the RMS velocities and the interval velocities. The two velocity windows show how the velocities varies as a function of TWT and CDP, where the velocities listed inside the two windows are the velocities for CDP 3124.

When the velocities are approved in IsoVel, the next step is to export the velocities to a velocity library in the Xps database. Thus, these can be used during the next processing jobs. By evaluating the result from the pre-stack migration, it is possible to evaluate whether the picked velocities are correct. Figure 5.2.9 shows a comparison between the final velocity and two other velocity fields, where one is scaled 10% up and the other 10% down. If the structures are better imaged with higher or lower velocities, it is possible to adjust them in IsoVel.

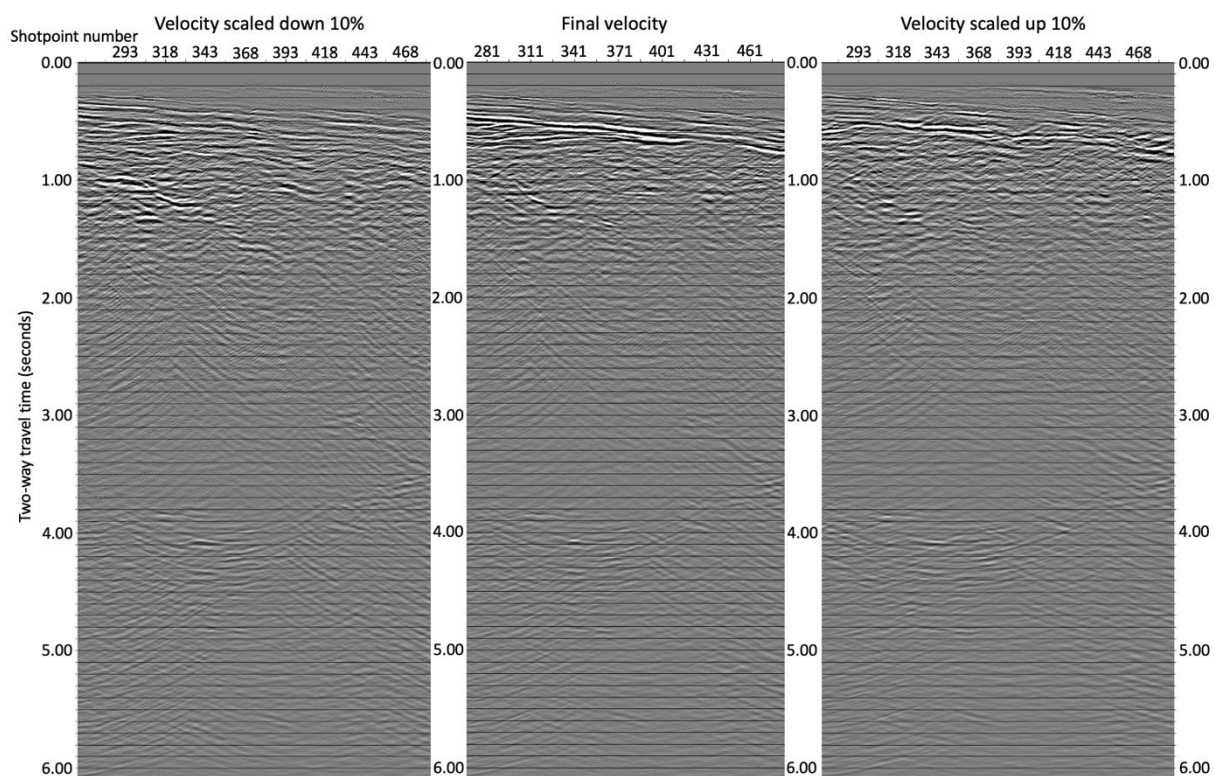


Figure 5.2.9: The figure compares the different velocities for line 2. The picked velocities from the velocity analysis represents the final velocity. The left window represents the seismic section when the velocity is scaled down 10%, whereas the right window represents the velocity scaled up 10%.

5.2.6 Stacking

After the velocity analysis, the data are stacked to get an overview of how the previous processing jobs have affected the seismic this far. It is a quick stack that uses the preliminary velocity model, and is commonly referred to as a brute stack. This step is only done as a quality control to get a quick result that can be used as a comparison for the subsequent processing jobs. The first step in the stacking is to do an external mute from incidence angle, where angles

above 40° are muted. Then an Ormsby filter with limits set to 5 Hz, 15 Hz, 75 Hz and 100 Hz, is applied to remove noise. The traces are then NMO corrected before they are stacked. This will be a simple stack, where the different velocity libraries are compared in Figure 5.2.10.

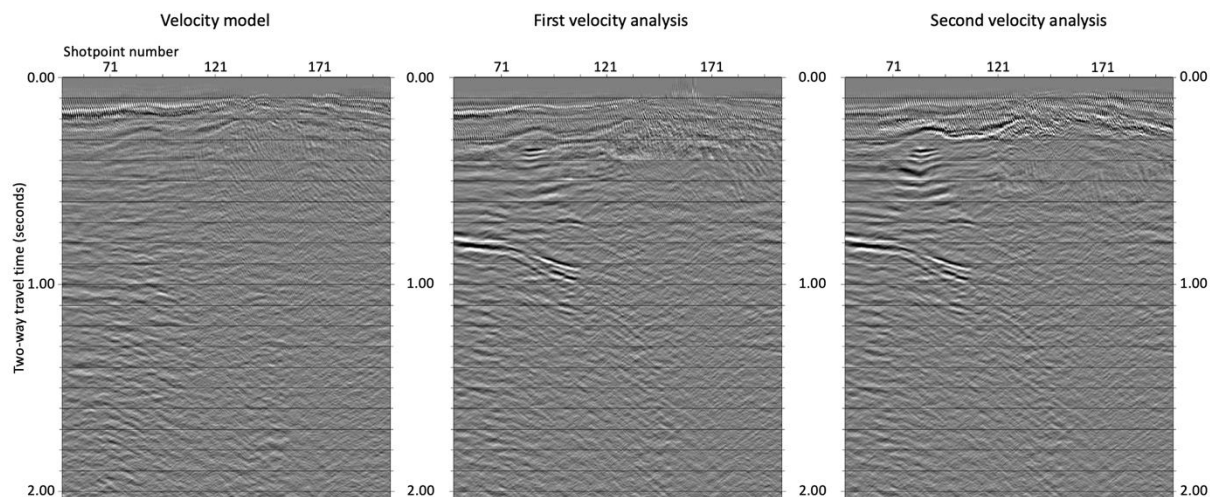


Figure 5.2.10: The figure compares the different velocity libraries used in the stacking of line 2. The window to the left shows a stacked section using the velocity library from the velocity model. The window in the middle shows the stacked section using the velocity library from the first velocity analysis, whereas the right window uses the velocity library from the second velocity analysis. The figure shows a clear improvement in using the velocity library from the second velocity analysis.

When comparing the stacked outputs from the different velocity libraries, it is clear that the outputs from the two velocity analyses provide a much better result than the output from the velocity model. When studying the outputs from the velocity analysis, the seabed is better imaged after the first velocity analysis compared to the second, whereas the other structures are better imaged after the second velocity analysis. Since this study focuses on structures below the seabed, the velocity library from the second velocity analysis is used in the final result.

5.2.7 Migration

After inspecting the stacked sections, the next step is to do a pre-stack migration of the data. The purpose of migration is to correct for dipping layers, by assigning the reflection points to their true locations in the subsurface. Pre-stack migration is preferred in areas of structural complexity with dipping interfaces and lateral variations in velocity (Yilmaz, 2001).

Before performing the migration an external mute from incidence angle, where the angle is set to 40° . Energy with incidence angle above 40° is muted, because it mainly represents refracted waves and other types of noise. Some CDP gathers are selected for display, NMO corrected and plotted to check if the selected angle in the previous step is too high or low and thereby needs to be adjusted. This step will not affect the further processing, and will just function as an additional step to control the selected parameters of the previous modules. After the external mute, amplitude scaling is performed on the data to gain a better balance between the amplitudes in the shallow and deeper parts of the section. The time-power method is used for this (Ruud, pers. comm.), where n is set to -0.2 . By using a negative value for n , amplitudes at shorter times are scaled up, whereas amplitudes for longer times are scaled down. The higher the negative value, the stronger the signals in the shallow sections. -0.2 was chosen, as higher values caused the signals in the deeper part of the section to become weaker.

The data are then migrated by Kirchhoff pre-stack time migration, where the traces were time corrected. The water bottom library and the final velocity library are also used during this process. The water bottom library is used as it is not necessary to migrate data above the seabed. An anti-alias low-pass filter with maximum frequency set at 115 Hz is used to remove noise that might have been introduced during the processing. The value indicates the highest frequency that is present in the datasets before filtering. How much energy that is removed is dependent on the velocities, reflector dip and CDP interval. The CDP distance was set to 50, and is supposed to correct for the 'stripes' in the seabed and shallow reflections which is caused by spatial aliasing. A value 100 was also tested but affected the horizontal resolution negatively.

After the migration was finished, it was decided to perform another velocity analysis to try to improve the velocity model. Figure 5.2.11 shows the migrated seismic section, where the velocity library from the second velocity analysis has been used. Looking at the figure, the seabed and shallow reflections are poorly imaged as a result of few traces with small offsets. However, this will be improved in the muting with stack job. Looking at the selected CDP gathers (Fig. 5.2.12), there are still some migration-stretching and refractions left at the ends.

This can be muted manually by opening the plot in Teamview and pick the affected area. The result is exported to a mute library that can be used in the subsequent muting job.

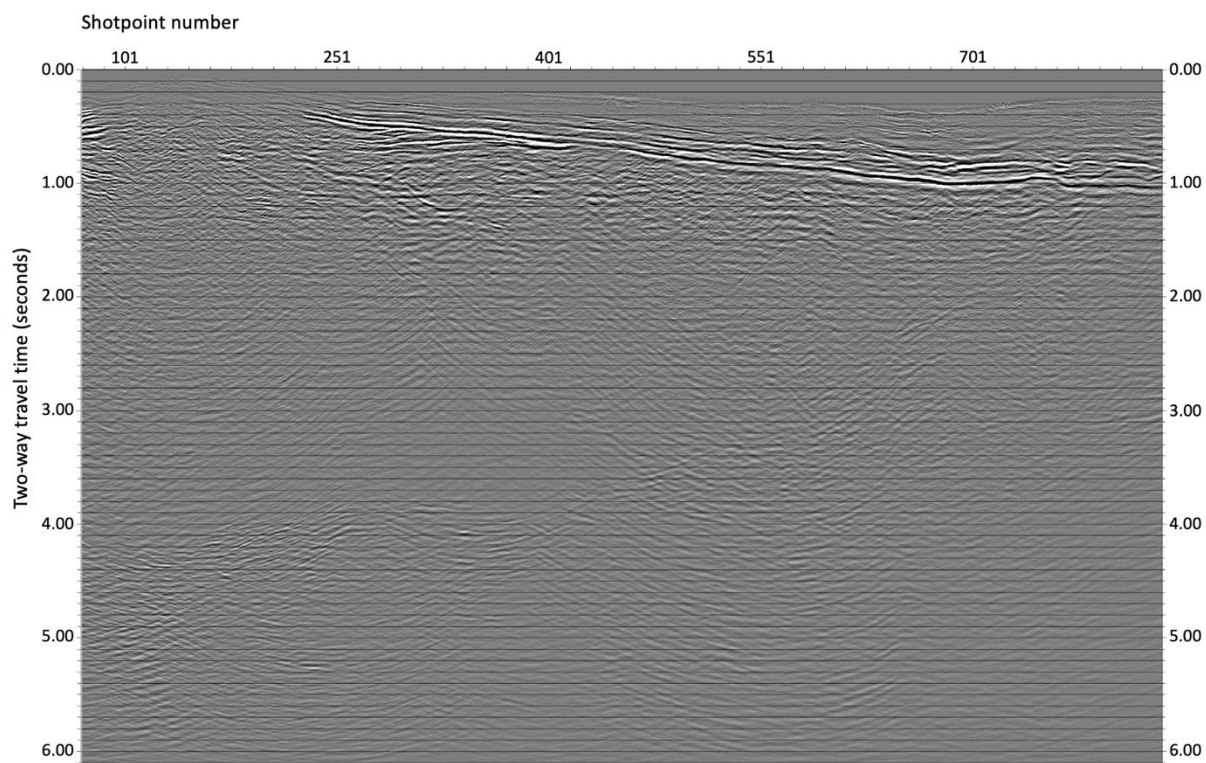


Figure 5.2.11: The figure shows the migrated seismic section from line 2. It is now possible to see real reflections, where they have been put to their true subsurface locations.

5.2.8 Muting with stack

The processing job aims at improving the seismic data, but will in return generate some artefacts (like NMO stretching) that reduce the data quality. Muting aims at reducing these affects and improving the overall quality of the seismic data by cutting the energy that represents noise. This processing job was done separately from the migration, as the mute functions had to be picked on the migrated gathers before the stacking.

The muting job starts by doing an internal mute, where the mute library created in the migration job is used. The purpose of this step is to remove the remaining refractions and migration-stretching that might occur as a result of the migration. Some CDP gathers are chosen for display and compared with the muted CDP output from the migration job in Figure

5.2.12. The figure shows how the picked manual mute significantly improves the gathers by removing the refraction and migration-stretching effects.

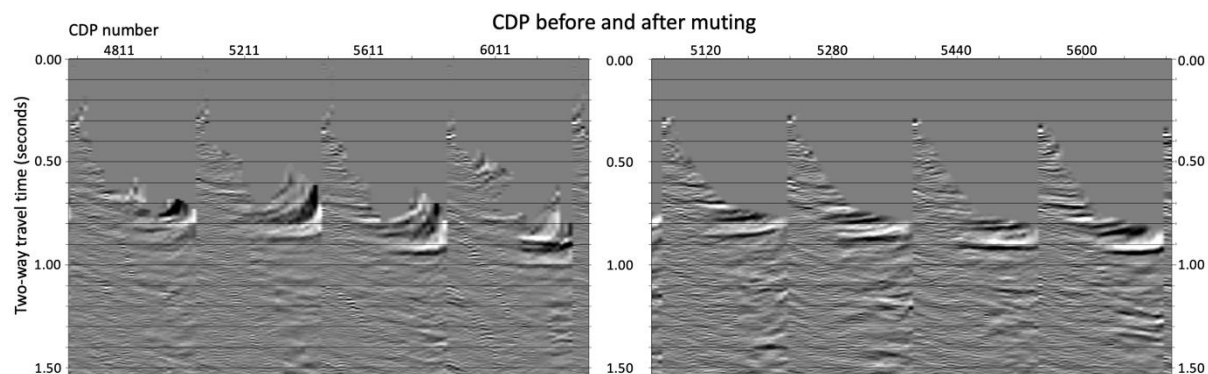


Figure 5.2.12: The figure shows a comparison of some selected CDP gathers before and after the mute library has been applied. The window to the left shows before, whereas after is displayed in the right window. The mute library removed the migration-stretching and remaining refractions that can be seen in the left window.

After the internal muting, the traces are stacked. Dip filtering in fk -domain is used to reduce the spatial aliasing in the seabed and shallow reflections, and serves the same purpose as the anti-alias filter that was applied during the migration. The result is displayed in Figure 5.2.13. The first velocity in the fk -filter is set to -3.0 km/s and the second to 3.0 km/s. As this is a seismic section, and not a shot or receiver gather, the velocity corresponds to the dip of a reflector. A time variable band-pass filter is added, where the filter values for the different time intervals are listed in Table 5.2.2. The filter varies as a function of time. As the section is assumed to have most low-frequency energy at the bottom of the section because of attenuation, the cut values become progressively lower with depth (Ruud, pers. comm.). Thus, the filter is supposed to cause deeper reflections to gain higher energy. At the end, the pulse shape is changed to zero-phase. Figure 5.2.13 shows a comparison of a section of the seismic before and after the muting. It is possible to view how the different modules have affected the seismic section by amplifying the signals and significantly reducing the stripes in the shallow parts. Additionally, noise has been removed, thus amplifying the reflected signals. The effect of the phase filter is also highly noticeable.

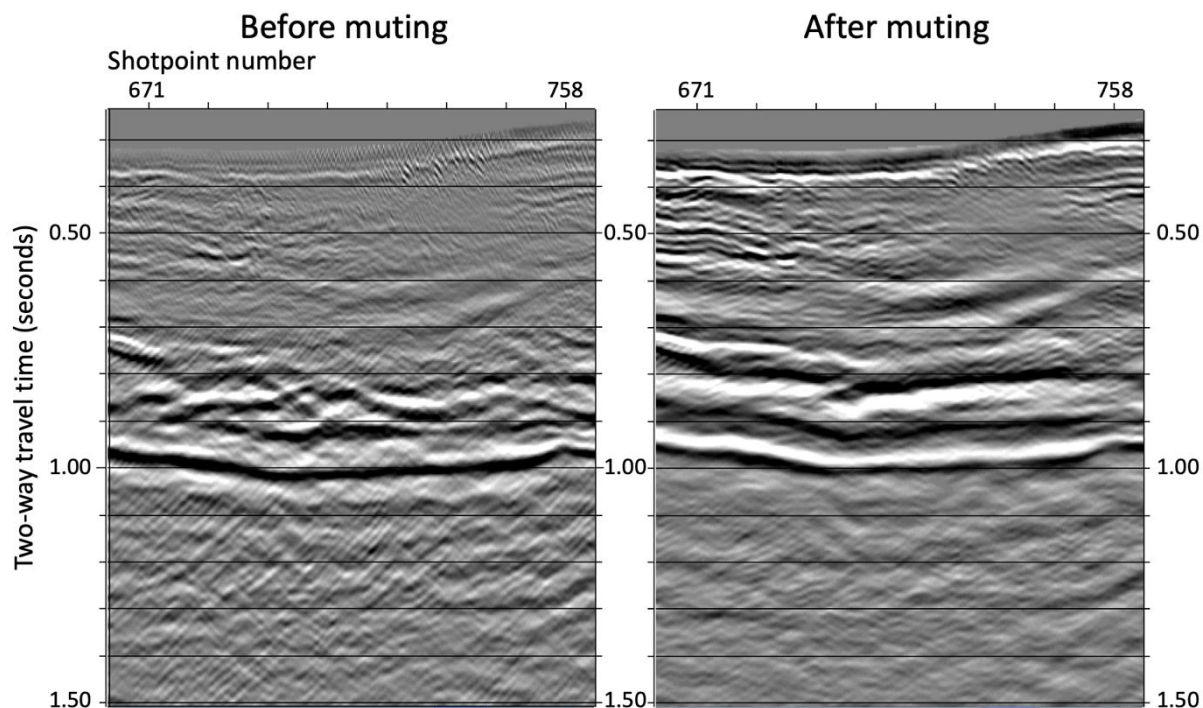


Figure 5.2.13: The figure shows a section of line 2 before and after application of anti-alias filter and f_k-filter. The different modules have amplified the signals significantly, where the seabed is much stronger after. Another significant improvement is the reduction in the spatial aliasing, which causes the 'stripes' that can be viewed in the left window.

Tabell 5.2.2: The table shows the filter values for the different time intervals of the time variable band-pass filter.

Start time (ms)	Low-cut (Hz)	High-cut (Hz)
4	12	100
300	10	85
700	8	70
1500	6	60

5.2.9 Converting to SEG-Y format

The final step in the processing sequence is to reformat the files from the internal Geocluster format to a SEG-Y file. The first step is to read the final data output from the muting. The next step is to access the coordinate system, which is UTM zone 33X, and tie it to the dataset. The coordinate system is defined from the shot-points to the individual lines and can therefore show the exact location of the lines. The values show north and east coordinates in meters, and thereby ensures that the lines are given the correct location relative to each other and the areas around. The final step is to write the SEG-Y file.

It is possible to display the result in Teamview to perform one last quality control of the data, in order to check whether there is anything else that can be improved. If the result is approved, the file is ready to be transferred to the next software, which in this case is Petrel, where the data can be interpreted. Figure 5.2.14 shows a comparison of the near trace plot before processing and the seismic section after processing. The figure shows the uppermost 3 seconds, and it is possible to view clear seismic reflections from the geological layering in the final result. All of the finished processed lines are displayed from Figure 5.2.15 to Figure 5.2.18.

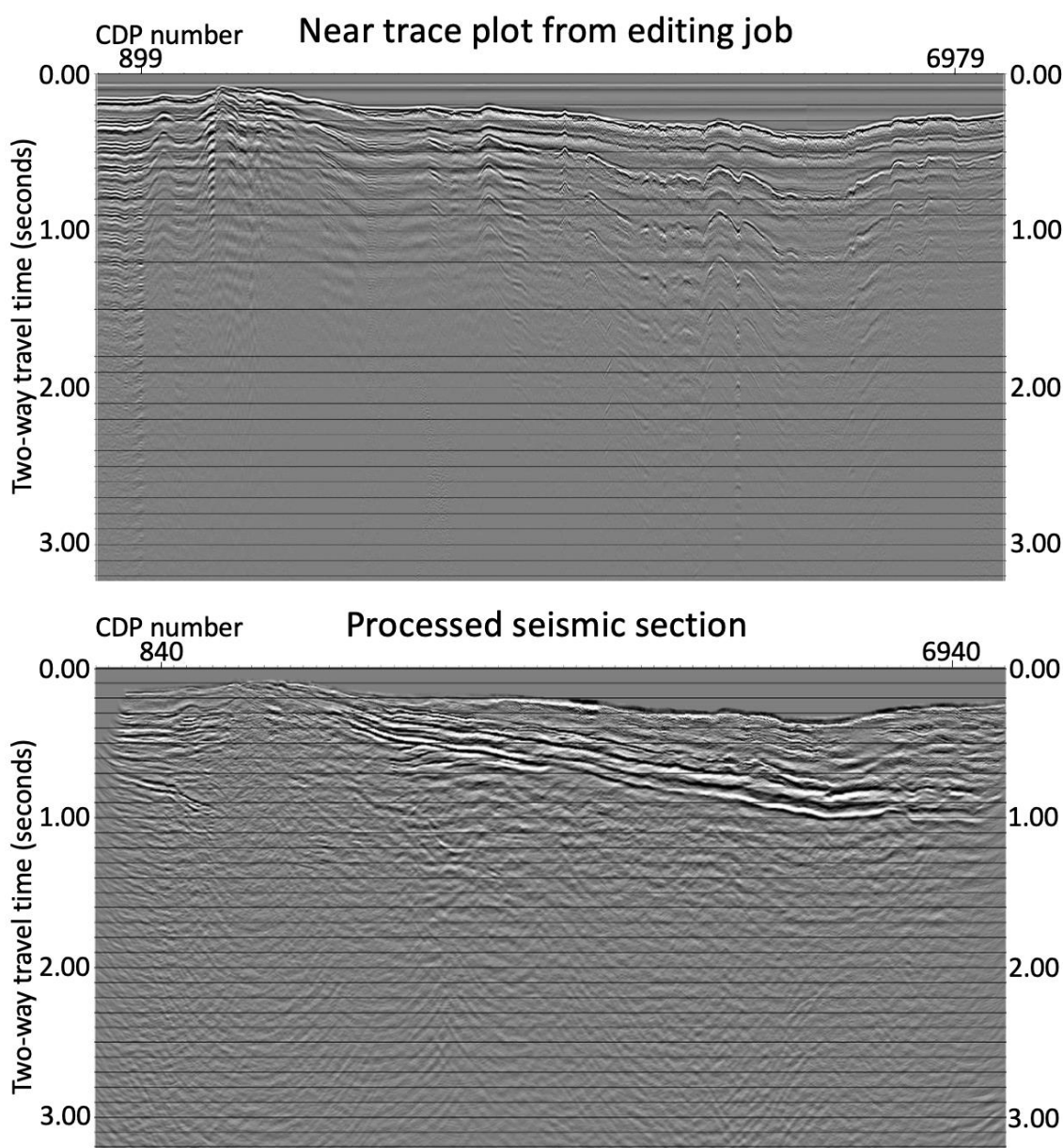


Figure 5.2.14: The figure shows a comparison of line 2 before and after processing. The upper window is before the processing, after the editing job. Whereas the lower window is after the processing is finished.

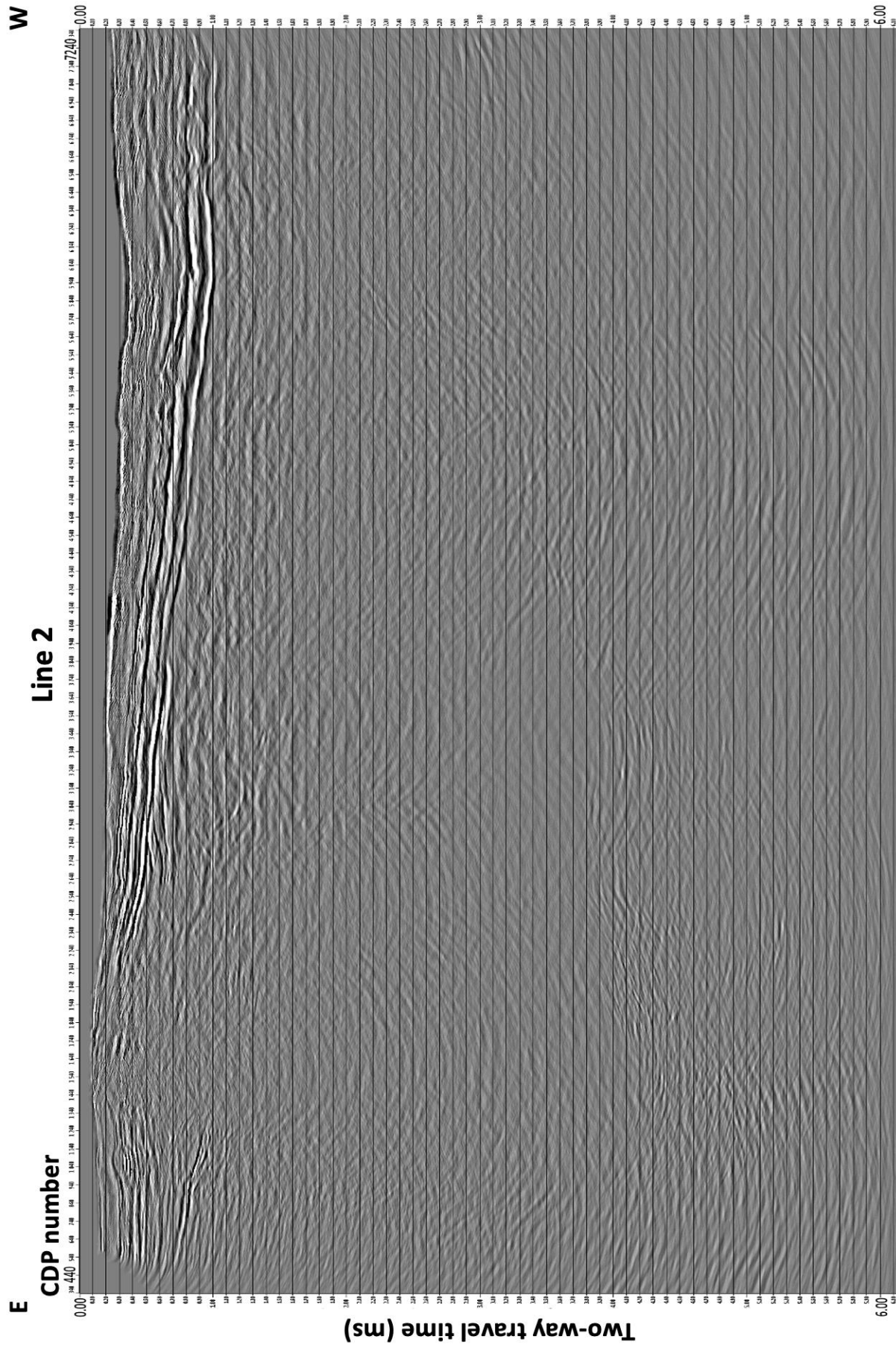


Figure 5.2.15: The figure shows line 2 after processing.

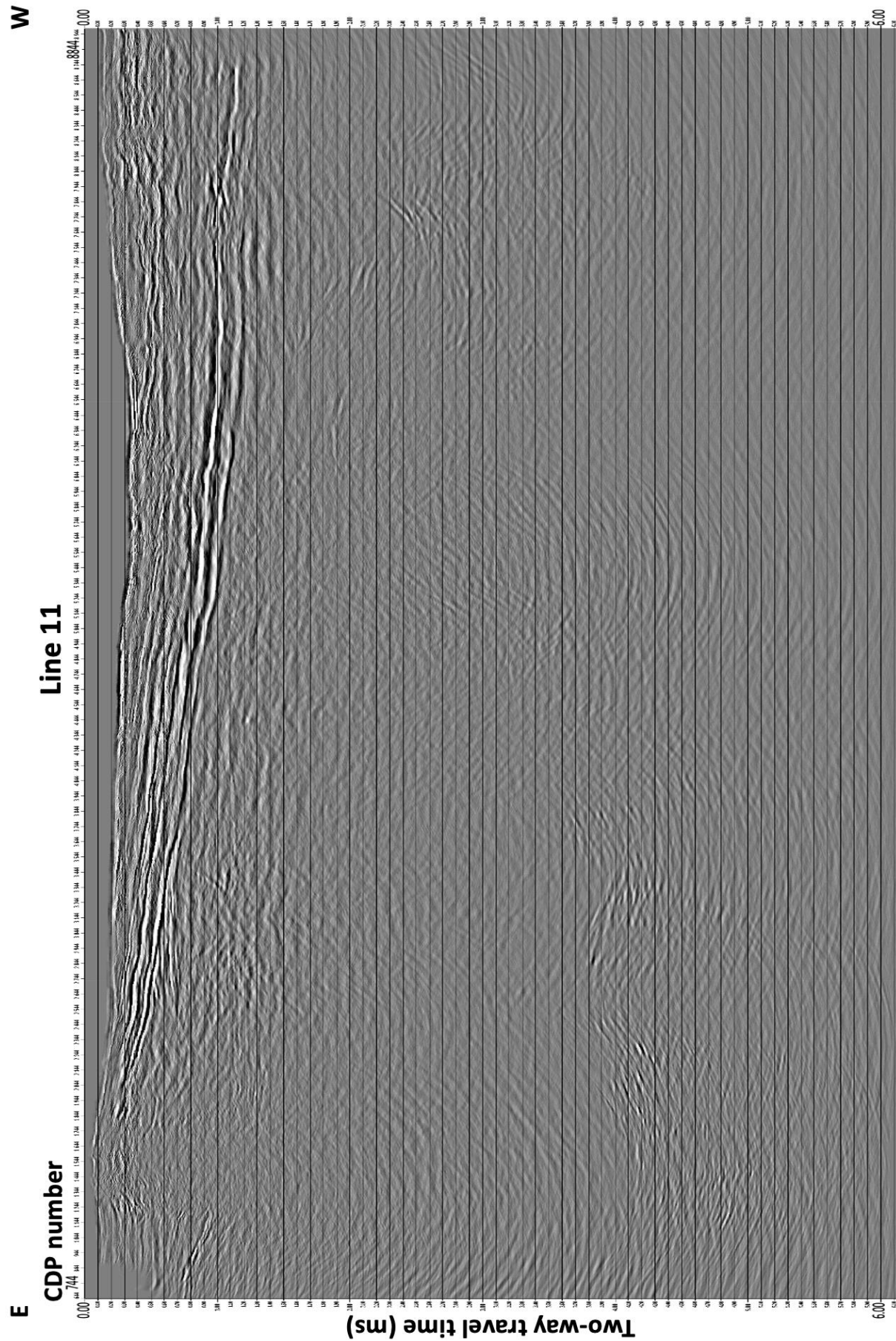


Figure 5.2.16: The figure shows line 11 after processing.

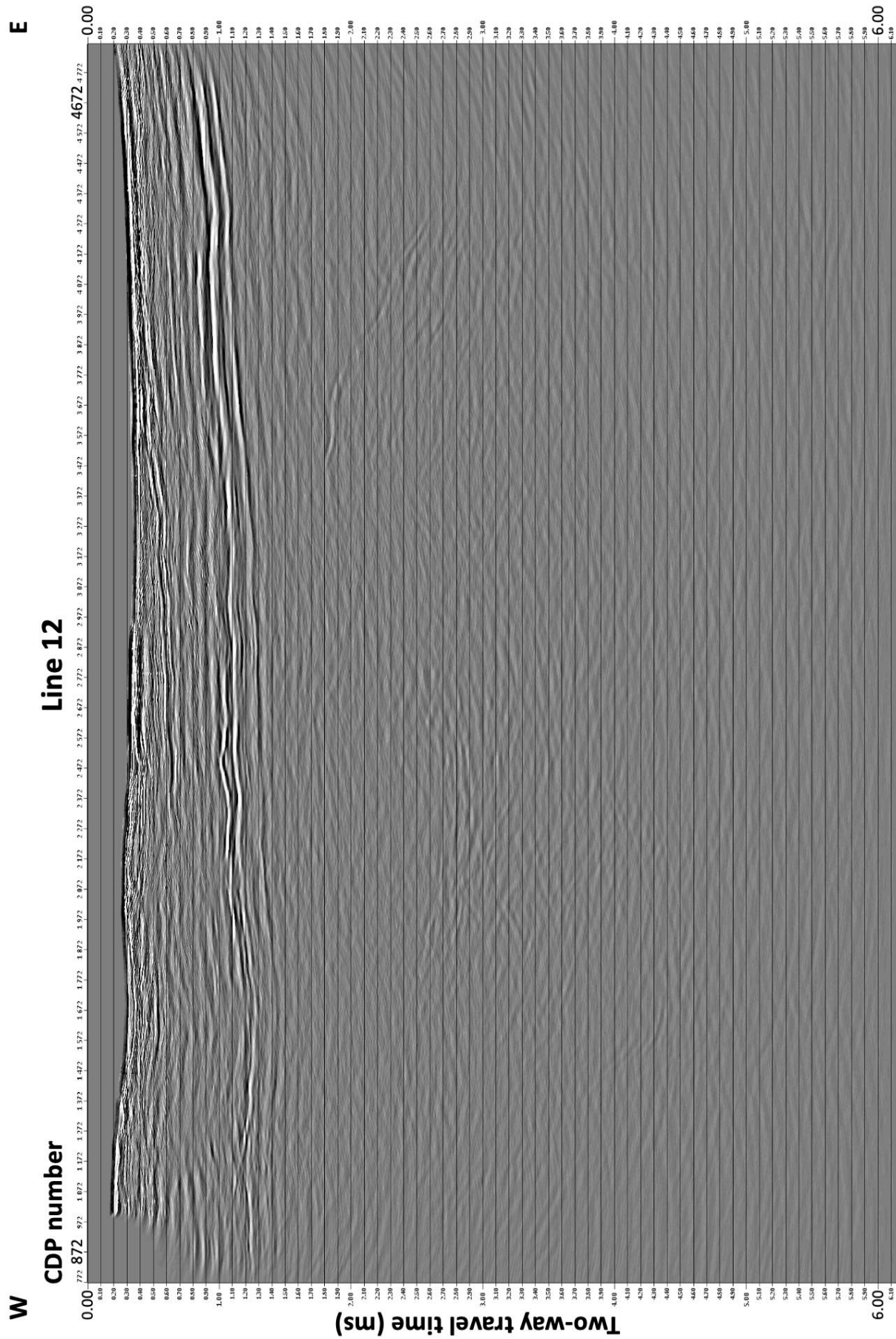


Figure 5.2.17: The figure shows line 12 after processing.

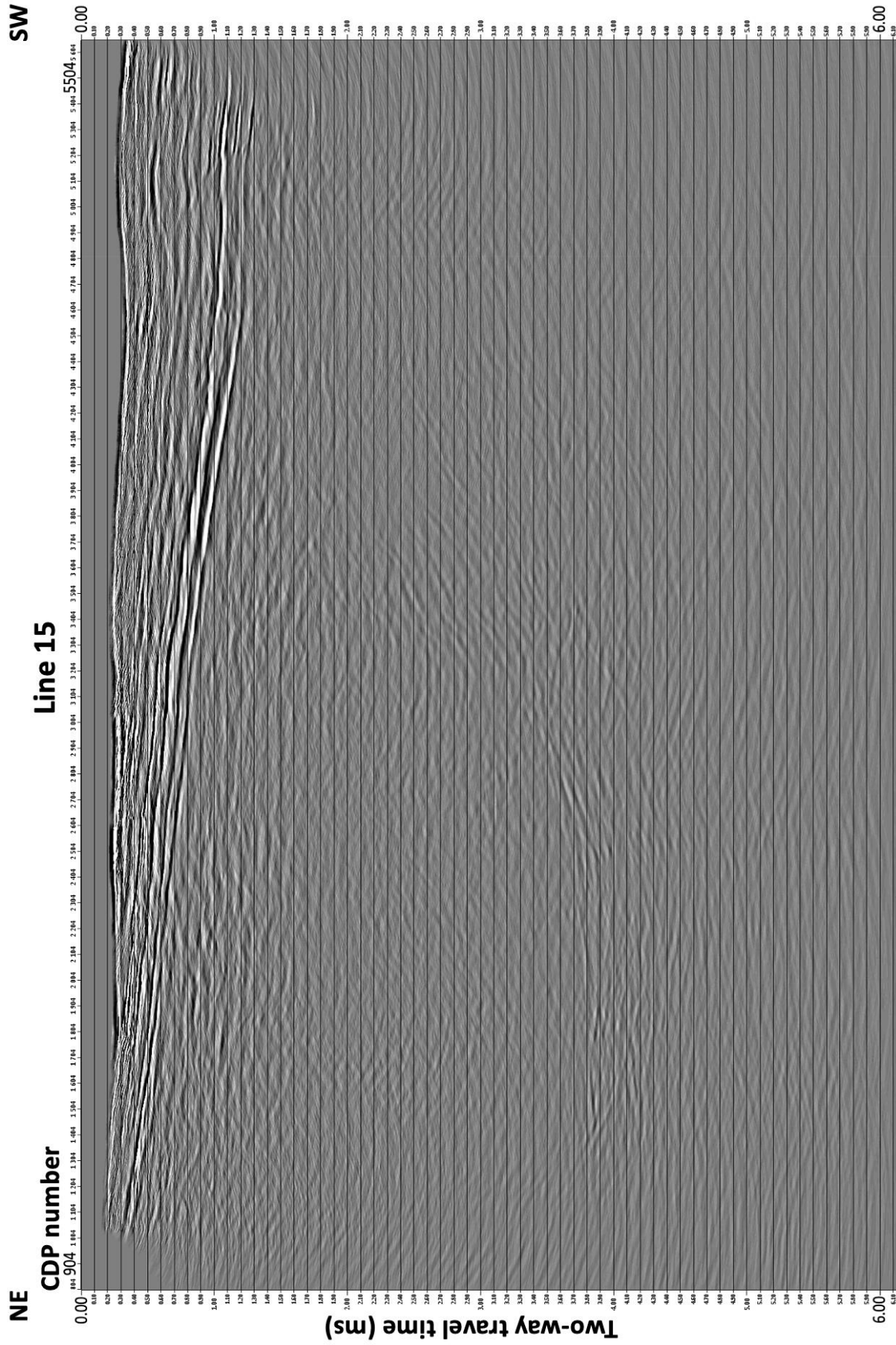


Figure 5.2.18: The figure shows line 15 after processing.

Chapter 6

Interpretation

In this chapter the interpretation of the seismic lines will be presented. The main goal with the interpretation is to map the different stratigraphic units and the most dominant structural features. The interpretation has been conducted in Petrel, and the next section contains a review of the software.

6.1 Software – Petrel

Petrel is a software developed by Schlumberger, and is the software used to perform all the interpretations in this study. The software is well recognized in both academic environments and in the industry. Petrel contains a variety of different tools that can be used within several areas of application, including interpretation of seismic data.

The processed lines were imported to Petrel in SEG-Y format to a coordinate system called ED50-UTM33. The colour table that was used is called 'Seismic (default)', and colours peaks (positive amplitude) in red. The colour tables can also be tailored by changing the colour scale, which can be done to highlight certain events or structures. Because faults are easier to see in a black-white scale, an outcrop attribute section was made for each of the lines using a colour table called 'Outcrop'. The outcrop attribute was used to quality control the various fault interpretations that were made. Due to discontinuous reflectors the horizons have largely been interpreted by using manual interpretation. In cases of continuous reflectors, seeded 2D autotracking has been used. The interpretations were made in a window called interpretation window, where a 2D or 3D window can be used to study and correlate the interpretations. Each horizon interpretation was used to generate a surface map, where two surface maps were used to generate an isopach map. These maps can be used to get an overview of large scale or local variations in and between the geological units.

6.2 Basis for the interpretation

6.2.1 Previous studies in the area

Several studies, which have been important for this study, have been conducted in this area. The interpretations that have been made in this thesis have been correlated with interpretations from these previous studies. The studies that have given an important basis for this study is listed below, where one article from Blinova et al. (2013) and a master thesis from Skaara (2020) have been used the most during the interpretation:

- Bergh et al. (1997): *Interaction of Basement-Involved and Thin-Skinned Tectonism in the Tertiary Fold-Thrust Belt of Central Spitsbergen Svalbard*. Describes multichannel seismic reflection data from Isfjorden.
- Amundsen et al. (2011): *The Cenozoic western Svalbard margin: sediment geometry and sedimentary processes in an area of ultraslow oceanic spreading*. Describes sedimentary processes and seismic character along the western Svalbard margin based on multichannel seismic reflection data.
- Blinova et al. (2012): *Seafloor expression and shallow structure of a fold-and-thrust system, Isfjorden, west Spitsbergen*. Describes bathymetric and multichannel seismic reflection data from Isfjorden, focusing on shallow structures.
- Bælum and Braathen (2012): *Along-strike changes in fault array and rift basin geometry of the Carboniferous Billefjorden Trough, Svalbard, Norway*. Describes the Billefjorden Fault Zone and the structures within.
- Blinova et al. (2013): *Analysis of structural trends of sub-sea-floor strata in the Isfjorden area of the West Spitsbergen Fold-and-Thrust Belt based on multichannel seismic data*. Describes multichannel seismic reflection data from Isfjorden, focusing on deep structures.
- Senger et al. (2013): *Geometries of doleritic intrusions in central Spitsbergen, Svalbard: an integrated study of an onshore-offshore magmatic province with implications for CO₂ sequestration*. Describes doleritic intrusions in central Spitsbergen.
- Braathen et al. (2017): *The Keisarhjelm detachment records Silurian-Devonian extensional collapse on Northern Svalbard*. Describes an extensional collapse detachment in north-western Svalbard.

- Skaara (2020): *Prosessering og tolkning av refleksjonsseismiske data fra Isfjorden, Svalbard*. Describes reflection seismic data from Isfjorden, Sassenfjorden and Billefjorden.

6.2.2 Seismostratigraphic framework

Previous studies have defined a seismostratigraphic framework (Fig. 6.2.1) that will be useful for the interpretations made in this study. The seismostratigraphic framework describes the seismic signature of the units.

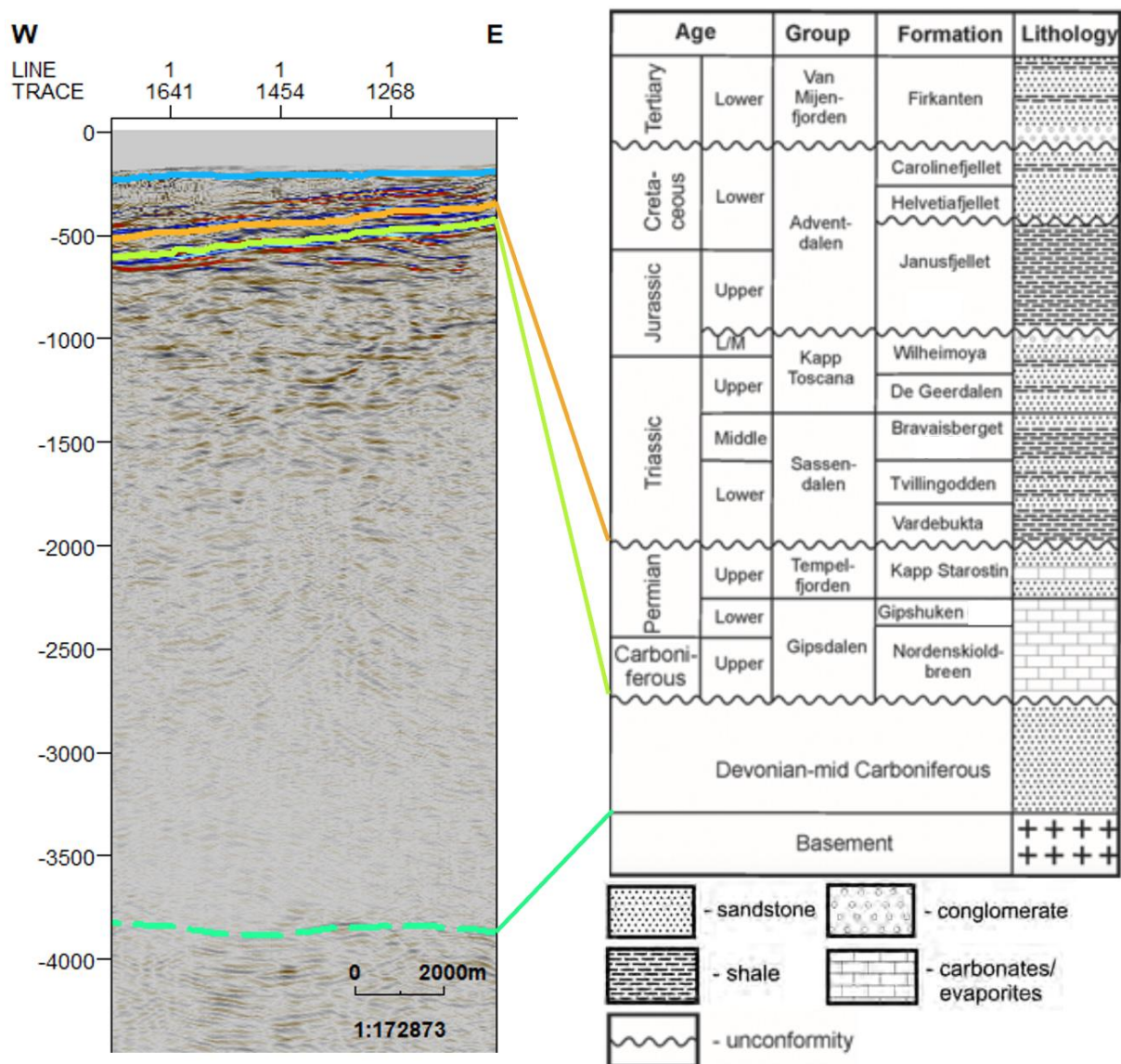


Figure 6.2.1: The figure shows the seismostratigraphic framework tied with the seismic units. The seismic example is from line 2 and the table is modified from Blinova et al. (2013).

The youngest sedimentary rocks found on Spitsbergen belong to the Van Mijenfjorden Group, which consists of alternating sandstones, siltstones and mudstones. The underlying Carolinefjellet Formation of the Adventdalen Group consist of a series of shale and sandstone successions with reflectors that are weak and laterally inconsistent. The transition from the Carolinefjellet Formation to Helvetiafjellet Formation is difficult to identify in seismic data as the boundary is transitional. The Helvetiafjellet Formation consists of high-velocity sandstones that create strong and continuous reflectors in the seismic section. The Janusfjellet Subgroup is in strong contrast to the overlying unit, as the low-velocity shales are characterised by chaotic and discontinuous seismic reflectivity pattern where the reflectors are almost transparent (Bælum and Braathen, 2012; Blinova et al., 2013).

The upper boundary of the Kapp Toscana Group creates a regional hiatus with the overlying Adventdalen Group. The sandstones of the Kapp Toscana Group create strong reflectors with a sharp impedance contrast to the overlying low-velocity shales (Blinova et al., 2013). The shales of the Sassendalen Group create weak and discontinuous reflectors and are in strong contrast to the underlying Permian-Upper Carboniferous succession. The Permian-Upper Cretaceous succession mainly consists of evaporites and carbonates that are characterised by strong, parallel, and continuous reflectors. Both the upper and lower boundary of the Permian-Upper Carboniferous succession are unconformities that create strong continuous reflectors (Blinova et al., 2013).

The Middle Carboniferous-Devonian succession comprises post-orogenic Old Red Sandstone and is characterised by a chaotic and discontinuous reflectivity pattern with weak, almost transparent, reflectors (Blinova et al., 2013). The Billefjorden Group of Early Carboniferous consists of sandstones and shales, and has no major reflectors. The group stands out compared to the overlying very reflective Permian-Upper Carboniferous succession, and the underlying chaotic and almost transparent Devonian unit (Bælum and Braathen, 2012). The basement rocks are referred to as Hecla Hoek and comprises highly deformed metamorphic rocks. The unit is characterised by discontinuous and chaotic reflectivity pattern, where the reflectors are stronger than the overlying Devonian unit.

Igneous intrusions have been documented in the inner Isfjorden area by outcrop observations, 2D seismic, bathymetric and well data (Bælum and Braathen, 2012; Senger et al., 2013). Planke et al. (2005) has found that igneous intrusions can be interpreted based on some characteristic features; high amplitude, saucer-shaped and/or abrupt terminations. The intrusions predominantly occur within the Triassic shale-sandstone succession. Sills and dykes are also present in the Permian succession where they are commonly seen in evaporites and shales. Some dykes cut as high as the Lower-Middle Jurassic succession, whereas other intrusions occur as low as the Devonian succession (Bælum and Braathen, 2012; Blinova et al., 2013; Senger et al., 2013).

6.2.3 Data quality

The quality of the data is dependent on a variety of different factors. Section 3.3.3 explained the importance of seismic resolution with regards to the imaging of a seismic section. Rough calculations on the resolution of the dataset can provide an indication of how the resolution changes through the seismic section (Table 6.2.1). The calculations indicate that the vertical resolution changes from 50 m just below the seabed, to 92 m at Hecla Hoek. The Fresnel zone changes from 158 m to 790 m from the seabed to Hecla Hoek.

Table 6.2.1: The table shows rough calculations of the resolution. The seabed and Hecla Hoek were chosen to show the change in resolution with increasing depth. Average values from the datasets have been used in the calculations.

	Depth, Z	Velocity, v	Dominant frequency, f	Wavelength: $\lambda = \frac{v}{f}$	Vertical resolution: $\frac{\lambda}{4}$	Fresnel zone (horizontal resolution): $\sqrt{\frac{\lambda Z}{2}}$
Seabed	250 ms	5000 m/s	25 Hz	200 m	50 m	~158 m
Hecla Hoek	3400 ms	5500 m/s	15 Hz	~367 m	~92 m	~790 m

The data quality is affected by the abnormally hard seabed in Isfjorden. The acoustic impedance obtains a strong contrast between the water layer and the seabed, which will result in a very large reflection coefficient and very small critical angles ($\sim 20^\circ$). A large reflection coefficient and low critical angle will cause large amounts of energy to reflect at the seabed, and thus only smaller amounts of energy to propagate through the subsurface. The same effect will occur at interfaces with high reflection coefficients, like intrusions. When less energy is used to image the subsurface, the data quality will be reduced and the features underneath that surface can be poorly imaged.

The seabed is generally very shallow, which results in water layer multiples to repeat at short intervals. Additionally, the large amounts of energy that reflect at the seabed will form multiples that travel through the water layer as guided waves. The amount of energy that reflect at the seabed that causes the multiples to become very strong. Yet, it looks like the water layer multiples have been attenuated effectively during the processing (Fig. 6.2.2). Some remaining multiples might interfere with real reflections, which can cause uncertain interpretations. The strength of the seabed reflection has been significantly reduced due to the processing steps that were taken to remove the water layer multiples. Initially, the seabed was continuous and had a high amplitude reflection. After the processing the seabed has become very weak and influenced by noise. Despite the amplitude recovery during the processing, it is clear that the data quality has been significantly reduced, especially regarding the shallowest areas. The quality of the shallowest areas could have been improved if less energy was removed during processing, but this would in return cause the multiples to become more dominating. If the goal of the survey was to image the shallow seabed, the acquisition geometry should have been changed to using a streamer with shorter offsets and group intervals.

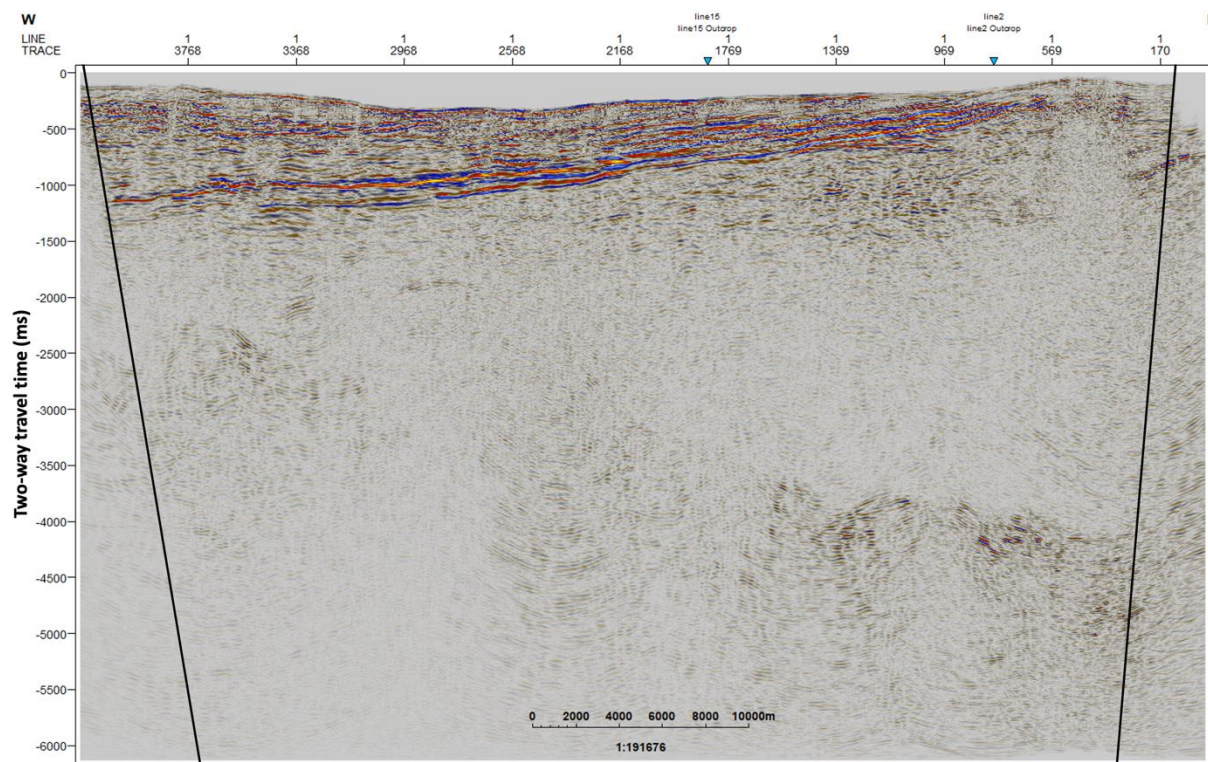


Figure 6.2.2: The figure shows the general seismic quality of the seismic sections, where line 11 have been used as an example. The black lines illustrate the area that is still affected by streamer noise.

The seismic is also influenced by streamer noise at the ends of the line (Fig. 6.2.2). The streamer noise is a result of the streamer not being fully extended when the vessel turns to start acquiring a new line. An attempt was made during processing to remove the streamer noise, but the quality of the processing varies. The noise will thus influence the seismic along the ends of the section, and this is illustrated for line 11 in Figure 6.2.2. The streamer noise at the beginning and end of the lines could have been avoided by excluding shots where the streamer is not fully extended along the line, but that would also have resulted in shorter lines. Some areas in the seismic section are also influenced by local transparent colours (Fig. 6.2.3). The transparency is outlined in the figure, and is caused by low amplitude, incoherent energy, or lacking reflectors. It is also important to note that the seismic data have not been depth converted, and have thus been interpreted in TWT. The interpretations will therefore not be 100% geologically accurate. Additionally, the effects that were attempted removed by static correction might not have been fully removed. It is therefore possible that a few local highs or lows might be slightly more pulled up or down compared to the real subsurface geology.

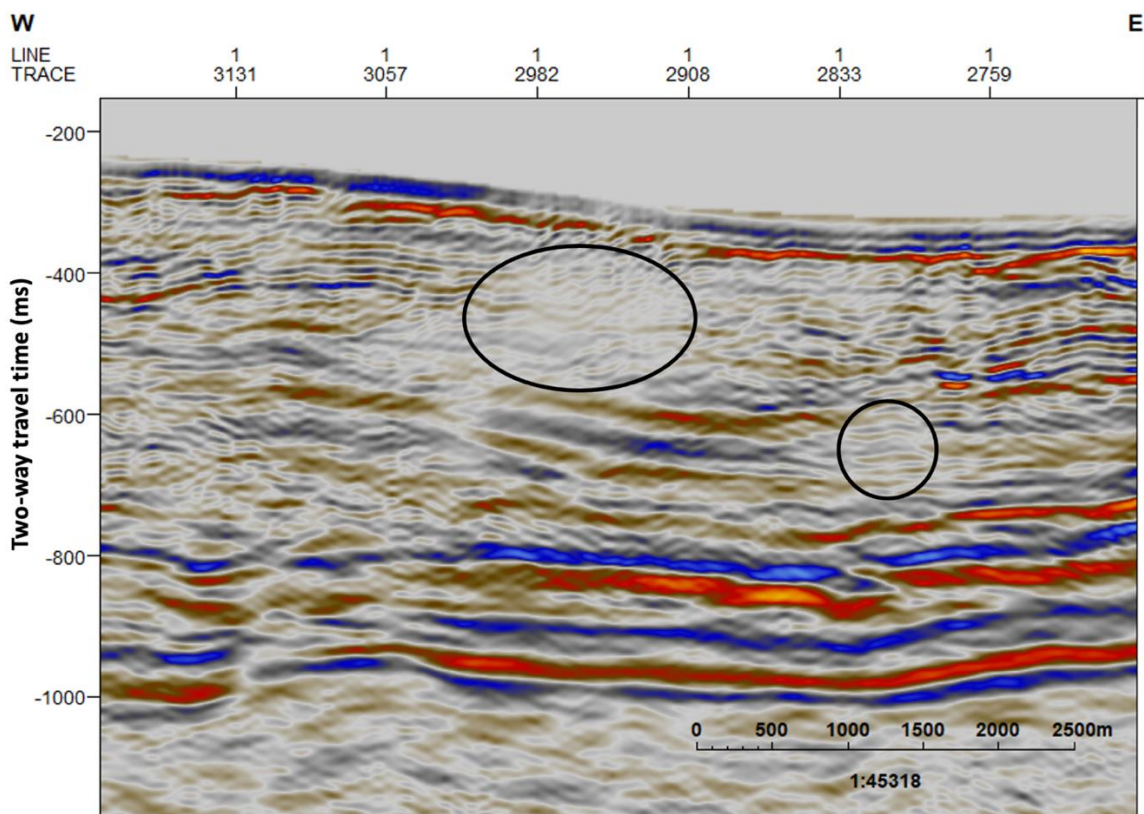
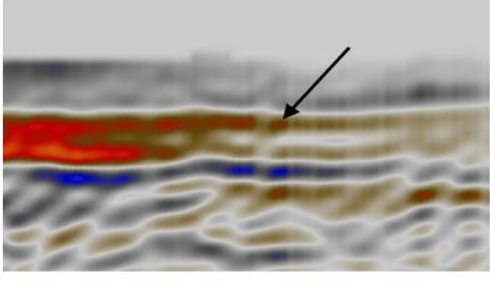
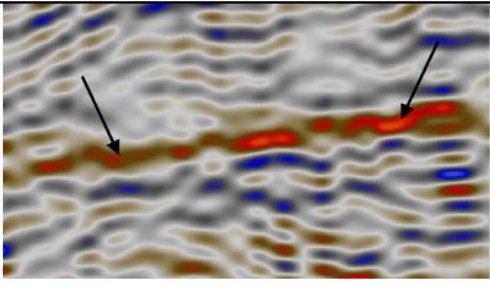
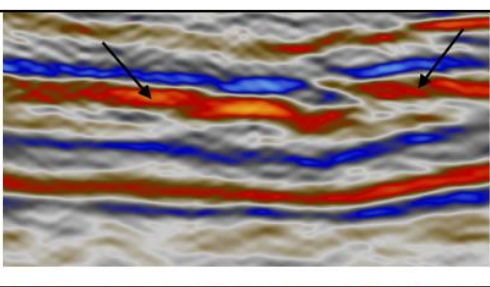
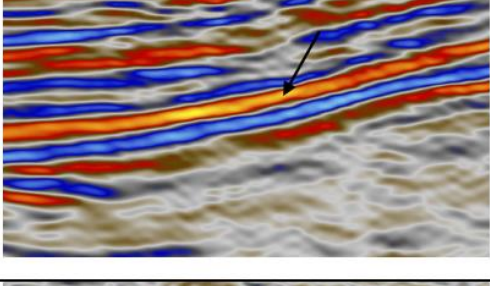
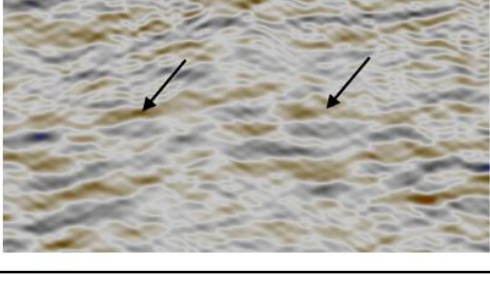


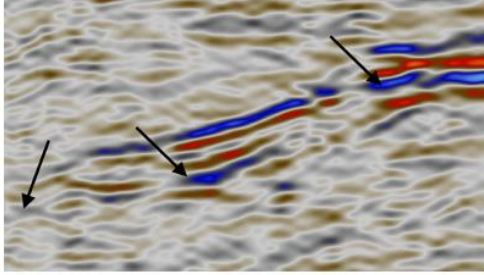
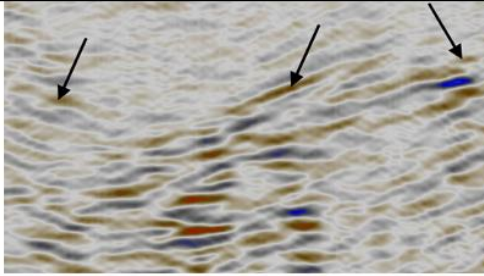
Figure 6.2.3: The figure shows the transparent areas for line 2, outlined with black circles.

6.3 Stratigraphic interpretation

The stratigraphic interpretation describes how the different horizons have been interpreted based on the seismic character of the reflections. In total, seven horizons have been interpreted from the seabed to the basement. Five of the horizons have been presented in this section and the remaining two are discussed in the next section, as they are strongly influenced by the Billefjorden Fault Zone. Some of the horizons have strong continuous reflections that were easy to interpret. Others were more challenging, as the reflections are weaker, discontinuous and disrupted by real structures or artefacts. The interpretation is supported by showing outcrops from the seismic section where the horizon is most evident. Table 6.3.1 shows the relationship between the horizon, phase, reflector characteristic and seismic signature.

Table 6.3.1: The table shows the relationship between the interpreted horizon, the phase, the reflector characteristic, and the seismic signature. The seismic signatures are taken from line 2 and 11.

Horizon	Phase	Reflector characteristic	Seismic signature
Seabed	Positive amplitude (peak)	Weak to strong amplitude, mainly continuous	
Reflection R	Positive amplitude (peak)	Weak to medium amplitude, varying continuity	
Top Permian	Positive amplitude (peak)	Strong amplitude, mainly continuous	
Top mid Carboniferous	Positive amplitude (peak)	Strong amplitude, continuous	
BFZ Horizon 1	Positive amplitude (peak)	Weak amplitude, mainly discontinuous	

BFZ Horizon 2	Negative amplitude (trough)	Medium amplitude, continuous to discontinuous	
Hecla Hoek	Positive amplitude (peak)	Weak amplitude, mainly discontinuous	

The stratigraphic horizons that have been interpreted are the seabed, an unknown horizon termed reflection R, top Permian, top mid Carboniferous and Hecla Hoek. The additional two horizons that have been interpreted and included in the structural interpretation are BFZ horizon 1 and BFZ horizon 2. The seismic character changes from line to line between the seabed horizon and the top Permian horizon, which makes the units between these horizons difficult to interpret. It was also difficult to interpret the horizons on the eastern part of the profile, as the seismic character changes due to influence from the BFZ.

Two different types of maps have been used during the stratigraphic interpretation. The first one is surface maps of the different horizons that show the variations in TWT. The colour distribution varies from red, that indicates the shallowest areas, to purple that indicate the deepest areas. The interpreted horizons form the basis for the surface map, where the area outside the interpreted lines contains artifacts due to interpolation between the lines. The interpolation might not be real and can create false topography in the maps. The second type is isopach maps. These are maps that show the thickness in TWT between two surfaces. The colour distribution varies from purple, that indicates the thickest areas to red, that indicates the thinnest areas. Figure 6.3.1 shows line 2 before interpretation, while Figure 6.3.2 shows the same line after the stratigraphic interpretation

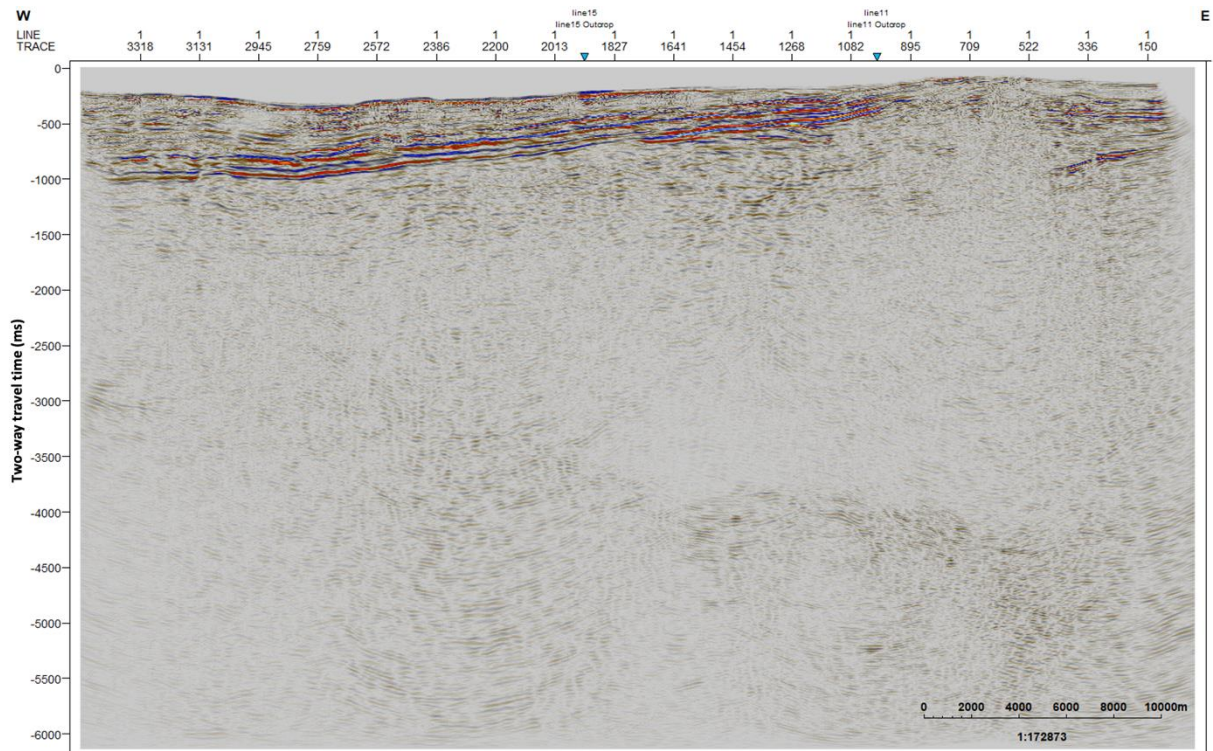


Figure 6.3.1: Line 2 before interpretation.

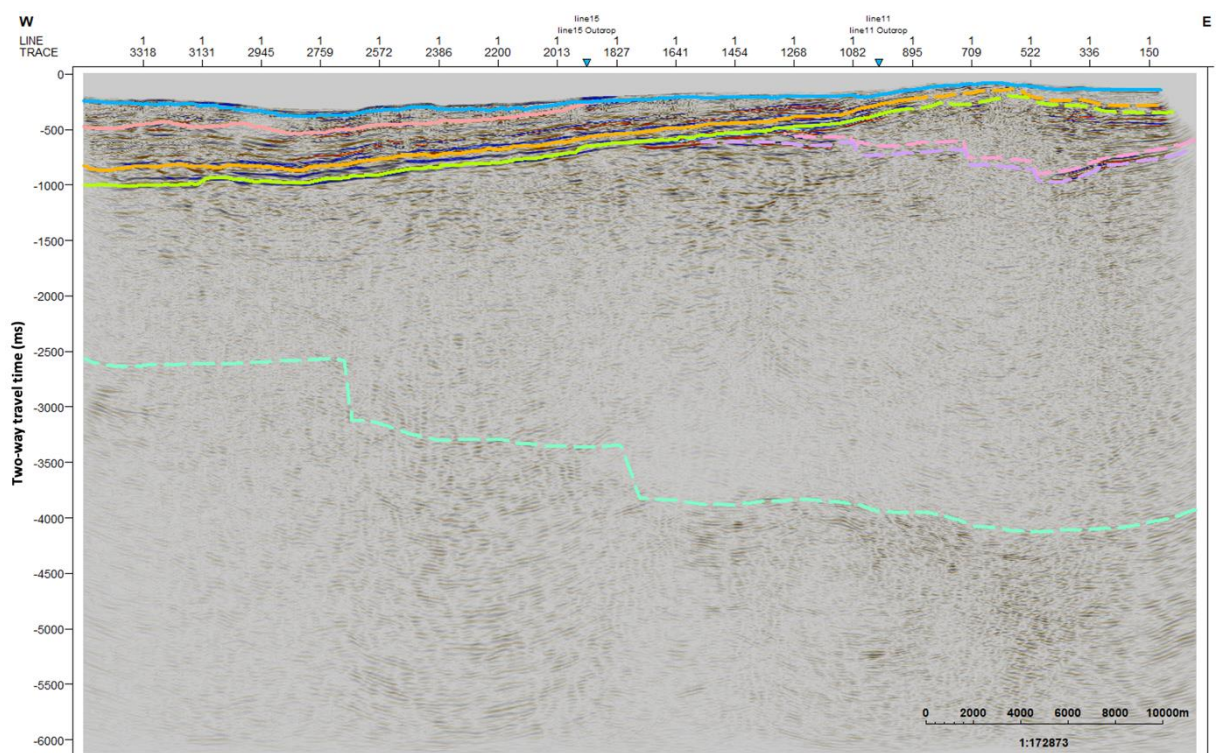


Figure 6.3.2: Line 2 after stratigraphic interpretation. The interpreted horizons are the seabed (blue), reflection R (light red), top Permian (orange), top mid Carboniferous (green) and Hecla Hoek (turquoise). BFZ horizon 1 (pink) and BFZ horizon 2 (purple) have also been interpreted and are described in Section 6.4.2. The dotted lines indicate uncertain interpretations.

6.3.1 Seabed

The seabed will normally be the horizon that is the easiest to interpret. However, the seabed has been strongly affected by the different steps that were taken during processing to remove the water layer multiples. The amplitude of the seabed reflection will therefore be weak several places and influenced by noise. Initially, the seabed will have a strong positive amplitude because of the large acoustic impedance contrast with the overlying water layer, which creates a positive reflection coefficient. However, the muting affects from the processing that muted reflectors above the picked seabed have almost completely removed the seabed reflector. Therefore, a trough is the first reflector that appears in the seismic section. Yet, the seabed reflector has been interpreted on the first peak reflector. Figure 6.3.3 shows a surface map of the picked seabed horizon. From the surface map it is possible to see that the seabed has large topographic variations, where the colour scale indicates that the TWT varies from 50 to 375 ms. The seabed is deepest in the central western parts and shallowest in NE where the BFZ is located.

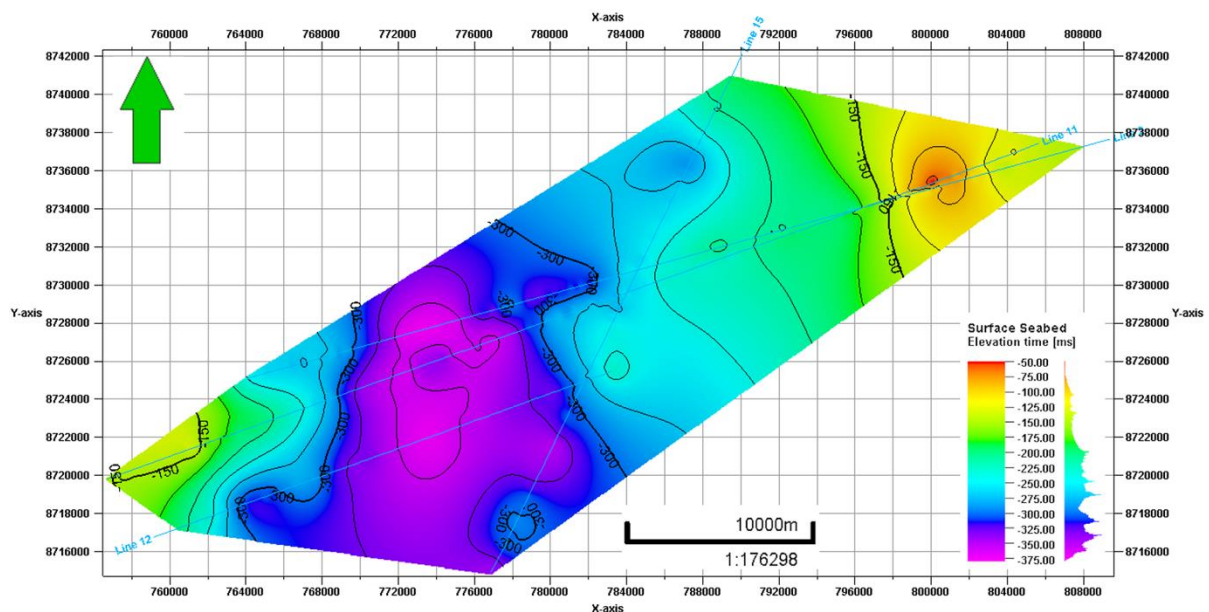


Figure 6.3.3: Surface map of the seabed horizon in TWT (ms).

6.3.2 Reflection R

It was decided to interpret an additional horizon between the seabed and top Permian horizon. As it was not clear from any of the previous studies in the area which stratigraphic layer this horizon represents, this will be investigated in the discussion (Chapter 7). The

reflector amplitude varies from weak to medium between the different seismic lines. For line 2 and 12 the reflector has a weak amplitude, for line 15 it is weak to medium, and for line 11 it is medium. The continuity of the reflector is varying along lines. The amplitude differences between the seismic lines and the varying continuity makes the horizon difficult to interpret and follow across the seismic section. Figure 6.3.4 shows a surface map of the picked reflection R horizon. The horizon dips towards SW, which is caused by a syncline in the central basin of Isfjorden. The colour scale on the figure indicates that the horizon has been interpreted between 250 and 850 ms TWT.

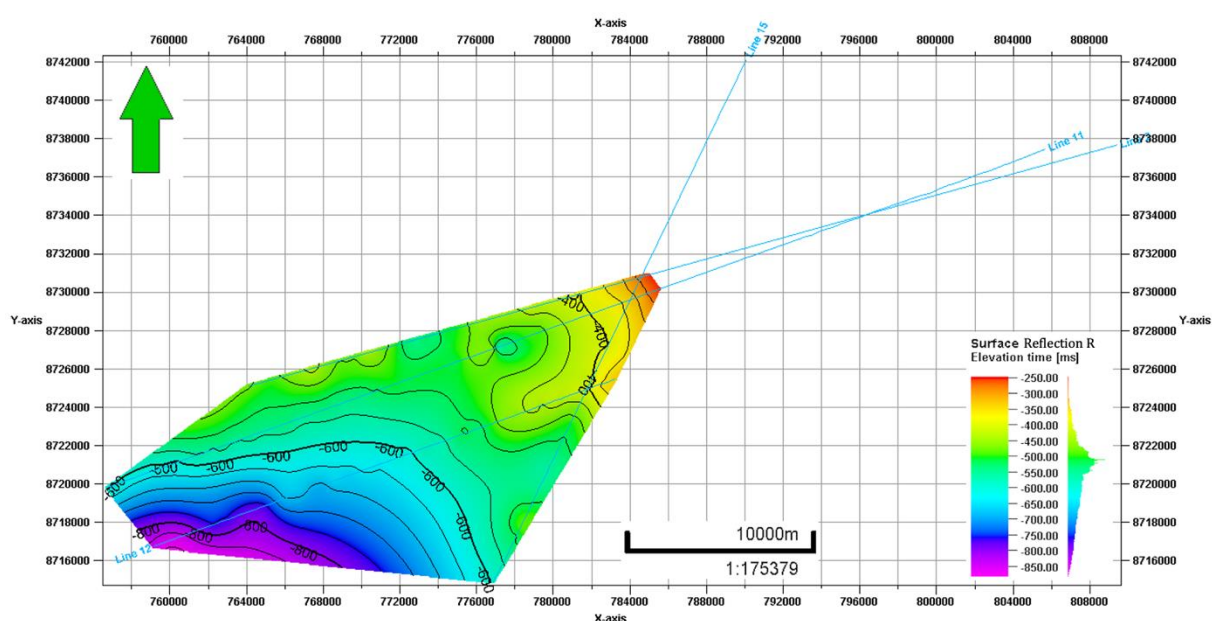


Figure 6.3.4: Surface map of the reflection R horizon in TWT (ms).

6.3.3 Top Permian

The top Permian horizon is interpreted as an unconformity. The Permian succession mainly consists of carbonates and evaporites, whereas the overlying succession consists of clastic rocks (Dallmann, 1999; Dallmann, 2015). This gives the top Permian reflector a strong peak amplitude. Initially, the reflector should be continuous. However, in this case, it is mainly continuous, where it in some locations is abruptly. Figure 6.3.5 shows a surface map of the picked top Permian horizon. The horizon dips towards SW and has been interpreted between 100 and 1300 ms TWT, where the shallowest part is above the BFZ.

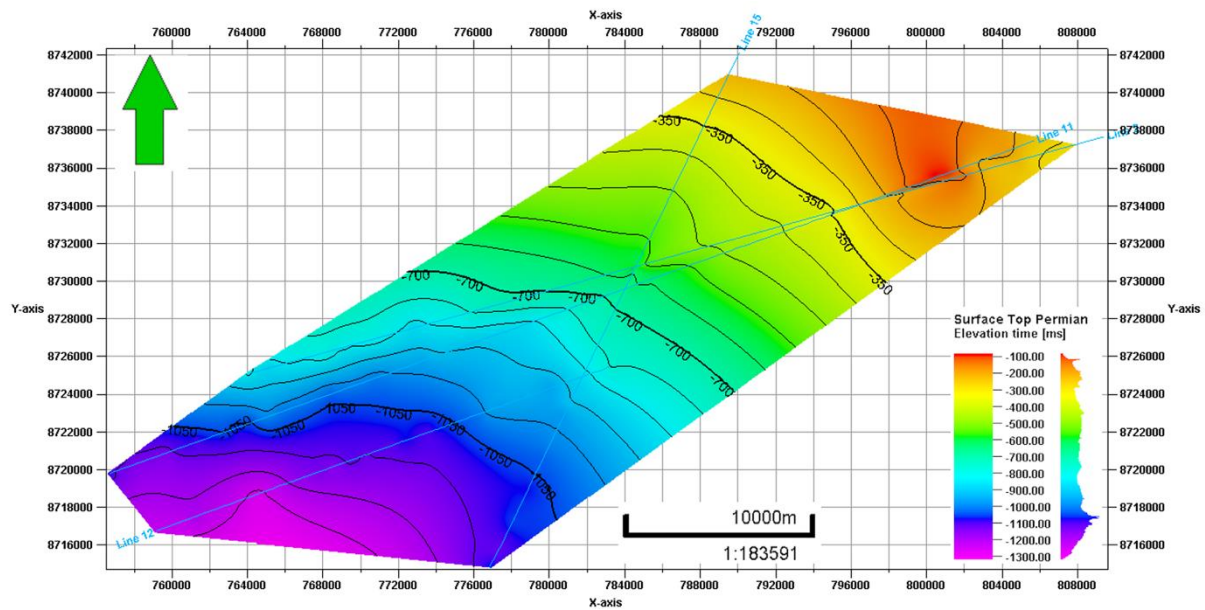


Figure 6.3.5: Surface map of the top Permian horizon in TWT (ms).

6.3.4 Top mid Carboniferous

Like the top Permian horizon, the top mid Carboniferous horizon is also interpreted as an unconformity. The underlying Devonian rocks truncates this horizon creating an angular unconformity. The reflector is continuous and has a strong peak amplitude, which together with the horizon being an angular unconformity, makes it very easy to identify in the seismic section. Figure 6.3.6 shows a surface map of the picked top mid Carboniferous horizon. The horizon dips towards SW and has been interpreted from 200 to 1400 ms TWT, where it is shallowest over the BFZ.

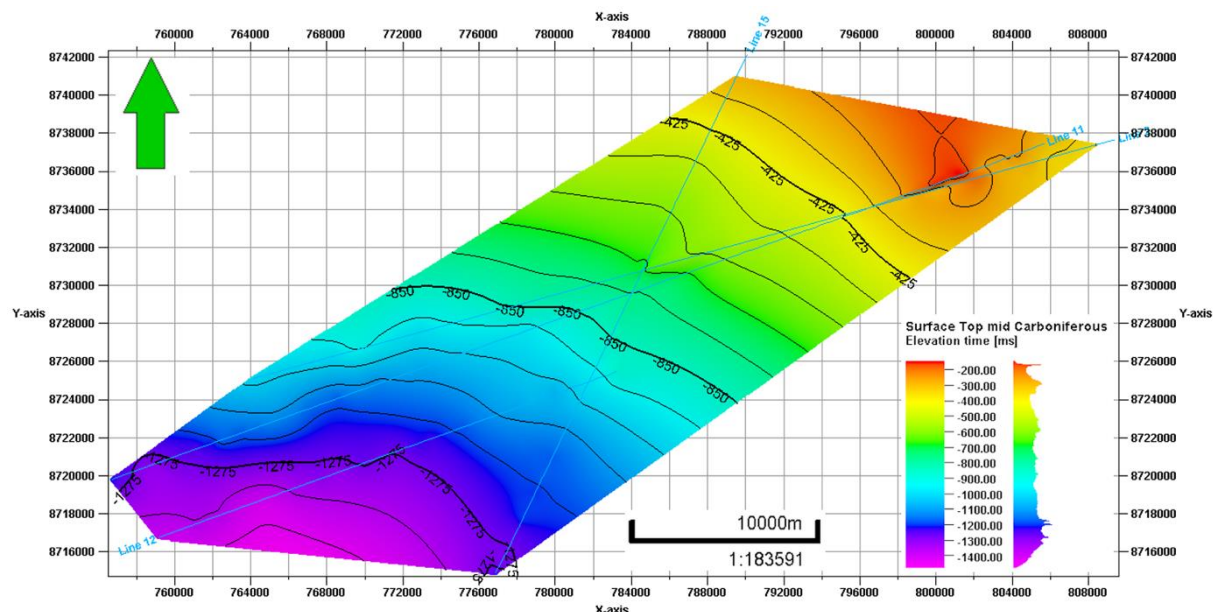


Figure 6.3.6: Surface map of the top mid Carboniferous horizon in TWT (ms).

6.3.5 Top Hecla Hoek

Top Hecla Hoek is the deepest interpreted horizon and represents the basement rocks. The basement is interpreted as a peak, as the density and velocity of the basement are high. The horizon is hard to interpret because it is discontinuous and has a weak amplitude. Figure 6.3.7 shows a surface map of the picked top Hecla Hoek horizon. The horizon is interpreted between 2200 and 4200 ms TWT. In contrast to the overlying horizons, except for the seabed, the horizon is shallowest in SW and deepest in NE. As illustrated in Figure 6.3.7, the horizon is undulating with two step increases in TWT from approximately 2500 to 3100 ms, which is from the yellow to green transition and 3100 to 3600 ms, which is from the turquoise to blue transition.

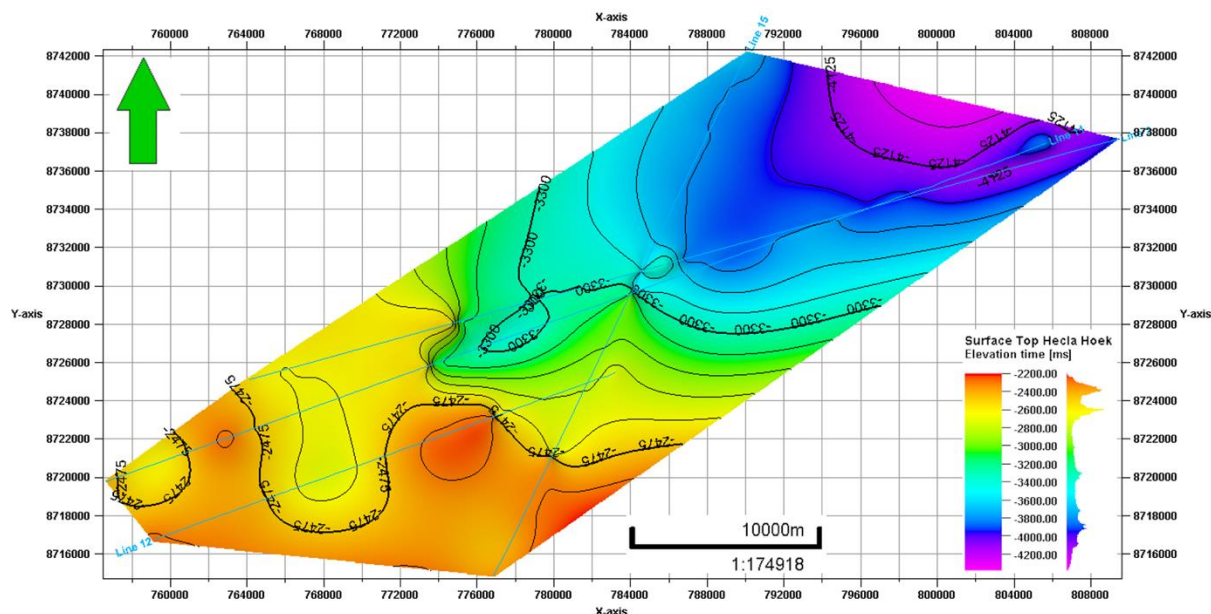


Figure 6.3.7: Surface map of the top Hecla Hoek horizon in TWT (ms).

6.3.6 Stratigraphic units

In addition to interpreting different horizons, it can also be useful to study the seismic character between them. Isopach maps can also provide useful information from the variation in thickness between the two horizons. This can tell something about how the sedimentation has varied across an area, and how the area has been influenced by different processes as uplift, erosion and deformation. Furthermore, eight different units have been described, for which associated isopach maps have been generated. Six of the units have been described below, whereas the remaining two have been described in the next section, as they are strongly influenced by the BFZ.

Unit 1: Seabed to reflection R

The unit covers the area deposited from an unknown Mesozoic age to today. The seismic character varies between being partly continuous to mainly discontinuous, where reflectors truncate the seabed as the unit gradually thins. Generally, the shallowest parts of the unit have very weak reflections, while the area above the reflection R horizon has stronger amplitudes. There are some variations in the seismic character between the different lines. Line 2, 12 and 15 have weak amplitudes with some local areas with medium to strong amplitudes. Line 11 has weak to strong amplitudes, where the majority of the reflections are of medium amplitude. For line 2, 11 and 15 the weaker amplitudes are at the top and the

stronger are near the bottom, while the opposite is the case for line 12, where the strongest amplitudes are at the top. For line 2 and 15 the unit is thinner compared with line 11 and 12. The difference in seismic character for line 2 are shown in Figure 6.3.8. The isopach map (Fig. 6.3.9) shows that the unit is thickest in SW and becomes gradually thinner towards NE. The thickness varies from 0 to 650 ms TWT, where zero values indicate where the reflection R reflector truncates the seabed.

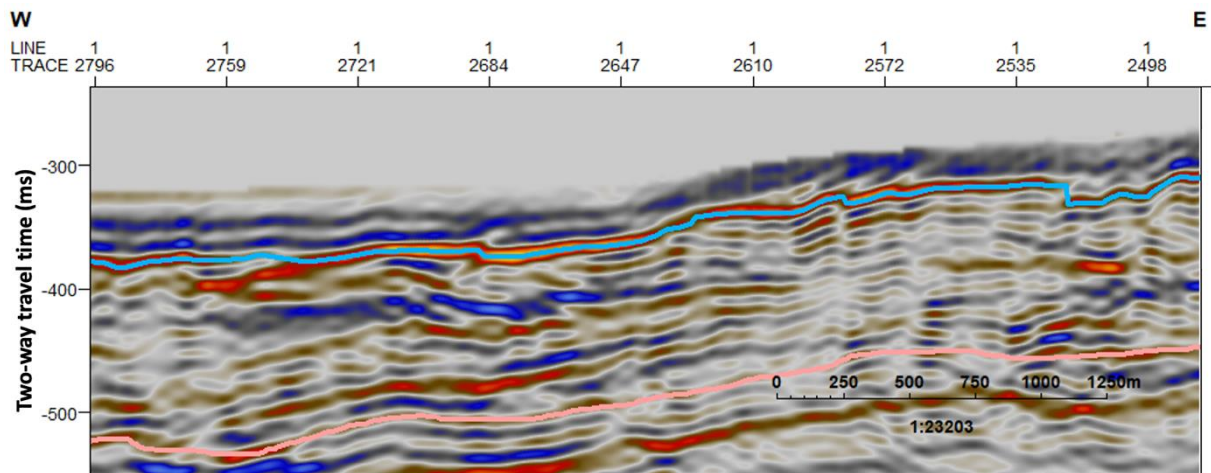


Figure 6.3.8: The figure shows the seismic character of unit 1 for line 2. The seabed horizon is indicated with blue and the reflection R horizon in light red. The reflection amplitudes are varying from weak to medium amplitudes, where some local areas have stronger amplitudes. The pattern varies from discontinuous to varying continuity in the areas with stronger amplitudes.

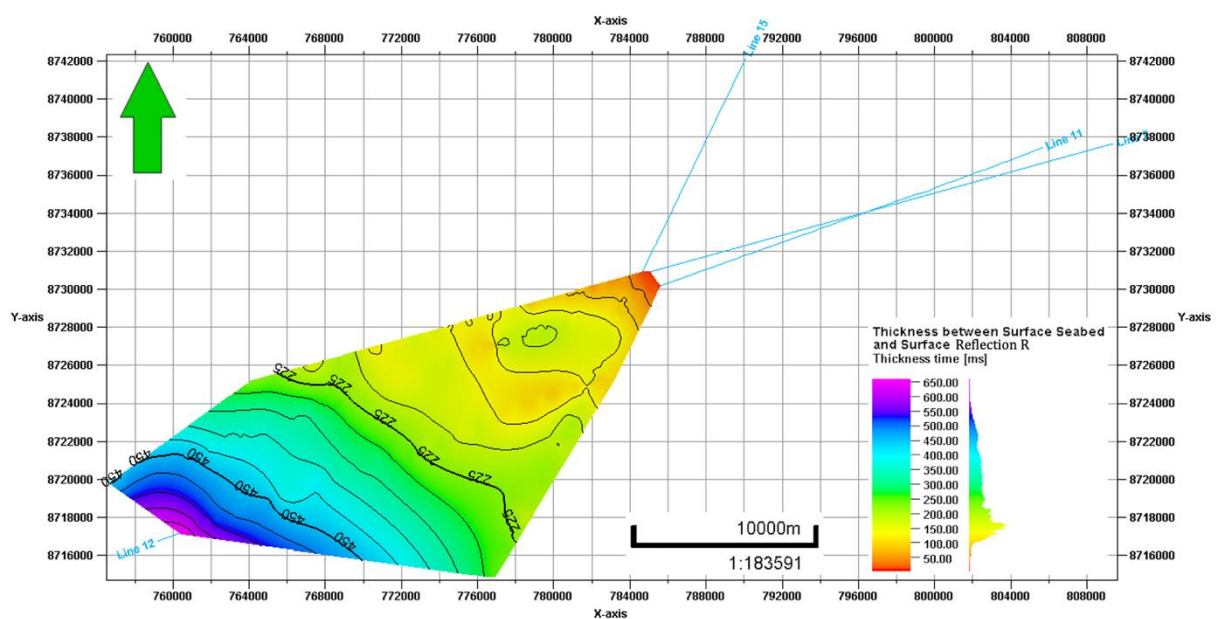


Figure 6.3.9: Isopach map between the seabed and reflection R in TWT (ms).

Unit 2: Reflection R to top Permian

The unit covers the area deposited from Early Triassic to an unknown Mesozoic age. The seismic character varies between being more discontinuous in the upper part of the unit to varying continuity in the lower part (Fig. 6.3.10). In the lower part it is possible to follow a few of the reflections across the seismic section. The seismic character varies across the seismic section and from line to line. For line 2 the amplitudes vary from weak to strong, where there are some very strong reflectors in the lower part of the unit. Line 12 predominantly has weak amplitudes with some medium amplitudes in the lower part. The same trends are seen for line 11 and 15, where the amplitudes vary from weak to medium at the western part of the section, and is dominated by medium to strong amplitudes towards east. The very high amplitudes seen in the different lines might be intrusions (Fig. 6.3.10). The differences in seismic character are shown in Figure 6.3.10, where line 2 is used as an example. The isopach map (Fig. 6.3.11) shows that the unit is thickest in the central to southern areas and thinnest in north. The thickness varies from 275 to 575 ms TWT.

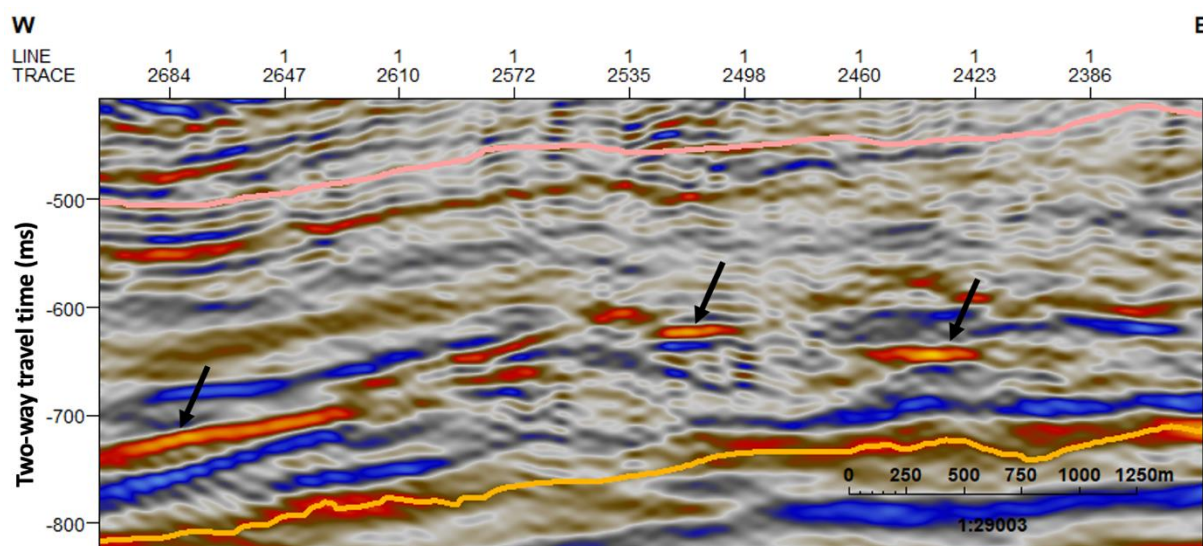


Figure 6.3.10: The figure shows the seismic character of unit 2 for line 2. The reflection R horizon is indicated with light red and the top Permian horizon in orange. The reflection character varies from discontinuous to varying continuity, where some of the reflectors have better continuity than others. The amplitudes are stronger in the bottom of the unit than near the top.

The arrows point at possible intrusions within the unit.

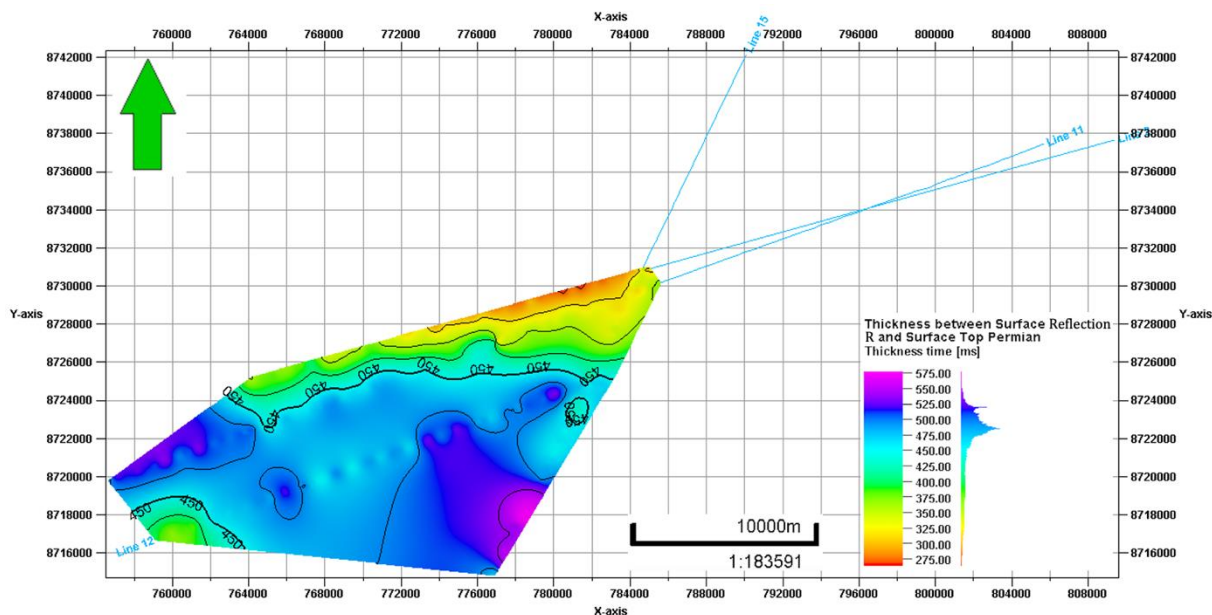


Figure 6.3.11: Isopach map between reflection R and top Permian in TWT (ms).

Unit 3: Seabed to top Permian

The unit combines unit 1 and 2, which is the area deposited from Early Mesozoic to today. The seismic character varies significantly (Fig. 6.3.12). On a general note, the amplitudes vary from weak to strong, where the reflectors are discontinuous to partly continuous. There are large variations in seismic character between the different profiles, which is demonstrated in Figure 6.3.12 where line 2 and 11 are compared. The isopach map (Fig. 6.3.13) shows that the unit is thickest in SW and gradually thins towards NE. The thickness varies from 100 to 1000 ms TWT, where it is thinnest directly above BFZ.

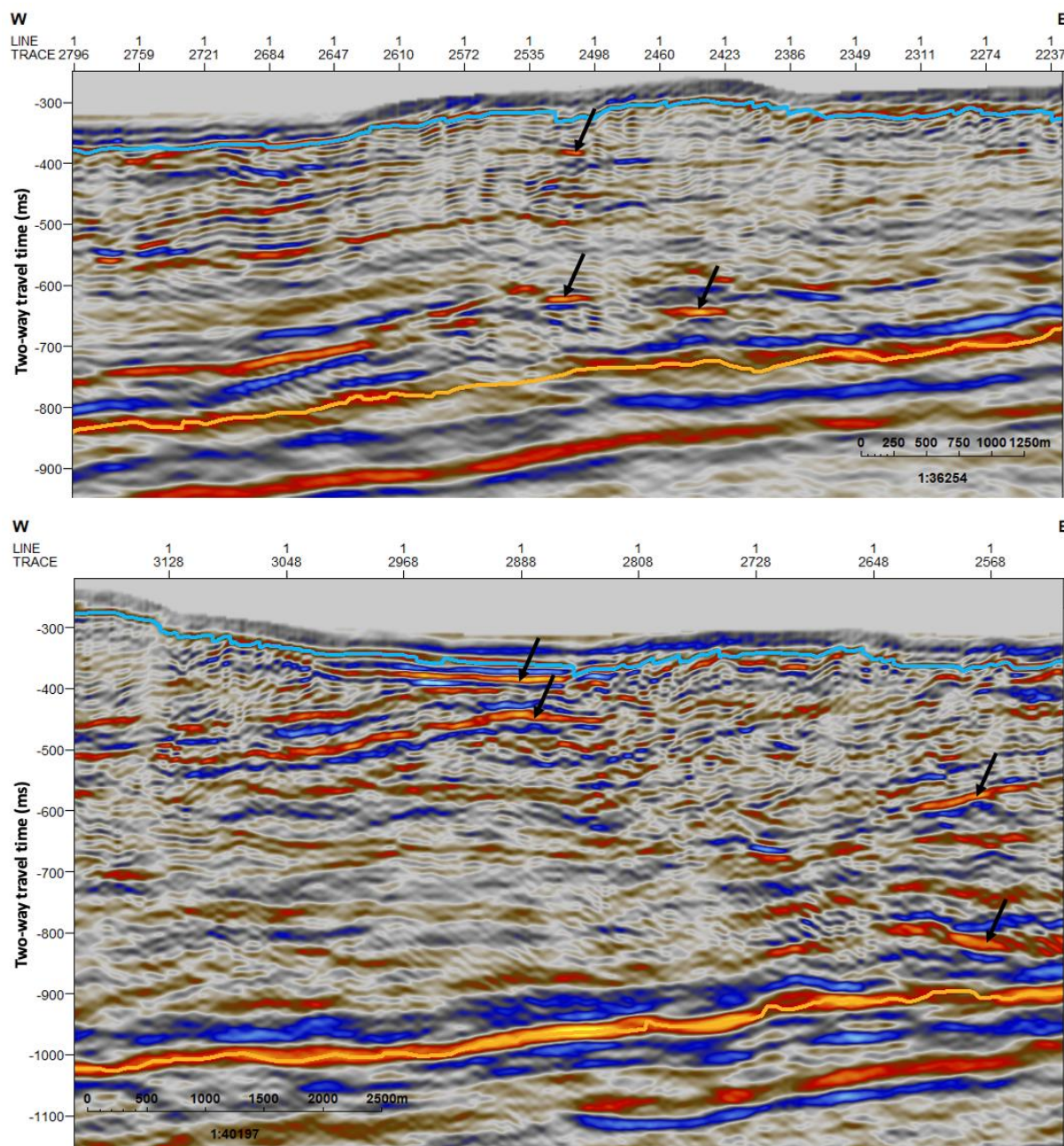


Figure 6.3.12: The figure shows the seismic character of unit 3 for line 2 (top) and line 11 (bottom). The seabed horizon is indicated with blue and the top Permian horizon in orange. Comparing the two lines it is possible to see that line 11 overall have higher amplitudes than line 2, but in return is more chaotic with more discontinuous reflectors. It is also possible to see that line 11 changes reflection character from west to east. The western part has higher amplitudes at the top of the unit, whereas the eastern part has higher amplitudes at the bottom of the unit. The reflection character also becomes more chaotic from west to east. Arrows point to possible intrusions, where both lines might have intrusions through the entire unit.

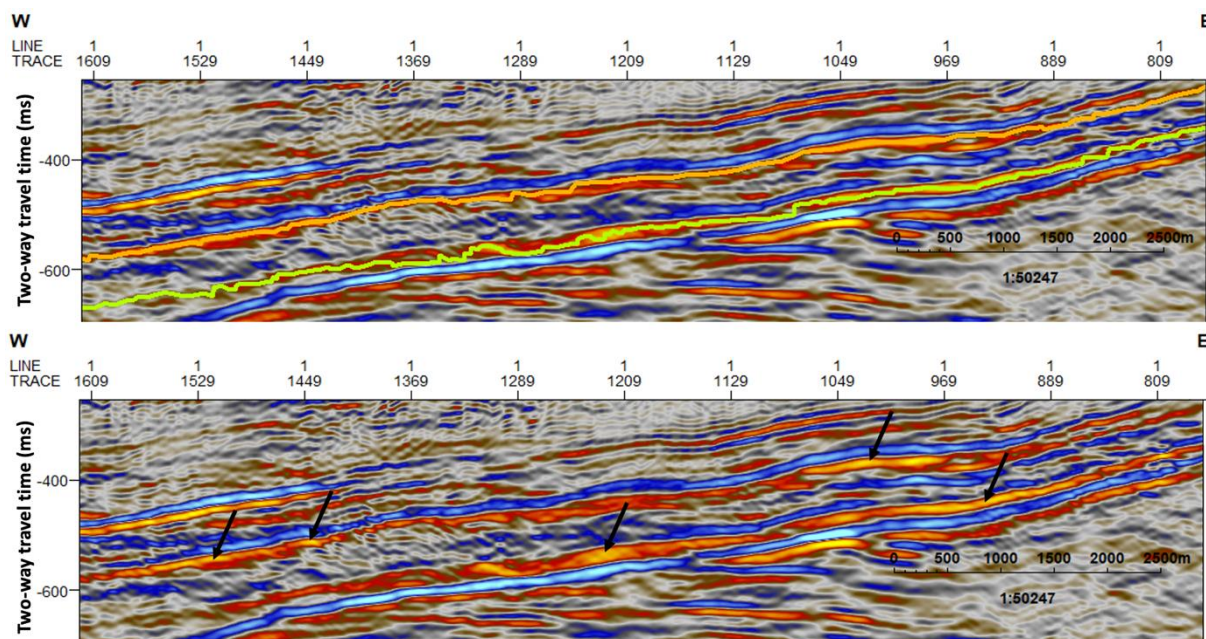


Figure 6.3.14: The figure shows the seismic character of unit 4 for line 2. The first figure shows the unit with the interpreted horizons, where top Permian is indicated with orange and top mid Carboniferous in green. The second figure shows the unit without the interpreted horizons, where the arrows point at possible intrusions.

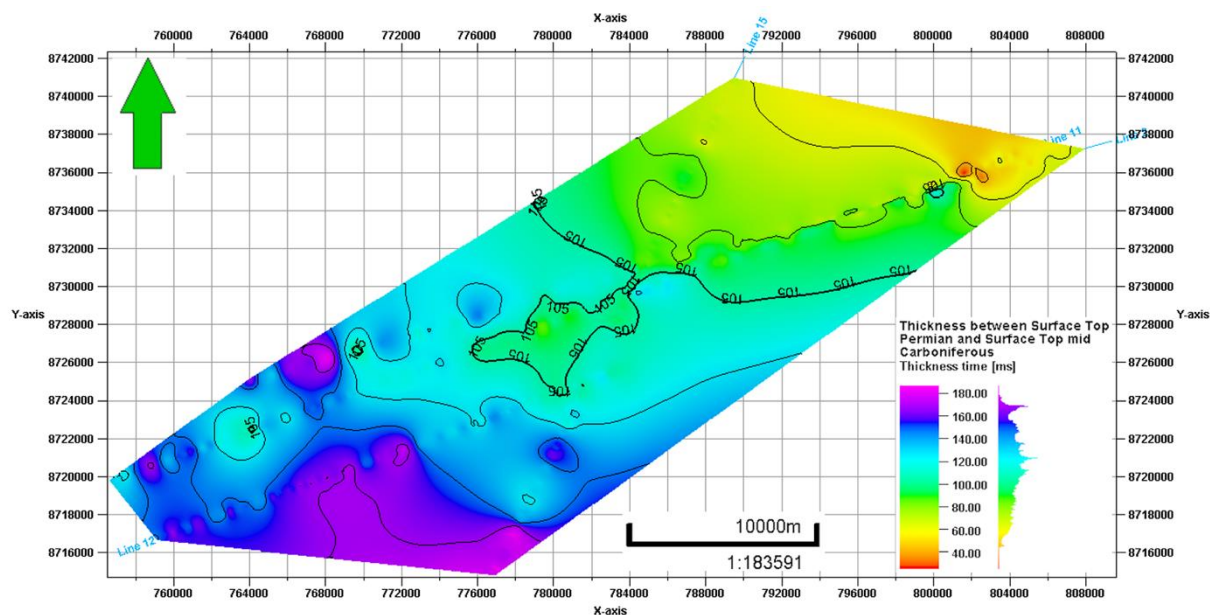


Figure 6.3.15: Isopach map between top Permian and top mid Carboniferous in TWT (ms).

Unit 5: Top mid Carboniferous to top Hecla Hoek

The unit covers the sediments that were deposited from Early Devonian to Middle Carboniferous. The unit truncates the top mid Carboniferous horizon, where the top of the unit has a different seismic character compared with the central and lower parts (Fig. 6.3.16).

The central and lower parts are characterized by low amplitude reflections from the Devonian Old Red sandstone. The seismic pattern is chaotic, where the upper parts contain some higher amplitude reflections (Fig. 6.3.16). The isopach map (Fig. 6.3.17) shows that the thickness varies from 1000 to 4000 ms TWT, increasing from SW to NE.

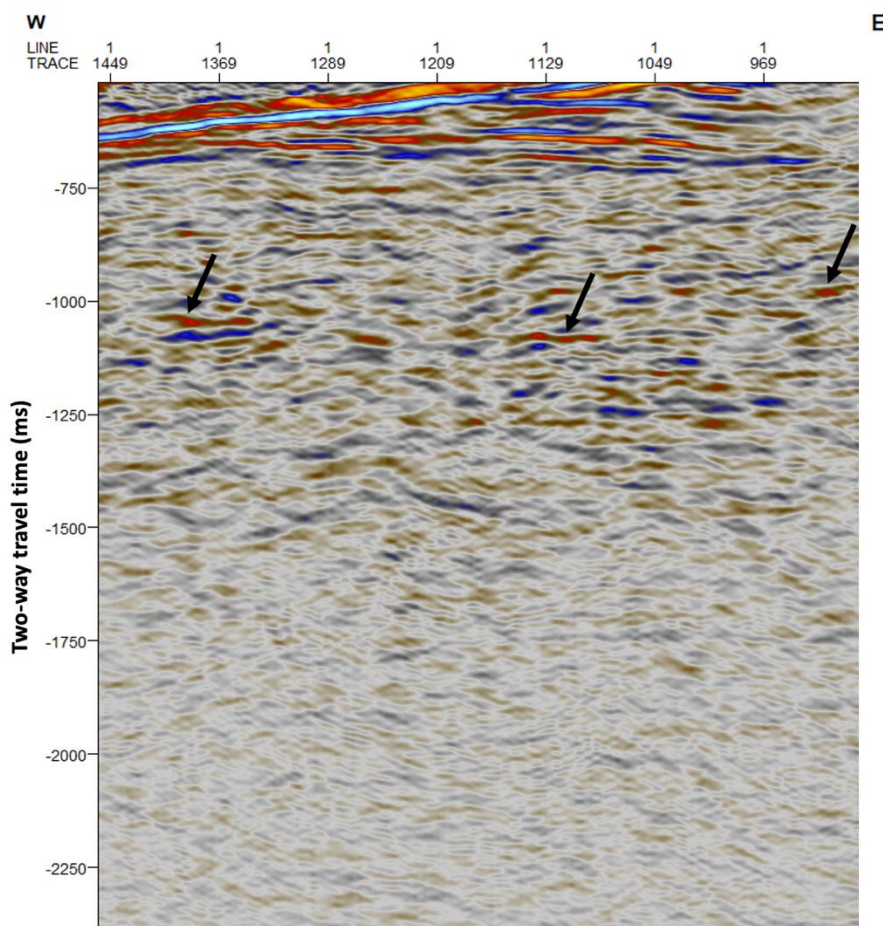


Figure 6.3.16: The figure shows an outcrop of unit 5 for line 11. The reflection pattern is chaotic and discontinuous with mainly low amplitudes. The arrows point at some higher amplitudes in the upper part of the unit.

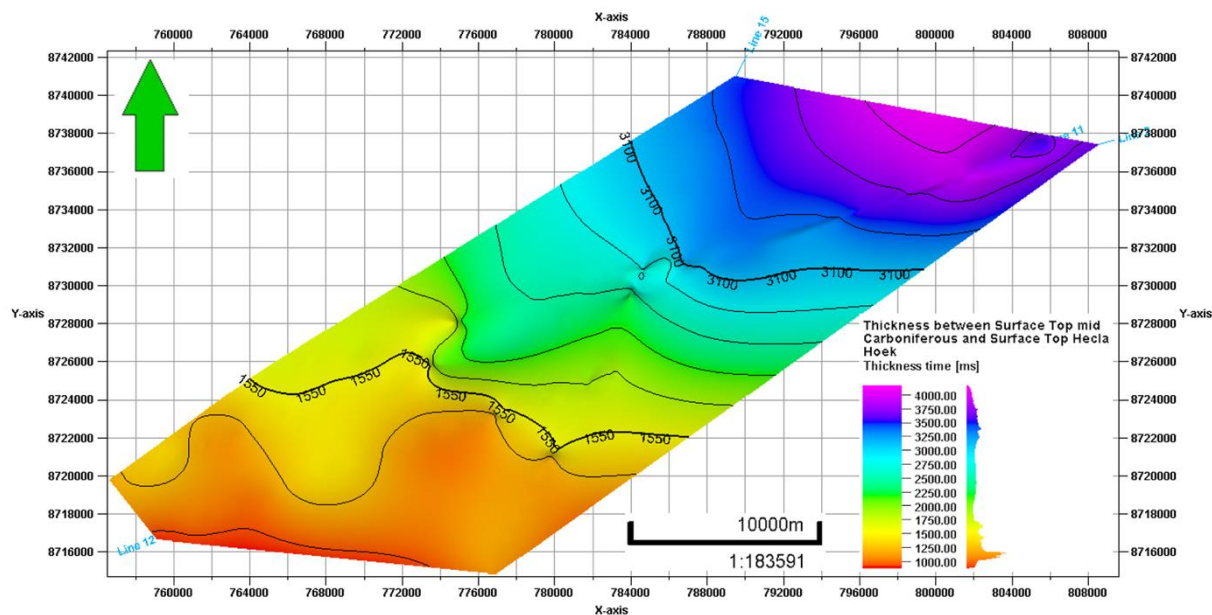


Figure 6.3.17: Isopach map between top mid Carboniferous and top Hecla Hoek in TWT (ms).

Unit 6: Hecla Hoek

The unit covers the basement rocks, which were deposited from late Proterozoic through Silurian. The unit comprises igneous and metamorphic rocks that generates some stronger reflections at the top of the unit (Fig. 6.3.18), because of the large impedance contrast with the overlying Devonian sandstones. The rocks were highly deformed during the Caledonian Orogeny (Hjelle, 1993), which makes the reflectors discontinuous and chaotic (Fig. 6.3.18).

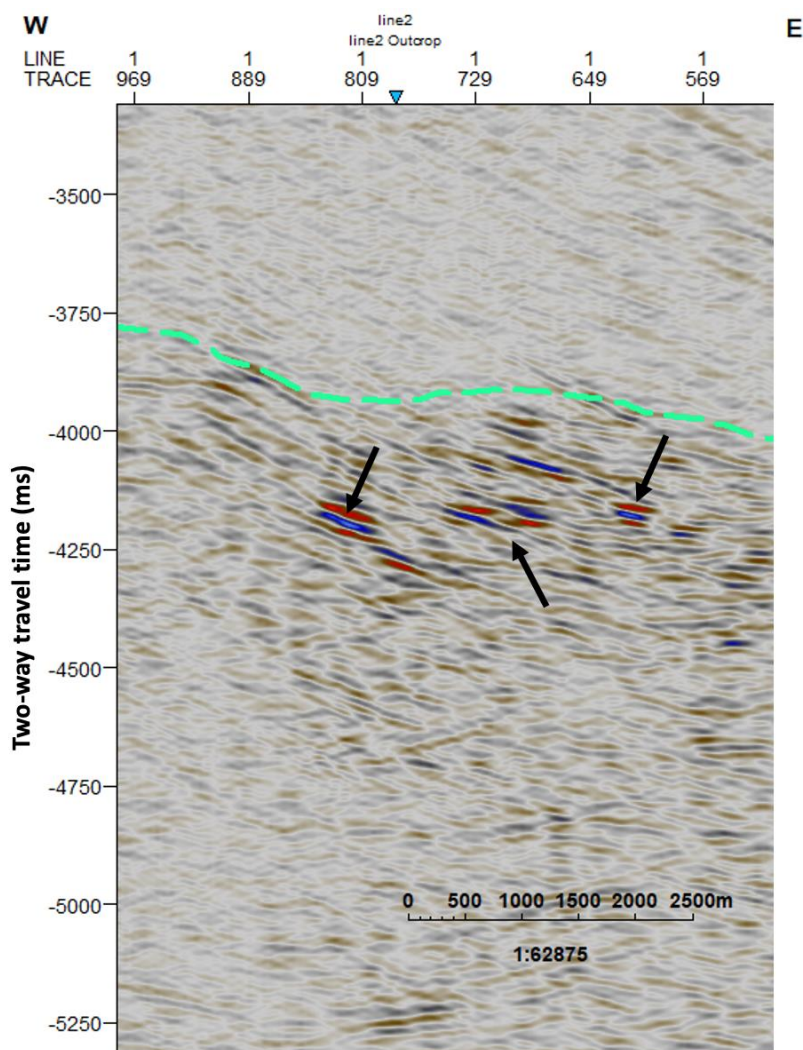


Figure 6.3.18: The figure shows the difference between the lower part of unit 5 and the upper part of unit 6 for line 11. The Hecla Hoek horizon is indicated with the turquoise dotted line. The arrows point at the stronger reflections at the top of the unit, which are a result of large impedance contrasts with the overlying unit.

6.4 Structural interpretation

The main focus of the structural interpretation has been to map dominant structural features in the Billefjorden Fault Zone and Hecla Hoek. Clear displacements in the seismic sections and interpreted horizons have been the main criteria when interpreting fault structures. The BFZ is only covered by two of the seismic lines, 2 and 11, whereas it is possible to map possible Hecla Hoek faults for all the lines. The structural features inside BFZ are very poorly imaged, as the faults have steep to vertical orientation and thus are not imaged properly by the seismic technique used. Two horizons have been interpreted across BFZ as a part of the structural interpretation. These horizons were selected because they are strongly influenced by the fault zone.

6.4.1 Fault structures in BFZ

The seismic character in the BFZ is very complex, where the reflection amplitudes are weak, discontinuous and chaotic (Fig. 6.4.1). The faults are difficult to recognize and interpret as they are poorly imaged because of their high angles. The interpretation thus depends on clear displacements in horizons and changes in seismic character. Figure 6.3.1 shows the fault interpretation in BFZ. Two normal faults (purple and light yellow) have been interpreted rooting in a scoop-shaped detachment (yellow). There are several possible interpretation options, which have been discussed in Chapter 7, along with possible structural models.

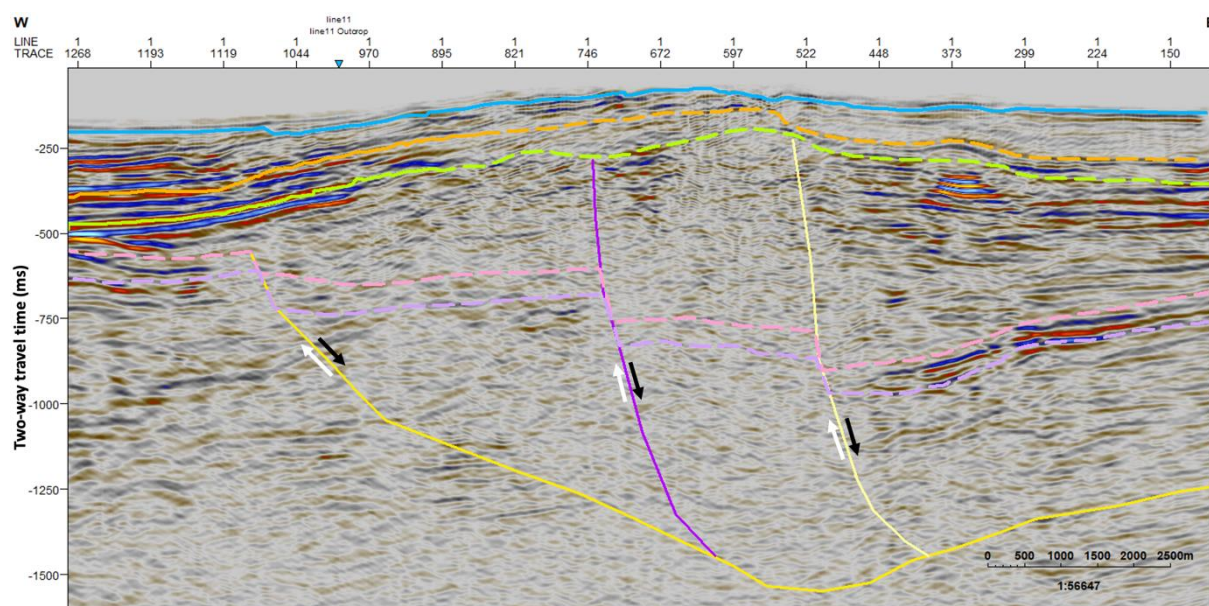


Figure 6.4.1: The figure shows the interpreted structures in the BFZ for line 2. The interpreted horizons in the section are the seabed (blue), top Permian (orange), top mid Carboniferous (green), BFZ H1 (pink) and BFZ H2 (purple). The interpreted structures are two high angle normal faults (purple and light yellow), and a detachment (yellow). The interpreted faults root in the detachment and displaces the BFZ H1 and BFZ H2 horizons. The arrows indicate the displacement direction of the two fault blocks, which indicates two normal faults. The seismic character inside the BFZ is chaotic, weak and discontinuous, with some stronger reflections to the west and east.

6.4.2 Stratigraphy in BFZ

The two horizons which have been interpreted across the BFZ, have been denoted as BFZ horizon 1 (BFZ H1) and BFZ horizon 2 (BFZ H2). The interpretations are represented by dotted lines, which means that the interpretations are uncertain, particularly in the central part, where the seismic character is very chaotic, with weaker amplitude and discontinuous

reflectors (Fig. 6.4.1). What makes the interpretations uncertain is the fact that the area is complex with numerous faults and folds.

BFZ horizon 1

The BFZ horizon 1 horizon is interpreted on a weak amplitude reflection, where the reflector is almost transparent in the middle of the fault zone. The reflector is mainly discontinuous, where the continuity is slightly better farthest east. The surface map (Fig. 6.4.2) shows that the surface is shallowest in SW and deepest in the middle of BFZ. The surface has been interpreted between 550 and 900 ms TWT and has varying topography, as a result from the faults that dominate the area.

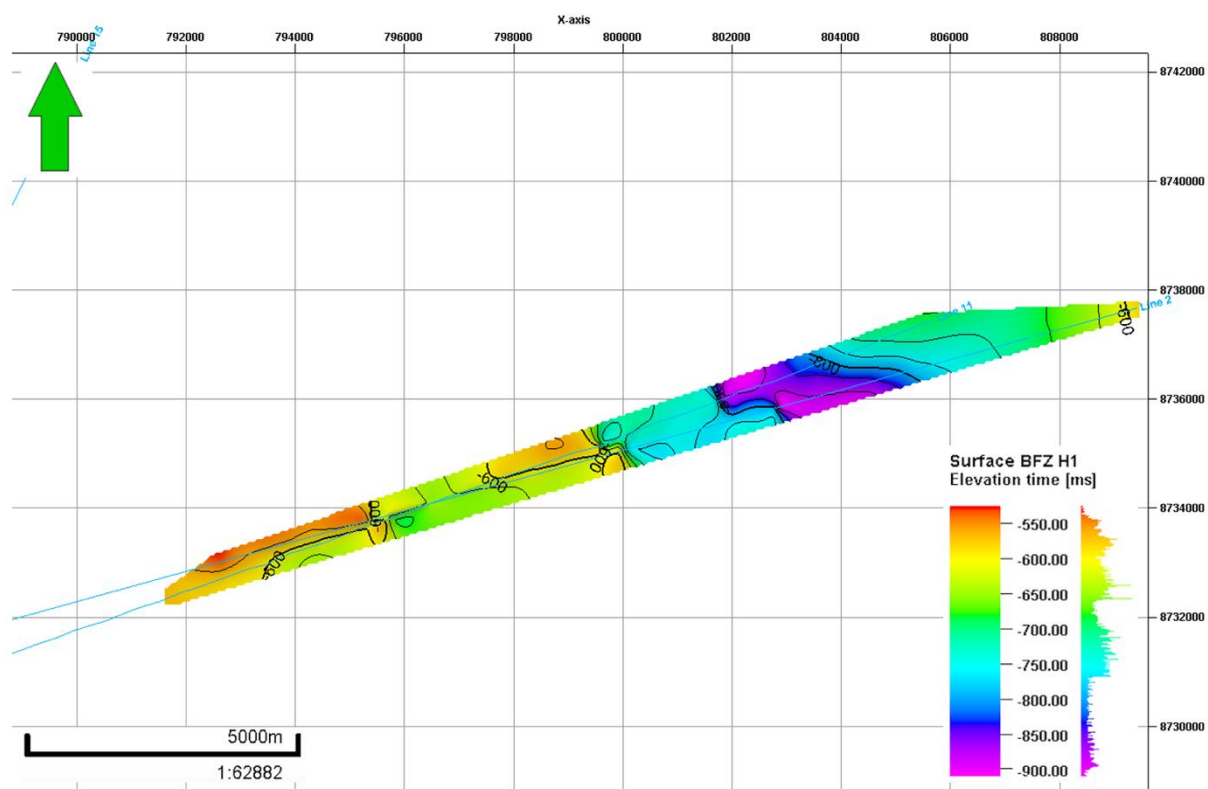


Figure 6.4.2: Surface map of the BFZ horizon 1 in TWT (ms).

BFZ horizon 2

BFZ horizon 2 have been interpreted on a medium amplitude reflector, with the strongest amplitudes to the west and east, and weakest amplitudes in the middle of BFZ. The reflector is continuous to discontinuous, with better continuity in the areas with stronger reflections. The surface map (Fig. 6.4.3) shows that the surface is shallowest in SW and deepest in the

middle of BFZ. The surface has been interpreted between 600 and 950 ms TWT and has varying topography resulting from the structural deformation in the area.

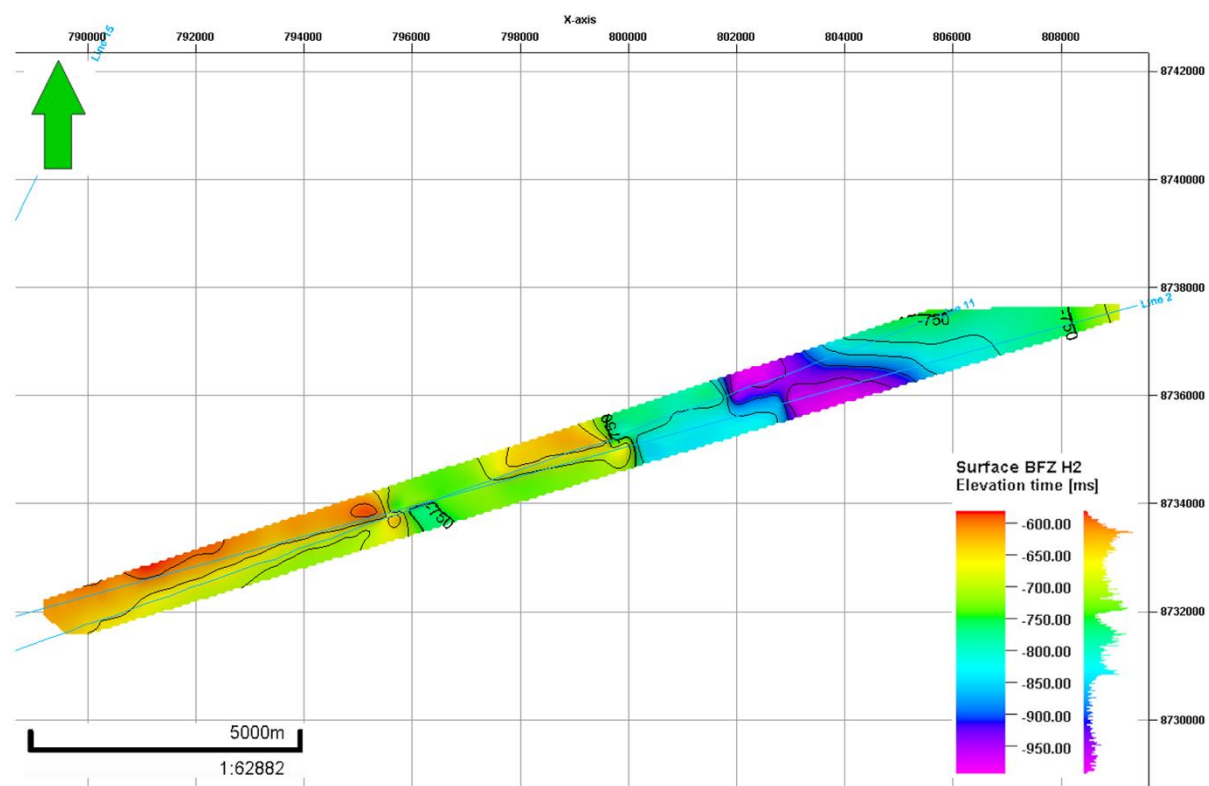


Figure 6.4.3: Surface map of the BFZ horizon 2 in TWT (ms).

Unit 7: Top mid Carboniferous to BFZ H1

The unit shows how the area appears between BFZ H1 and the top mid Carboniferous unconformity. The amplitudes are mainly weak with some medium amplitudes at the top of the unit, whereas the reflectors are discontinuous and chaotic in the middle. The reflection pattern changes farthest east, where the continuity is varying with tendencies of parallel reflectors. The isopach map (Fig. 6.4.4) shows that the unit is thinnest in SW, where BFZ H1 truncates the unconformity. The thickest part is in the middle of BFZ where BFZ H1 is faulted down, and top mid Carboniferous is uplifted above the fault zone. The figure indicates that the thickness increases rapidly at some locations, which is caused by faulting. The thickness varies from 50 to 650 ms TWT.

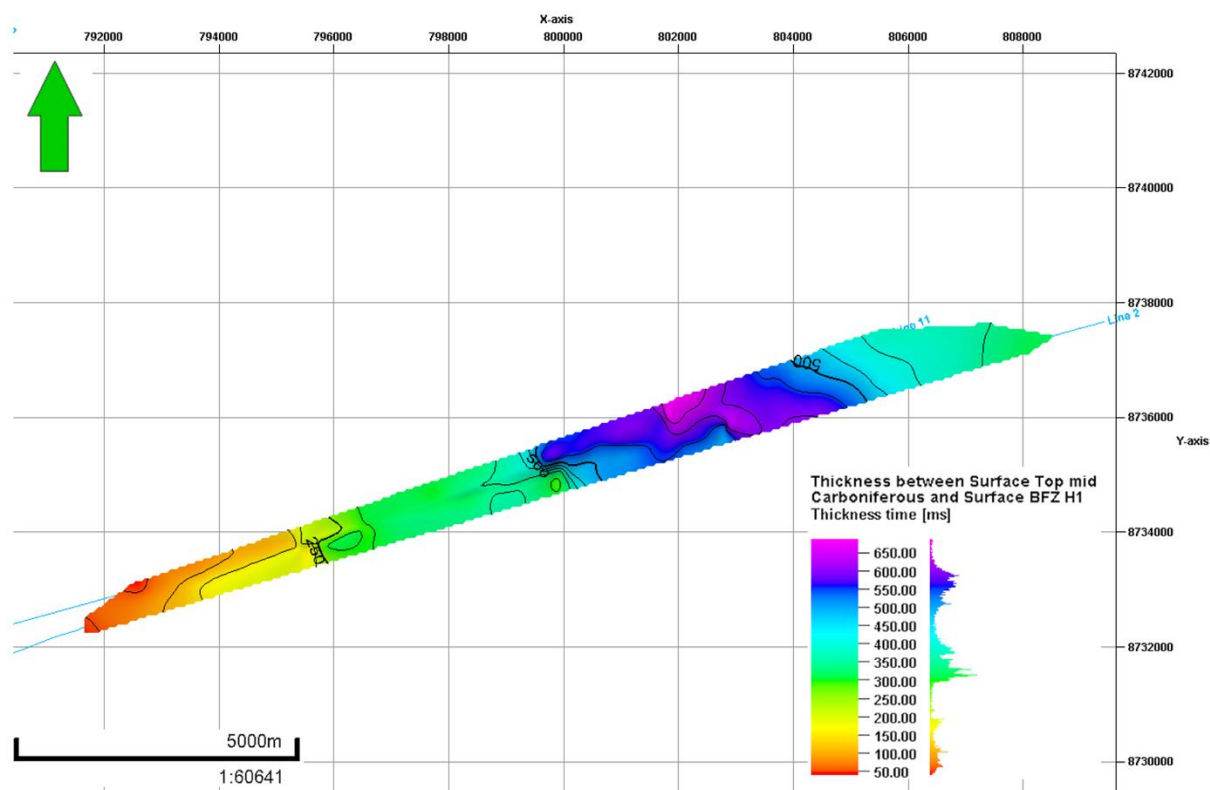


Figure 6.4.4: Isopach map between top mid Carboniferous and BFZ horizon 1 in TWT (ms).

Unit 8: BFZ H1 to BFZ H2

The unit shows how the area appears between the two BFZ horizons. The amplitudes are mainly weak with some stronger amplitudes in W and E. The seismic pattern is chaotic with discontinuous reflectors in the middle. The pattern changes towards each end of the unit, where the continuity is varying with tendencies of parallel reflectors. The isopach map (Fig. 6.4.5) shows that the thickness varies from 0 to 130 ms TWT. The thickness is relatively constant at around 80 ms TWT. The figure shows that there are three locations with anomalies at the three fault locations. As the lines (2 and 11) image the fault zone from different angles, the interpretations are difficult to correlate due to differences in the seismic pattern.

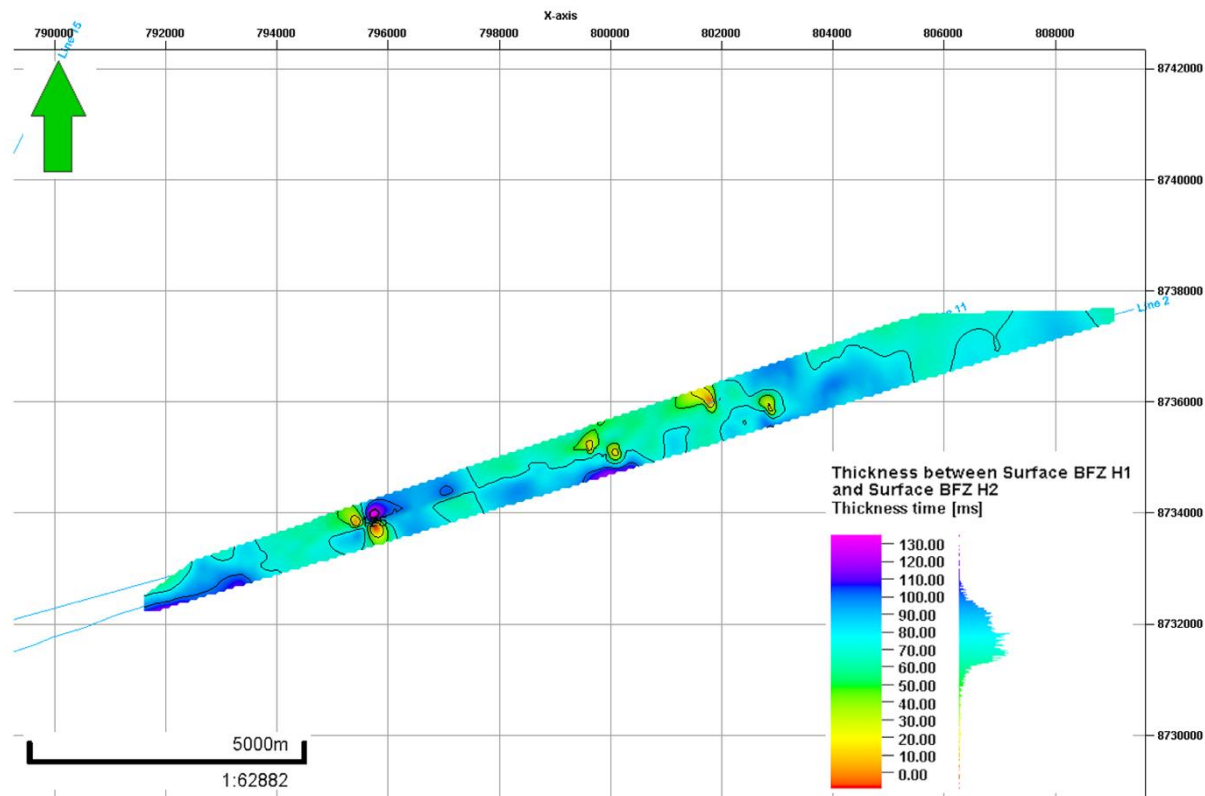


Figure 6.4.5: Isopach map between BFZ horizon 1 and BFZ horizon 2 in TWT (ms).

6.4.3 Structures in Hecla Hoek

From the stratigraphic interpretation the top Hecla Hoek horizon is described as undulating, which during the structural interpretation has been interpreted as folding. From this interpretation it is possible to infer that the entire Hecla Hoek unit is folded. The horizon and surface map (Fig. 6.3.7) also shows that there are two steep inclines in TWT, which have been interpreted as faults (Fig. 6.4.6). There are several possible interpretations for the fault structures in this unit, where this interpretation was considered the most probable. The other alternatives are discussed in Chapter 7.

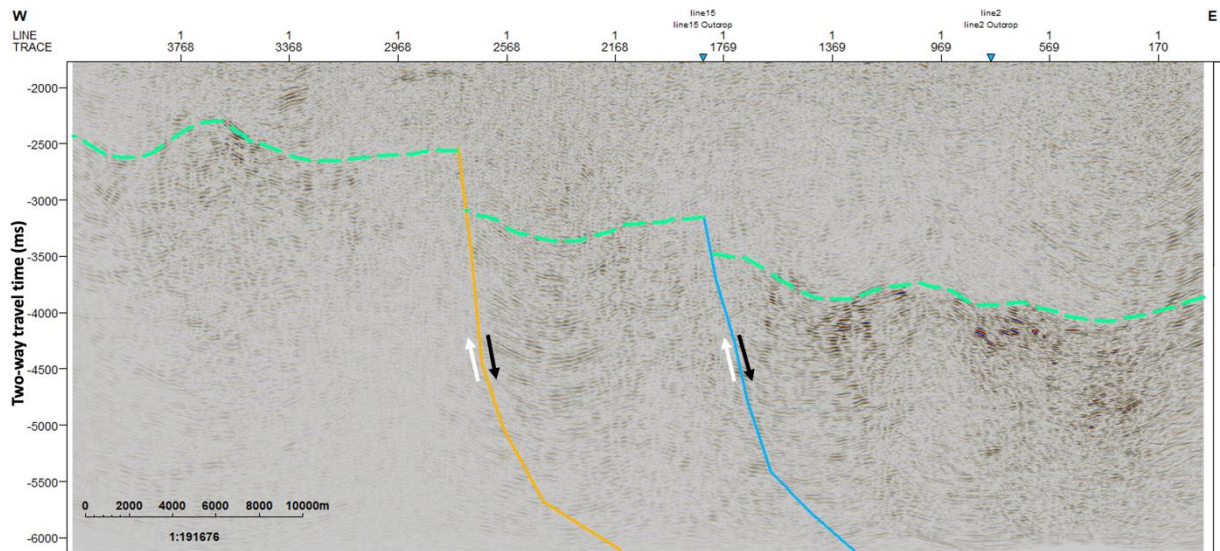


Figure 6.4.6: The figure shows the interpreted structures for line 11. The interpreted top Hecla Hoek horizon (turquoise) is folded, which can be seen from the undulating line. The two interpreted faults (orange and blue) clearly displace the horizon. The arrows indicate the displacement direction, which indicates two normal faults.

Chapter 7

Discussion

In this chapter different elements from the processing and interpretation results will be discussed. For the processing, it has been important to evaluate how it has affected the overall data quality, and to identify changes that could or should have been made. For the interpretation, the different stratigraphic units and interpreted structures have been discussed in accordance with other interpretation options and previous studies in the area.

7.1. Processing

One of the largest challenges when acquiring marine seismic reflection data is multiples, which have significantly influenced the quality of the datasets. The process of removing the water layer multiples started with velocity filtering and surface consistent predictive deconvolution. The velocity filters are used to remove the multiples with low critical angles, the remaining multiples travel almost vertically in the water layer and can effectively be removed by deconvolution. The two methods removed most of the multiples, however, some multiple energy remained. By adjusting the velocity filter values, more of the multiples could have been removed, but this would in return cause some of the reflected energy to be removed. The filter values were not changed, as removing reflected energy could negatively affect the quality of the data, and later processing steps like migration, mute and stacking would attenuate the multiple energy further.

Initially, the seabed had a strong and continuous reflection (Fig. 5.2.2). However, the processing has caused the seabed to become weaker, more discontinuous and influenced by noise. The significant reduction in the quality of the seabed is caused by the effects of the velocity filters that were used to remove the water layer multiples. The water layer multiples repeat at short intervals and are more dominating in the shallow parts. Because more energy has to be removed in the shallow parts, the quality will become poorer compared to the deeper parts. Muting has also contributed to the reduction in the quality of the seabed, where

the muting caused large parts of the seabed reflector to be removed. Additionally, time correction during pre-stack migration cause stretching of traces and automatic 'stretch-mute'.

Amplitude recovery has been used to amplify the energy in the shallower parts of the section. In addition to amplifying reflections, amplitude recovery will also amplify the noise that have been generated during the processing. More careful use of amplitude recovery could have caused the section to become less influenced by noise. Yet, the process is necessary to be able to interpret the shallower parts of the section. The amplitude scaling used during the migration could be scaled up even more to strengthen the amplitudes in the shallow section. However, when the shallow parts are scaled up, the amplitudes for the deeper parts are scaled down. It was therefore important to choose a value that did not significantly affect the amplitudes of the deeper parts of the section.

The seabed and shallow parts of the section were also strongly influenced by spatial aliasing prior to the application of an anti-alias low-pass filter and a velocity filter that were used during the migration and muting. Most of the spatial aliasing was removed by the two filters, but some remained. More of the aliasing could have been removed by increasing the CDP distance in the anti-alias filter, but this would in return affect the horizontal resolution negatively. As the spatial aliasing was not a big problem, it was decided that the result after the migration and muting was satisfactory.

The quality of the data was discussed in Section 6.2.3, where it was demonstrated that the quality of the data was significantly improved because of the processing. Yet, noise have been generated through the seismic section because of the processing, where amplitude recovery has amplified the noise. Noise has also been generated near the ends of the sections as a result of the streamer turning. Despite the attempt that was made to scale down the streamer noise, it is still clear in the seismic sections. Inaccurate picking of velocities during the velocity analysis can influence the primary reflections and cause them to become weaker. The bigger the difference between the picked velocity and the true velocity of the reflection, the weaker it will appear in the seismic section.

The quality of the seabed and shallow reflections have been most influenced by the processing. However, the data have been acquired with respect to imaging of deeper structures, which is the target area for this study. The poorer quality of the shallower sections is thus not a significant problem. The removal of the water layer multiples is also important to ensure that they do not dominate the seismic section. Thus, it is possible to interpret the processed sections as they contain a lot of information about real seismic events.

7.2 Interpretation

7.2.1 Stratigraphic units

Unit 3: Seabed to top Permian

The unit comprises both unit 1 and unit 2 and is thickest in the south-western area. The unit gradually thins towards northeast and is thinnest over the BFZ (Fig. 6.3.13), where erosion and uplift during Tertiary have affected the unit. From the bedrock geology at Svalbard (Fig. 2.1.2) it can be seen that rocks deposited during Middle Jurassic-Early Cretaceous and Triassic-Middle Jurassic are present at the land areas surrounding inner Isfjorden and outer Sassenfjorden. However, these rock units might not be present in the fjord due to erosion. The seismic lines in this study are compared to the study from Blinova et al. (2012, 2013). From their studies it is possible to infer that the Middle Jurassic-Early Cretaceous unit is probably not present in this study, whereas the Triassic-Middle Jurassic unit most likely is present.

The Sassendalen Group contains low-velocity shales that cause weak and discontinuous reflections, with some intervals that have higher velocities. The Kapp Toscana group contains folded and over-thrusted sandstones of higher reflectivity and velocity compared to the underlying group (Bergh et al., 1997; Bælum and Braathen, 2012; Blinova et al., 2012, 2013). The descriptions of the reflectivity patterns from the previous studies can be used to identify the reflection R horizon and to infer which groups that are present in unit 3. In this study, unit 1 has been described as having stronger reflections compared to unit 2, and both units have discontinuous to varying reflection continuity (Fig. 7.2.1). When comparing the interval velocities from the velocity analysis with the interpreted stratigraphy (Fig. 7.2.1), it is found that unit 1 has higher velocities than unit 2. The changes in seismic character and velocity

indicate that unit 1 corresponds to the Kapp Toscana Group, and unit 2 to the Sassendalen Group. It is therefore suggested that reflection R is the boundary between the two groups. However, this is only one alternative interpretation.

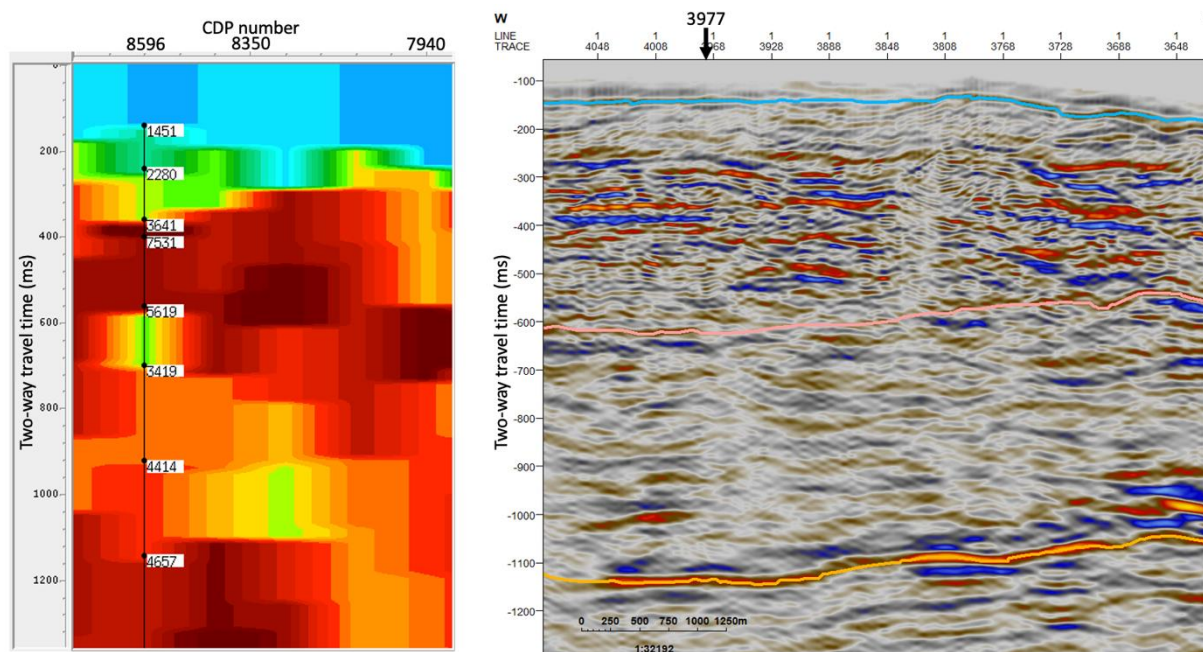


Figure 7.2.1: The left window shows an outcrop from IsoVel from line 11. The velocity numbers (ms) are for CDP 8596, which corresponds to trace 3977 in the right window. The right window shows an outcrop from Petrel from line 11. The seabed is illustrated in blue, reflection R in light red, and top Permian in orange. Unit 1 is from the seabed to reflection R, whereas unit 2 is from reflection R to top Permian.

Unit 4: Top Permian to top mid Carboniferous

The unit progressively thins and becomes shallower from SW to NE (Fig. 6.3.15). The unit is shallowest and thinnest over the BFZ, indicating that the unit has been subjected to uplift. The middle Carboniferous unconformity is easily recognisable as an angular unconformity, where the underlying reflectors truncate at this horizon. The top Permian unconformity has no visible truncation, but there might be some slight indications of the overlying reflectors onlapping on the horizon. However, it is very difficult to see, as the reflectivity pattern of the overlying unit can be very discontinuous. The top Permian unconformity developed in association with a regional uplift during the Permian-Triassic transition (Blinova et al., 2013). The strong, continuous and parallel reflection pattern that dominates the unit is due to the accumulation of carbonates and evaporites that create a strong acoustic impedance contrast with the overlying and underlying successions (Blinova et al., 2013).

Unit 5: Top mid Carboniferous to top Hecla Hoek

Unit 5 is thinnest in SW and progressively thickens towards NE (Fig. 6.3.17), this is also seen in the study from Skaara (2020). The thickest part of the unit is where the top mid Carboniferous horizon is uplifted above the BFZ, and where top Hecla Hoek has been faulted down by what has been interpreted as normal faults. The significant thickness of the unit has been caused by the large amounts of molasse sediments that were deposited during the Devonian period in association with the collapse of the Caledonian mountain range (Dallmann, 2015). The sedimentary unit was involved in Late Devonian contraction related to the Svalbardian Phase, which can explain the chaotic reflectivity pattern observed in the unit (Blinova et al., 2013).

In Chapter 6, the unit was described to have stronger reflections at the top eastern part of the unit just west of the BFZ (Fig. 7.2.2). From interpretations made by Blinova et al. (2012, 2013) it might be inferred that these stronger reflections are a result of sedimentary deposition from lower to middle Carboniferous. This might suggest that the Billefjorden Group are present in this area. Bælum and Braathen (2012) has described the Billefjorden Group to have no major seismic reflections inside the unit, but that it stands out compared to the very reflective overlying Gipsdalen Group, and the underlying chaotic reflection pattern found in the basement rocks. In the study from Bælum and Braathen (2012), the Billefjorden Group was only found on the eastern side of BFZ, where the Devonian rock unit is not present. In a study from the Nordfjorden High made by Braathen et al. (2012), they have possibly interpreted a unit that corresponds to the Billefjorden Group to the west of BFZ, overlying the Devonian rock unit. Thus, an alternative interpretation to the stronger reflections described in this study is that they might be a part of the Billefjorden Group.

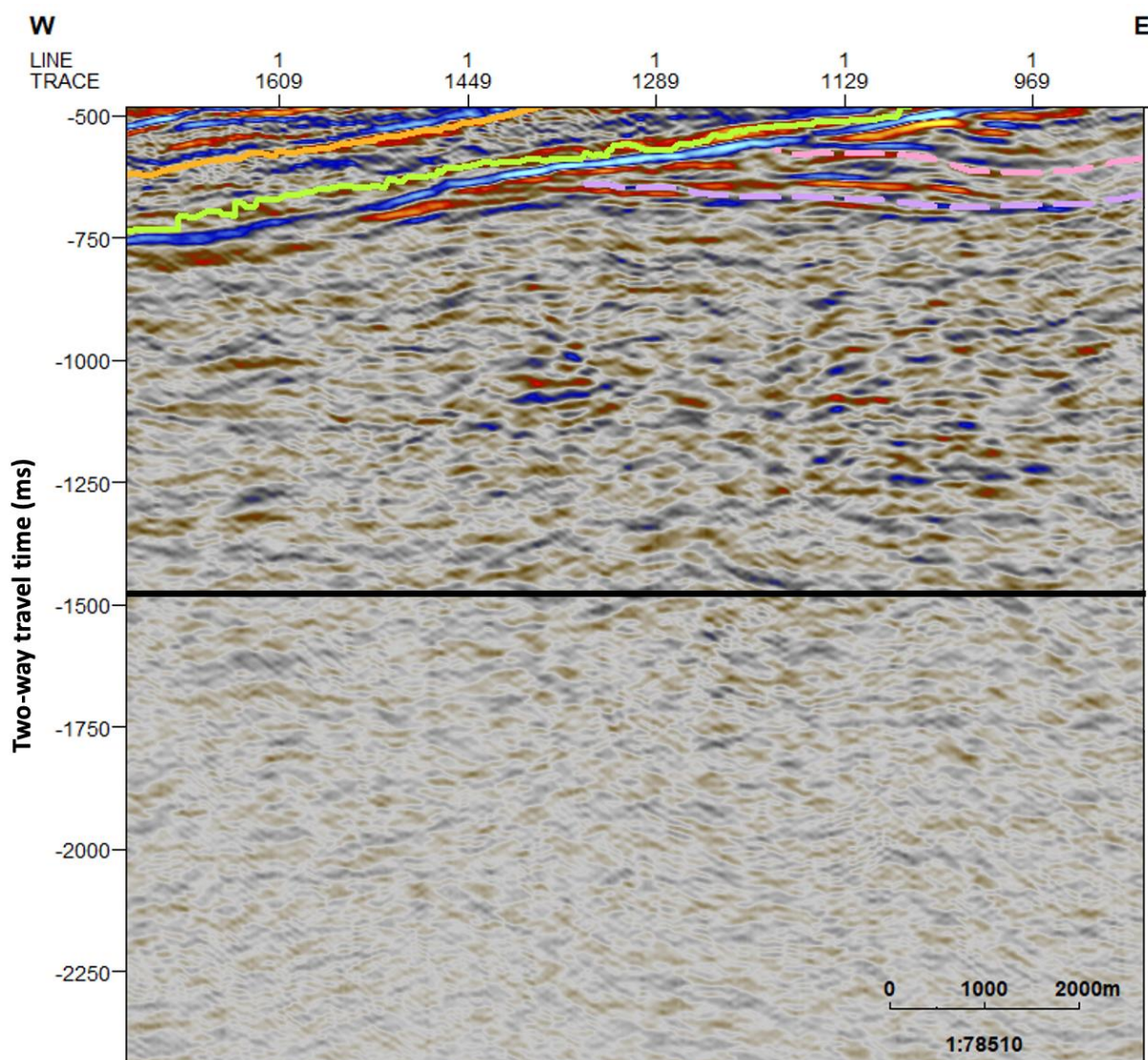


Figure 7.2.2: The figure shows the difference in reflection character on the upper part of unit 5 compared to the lower part, for line 11. The black line is used to illustrate where the reflection pattern approximately changes from stronger reflections to almost transparent reflections in the lower part. The top mid Carboniferous horizon is interpreted with the green line.

7.2.2 Stratigraphy and structures in BFZ

The Billefjorden Fault Zone has a complex fault geometry and consists of multiple major fault strands and smaller faults. The evolution of the fault zone stretches from the Caledonian to Devonian transcurrent and contractional faulting, where the BFZ initially formed as a strike-slip fault zone (Bælum and Braathen, 2012; Dallmann, 2015). During the Carboniferous period the fault zone was involved in rifting, whereas in Tertiary, the fault zone was involved in contractional reactivation (Bælum and Braathen, 2012). This creates a possibility for strike-slip, normal and reverse faults in the fault zone. This section will discuss the geometry of the BFZ and tie the interpretations to possible formation models.

Unit 7 and unit 8: Top mid Carboniferous to BFZ H2

The two units have been interpreted across the Billefjorden Fault Zone. In total, there are three locations with steep inclines in the two units which have been caused by faulting (Fig. 6.4.1). The figure also shows that the units are thickest in the central north-eastern part, where BFZ H1 and BFZ H2 have been faulted down, and the top mid Carboniferous horizon has been uplifted above the fault zone. The reflection pattern inside the fault zone, where the two units have been interpreted, are chaotic with mainly weak and discontinuous reflections. The amplitudes are stronger towards the western and eastern parts of the section (Fig. 6.4.1).

The interpretations made in this study partly coincides with the interpretations made by Skaara (2020), which was the first to interpret the horizons in this area. However, the seismic character inside the BFZ is different for the present study, where the amplitudes are found to be lower and the reflectors are more discontinuous. The difference in seismic character makes it difficult to compare the interpretations. Both studies have interpreted the horizons on what seems like the same reflectors in the west where they truncate the top mid Carboniferous horizon. For both studies, the horizons have been faulted down by the detachment (Fig. 7.2.5) and the two western faults. However, (Skaara, 2020) has interpreted five faults in the BFZ, whereas this study only has interpreted two. Additionally, this study has interpreted the two horizons to be located at an average of about 750 ms TWT (Fig. 6.4.2 and Fig. 6.4.3), whereas Skaara (2020) has an average of about 500 ms TWT. This indicates that there are several interpretation alternatives for the two horizons, or it might indicate that the horizons are located deeper towards the south.

Interpretation options

There are several possible interpretation options for the fault structures in the BFZ. The structures were especially difficult to interpret in this area, as the reflection pattern is chaotic, weak and discontinuous. The reflection pattern makes it difficult to see clear displacements in the seismic sections, and it is thus difficult to make an interpretation. It is important to recognize that several interpretation alternatives are possible inside the BFZ, where some will be discussed and compared to previous studies. Figure 7.2.3 shows interpretation alternative 1, where two normal faults have been interpreted to root in one detachment. Interpretation

alternative 2 indicates a more complex fault geometry in the BFZ and is shown in Figure 7.2.4, where four normal faults have been interpreted to root in two detachments.

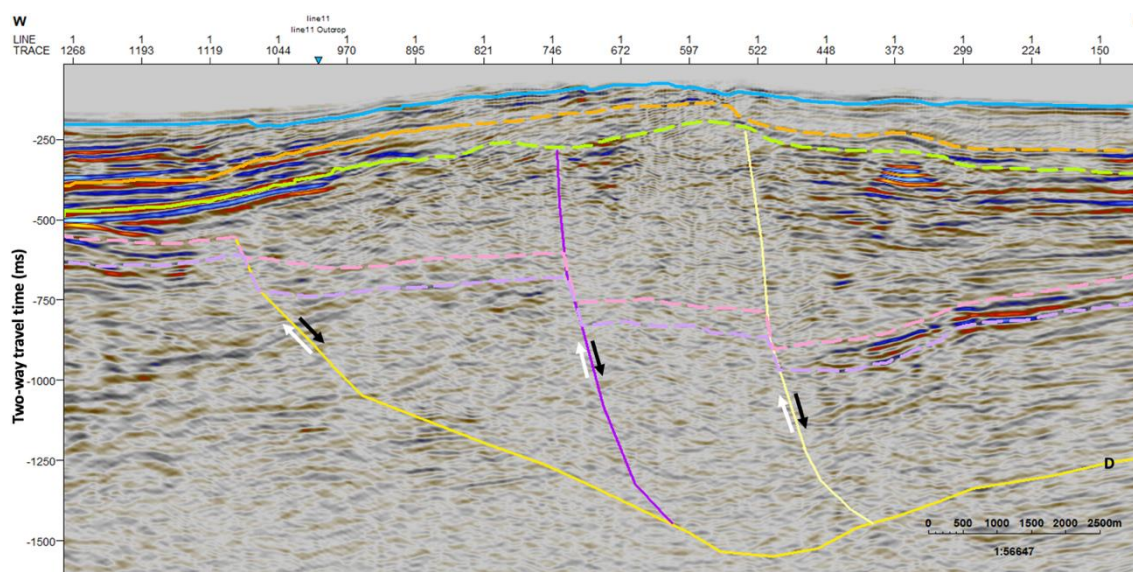


Figure 7.2.3: The figure shows interpretation alternative 1 in the BFZ for line 2. The interpreted horizons in the section are the seabed (blue), top Permian (orange), top mid Carboniferous (green), BFZ H1 (pink) and BFZ H2 (purple). The interpreted structures are two high angle normal faults (purple and light yellow), and a detachment (yellow). The interpreted faults root in the detachment and displace the BFZ H1 and BFZ H2 horizons. The arrows indicate the displacement direction of the two fault blocks, which indicates two normal faults.

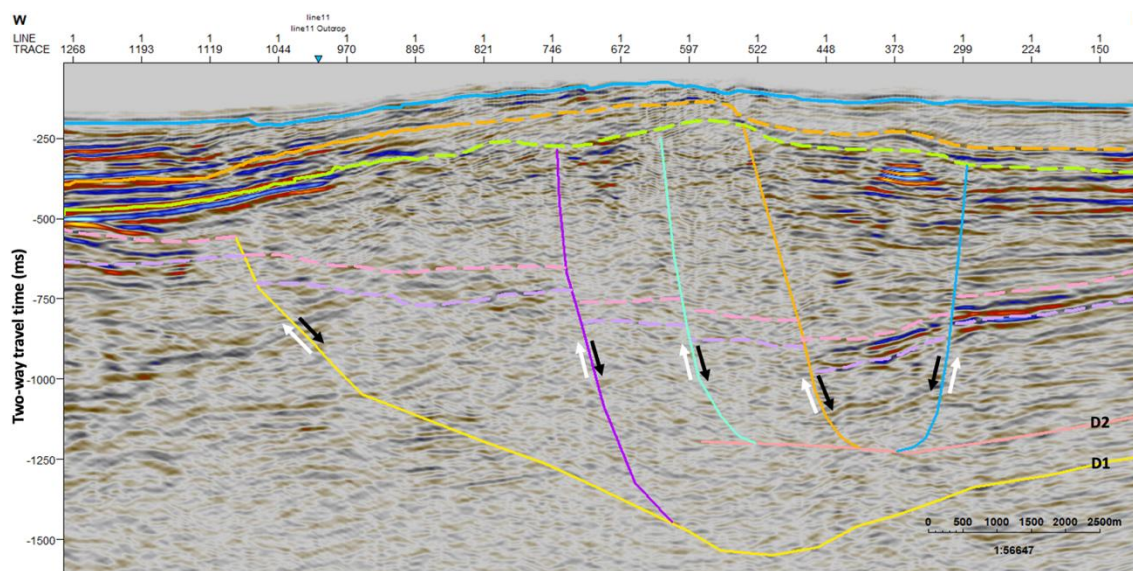


Figure 7.2.4: The figure shows interpretation alternative 2 in the BFZ for line 2. The interpreted horizons in the section are the seabed (blue), top Permian (orange), top mid Carboniferous (green), BFZ H1 (pink) and BFZ H2 (purple). The interpreted structures are four high angle normal faults (purple, turquoise, orange and blue), and two detachment (D1: yellow, and D2: light red). The interpreted faults root in the two detachments and displace the BFZ H1 and BFZ H2 horizons. The arrows indicate the displacement direction where all have been interpreted as normal faults.

Bælum and Braathen (2012) have interpreted three major fault strands in the BFZ that dips towards the east; the Odelfjellet, Balliolbreen and Drønbreen faults. A seismic line from Sassenfjorden were interpreted to be affected by two of the major fault strands, the Balliolbreen and Drønbreen faults (Bælum and Braathen, 2012). The Balliolbreen fault has been interpreted as a normal fault, whereas the Drønbreen fault has been interpreted as a reverse fault. Several minor faults have also been interpreted between the two major faults. The interpretations made by Bælum and Braathen (2012) support interpretation alternative 1 for two major faults. However, the displacement character of the faults is different. This study have interpreted two normal fault, whereas Bælum and Braathen (2012) have interpreted one normal and one reverse fault. The different displacement character is caused by different interpretations of the stratigraphic layers east of BFZ. Bælum and Braathen (2012) have interpreted the basement to be placed on top of the Devonian sedimentary succession to the east, which challenge the interpretations made in this study.

The difference in seismic character on the eastern and western side of the BFZ might be a possible indication that the area is affected by strike-slip movements. As the BFZ initially formed as a strike-slip fault zone, these faults can have been reactivated during a later stage as high angle dip-slip faults. The interpreted normal faults have probably been reactivated several times throughout the geological history of the area. If the fault, for instance, first initiated as a reverse fault with major displacement, then reactivated as a normal fault with minor displacement, one stratigraphic layer might be faulted down, whereas a deeper layer might be faulted up. Thus, the interpreted fault can appear as both a normal and a reverse fault depending on the interpreted stratigraphic units. This might be a possible explanation for why this study have interpreted the faults as normal due to the displacement of the two BFZ horizons, whereas Bælum and Braathen (2012) have interpreted one fault as reverse due to the displacement of the basement rocks.

A study from Braathen et al. (2017) northwest of the BFZ have interpreted a crustal-scale extensional detachment that separates the Old Red Sandstones of the Devonian succession from a underlying metamorphic core complexes. The study has also interpreted normal faults that root in the detachment. The interpretations made in this study coincides with the interpreted detachment geometry seen in the studies from Braathen et al. (2017) and Skaara

(2020). Skaara (2020) has interpreted two detachments in the fault zone, where the second detachment (D2) have been included in interpretation alternative 2, to illustrate the possibility of a second detachment. However, it was not possible to find any clear indications of a second detachment in this study due, which might be a result differences in the quality of the seismic data.

Based on previous studies and the observed seismic character, interpretation alternative 1 has been chosen as the preferred interpretation. The two interpreted faults might correspond to the Balliolbreen and Dønbreen faults interpreted by Bælum and Braathen (2012), where several minor faults might be present in the fault zone. The interpreted normal faults that root in the detachment correspond well with the supra-detachment formation model, which will be discussed in the next section. However, several models have been suggested, where the strike-slip model might be another possible formation model for the BFZ.

Supra-detachment model

During the Devonian extensional collapse of the Scandinavian Caledonides, supra-detachment basins formed. Supra-detachment basins form in the hanging-wall of low-angle normal faults where they have formed along a listric breakaway zone of a major detachment fault system (Vetti and Fossen, 2012). This model has been used to describe the formation of the scoop-shaped Hornelen basin, which is located on the western coast of Norway. Braathen et al. (2017) has studied the Keisarhjelmen detachment on north-western Svalbard, and points to Devonian extensional systems along the western coast of Norway as highly relevant to the Keisarhjelmen detachment. The study links the formation of the detachment to the extensional collapse of the Scandinavian Caledonides and infer that other parts of Svalbard are affected by late to post Caledonian detachments (Fig. 7.2.5). It is therefore likely that the same model used to describe the Hornelen basin can be used to describe the formation of the Billefjorden Fault Zone.

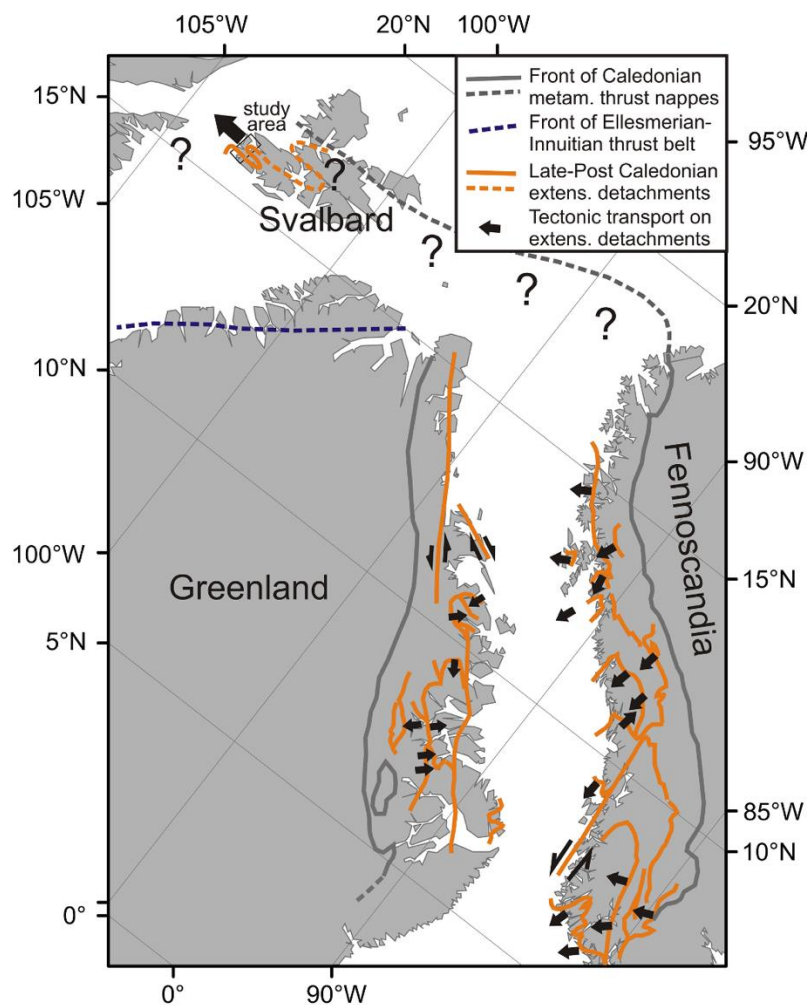


Figure 7.2.5: The figure illustrates a reconstruction of the North Atlantic-Arctic domain at 400 Ma, showing late to post Caledonian extensional detachments and the transport of their hanging-wall nappes. Modified by Braathen et al. (2017) from Fossen (2010).

Crustal scale extension played a significant role in the Silurian-Devonian history in the North Atlantic (Braathen et al., 2017). Figure 7.2.5 shows the area where Braathen et al. (2017) imply that extensional detachment basins have formed on Svalbard. As seen from the figure, the detachment is supposed to be located in the eastern parts of Isfjorden, across Billefjorden and Sassenfjorden. Thus, making it highly probable that the supra-detachment model can be used to describe the formation of the BFZ. Braathen et al. (2017) have interpreted arrays of normal faults that root in the detachment. Dallmann and Piepjohn (2018) commented on the study by Braathen et al. (2017), where they did not reject the idea of an extensional detachment, but better documentation was needed.

The supra-detachment interpretation alternative for BFZ is shown in Figure 7.2.6. This is the interpretation option that has been presented in Chapter 6. The interpretation shows a scoop-shaped detachment with two large normal faults (purple and light yellow) with a steep dip towards the east. The steep faults correspond well with the supra-detachment model, which normally have very steep faults. The interpreted structures are evident in the seismic section and were first interpreted for line 2, then correlated with line 11. Figure 7.2.7 shows a geological model for the interpreted supra-detachment alternative, which is represented as a supra-detachment model.

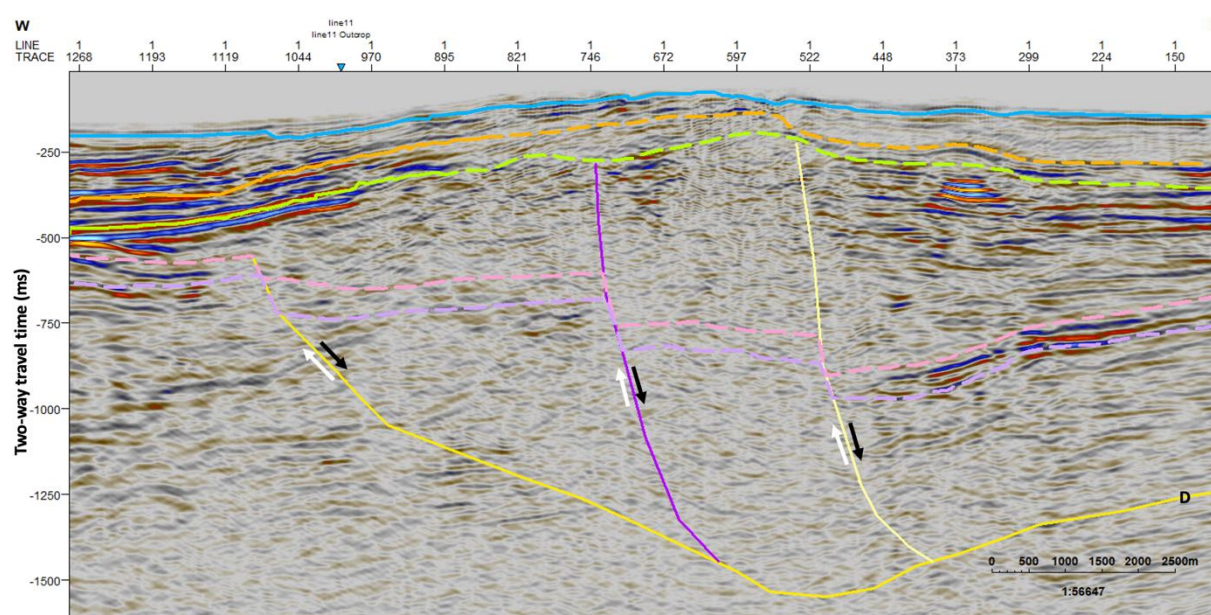


Figure 7.2.6: The figure shows the supra-detachment interpretation alternative in the BFZ for line 2. The figure was used to make a geological model of the BFZ, which represents the supra-detachment model.

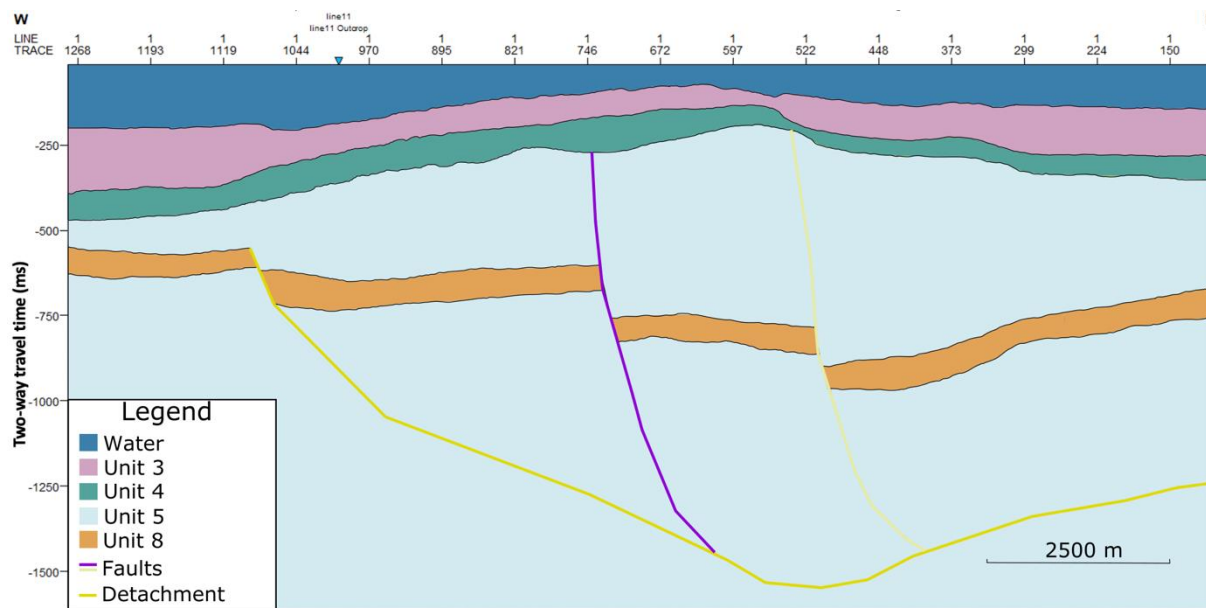


Figure 7.2.7: The figure shows the supra-detachment model of the BFZ for line 2.

Strike-slip model

As the BFZ initially formed as a strike-slip fault zone, a strike-slip formation model also needs to be discussed as a possible formation model for the BFZ. The model implies that the basin formed in a restricted regime of a strike-slip fault system. The model was developed by Crowell (2003), who studied the tectonics of Ridge Basin, which is a part of the San Andreas transform belt in southern California. When the geology is different on one side of a fault compared to the other, which is the case for the seismic character on either side of the BFZ, Crowell (2003) stated that this is the first clue to the probability of strike-slip faulting. The strike-slip model was supported by Steel and Gloppen (1980) as a possible formation model for the Hornelen basin. It is possible to make interpretations in the BFZ that support the strike-slip model as a possible formation model, which is why it has been presented as a possible interpretation alternative.

The BFZ does not follow a straight line in the north-south direction, which makes it possible for the fault zone to be affected by transpression and transtension. As strike-slip faults are difficult to image with seismic reflection data because of the steep angles, it is possible to look for restraining and releasing bends where the vertical movements are associated with dip-slip faults or folds. These structures are called flower structures and are characterised by their tendency to split and widen towards the surface (Fossen, 2010). The flower structures can be

either positive or negative depending on the tectonic setting, where positive structures are associated with contraction, and negative with extension.

The interpretations that have been made indicate a positive flower structure (Fig. 7.2.8) which might have originated from the Caledonian to Devonian transcurrent and contractional faulting. The interpreted faults vary from steep reverse faults to normal faults, and are restricted by two boundary faults that gather towards the centre of the basin at 2250 ms TWT (Fig. 7.2.8). The basin is faulted down compared to the areas around, which might be related to post-orogenic extension. Figure 7.2.9 shows a geological model for the interpreted strike-slip alternative, which is represented as a strike-slip model.

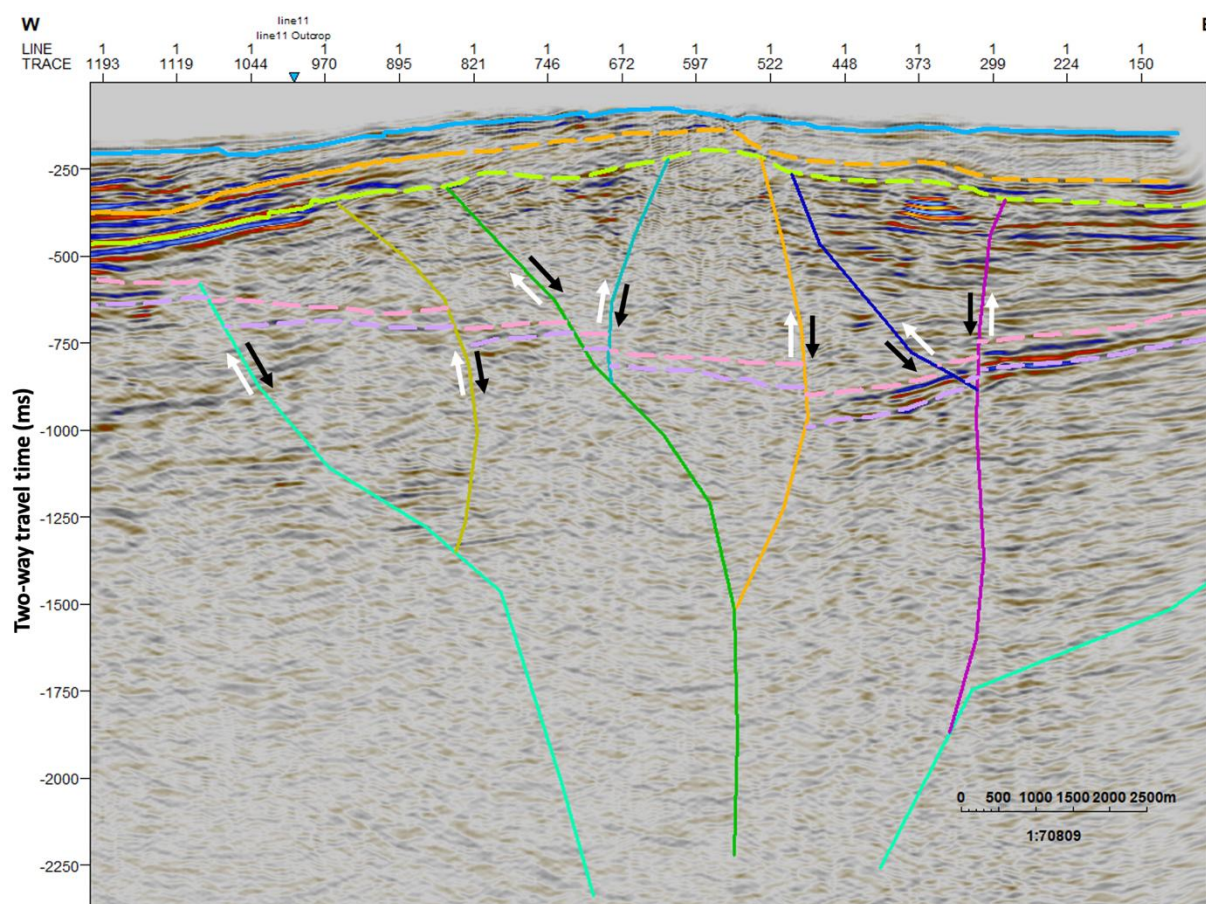


Figure 7.2.8: The figure shows the strike-slip interpretation alternative in the BFZ for line 2. The figure was used to make a geological model of the BFZ, which represent the strike-slip model.

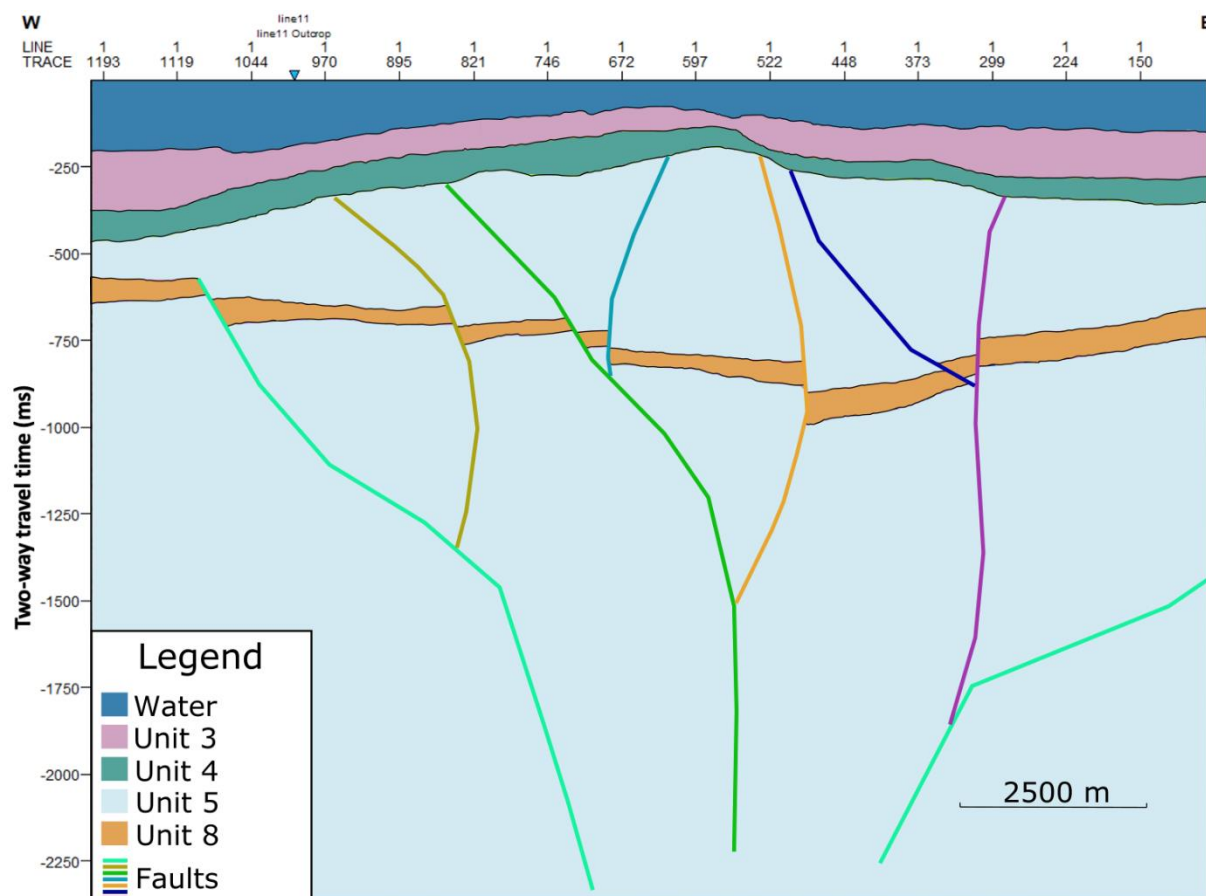


Figure 7.2.9: The figure shows the strike-slip model of the BFZ for line 2.

7.2.2 Stratigraphy and structures in Hecla Hoek

Unit 6: Hecla Hoek

The top Hecla Hoek horizon is shallowest in SW and deepest in NE (Fig. 6.3.7). There are two locations with a steep incline in TWT, that have been interpreted as normal faults (Fig. 6.4.6). Some fault interpretation alternatives will be discussed in the next section. The Hecla Hoek unit comprises igneous and metamorphic rocks that have a strong impedance contrast with the overlying Devonian sandstones. This impedance contrast have resulted in stronger reflections in the upper part of the Hecla Hoek unit, which corresponds to the findings made by Skaara (2020). The reflection pattern is discontinuous to chaotic, which is a result from the mid-Silurian to early Devonian Caledonian Orogeny, that caused the basement rocks to become highly deformed (Blinova et al., 2013).

Interpretation options

There are several possible interpretation options for the fault structures in the Hecla Hoek unit, and three of these will be discussed here. The first interpretation alternative (Fig. 7.2.10) is that there are no fault structures in the area where the lines have been collected. As it is possible to see from the figure, there are two areas with nearly transparent reflectors. For the rest of the area, the horizon is easier to interpret due to the stronger amplitudes located just underneath the horizon. It is possible to draw an approximated line through the areas with weaker reflections by following discontinuous reflectors. The second and third alternative are that the area with weak amplitudes have been displaced, where the very weak amplitudes might have been caused by poor imaging due to high angle faults. The second alternative (Fig. 7.2.11) is that the displacement represents normal faults dipping towards east, whereas the third alternative (Fig. 7.2.12) is that the displacement represents reverse faults dipping towards west.

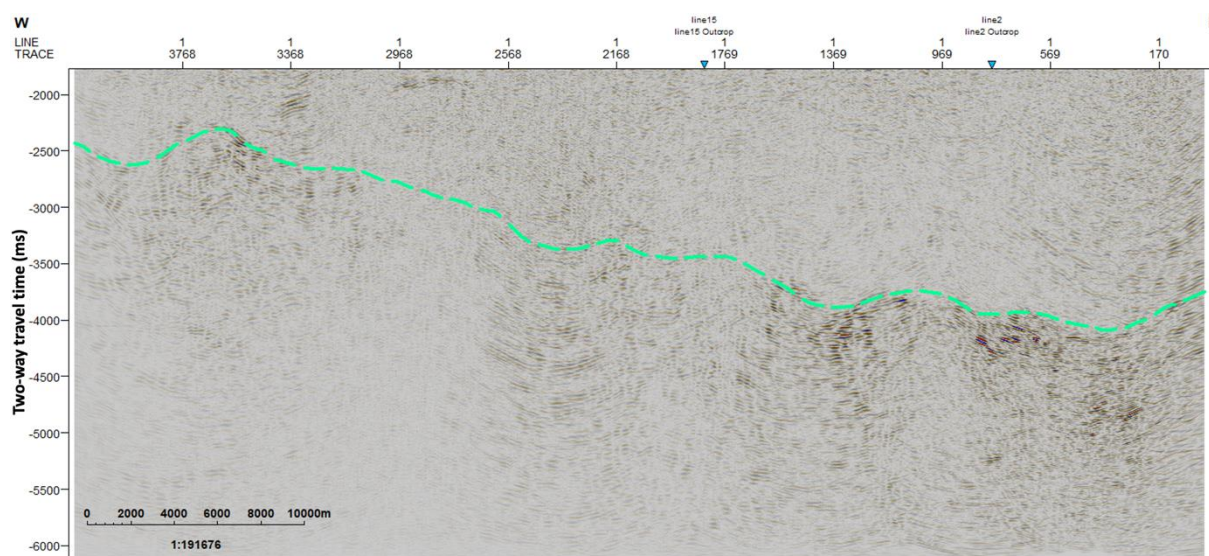


Figure 7.2.10: The figure shows interpretation alternative 1 for line 11. The top Hecla Hoek horizon (turquoise) has been interpreted without fault structures.

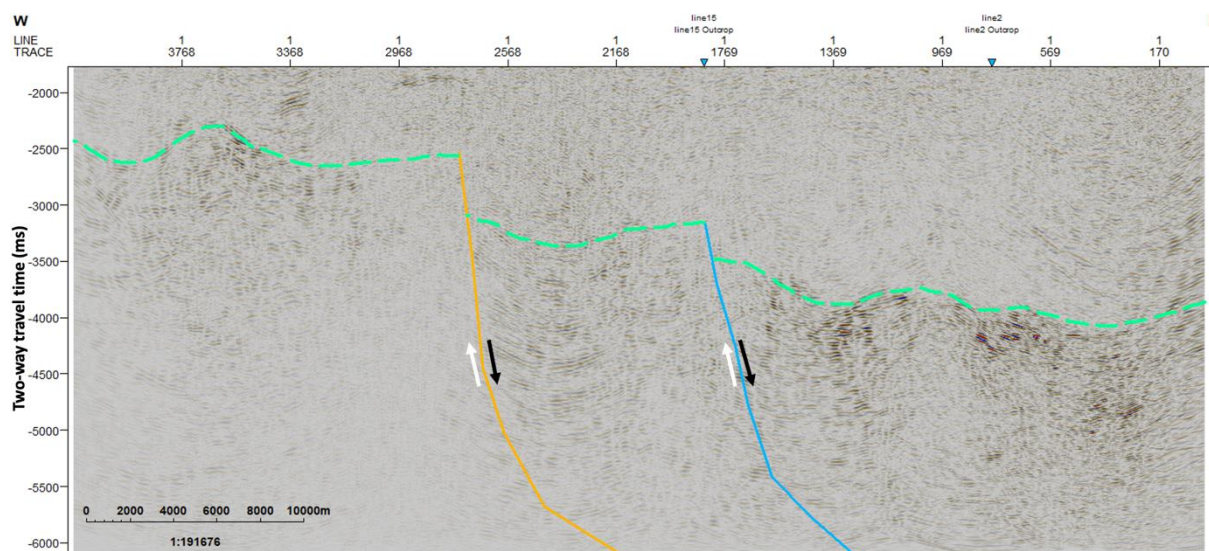


Figure 7.2.11: The figure shows interpretation alternative 2 for line 11. The top Hecla Hoek horizon (turquoise) has been interpreted with two normal faults (orange and blue). The arrows indicate the displacement direction of the two fault blocks on either side of each fault.

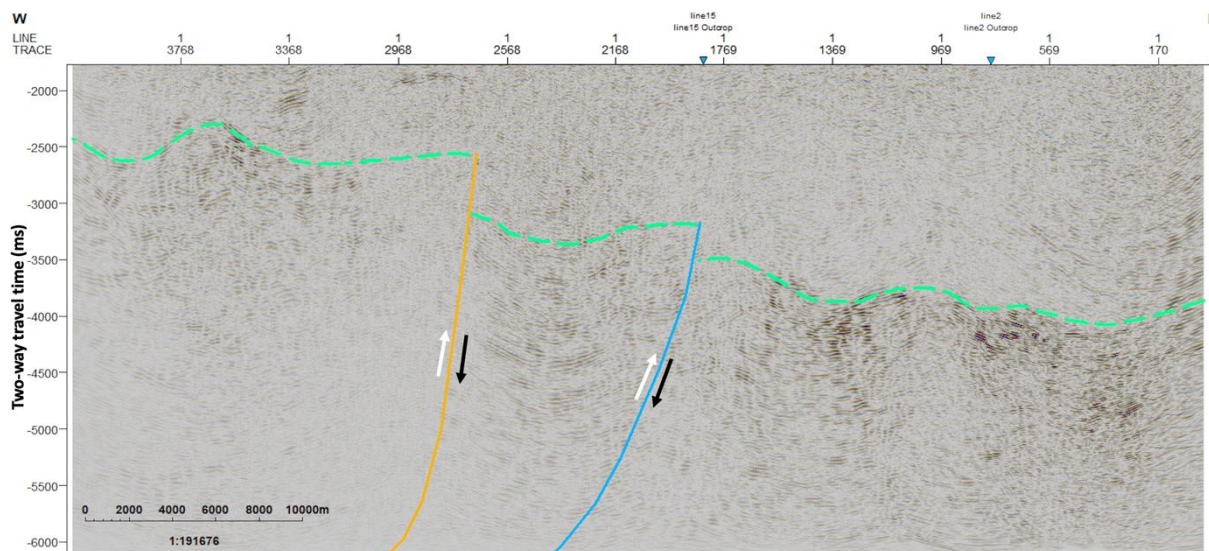


Figure 7.2.12: The figure shows interpretation alternative 3 for line 11. The top Hecla Hoek horizon (turquoise) has been interpreted with two reverse faults (orange and blue). The arrows indicate the displacement direction of the two fault blocks on either side of each fault.

Previous studies like Bergh et al. (1997), Blinova et al. (2012, 2013) and Skaara (2020), have all reported and interpreted fault structures in the Hecla Hoek unit. Thus, alternative 1 does not seem like a probable interpretation of the unit. The study from Bergh et al. (1997) have documented normal faults on land, whereas the studies from Blinova et al. (2012, 2013) and (Skaara, 2020) have interpreted normal faults from seismic sections collected in the fjord.

Because all of these studies have reported findings of normal faults, interpretation alternative 2 was considered the most probable interpretation alternative. The normal faults are likely to be a result of Devonian extension after the formation of the Caledonian mountain range, and might be a part of a bigger fault-bounded rift basin (Dallmann, 2015).

7.2.4 Other observations

Intrusions

A study from Senger et al. (2013) has described dolerite intrusions in central Spitsbergen on Svalbard. This study reports that the igneous intrusions predominantly occur within the Triassic succession, but that sills and dykes also are present in the Permian and Lower-Middle Jurassic succession. The identification criteria for intrusions in seismic sections defined in Planke et al. (2005) bases the main criteria on high amplitude, saucer-shape and/or abrupt terminations. These criteria correspond well with the observed characteristics in this study.

Digranes and Kristoffersen (1995) discovered that an interpreted dolerite intrusion partly coincides with the top Permian reflector. Senger et al. (2013) and Skaara (2020) have made the same interpretations of an extensive, layer-parallel, high-amplitude reflection that partly coincides with the top Permian reflector. The same interpretations can also be made in this study, where the seismic sections cover the same area. Figure 7.2.13 shows what is assumed to be the same dolerite intrusion. Blinova et al. (2013) and Senger et al. (2013) have also interpreted some short high-amplitude reflections in the Triassic and Devonian units to be related to dolerite intrusions, which support the intrusion interpretations that were made in Chapter 6. More intrusions might be present in the seismic sections even though they are not prominent. Some intrusions might be smaller than the seismic data are able to resolve, which is caused by a limit to the bed thickness related to the seismic resolution. The seismic resolution for the seabed and Hecla Hoek was calculated in Table 6.2.1. The vertical resolution for the seabed was calculated to be 50 m, and the Fresnel zone to be 158 m. For Hecla Hoek, the vertical resolution was calculated to be 92 m, and the Fresnel zone to be 790 m. Stratigraphic or structural features that are not larger than the seismic resolution will thus not be detected and visible in the seismic section.

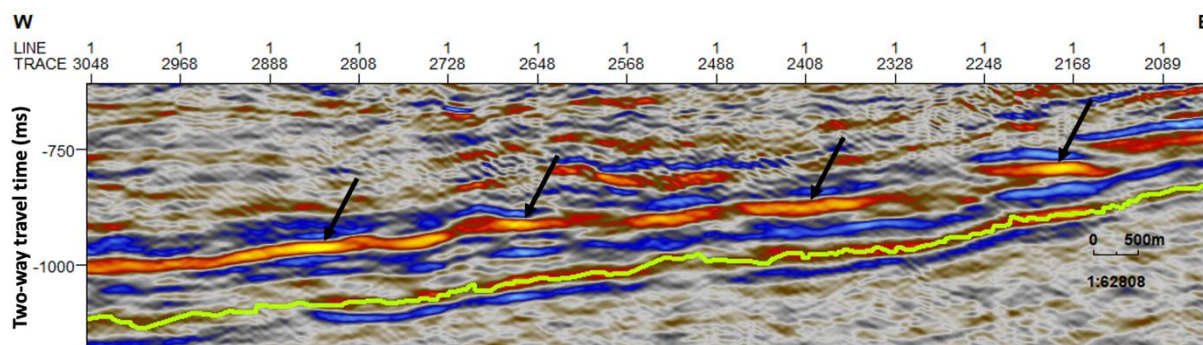


Figure 7.2.13: The figure shows a section from line 11 where the arrows point to the strong parallel reflection that have been interpreted to be dolerite intrusion. The arrows also point at the interpreted top Permian horizon.

Fault structures

A study from Blinova et al. (2012) has mapped the shallow structures of the fold-and-thrust belt in Isfjorden. The study describes detachments with related faults that have been found in three different layers; D1 in the Jurassic-Cretaceous succession, D2 in the Triassic-lowermost Jurassic succession, and D3 in the Carboniferous-Permian succession. It is important to note that these detachments are not the same as those discussed for the BFZ. It will not be possible to find D1 in the seismic sections in this study, as the sedimentary succession where the detachment is located truncates the seabed west of the study area.

Several small reverse faults have been interpreted in the Carboniferous to lowermost Jurassic succession and might be related to the interpretations made by Blinova et al. (2012). Figure 7.2.14 shows two interpreted small reverse faults that roots in a reflector just below the interpreted reflection R horizon, which is thought to be the top Sassendalen reflector. The reflector where the two faults root might be the D2 detachment, which corresponds well with the interpretations made by Blinova et al. (2012), where D2 is inferred to be located in the Bravaisberget Formation, which is the uppermost formation of the Sassendalen Group in this area. Three small reverse faults have been interpreted to root in one detachment in the Carboniferous-Permian succession (Fig. 7.2.15). The interpreted detachment might correspond to D3 interpreted by Blinova et al. (2012), inferred to be located in the Gipshuken Formation of the Gipsdalen Group.

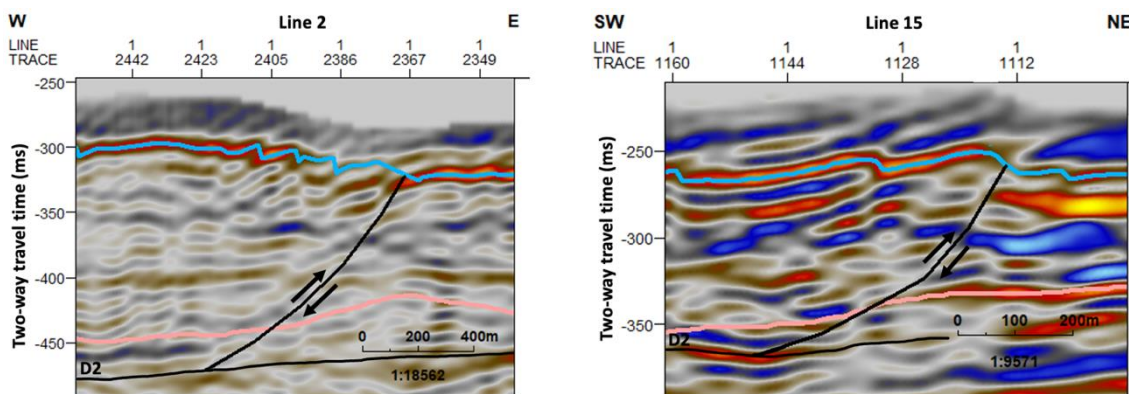


Figure 7.2.14: The figure shows the two interpreted reverse faults (black) that root in the same detachment just below the reflection R horizon (light red). The detachment has been interpreted to correspond to D2 from Blinova et al. (2012).

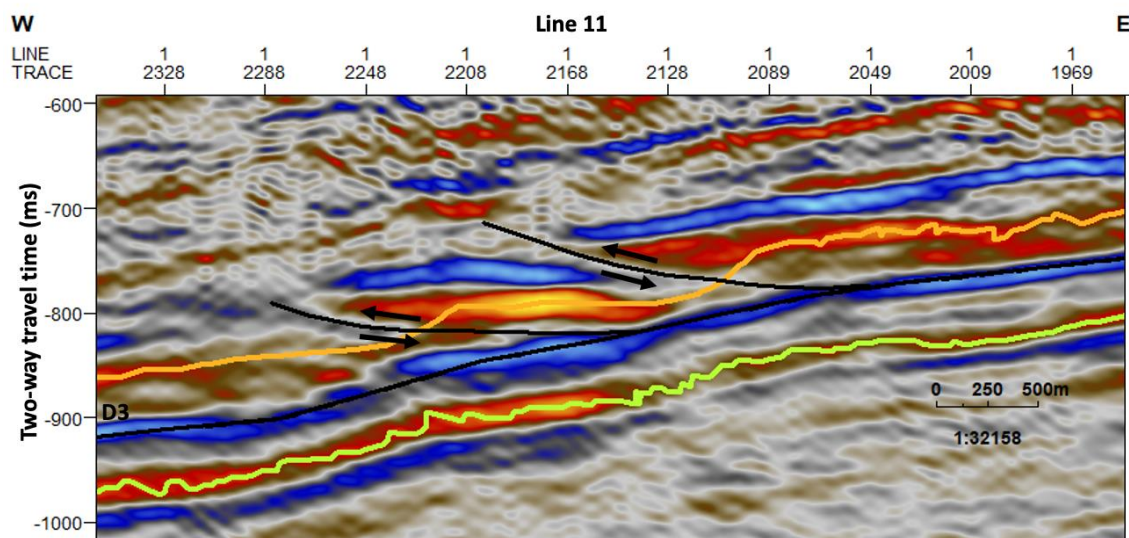
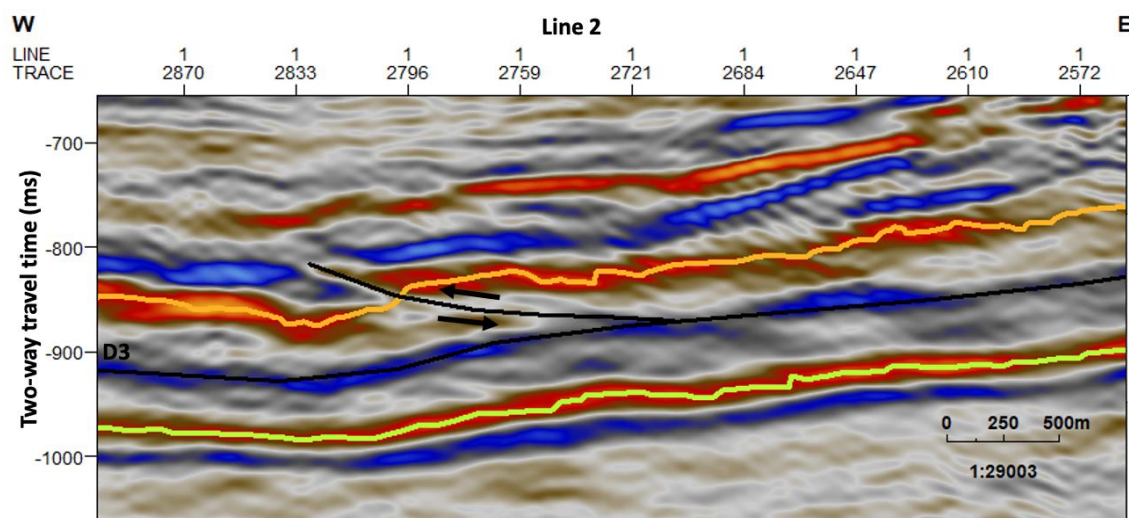


Figure 7.2.15: The figure shows the three interpreted reverse faults (black) that root in the same detachment between the top Permian (orange) and top mid Carboniferous (green) horizons. The detachment has been interpreted to correspond to D3 from Blinova et al. (2012).

Chapter 8

Conclusion

8.1 Processing

In this study four 2D multichannel seismic reflection lines from the inner Isfjorden and Sassenfjorden have been processed. Because of the very hard and shallow seabed, the seismic sections are dominated by strong water layer multiples that repeat at short intervals. The main focus has been to remove these effects with a goal of providing a processing sequence that effectively removes the multiples without significantly affecting the quality of the data.

- The processing sequence includes editing, deconvolution, band-pass filtering, velocity filtering, static correction, velocity analysis, brute stack, Kirchhoff pre-stack time migration, mute and stack.
- During the filtering and deconvolution, several methods have been used to remove as much multiple energy and noise as possible. Multiple velocity filters in fk -domain and surface predictive deconvolution have been used to remove most of the multiple energy. The remaining multiple energy has been attenuated through migration, mute and stacking.
- The velocity filters were first applied to the shot gathers, then to the receiver gathers. This was done to prevent an asymmetrical effect in the fk -spectra. By choosing values slightly higher than the measured velocities, the multiples are effectively attenuated or removed along with the aliasing and linear noise.
- Surface consistent predictive deconvolution has been used to remove the multiples that remain after the velocity filtering. The method uses statistics where separate filters are calculated for each source and receiver location.

- The processing sequence have significantly improved the quality of the data. However, the data are not well suited for imaging shallow structures in areas with small water depths (<100 m), which is a result of the acquisition geometry.
- Amplitude recovery have been used to amplify the energy in the shallow parts, and applications of an anti-alias low-pass filter and fk-filter was used to remove the spatial aliasing.
- The results show that the processing sequence has been successful in removing the water layer multiples, thus providing a good image of the subsurface.

8.2 Interpretation

The processed lines were used to interpret the subsurface geological features in the study area. The focus has been to get an overview over and map the stratigraphical horizons and units that are present in the area, in addition to interpreting the fault geometry in the basement and Billefjorden Fault Zone. These interpretations will in return provide a better understanding of how the geological history has affected the stratigraphical and structural development of the area. The interpretations that have been made corresponds well with previous studies.

- Stratigraphic horizons and units from the seabed to Hecla Hoek have been interpreted. The units from the reflection R horizon to top mid Carboniferous dip towards the southwest.
- The top Permian and top mid Carboniferous horizons have been interpreted as unconformities. The interpretations of the horizons are reminiscent of an anticline, where the horizons are located very shallow over the BFZ, and deeper on either side of the fault zone.
- The top Sassendalen horizon and Billefjorden Group are present in the study area. Descriptions of seismic characters from previous studies were used in the

identification, where the top Sassendalen horizon corresponds to the interpreted reflection R horizon. The strong reflection at the top of the Devonian-Middle Carboniferous succession corresponds to the Billefjorden Group.

- The Hecla Hoek horizon has been displaced by normal faults with steep dips towards the east. The faults are probably a part of a larger graben structure that characterises the basement on Svalbard.
- The Billefjorden Fault Zone has been interpreted as a supra-detachment basin of Devonian age. The basin is dominated by steep normal faults that root in a scoop-shaped detachment. The formation of the BFZ started in Late Silurian and continued through the Devonian period, where the fault geometry is caused by crustal scale extension related to the Caledonian orogenic collapse.
- Possible intrusions have been interpreted in the units from the seabed to the top mid Carboniferous horizon. The interpretations coincide with previous studies and are probably related to volcanism from the latest Jurassic through the Early Cretaceous periods.
- The interpreted small reverse faults in the Triassic-lowermost Jurassic and Carboniferous-Permian successions root in two separate detachments. The formation of the detachments and reverse faults are related to the Tertiary contractional reactivation of the West Spitsbergen Fold-and-Thrust Belt.

The interpretations that have been presented in this study only represents a possible interpretation of the study area. It is therefore possible that other interpretations are applicable, and the accessibility to more information and data would have contributed to a more reliable interpretation. The data quality that is obtainable with 2D multichannel reflection seismic data is limited. However, the interpretations that have been presented in this study are supported by several other studies and will therefore represent a highly probable interpretation.

References

- Amundsen, I. M. H., Blinova, M., Hjelstuen, B., Mjelde, R. and Haflidason, H. (2011). The Cenozoic western Svalbard margin: sediment geometry and sedimentary processes in an area of ultraslow oceanic spreading. *Marine Geophysical Research*, 32 (4), 441–453.
- Bergh, S. G., Braathen, A. and Andresen, A. (1997). Interaction of Basement-Involved and Thin-Skinned Tectonism in the Tertiary Fold-Thrust Belt of Central Spitsbergen, Svalbard. *AAPG Bulletin*, 81 (4), 637–661.
- Blinova, M., Faleide, J. I., Gabrielsen, R. H. and Mjelde, R. (2012). Seafloor expression and shallow structure of a fold-and-thrust system, Isfjorden, west Spitsbergen. *Polar Research*, 31 (1), 11209–11213.
- Blinova, M., Faleide, J. I., Gabrielsen, R. H. and Mjelde, R. (2013). Analysis of structural trends of sub-sea-floor strata in the Isfjorden area of the West Spitsbergen Fold-and-Thrust Belt based on multichannel seismic data. *Journal of the Geological Society*, 170 (4), 657–668.
- Blinova, M., Thorsen, R., Mjelde, R. and Faleide, J. I. (2009). Structure and evolution of the Bellsund Graben between Forlandsundet and Bellsund (Spitsbergen) based on marine seismic data. *Norwegian Journal of Geology*, 89, 215–228.
- Braathen, A., Bergh, S. G. and Maher Jr, H. D. (1999). Application of a critical wedge taper model to the Tertiary transpressional fold-thrust belt on Spitsbergen, Svalbard. *Geological Society of America Bulletin*, 111 (10), 1468–1485.
- Braathen, A., Bælum, K., Maher, H. and Buckley, S. J. (2012). Growth of extensional faults and folds during deposition of an evaporite-dominated half-graben basin; the Carboniferous Billefjorden Trough, Svalbard. *Norwegian Journal of geology*, 91 (3), 137-160.

Braathen, A., Osmundsen, P. T., Maher, H. and Granerød, M. (2017). The Keisarhjelmen detachment records Silurian–Devonian extensional collapse in Northern Svalbard. *Terra Nova*, 30 (1), 34–39.

Bælum, K. and Braathen, A. (2012). Along-strike changes in fault array and rift basin geometry of the Carboniferous Billefjorden Trough, Svalbard, Norway. *Tectonophysics*, 546–547, 38–55.

CGGVeritas (2008). *Geocluster 5.0 Release Notes*.

Crowell, J. C. (2003). Tectonics of Ridge Basin region, Southern California. *Geological Society of America, Special Paper*, 367, 157–204.

Dallmann, W. K. (1999). *Lithostratigraphic lexicon of Svalbard : review and recommendations for nomenclature use : Upper Palaeozoic to Quaternary bedrock*. Tromsø: Norwegian Polar Institute, Polar Environmental Centre.

Dallmann, W. K. (2015). *Geoscience Atlas of Svalbard*. Tromsø: Norwegian Polar Institute.

Dallmann, W. and Piepjohn, K. (2018). *Comment on “The Keisarhjelmen detachment records Silurian–Devonian extensional collapse in Northern Svalbard”*.

Digranes, P. and Kristoffersen, Y. (1995). Use of Mode-converted Waves in Marine Seismic Data to Investigate the Lithology of the Sub-bottom Sediments in Isfjorden, Svalbard. *Pure and applied geophysics*, 145 (2), 313–325.

Faleide, J. I., Tsikalas, F., Breivik, A. J., Mjelde, R., Ritzmann, O., Engen, O., Wilson, J. and Eldholm, O. (2008). Structure and evolution of the continental margin off Norway and the Barents Sea. *Episodes*, 31 (1), 82–91.

Fossen, H. (2010). *Structural Geology*. Cambridge: Cambridge University Press Textbooks.

Gelius, L. J. and Johansen, T. A. (2010). *Petroleum geophysics*. Bergen: UniGEO.

Hart, B. S. (2000). *3-D seismic interpretation: A primer for geologists*, SEPM Short Course 48. Tulsa, Okla: Society for Sedimentary Geology.

Herron, D. A. (2011). *First steps in seismic interpretation*, 16. Tulsa, Okla: Society of Exploration Geophysicists.

Hjelle, A. (1993). *Geology of Svalbard*, Polarhåndbok 7. Oslo: Norsk Polarinst.

Kearey, P., Brooks, M. and Hill, I. (2002). *An introduction to geophysical exploration*. 3rd ed. Oxford: Blackwell Science.

Mjelde, R. (2003). *Cruise report: SVALEX 2002: MCS survey Isfjorden and shelf by use of Håkon Mosby*.

Mjelde, R. (2010). *Seismic Equipment*. [Online]. Available at: <http://buster.geo.uib.no/emodules/modules/Seismic%20equipment/index.html> [Accessed 7 May 2021].

Mjelde, R. (2011). *Seismic Acquisition: Geophysical Principles*. [Online]. Available at: <http://buster.geo.uib.no/emodules/modules/Seismic%20acquisition%20principles/index.html> [Accessed 7 May 2021].

Obeid, H., Khettab, H., Marais, L., Hallab, M., Laurent, S. and Boutouyrie, P. (2017). Evaluation of arterial stiffness by finger–toe pulse wave velocity: optimization of signal processing and clinical validation. *Journal of Hypertension*, 35 (8), 1618–1625.

Piepjohn, K. and Dallmann, W. K. (2014). Stratigraphy of the uppermost Old Red Sandstone of Svalbard (Mimerdalen Subgroup). *Polar Research*, 33 (1), 19998.

Planke, S., Rasmussen, T., Rey, S. S. and Myklebust, R. (2005). Seismic characteristics and distribution of volcanic intrusions and hydrothermal vent complexes in the Vøring and Møre basins. *Geological Society, London, Petroleum Geology Conference series*. 6 (1), 833–844.

Samson, C. and West, G. F. (1992). Correction for water depth variations of marine crustal reflection seismic data using refraction statics. *Marine Geophysical Research*, 14 (1), 65–76.

Senger, K., Roy, S., Braathen, A., Buckley, S., Bælum, K., Gernigon, L., Mjelde, R., Noormets, R., Ogata, K., Olausson, S., Planke, S., Ruud, B. O. and Tveranger, J. (2013). Geometries of doleritic intrusions in central Spitsbergen, Svalbard: an integrated study of an onshore-offshore magmatic province with implications for CO₂ sequestration. *Norwegian Journal of Geology*, 93, 143–166.

Senger, K., Tveranger, J., Ogata, K., Braathen, A. and Planke, S. (2014). Late Mesozoic magmatism in Svalbard: A review. *Earth-Science Reviews*, 139, 123–144.

Sheriff, R. E. and Geldart, L. P. (1995). *Exploration seismology*. 2nd ed. Cambridge University Press.

Simm, R. and Bacon, M. (2014). *Seismic Amplitude: An interpreter's handbook*. Cambridge University Press.

Skaara, S. (2020). *Prosessering og tolkning av refleksjonsseismiske data fra Isfjorden, Svalbard*. Mastergrad i Geovitenskap, Institutt for Geovitenskap: Universitetet i Bergen.

Steel, R. and Gloppen, T. G. (1980). Late Caledonian (Devonian) Basin Formation, Western Norway: Signs of Strike-Slip Tectonics during Infilling. *Tectonophysics*, 36, 79–103.

Van Der Pluijm, B. A. and Marshak, S. (2004). *Earth structure: An introduction to structural geology and tectonics*. WW Norton.

Vetti, V. V. and Fossen, H. (2012). Origin of contrasting Devonian supradetachment basin types in the Scandinavian Caledonides. *Geology*, 40 (6), 571–574.

Worsley, D. (1986). *The geological history of Svalbard: evolution of an Arctic archipelago*. Stavanger: Den norske stats oljeselskap a.s.

Worsley, D. (2008). The post-Caledonian development of Svalbard and the western Barents Sea. *Polar research*, 27 (3), 298–317.

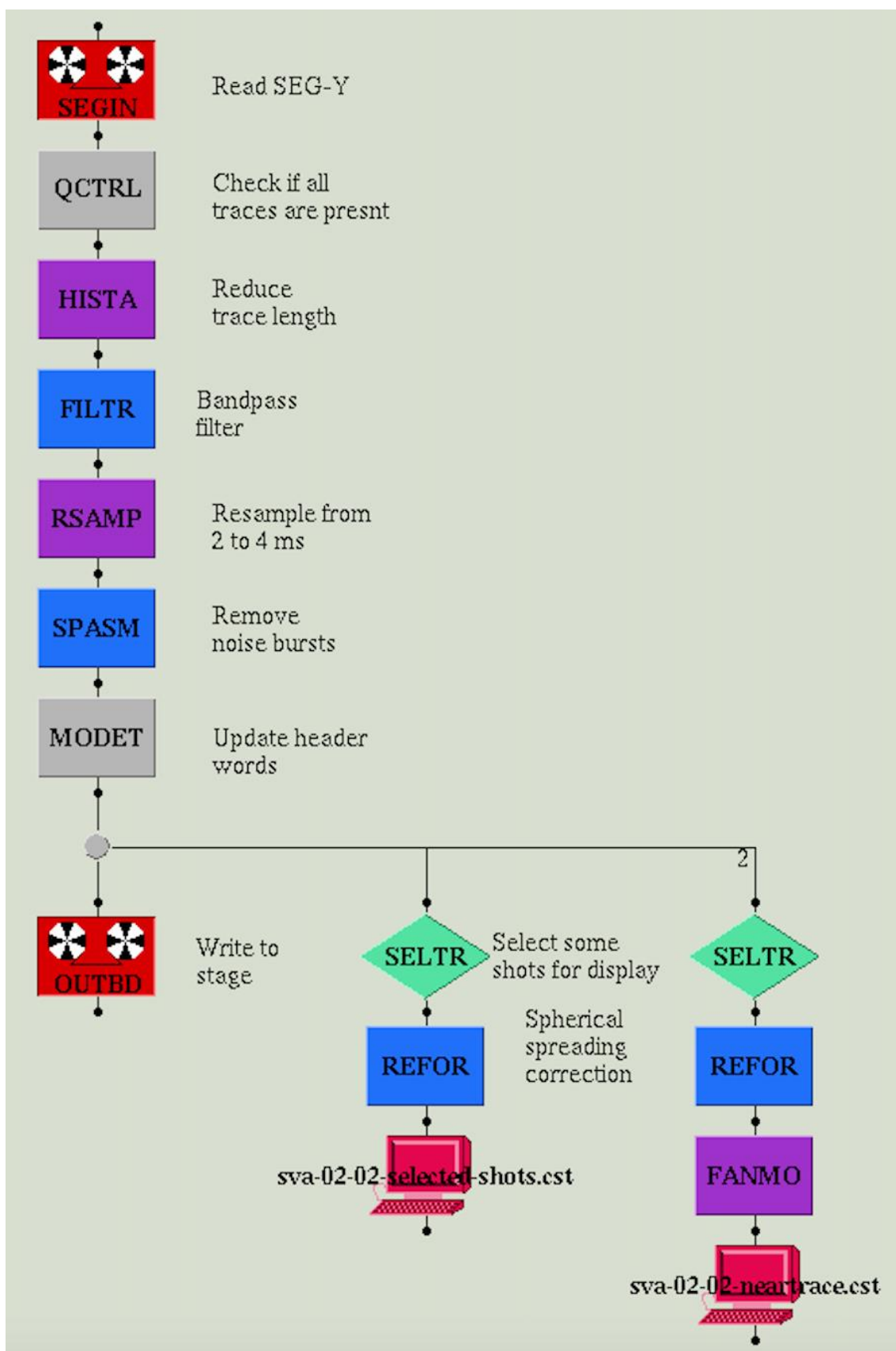
Yilmaz, Ö. (2001). *Seismic data analysis: Processing, inversion, and interpretation of seismic data*. 2nd ed. Tulsa, Okla: Society of Exploration Geophysicists.

Appendix A

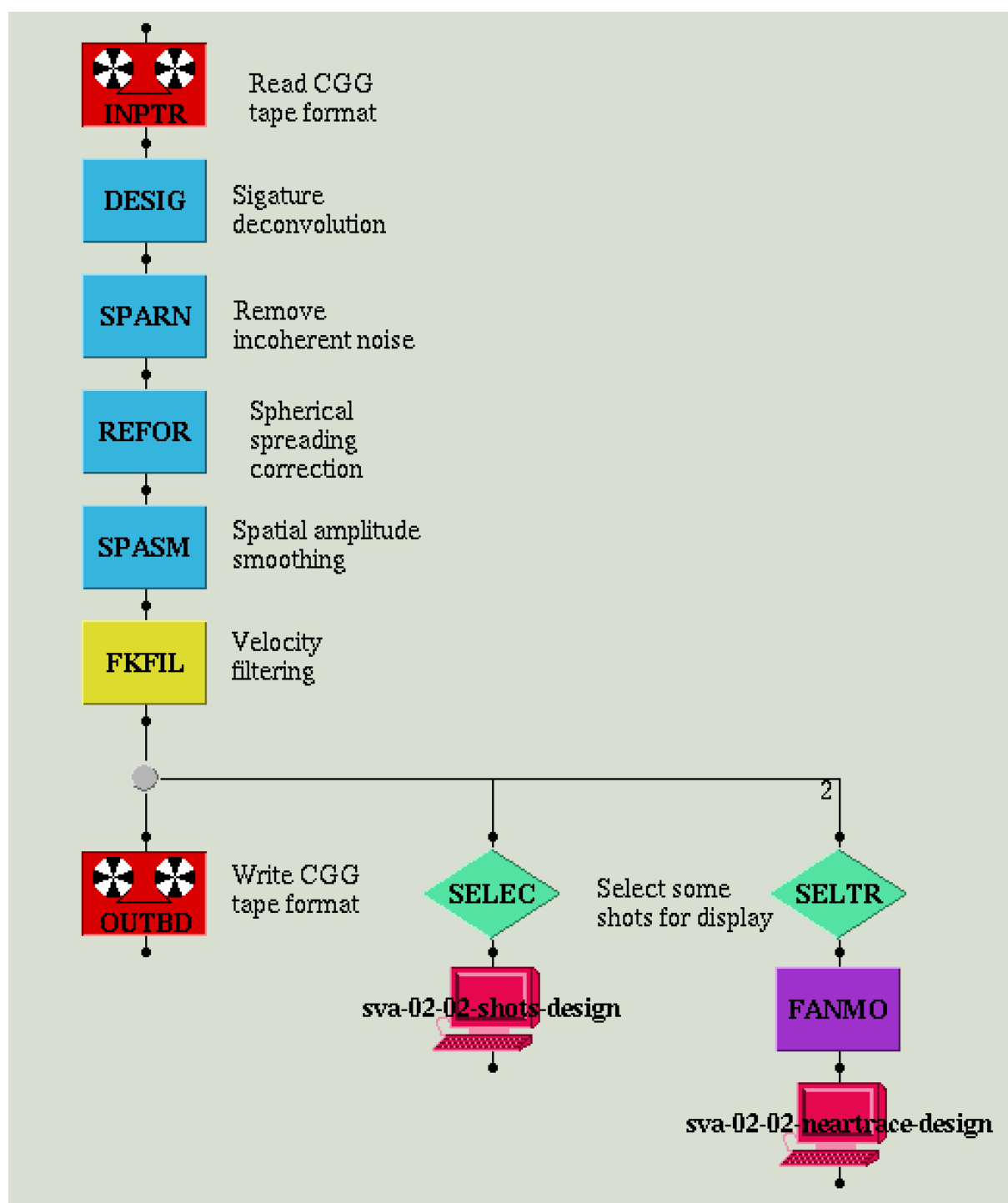
Processing jobs

The processing jobs that have been used during the processing sequence, from Xjob.

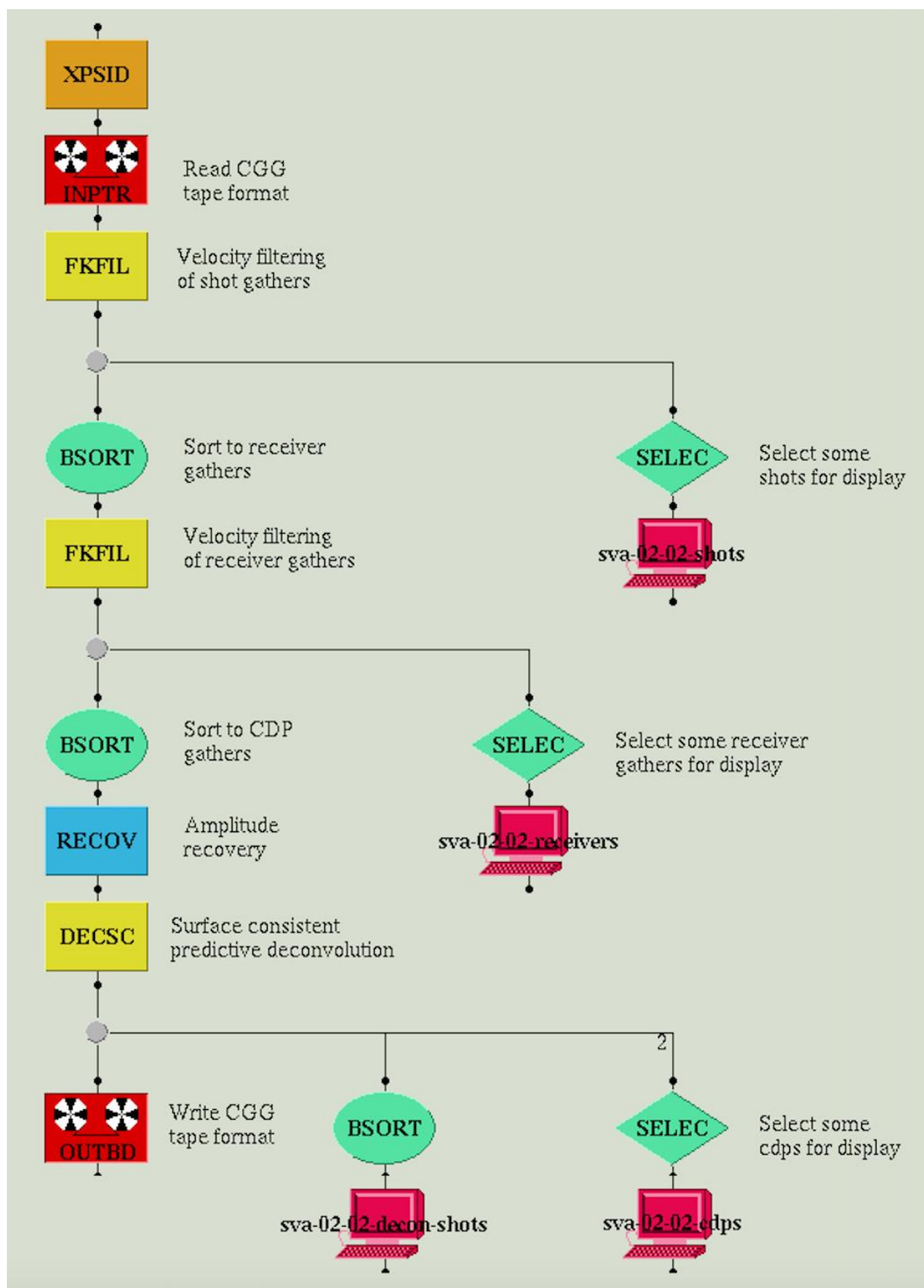
Editing



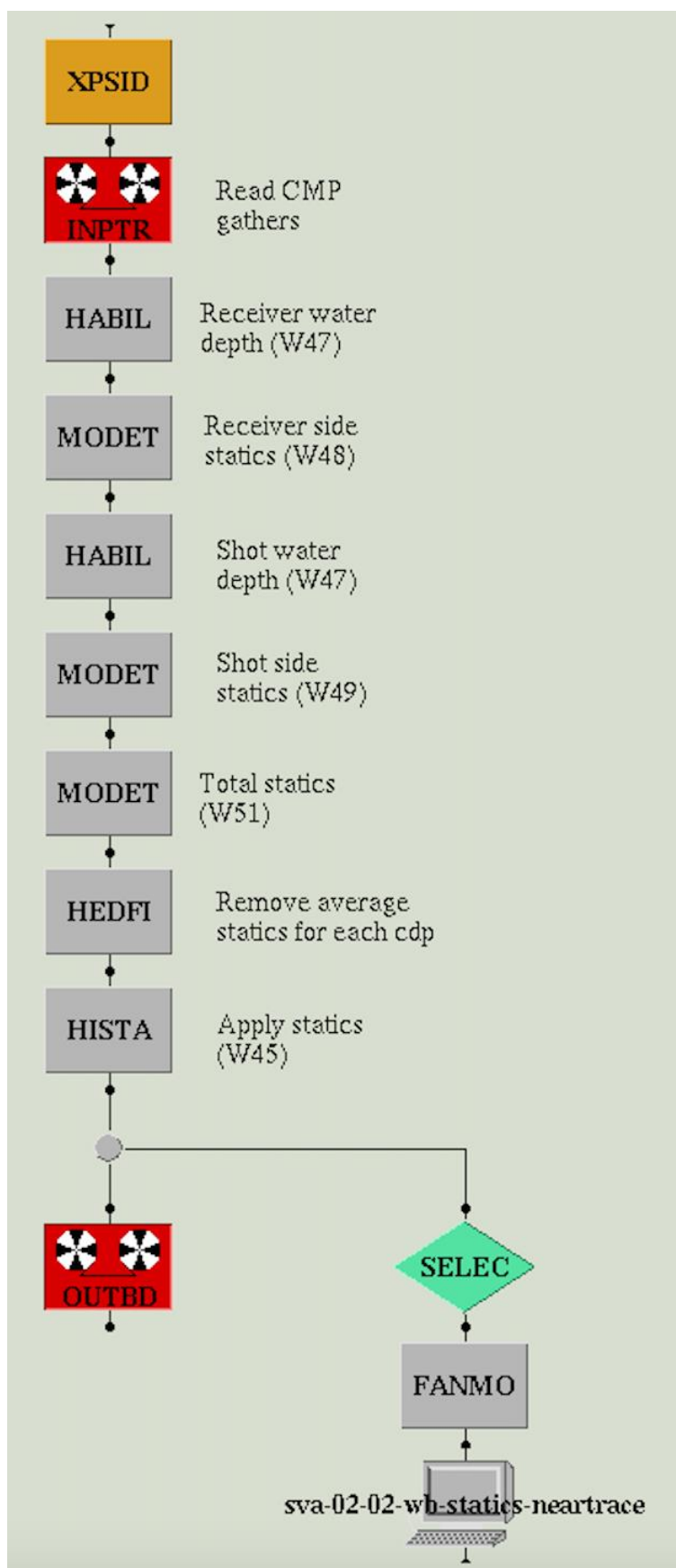
Signature deconvolution



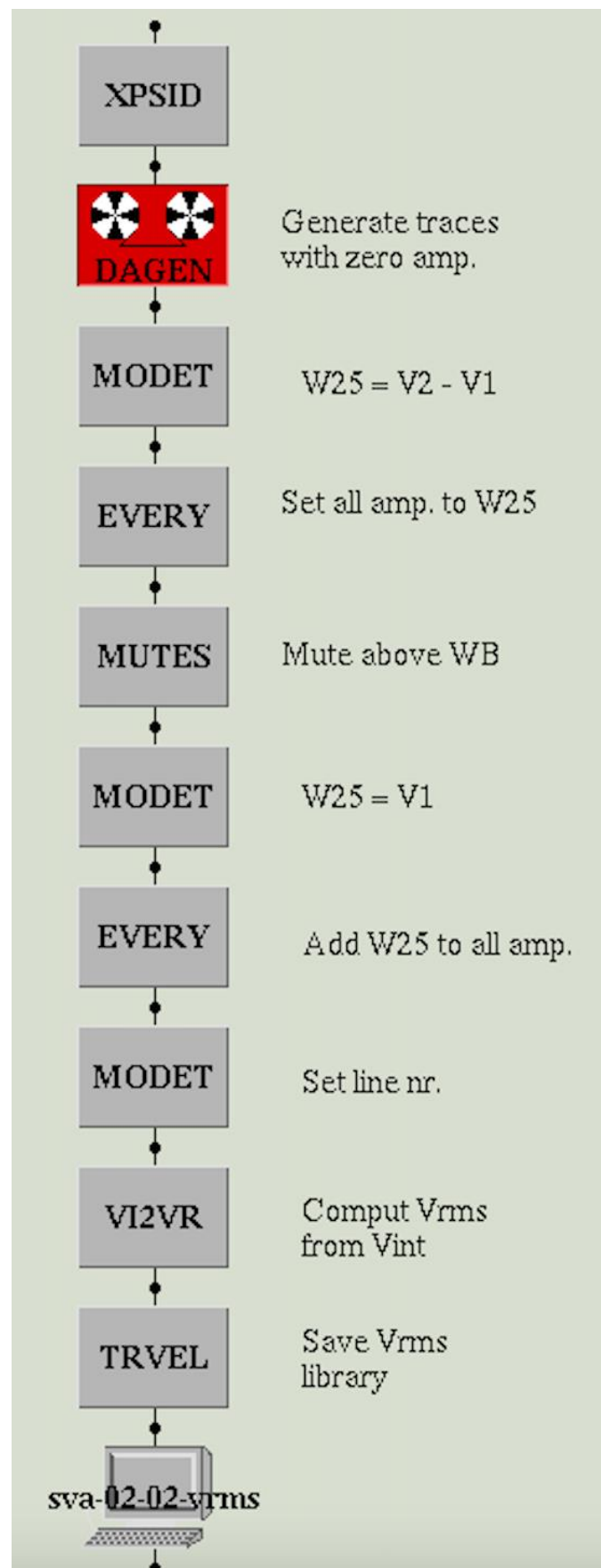
Filtering



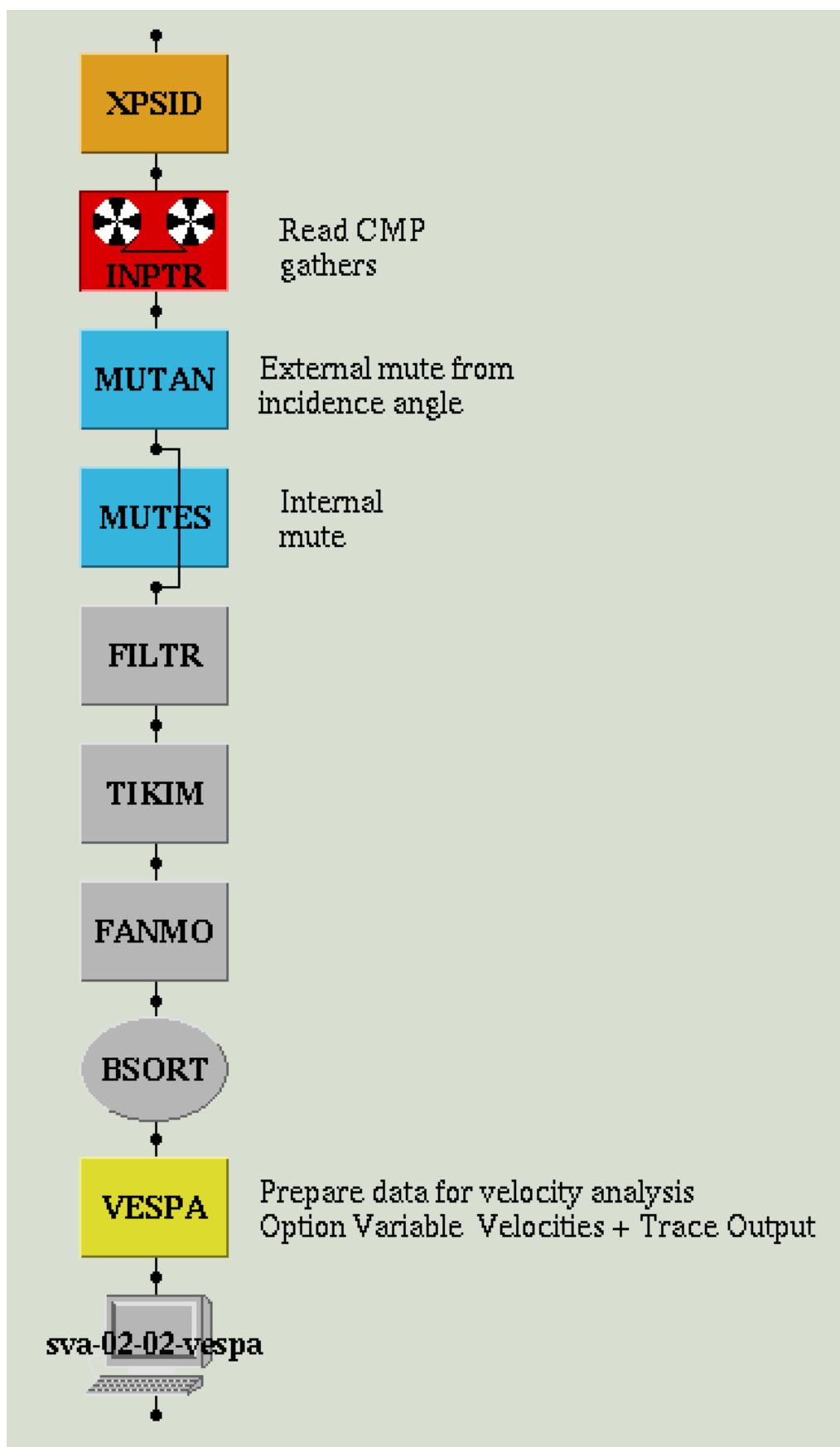
Static correction



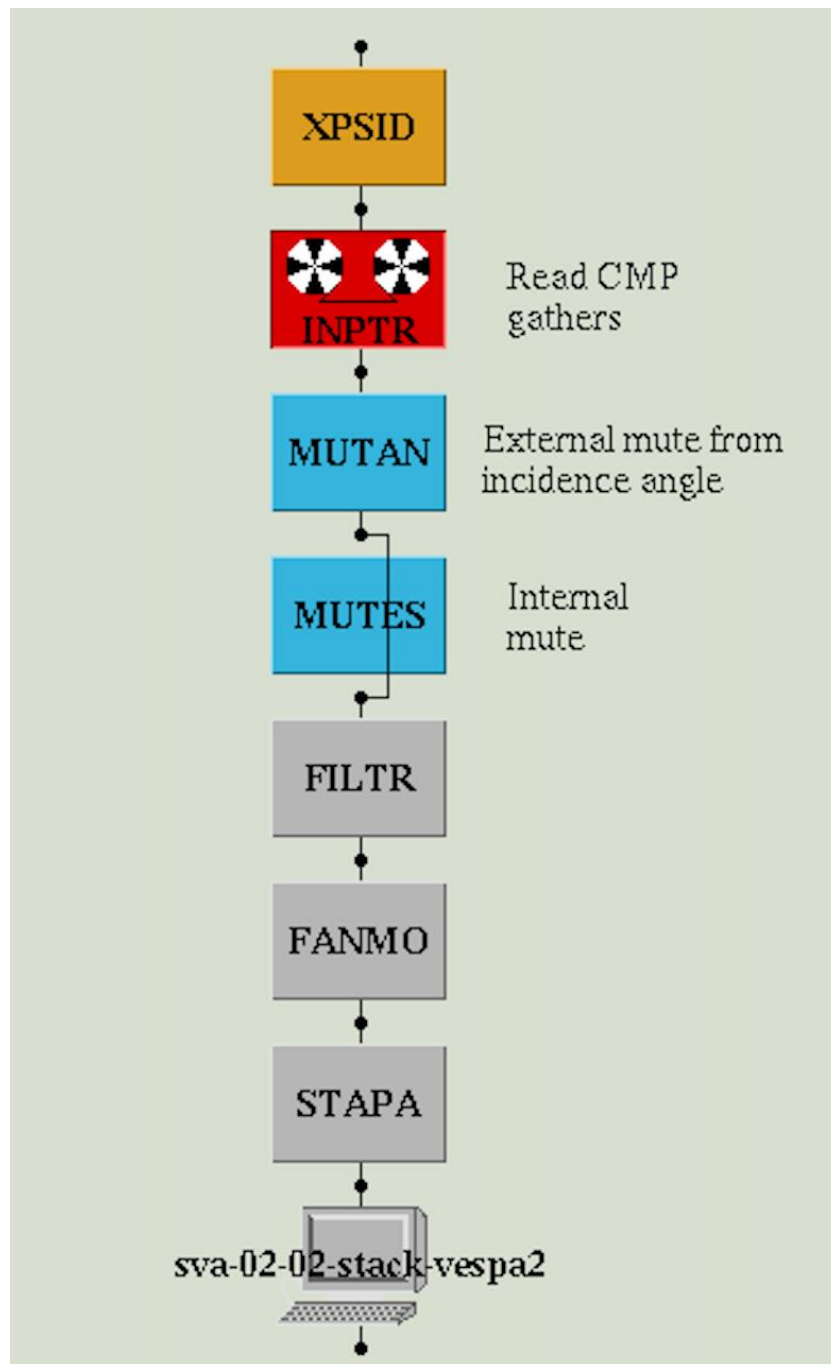
Velocity model



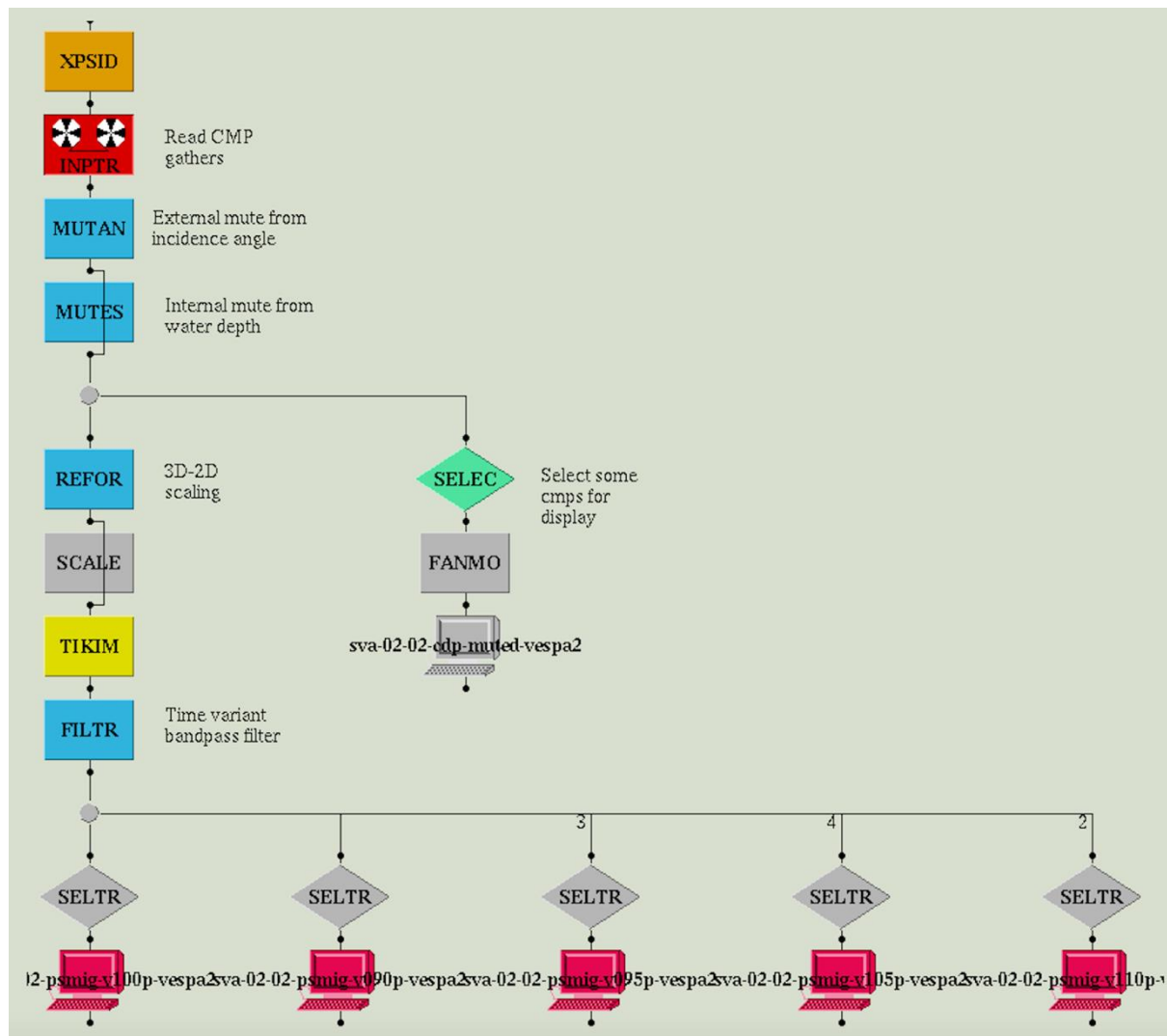
Velocity analysis preparation



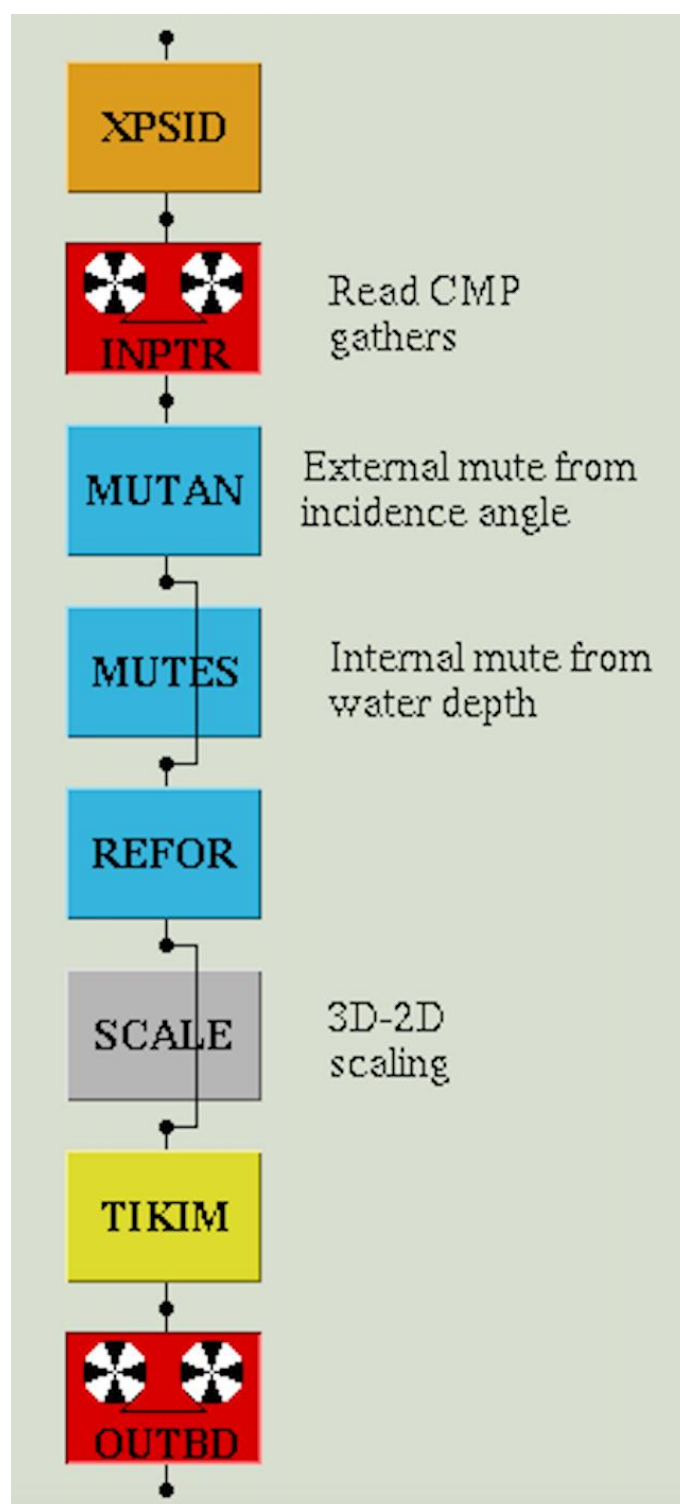
Stacking



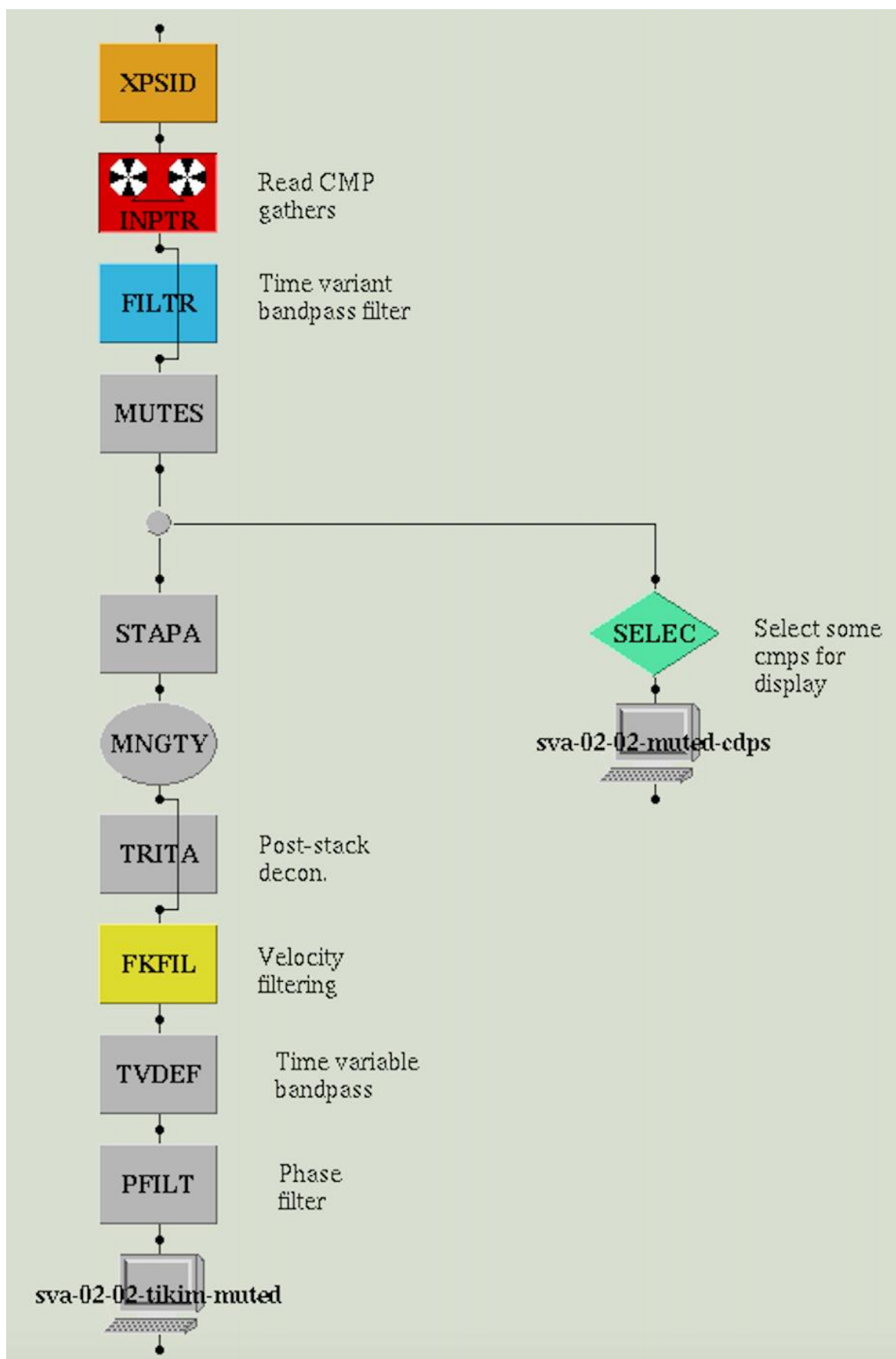
Migration I



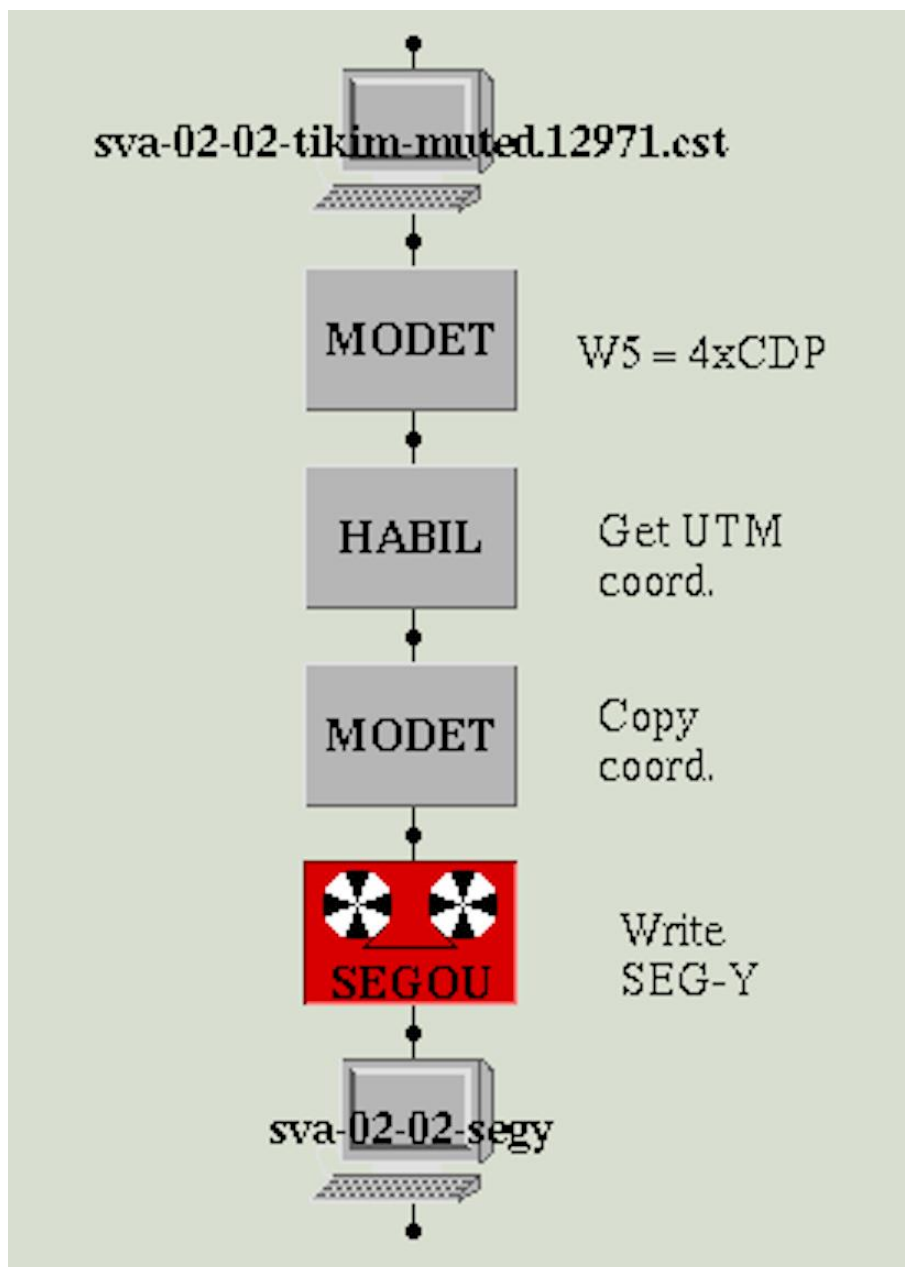
Migration II



Mute with stack



Write SEG-Y

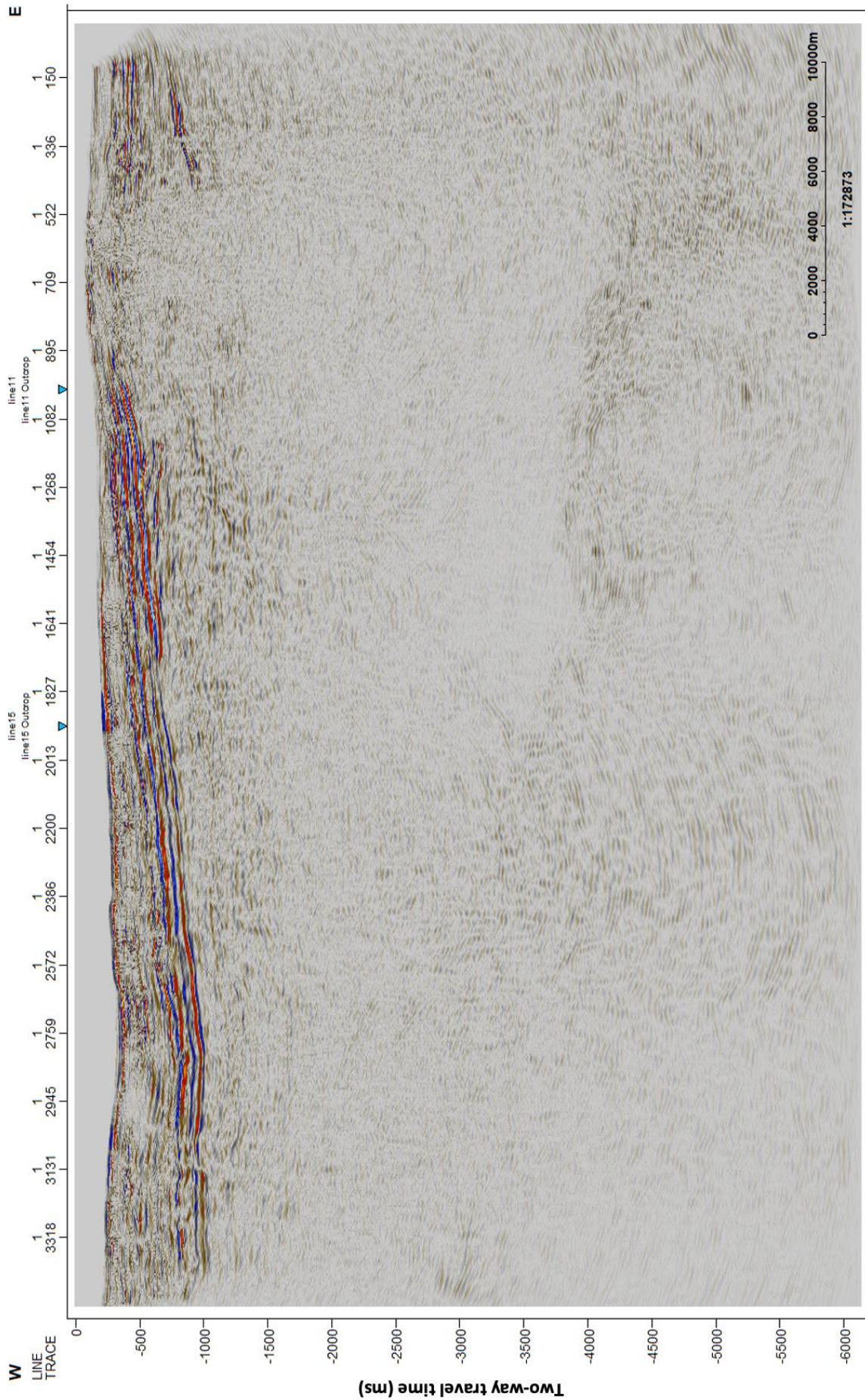


Appendix B

Interpreted lines

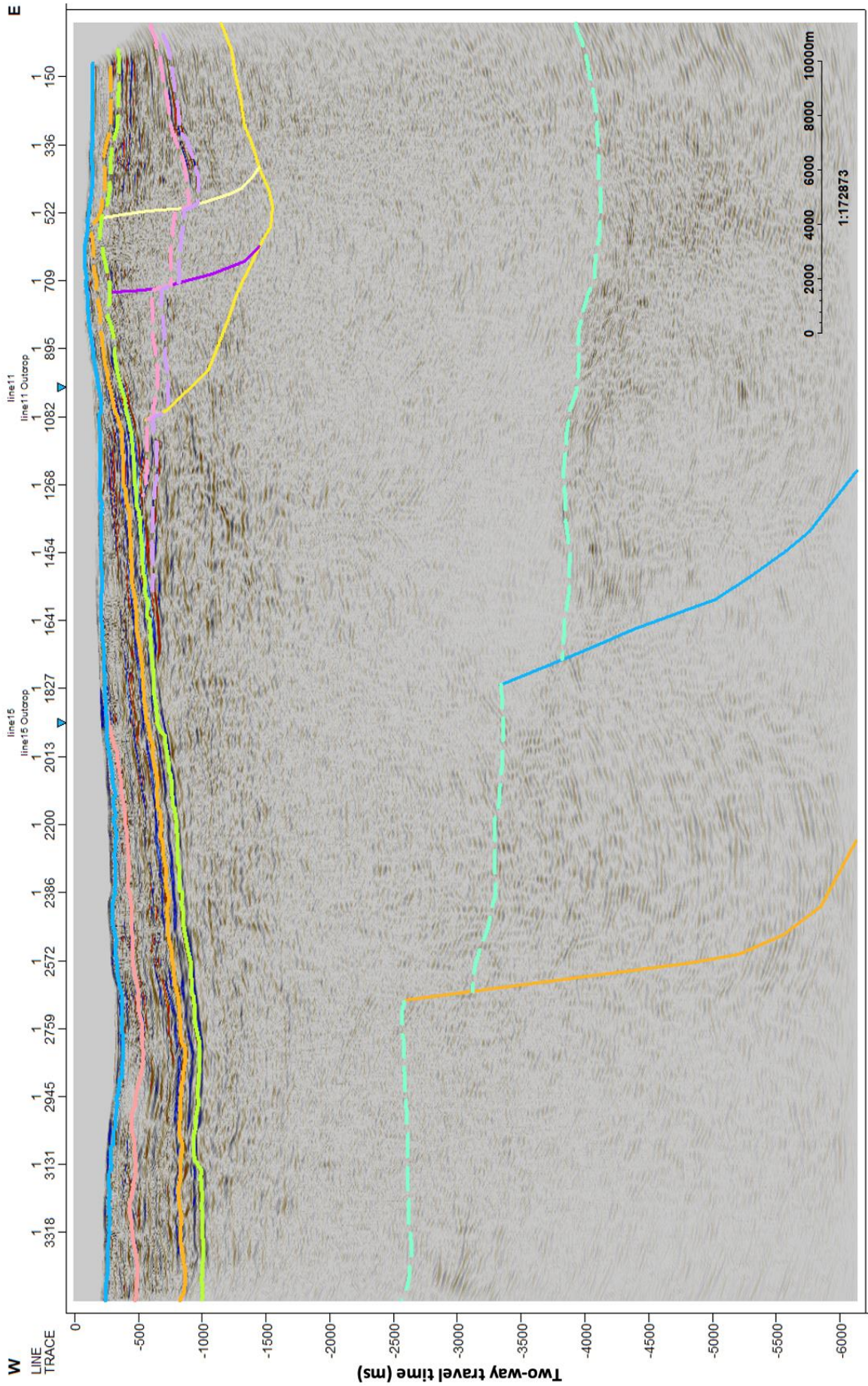
The seismic lines before and after interpretation.

Line 2



W
LINE TRACE
E

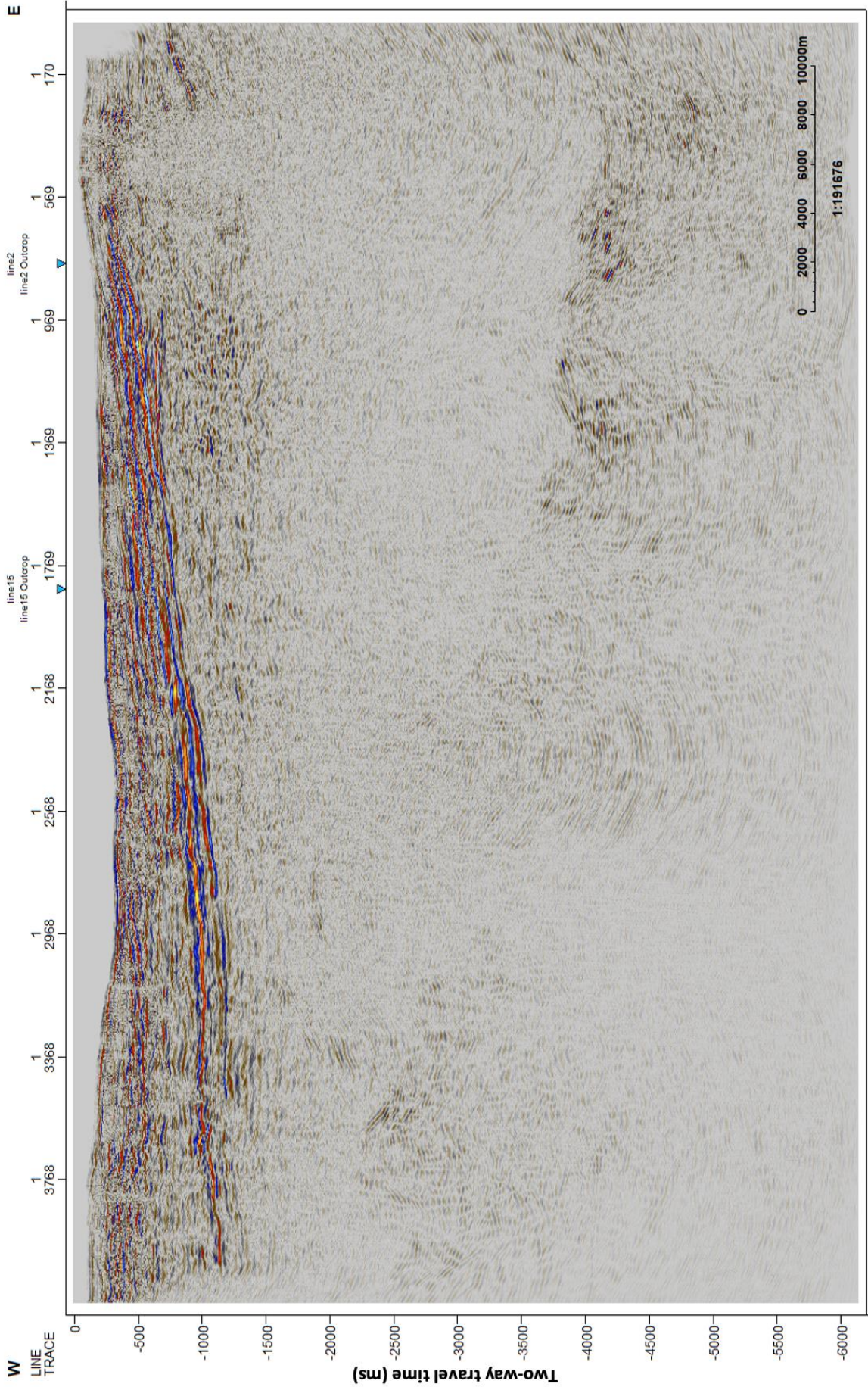
Line 2



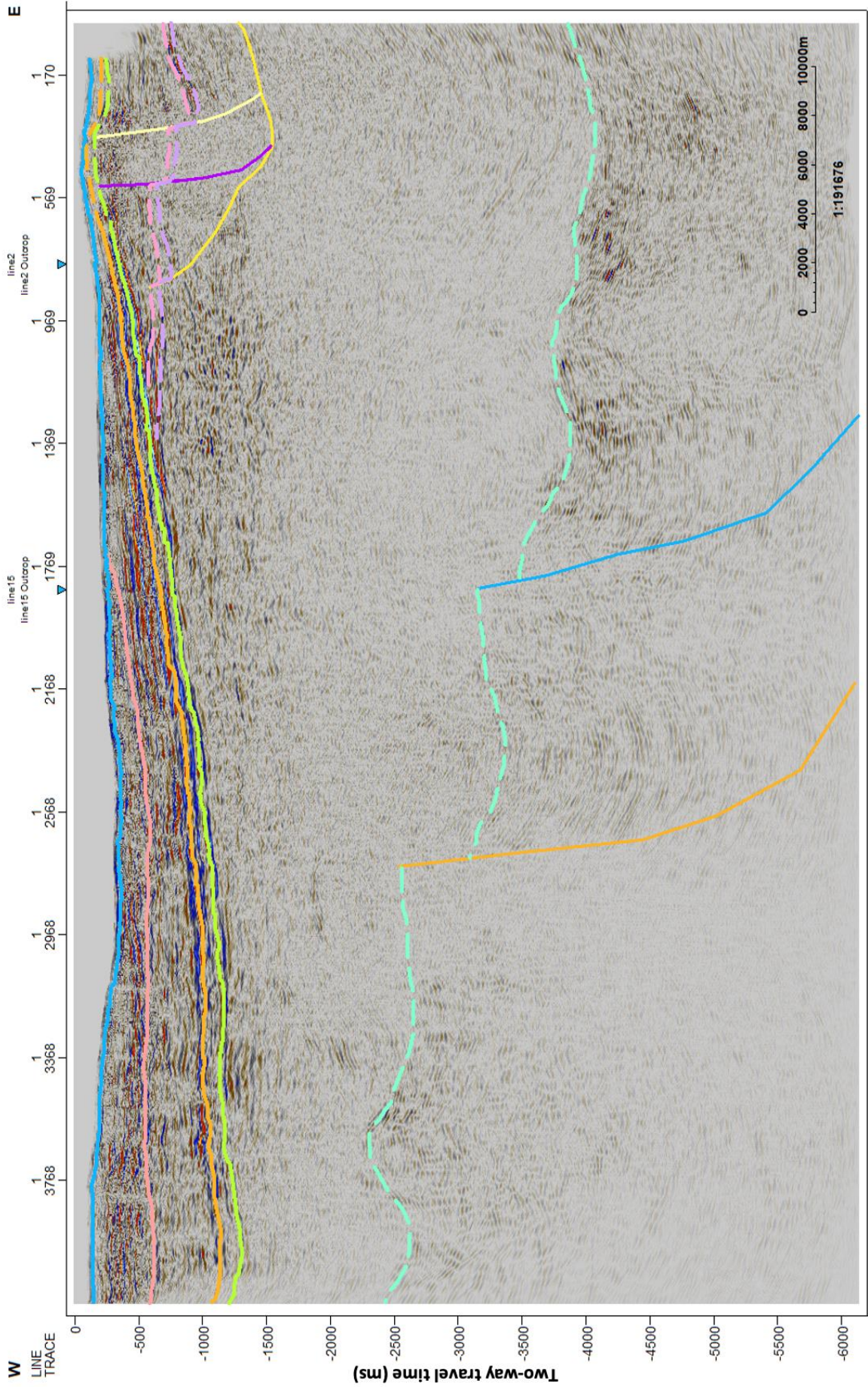
E

W

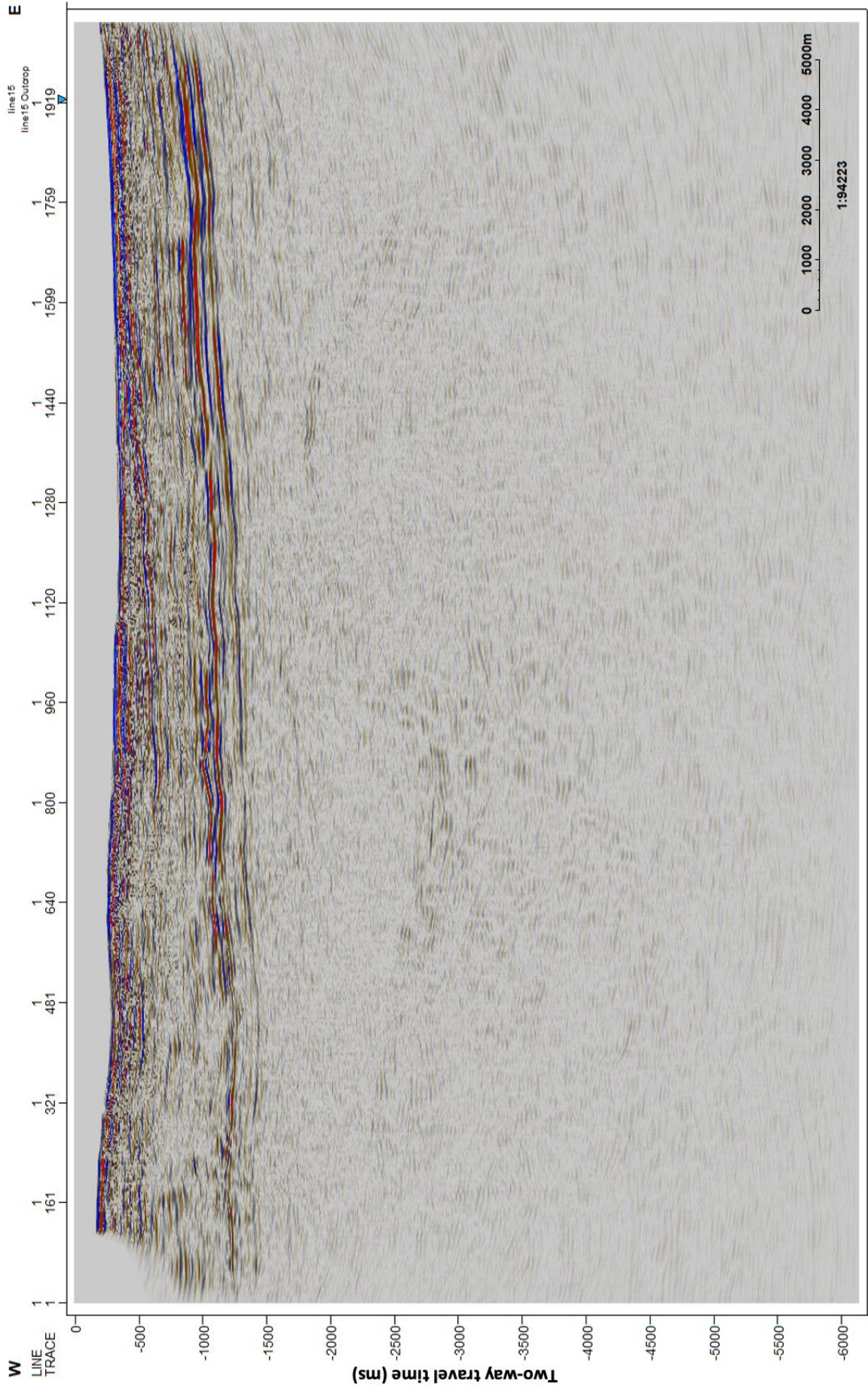
Line 11



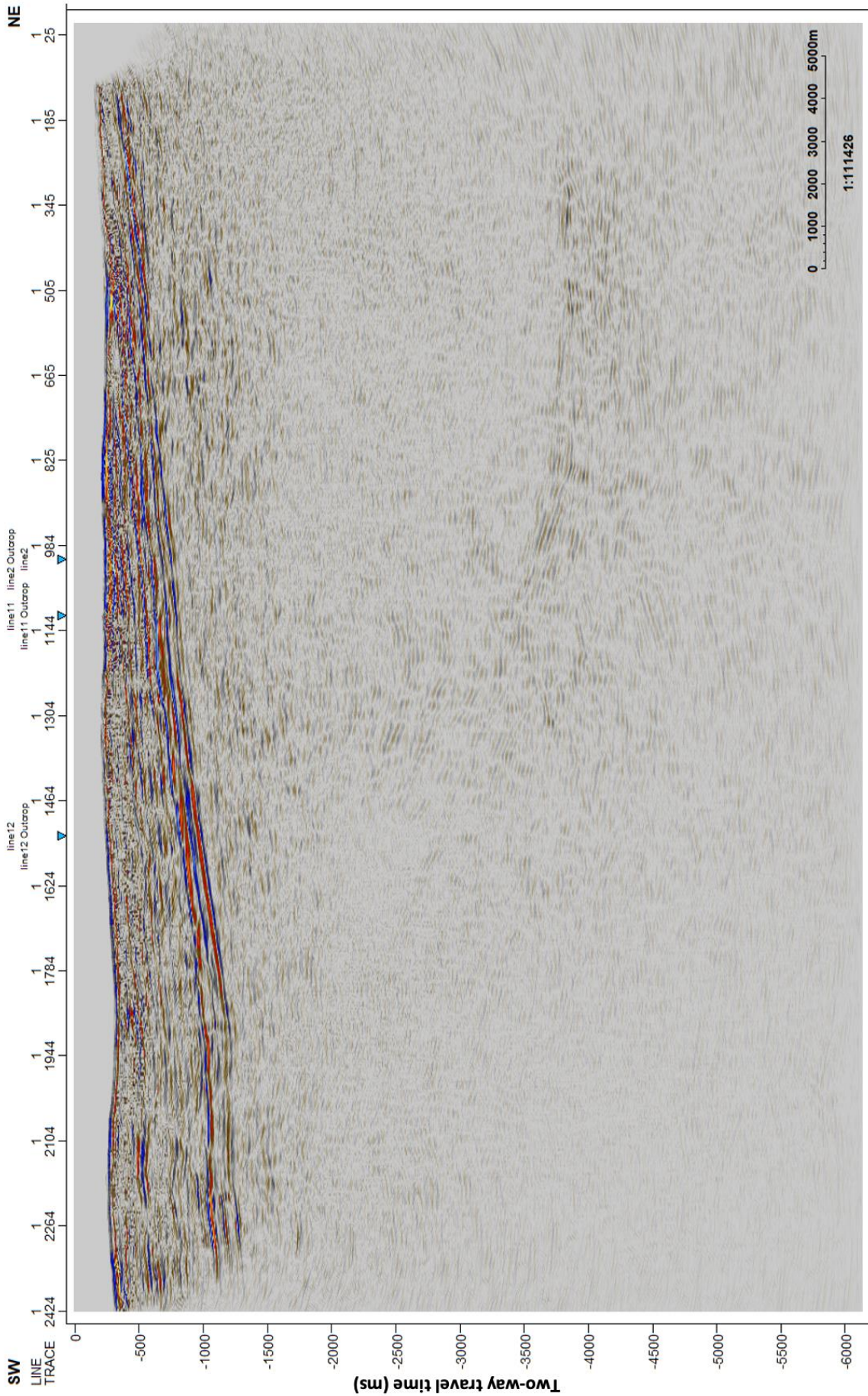
Line 11



Line 12



Line 15



NE

SW

LINE TRACE

1

2424

2264

2104

1944

1784

1624

1464

1304

1144

984

825

665

505

345

185

1

1

1

1

1

1

0

-500

-1000

-1500

-2000

-2500

-3000

-3500

-4000

-4500

-5000

-5500

-6000

Two-way travel time (ms)

0

1000

2000

3000

4000

5000m

1:111426

Line 15

